ANGULAR DISTRIBUTION OF J/PSI DECAYS IN DIMUON CHANNEL IN 800 GEV PROTON-COPPER COLLISIONS

BY

TING-HUA CHANG

A Dissertation submitted to the Graduate School
in partial fulfillment of the requirements
for the Degree
Doctor of Philosophy

Subject: Physics

New Mexico State University
Las Cruces, New Mexico
July 1999

"Angular distribution of J/psi decays in dimuon channel in 800 GeV proton copper collisions," a dissertation prepared by Ting-Hua Chang in partial fulfillment of the requirements for the degree, Doctor of Philosophy, has been approved and accepted by the following:

Timothy J. Pettibone
Dean of the Graduate School

Vassili Papavassiliou
Chair of the Examining Committee

Date

Committee in charge:

Dr. Vassili Papavassiliou, Chair

Dr. Sidney A. Coon

Dr. Gary S. Kyle

Dr. Robert J. Liefield

Dr. Richard L. Long

DEDICATION

To all of you who read this thesis.

ACKNOWLEDGEMENTS

I would like to thank all the members of the FNAL E866/NuSea Collaboration who made this experiment, and hence this thesis, possible.

I would like to thank my thesis advisor Prof. Vassili Papavassiliou for his guidance on my thesis work. Everything I know about QDC is from him. Without his constant help and knowledge, I would have never understood this subject.

I would like to thank Prof. Gary Kyle for his non-stop supporting during the last seven years, financially and personally. I never had to worry about any budget problems on travelling or attending conferences during the time of study. He was also my formal advisor, who introduced me into the career of high energy physics. Without his support, I don't know to where I would have ended up now.

I would like to thank Dr. Thomas Carey. We worked together on E866 DAQ upgrade project at LANL for more than a year. He has taught me so many special skills about hardware electronics and software coding which are nowhere to learn in campus. He is a great teacher and I enjoyed the time we spent together very much.

I would like to thank Dr. Patrick McGaughey and Dr. Chuck Brown, for their work on the angular distribution analysis. They have provided me with many valuable suggestions and ideas. Especially for Dr. Patrick McGaughey for his deep physics insight on this subject, I have gained a lot.

I would like to thank Dr. Mike Leitch and Dr. Paul Reimer, who maintained the analysis and Monte Carlo code. Without their efforts, the data analysis would be impossible.

I would like to thank Prof. Carl Gagliardi and Dr. Don Geesaman, for their careful reading of my thesis draft and giving critical comments.

I would like to give thanks to the following list of people, for their help in many ways during the past days: Jim Bread, Siguud and Ingrid Smitz, Bob and Rona Paz, Ho-Fu and Lily Dai, Paul and Lily Horng, Job and Grace Lee, John Powell, Ron and May Guo, Prof. Twan-Wu Chen, and Jason Webb.

I would like to give special thanks to my parents Zhe-Yu and Pi-Tao Chang for their spiritual and financial support.

Last but not least, I would like to thank my loving wife Yan, for her patient and constant encouragement. She is the behind-unseen author of this thesis.

VITA

September 28th, 1967–Born in Changhua, Taiwan

1989–B.S., Tunghai University, Taichung, Taiwan

1991–M.S., New Mexico State University, Las Cruces, New Mexico

PUBLICATIONS

Pion-induced nucleon knockout from a polarized ^7Li *target*, M.G. Khayat *et al.*, Bull. Am. Phys. Soc. **39**, 1146 (1994).

π^-*-induced single charge exchange on polarized* ^3He, Q. Zhao *et al.*, Bull. Am. Phys. Soc. **40**, 963 (1995).

Analyzing powers for polarized $^1H(\pi^+, \pi^- p)$ *at* T_π *= 165 MeV and 240 MeV*, B. A. Raue *et al.*, Phys. Rev. **C53**, 1005 (1996).

Anti-D/Anti-U asymmetry and the origin of the nucleon sea, FNAL E866/NuSea Collaboration, J. C. Peng *et al.*, Phys. Rev. **D58**, 2004 (1998).

Measurement of the light anti-quark flavor asymmetry in the nucleon sea, FNAL E866/NuSea Collaboration, E. A. Hawker *et al.*, Phys. Rev. Lett. **80**, 3715 (1998).

Measurement of J/ψ *decay angular distribution in dilepton channel in 800 GeV p+Cu collisions*, to be published.

FIELD OF STUDY

Major Field: Physics

Minor Field: Chemical Engineering

ABSTRACT

ANGULAR DISTRIBUTION OF J/PSI DECAYS IN DIMUON CHANNEL IN 800 GEV PROTON-COPPER COLLISIONS

BY

TING-HUA CHANG

Doctor of Philosophy in Physics

New Mexico State University

Las Cruces, New Mexico, 1999

Dr. Vassili Papavassiliou, Chair

The angular distribution of J/ψ decays in the $\mu^+\mu^-$ channel in 800 GeV proton-copper collisions has been measured for $x_F > 0.25$. The polarization parameter λ is extracted in 1 GeV of p_T and 0.1 of x_F bins for two magnet configurations with different acceptances. The data indicate that the J/ψ's are produced with a slight transverse polarization at small x_F, which turns to longitudinal at $x_f > 0.6$. No p_T dependence of λ is observed. Theoretical calculations are needed in order to interpret the measurements.

TABLE OF CONTENTS

LIST OF TABLES

LIST OF FIGURES

1. INTRODUCTION

Since the 1970s the Standard Model has provided a satisfactory description of the interactions of all known elementary particles. The underlying theory for describing the electromagnetic force in the sub-atomic world is known as Quantum Electrodynamics (QED), while Quantum Chromodynamics (QCD) describes the strong force. QED has been tested to be a valid theory by its amazing predictions of the lepton magnetic moments and atomic energy spectra. But unlike QED, even though QCD was developed following the same fundamental idea of gauge invariance and seems to be a straightforward extension of QED, QCD is facing the difficulties associated with non-perturbative calculations in the low-energy regime. After decades of effort physicists have developed techniques, such as renormalization and resummation, as well as non-perturbative ones, such as effective theories, to help solve some of the mathematical difficulties. And nowadays we are able to compare many experimental results with QCD predictions, and indeed QCD has proved to be the best candidate theory for describing the strong interaction.

There are many successful examples of QCD. The earliest and most profound one is the prediction of the evolution of the structure functions in Deep Inelastic Scattering (DIS). Given the quark and gluon distributions at a fixed energy-momentum transfer Q_0^2, QCD can actually predict the nucleon structure functions at arbitrary Q^2 using the Evolution Equations [Pic 95]. Later in collider experiments, Next-to-Leading Order (NLO) QCD calculations predicted the inclusive jet-production cross section over several orders of magnitude and over a wide range of center-of-mass (COM) energy and jet transverse momentum [Arn 86, Ali 91, Abe 93] using the Parton Distribution Functions (PDFs) extracted from the DIS data. Another example is the Drell-Yan process [Dre 70]. The Drell-Yan process, massive lepton-pair production via electroweak quark-antiquark annihilation into vector bosons (photon, $W^{\pm}$, or Z) and then decay, is one of the few processes which have been calculated up to next-to-next-to-leading order (NNLO) in perturbative QCD. A recent calculation [Rij 95] including some of the NNLO terms has shown a good agreement with the data. Another example is the inclusive heavy quark production. Fixed-target studies of heavy-flavor production have provided a wealth of data. Total cross sections, single-inclusive distributions, correlations between the quark and the antiquark have been measured in both hadro- and photoproduction. All experimental results are in qualitative agreement with perturbative QCD calculations. A detailed comparison of the fixed-target data and NLO QCD predictions can be found in [Fri 97].

Throughout the entire thesis the following symbols are used to describe the kinematic variables:

S: center-of-mass energy of the beam-target system.

m: rest mass of the dimuon pair.

p_T: transverse momentum of the dimuon pair.

x_F: dimensionless longitudinal momentum of the dimuon pair. It is defined as the pair longitudinal momentum P_L divided by its maximum kinematically allowed value $P_{L,max}$ in the beam-target COM frame. It relates to the Bjorken x, the fraction of the hadron momentum carried by the parton in the hadron boosted to the infinite-momentum frame, of the beam parton x_1 and of the target parton x_2 by $x_F(1 - m^2/S) = x_1 - x_2$.

θ and ϕ: polar and azimuthal angles of the dimuon pair; described in section 1.2.3.

1.1 Failure of Perturbative QCD in Charmonium Production

While QCD has provided successful descriptions of many aspects of the experimental data, there are still some phenomena which could not be described. The production of charmonium at large transverse momentum is one of such processes: the observed production cross sections have differed from QCD predictions by more than an order of magnitude, even though in [Fri 97] it has been shown that the charm production total cross section can be calculated from QCD. This discrepancy between experiment and theory has revealed a more complicated picture for heavy quarkonium production.

Quarkonium production was conventionally calculated based on the color-singlet model (CSM) before 1993. However this model has failed to describe charmonium-hadroproduction data [Sch 94]. In hadroproduction of charmonium at fixed target energy, $\sqrt{S} < 50$ GeV, the ratio of the number of J/Ψ's produced directly to those arising from decays of higher charmonium states is under-

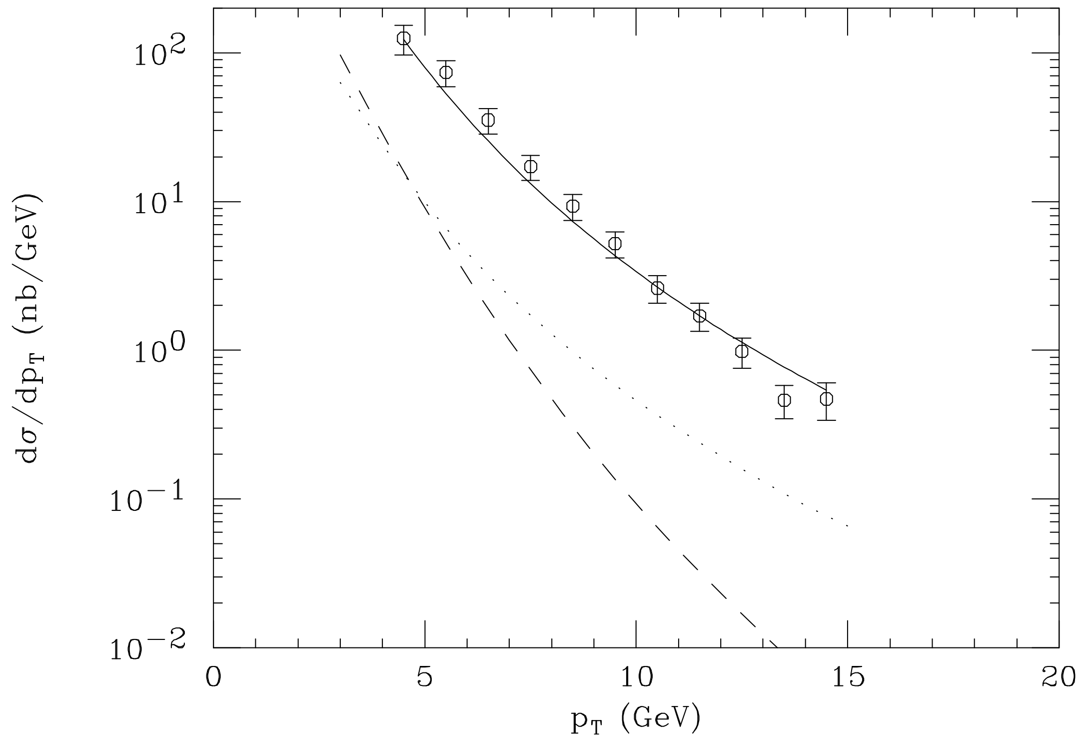

Figure 1.1: CDF data on the differential cross section for prompt ψ's. The curves are the LO predictions of the color-singlet model (dashed curve), predictions including fragmentation in the color-singlet model (dotted curve), and including contributions from gluon fragmentation via the color-octet mechanism (solid curve) with the normalization adjusted to fit the CDF data. (Taken from [Bra 96])

predicted by at least a factor of five [Van 95]. At Tevatron collider energies, the excess of direct ψ' production compared to the CSM prediction is a factor of 30 [Bra 94, Roy 94]. This excess has been referred to as the ψ'-anomaly. Figure 1.1 compares the CDF ψ' data and some theoretical predictions. Figure 1.2 shows the comparison with the fixed-target data.

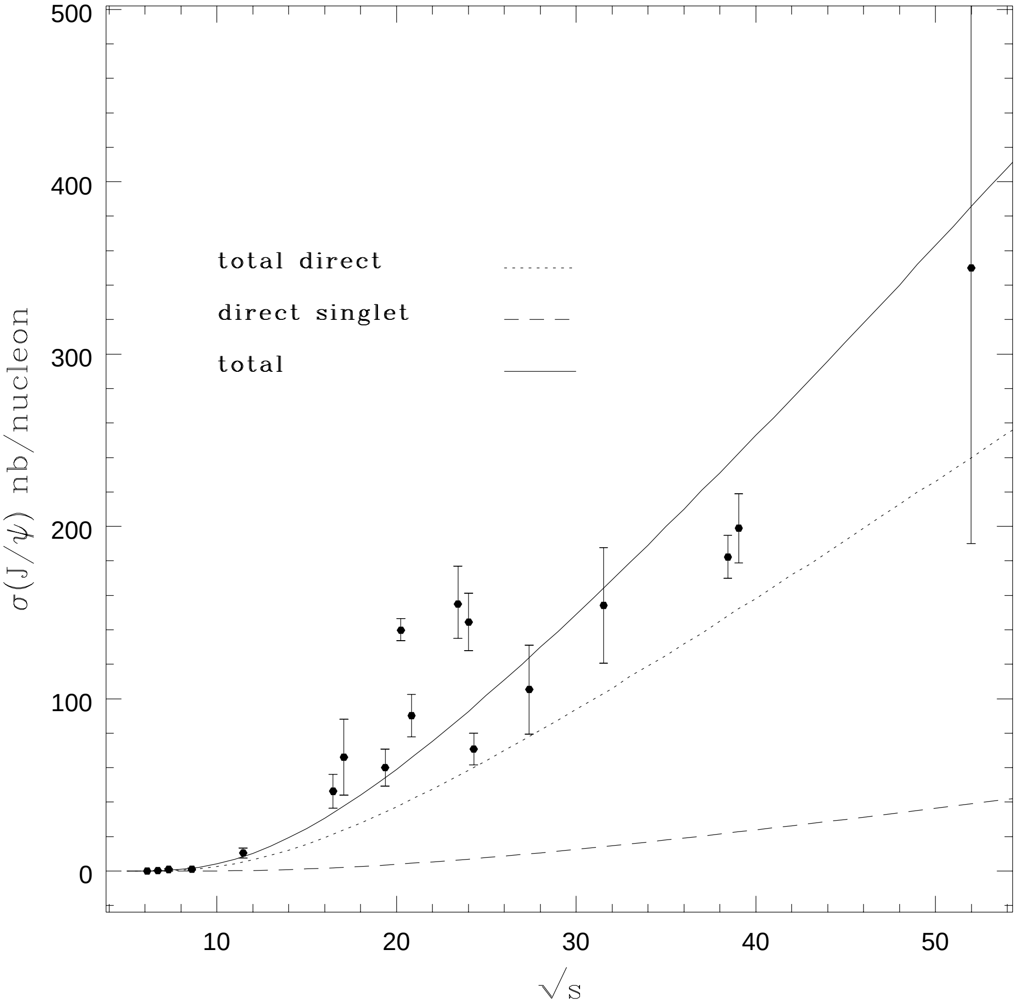

Figure 1.2: J/ψ production cross section ($x_F > 0$) in proton-nucleon collisions. Solid line: Fit to the total cross section including radiative feed-down from the χ_c states and ψ'. Dashed line: Direct J/ψ cross section. Dotted line: Direct J/ψ production, color-singlet only. (Taken from [Bnk 97])

1.2 Developments of Theoretical Models

Data from the Tevatron have revealed that the production rate of ψ' at large transverse momentum is more than an order of magnitude larger than the early theoretical predictions. These results can be understood by taking into account two more mechanisms. The first is the realization that fragmentation must dominate at large transverse momentum, which implies that most charmonium in the large p_T region is produced by the hadronization of individual high-p_T partons. The second is the development of a factorization formalism for quarkonium production based on non-relativistic QCD (NRQCD) that allows the formation of charmonium from color-octet $c\bar{c}$ pairs to be treated systematically. In this section we will summarize these theoretical developments. A more complete review of the development was given by Braaten et al. [Bra 96].

1.2.1 Color Singlet Model

A thorough review of the applications of the color-singlet model to heavy-quarkonium production was given by Schuler [Sch 94]. To describe the color-singlet model, we can think of the production of charmonium as proceeding in two steps. The first step is the production of a $c\bar{c}$ pair, and the second step is the binding of the $c\bar{c}$ pair into a charmonium state.

We first consider the production of the $c\bar{c}$ pair. The $c\bar{c}$ pair must be produced with relative momentum that is small compared to the mass of the charm quark in order to have a significant probability to be bound together. Assuming that the c and $\overline{c}$ do not exist in the initial state, the production of a $c\overline{c}$ pair must involve virtual particles which are off-shell by amounts of order m_c or larger. This part of the amplitude is called the short-distance part, because the spatial separation of the c and $\overline{c}$ is of order $1/m_c$ or smaller. On the other side, the formation of the bound state is considered to be the long-distance part of the amplitude. The total amplitude of charmonium production is expected to be dependent on the charmonium state H and on the quantum numbers of the $c\overline{c}$ bound pair.

For any charmonium state, the dominant Fock state is a color-singlet $c\overline{c}$ pair in a definite angular-momentum state. We introduce the following notation, for example, the dominant Fock state for the J/ψ is $|c\overline{c}(\underline{1},{}^3S_1)\rangle$, while for the χ_{cJ} it is $|c\overline{c}(\underline{1},{}^3P_J)\rangle$. The color states are denoted by $\underline{1}$ for color-singlet and $\underline{8}$ for color-octet, and the angular momentum states are denoted using the standard spectroscopic notation ${}^{2S+1}L_J$. The color-singlet model requires that, only the $c\overline{c}$ pair in a color-singlet ${}^{2S+1}L_J$ state can bind to form the charmonium with $|c\overline{c}(1^{2S+1}_{,}L_J)\rangle$ as the final Fock state.

The color-singlet model has enormous predictive power. The cross section for producing a quarkonium state is predicted in terms of a single nonperturbative parameter for each orbital angular momentum multiplet. The amplitude for producing a color-singlet $c\overline{c}$ pair with small relative momentum (the short distance part) can be calculated using perturbative QCD, while the long-distance part parameters can be determined from experiments and are expected to be process-independent. Thus the long-distance parameters determined from decays of the charmonium states can be used to predict the normalized production rate of charmonium states.

We should keep in mind that the color-singlet model is only a model. The most basic assumption, the factorization picture, has never been proven to be correct, and the relativistic corrections which account for the relative velocity of the quark and antiquark are neglected. The color-singlet model also assumes that a $c\overline{c}$ pair produced in a color-octet state will never form the final charmonium. However it might be possible that a color-octet $c\overline{c}$ pair can transit to a color-singlet state by radiating soft gluons. We will include the color-octet mechanism in the coming section.

1.2.2 Gluon Fragmentation

The first major conceptual advance in recent theoretical developments of quarkonium production was the idea of "fragmentation." Fragmentation is the formation of a hadron within a jet produced by a parton with large transverse momentum. But here this term is used to include general hadronization processes.

The real revolution about the fragmentation mechanism is the realization that a colored parton, generally a gluon, can result in a color-singlet final state via soft-gluon emissions. This possibility was not considered in the conventional wisdom. Once it was accepted, the color-octet $c\overline{c}$ state could also result in the color-singlet final quarkonium by the same argument, and thus the contributions from color-octet components become possible, as opposed to the color-singlet model.

When the CSM includes the contributions from gluon-fragmentation, its prediction qualitatively agrees with the shape of the CDF ψ' data, but is still off in normalization by an order of magnitude, in the ψ' p_T differential cross section. The prediction from the CSM failed completely in the high p_T region without including the gluon-fragmentation mechanism [Bra 95]. Figure 1.1 shows the predictions and data.

1.2.3 Color-Octet Mechanism

The second major conceptual advance is to realize that the color-octet mechanism can be important. Contrary to the basic assumption of the color-singlet model, a $c\bar{c}$ pair that is produced in a color-octet state can bind to form the charmonium final state.

By including the contribution from the color-octet object in the matrix element, one can make the prediction agree well with the experimental data by leaving the relative size of the color-octet contribution as an adjustable parameter. Its verification now requires considering quarkonium production in other processes in order to demonstrate process-independence of the long-distance part of the color-octet matrix element. Now the data available from different processes are CDF data, fixed-target data, and photo-production data. The size of color-

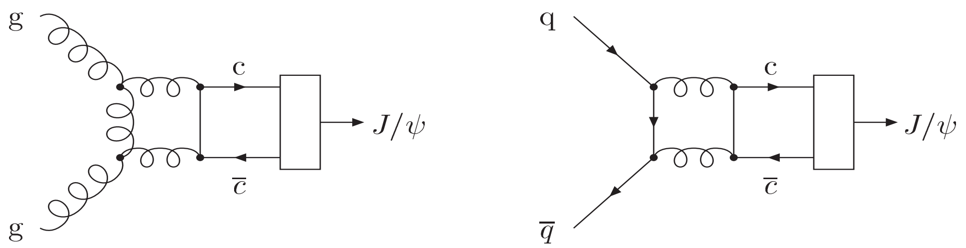

(a) Color-Singlet Feynman Diagrams

(b) Gluon-Fragmentation diagram
(for high p_T gluons only)

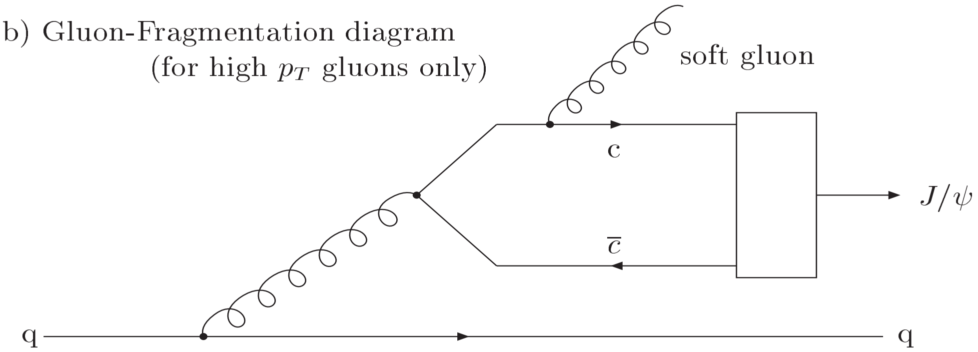

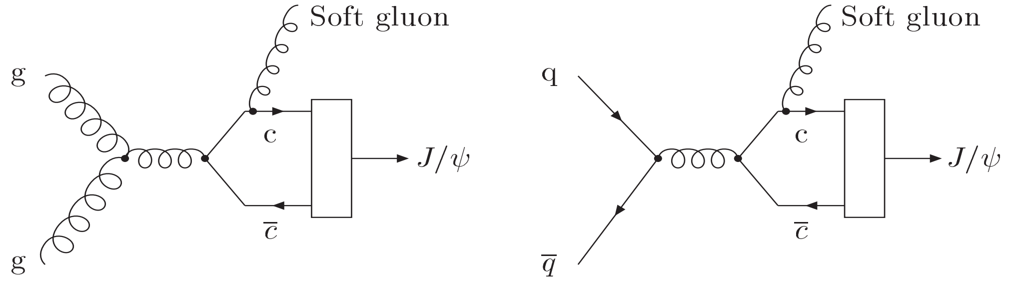

(c) Color-Octet Feynman Diagrams

Figure 1.3: Feynman diagrams of J/ψ production mechanisms. (a) Color-Singlet mechanism, (b) Gluon fragmentation, (c) Color-Octet mechanism.

octet contributions from these data are not obviously in agreement with each other and more sophisticated explanations are needed.

Other problems associated with the color-octet mechanism are the discrepancies with the χ_{c1}/χ_{c2} production ratio and the $J/\psi(\psi')$ polarization: the χ_{c1}/χ_{c2} production ratio remains almost an order of magnitude too low, and the predicted transverse polarization of the J/ψ and ψ' is too large compared to the existing pion data in fixed-target experiments [Ben 96]. All of these suggest that higher-twist effects may be substantial even after including the octet mechanism.

A polarization measurement is a crucial test for the color-octet mechanism. Since the octet production matrix elements of NRQCD lead to a polarization pattern different from the CSM, a polarization measurement can provide us with significant information on quarkonium production. For example, J/ψ's produced at the Tevatron at large p_T are predicted to be almost fully transversely polarized, i.e. $\lambda(J/\psi) \sim 1$ [Cho 95], as a result of production via gluon fragmentation. At smaller p_T, the J/ψ's are predicted to be produced essentially unpolarized around $p_T \sim 5$ Gev [Ben 97]. The observation of this polarization pattern would test the underlying theory (the Factorization Approach). To limit the introduction, we will concentrate our attention on fixed-target experiments from now on since FNAL E866 is a fixed-target experiment.

The polarization of the quarkonium, measured by analyzing the angular distribution of the quarkonium decay products in its rest frame, is of the form

$$d\sigma/d\cos\theta \sim 1 + \lambda \cos^2\theta \tag{1.1}$$

where θ is the polar angle measured in the rest frame of the quarkonium. The quarkonium rest frame is well specified except for arbitrary three-dimensional rotations. The Collins-Soper frame [Col 77], in which the Z-axis is defined to be parallel to the bisector of the angle between the directions of the interacting hadrons in the quarkonium rest frame, is used in this analysis. In all other earlier fixed-target experiments the Gottfried-Jackson frame, in which the Z-axis is defined to be parallel to the incoming beam axis in the quarkonium rest frame, was used. These two frames are equivalent if the quarkonium has zero p_T [Fal 86]. For the p_T range of fixed-target experiments, of the order of 1 GeV, compared to hundreds of GeV of longitudinal momentum, the two frames are approximately the same [Gee 98].

1.3 Fixed-Target Polarization Experiments and Predictions

Polarization measurements have been performed for J/ψ and ψ' production in pion and proton scattering fixed-target experiments. From a theoretical point of view, the ψ' decay has been more extensively studied because all the ψ' data samples are direct ψ's. The observed value of λ for ψ' is 0.02 ± 0.14, measured at $\sqrt{s} = 21.8$ GeV in the region $x_F > 0.25$ by Heinrich et al. [Hei 91]. When studying the polarization of the J/ψ decay one has to take the polarization inherited from decays of the higher charmonium states χ_{cJ} and ψ' into account and this leaves some ambiguity in the interpretation of the results. In the following sections we will only review J/ψ polarization experiments to compare with the E866 results.

1.3.1 Model Predictions of Polarization at Fixed-Target Energies

1.3.1.a Color-Singlet Model

The polarization of J/ψ has been calculated from perturbative QCD by Vanttinen et al. [Van 95]. The parameter λ in Equation 1.1 was calculated from the $c\bar{c}$ production amplitude and the electric dipole approximation of radiative χ decays.

Figure 1.4a shows the predicted values of the parameter λ in Equation 1.1 in the Gottfried-Jackson frame as a function of x_F, for the direct J/ψ and the $\chi_{1,2} \rightarrow J/\psi + \gamma$ processes separately. The dashed lines indicate the effect of a Gaussian smearing in the transverse momentum of the beam partons. The overall $\lambda(x_F)$ including direct and indirect J/ψ processes is shown in Figure 1.4b and compared with the Chicago-Iowa-Princeton [Bii 87] and E537 data [Ake 93]. The QCD calculation gives $\lambda \sim 0.5$ for $x_F < 0.6$, significantly larger than the measured value. The lower curve in Figure 1.4b shows the effect of multiplying the partial J/ψ cross section with the K-factors obtained from experiments. The discrepancies between the calculated and measured values of λ suggest that the

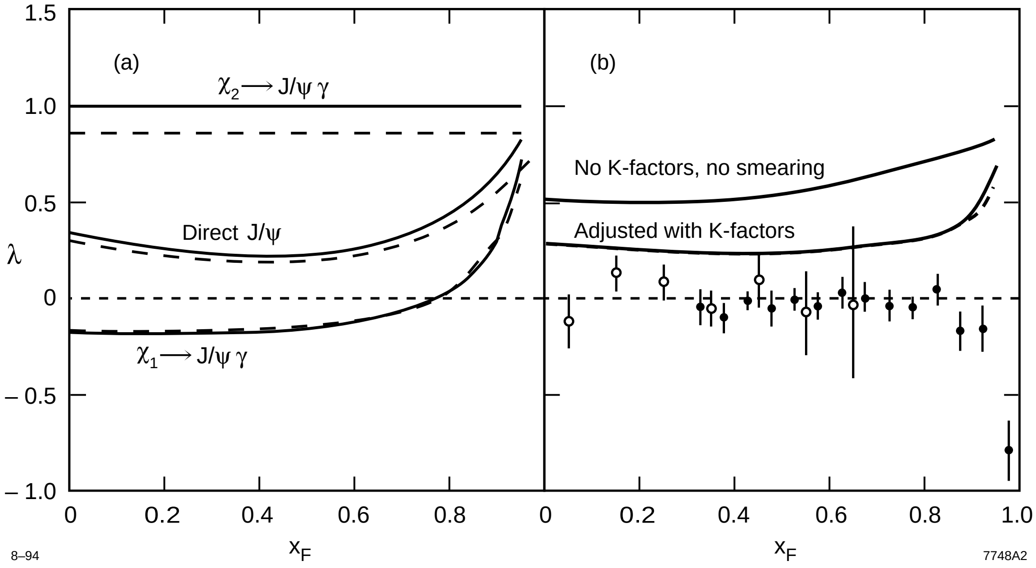

Figure 1.4: Leading-twist predictions of $\lambda(x_F)$ in πN collisions. The beam energy $E_{lab} = 300$ GeV. (a)The three solid curves show the decay distributions of J/ψ's produced via radiative decays of the χ_2 and χ_1 states and "directly" in gluon fusion. The dashed curves show the effect of smearing the transverse momentum distribution of the beam parton by a Gaussian function exp[-$(k_\perp/500\text{ MeV})^2$]. (b)The combined decay distribution of all J/ψ's, including contributions from $\chi_{1,2}$ decays and direct production, is shown here. The lower curve shows the effect of adjusting the relative normalization of the different contributions to their measured values by appropriate K-factors. The dashed curve shows the effect of transverse-momentum smearing and K-factors adjustments. The data are from the Chicago-Iowa-Princeton (full circles) and E537 (open circles) experiments. (Taken from [Van 95]).

leading-twist processes considered in the calculation are not adequate for explaining charmonium production.

1.3.1.b Color-Evaporation Model

The color-evaporation model [Fri 77, Hal 77] assumes that the $c\overline{c}$ pair in $^3S_1$ state can transit to $^1S_0$ state via soft gluon emission, so J/ψ is always produced unpolarized. In this model the color and spin quantum numbers of the $c\overline{c}$ pair are irrelevant. The fraction of the $c\overline{c}$ pairs bound into J/ψ is described by a phenomenological parameter $f_{J/\psi}$.

The color-evaporation model is considered to be an over-simplified model, because it is not concerned with the details of the particles which initiate the reaction. The evident failure is the prediction of the fraction of J/ψ coming from χ_c decays. According to the color-evaporation model, the fraction of J/ψ coming from χ_c decays should be process-independent. But the experimental data both in fixed-target experiments in pN and πN collisions and also in $p\overline{p}$ collisions at the Tevatron gather around a central value of 0.3-0.4, while in γ-p collisions an upper limit of 0.08 was obtained [Bar 87].

Since this model gives trivial prediction on J/ψ polarization and fails in predicting ratios of quarkonium production, we will not discuss this model in later discussions.

1.3.1.c Non-Relativistic QCD

The polarization of J/ψ has been calculated in non-relativistic QCD by Beneke and Rothstein [Ben 96]. The production cross section for a quarkonium state H in the process

$$A + B \longrightarrow H + X \tag{1.2}$$

can be written as

$$\sigma_H = \sum_{i,j} \int_0^1 dx_1 dx_2 f_{i/A}(x_1) f_{j/B}(x_2) \hat{\sigma}(ij \to H) \tag{1.3}$$

$$\hat{\sigma}(ij \to H) = \sum_n C^{ij}_{\overline{Q}Q[n]} \langle O^H_n \rangle \tag{1.4}$$

In Equation 1.3 the summation sums up the contributions by all partons in the colliding hadrons, and the $f_{i/A}$ and $f_{j/B}$ are the corresponding parton distribution functions (PDF). The coefficients $C^{ij}_{\overline{Q}Q[n]}$ in Equation 1.4 describe the production of a quark-antiquark pair in a state n and have expansions in $\alpha_s(2m_Q)$. The parameters $\langle O^H_n \rangle$ describe the subsequent hadronization of the $Q\overline{Q}$ pair into the quarkonium state H. It is important to test the universality of the production matrix elements $\langle O^H_n \rangle$ because this is an essential prediction of the factorization formula (1.4).

In the calculation of Beneke and Rothstein, the following intermediate $c\overline{c}$ states are considered: $(\underline{1}, {}^3S_1)$, $(\underline{8}, {}^1S_0)$, $(\underline{8}, {}^3P_J)$, and $(\underline{8}, {}^3S_1)$. For each intermediate state the ratios of longitudinal to transverse polarized quarkonia were computed. To obtain the total polarization, the various subprocesses have to be weighted by their partial cross sections. Weighting all subprocesses by their partial cross sections and neglecting the small ψ' feed-down, a sizable polarization is obtained:

$$0.31 < \lambda < 0.63$$

However the existing data show no sign of polarization. Thus NRQCD including the color-octet contributions also gives a wrong prediction on the J/ψ polarization problem, and one has to seek for explanations from higher-twist processes.

1.3.2 Fixed-Target J/ψ Polarization Experiments

1.3.2.a E537

Fermilab experiment E537 has measured the differential cross section $d\sigma/d\cos\theta$ for J/ψ production in π^-N interactions and in $\overline{p}$N interactions at $\sqrt{S} = 15.3$ GeV in the region $x_F > 0$ [Ake 93]. Fitting the angular distribution to the form of Equation 1.1, $\lambda = -0.115 \pm 0.061$ for $\overline{p}$ and $\lambda = 0.028 \pm 0.004$ for π^- were obtained. The data sample used to obtain this result contained 12530 J/ψ events produced by the $\overline{p}$ beam and 33820 J/ψ events by the π^- beam.

1.3.2.b E672/E706

Fermilab experiments E672/E706 have measured the differential cross section $d\sigma/d\cos\theta$ for J/ψ production in π^-Be collisions at $\sqrt{S} = 31.5$ GeV in the region

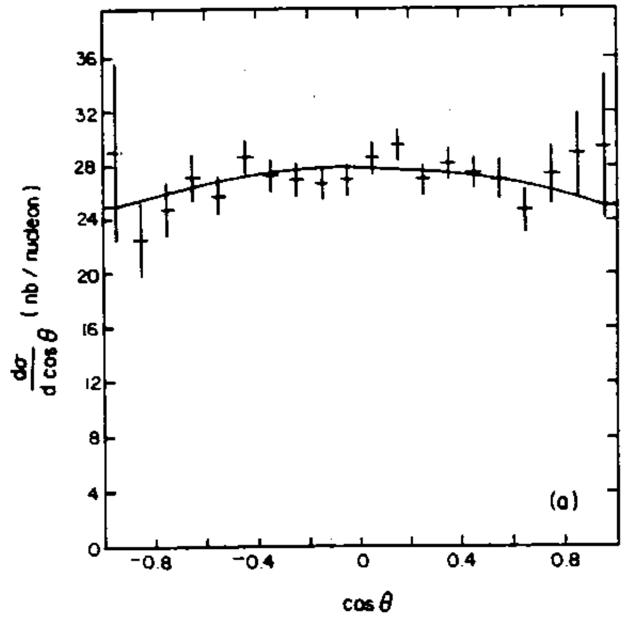

Figure 1.5: cosθ distribution for E537 $\overline{p}W$ data. (Taken from [Ake 93])

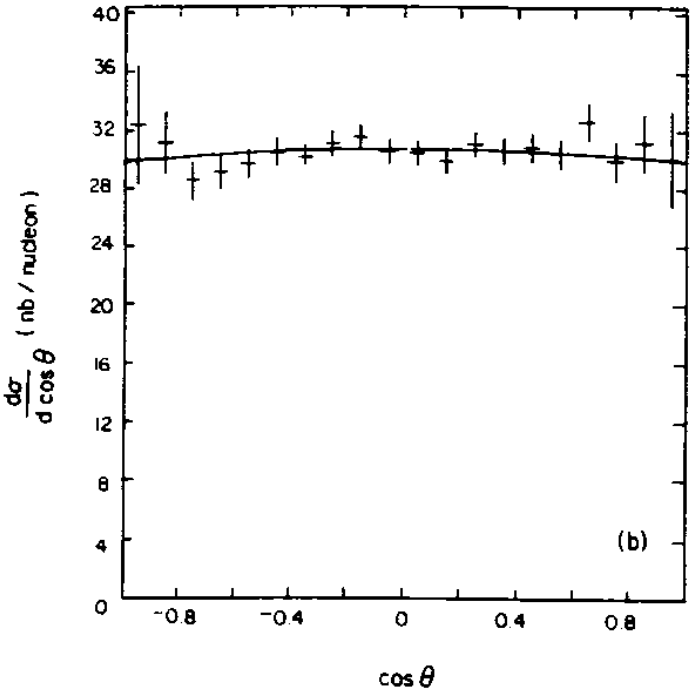

Figure 1.6: cosθ distribution for E537 $\pi^- W$ data. (Taken from [Ake 93])

$0.1 < x_F < 0.8$ [Gri 96]. Fitting the angular distribution to the form of Equation 1.1, $\lambda = -0.01 \pm 0.08$ was obtained. The data sample used to obtain this result contained 9600 J/ψ's.

1.3.2.c E771

Fermilab experiment E771 has measured the differential cross section $d\sigma/d\cos\theta$ for J/ψ production in pSi collisions at $\sqrt{S} = 38.8$ GeV in the region $-0.05 < x_F < 0.25$ [Ale 97]. This is the only published polarization measurement for J/ψ produced with a proton beam. Fitting the angular distribution to the form of

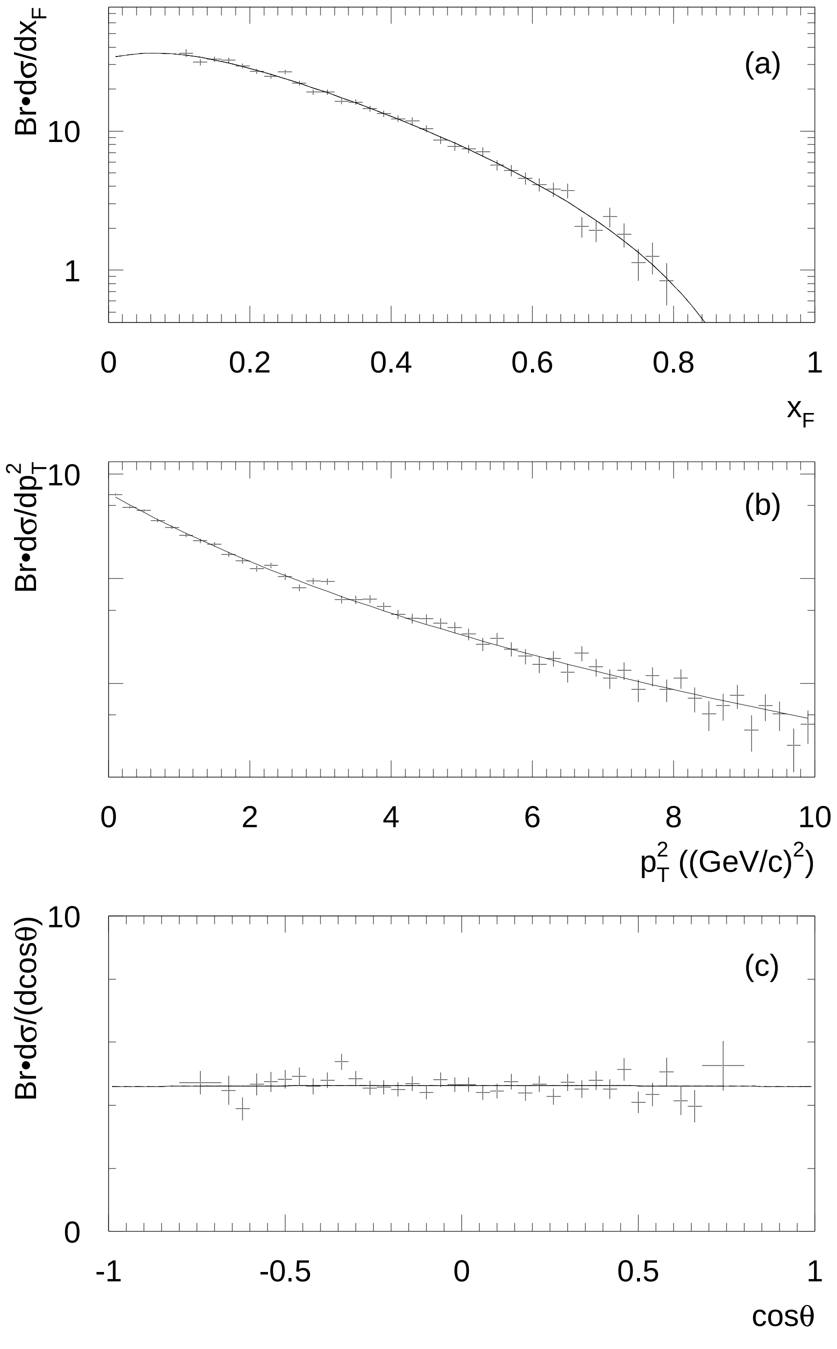

Figure 1.7: x_F, p_T, and $/cos\theta$ distribution for the E672/706 $\pi^- Be$ data. (Taken from [Gri 96])

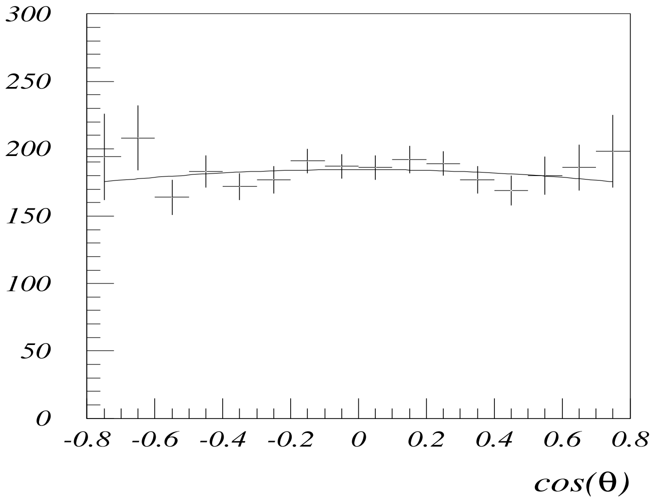

Figure 1.8: $\cos\theta$ distribution for E771 pSi data. (Taken from [Ale 97])

Equation 1.1, $\lambda = -0.09 \pm 0.12$ was obtained. The data sample used to obtain this result contained 11660 J/ψ's.

1.3.2.d Chicago-Iowa-Princeton

A dedicated J/ψ decay angular distribution measurement was performed at Fermilab using a 252 GeV pion beam incident on a tungsten target [Bii 87]. The data sample contains 1600000 J/ψ events from a π^- beam and 600000 J/ψ events from a π^+ beam. The data are in the kinematic range $x_F > 0.25$ and $p_T < 5.0$ GeV. To determine the J/ψ decay angular distribution, the data were divided into fifteen regions of x_F, five regions of $\cos\theta$, and five regions of ϕ in the kinematic range $x_F > 0.25$, $-1 < \cos\theta < 1$, and $-\pi < \phi < \pi$. For each bin of x_F, $\cos\theta$, and ϕ the raw $\mu^+\mu^-$ mass distribution was fitted by a seven-parameter function involving a Gaussian distribution for the J/ψ and ψ' and a quadratic polynomial

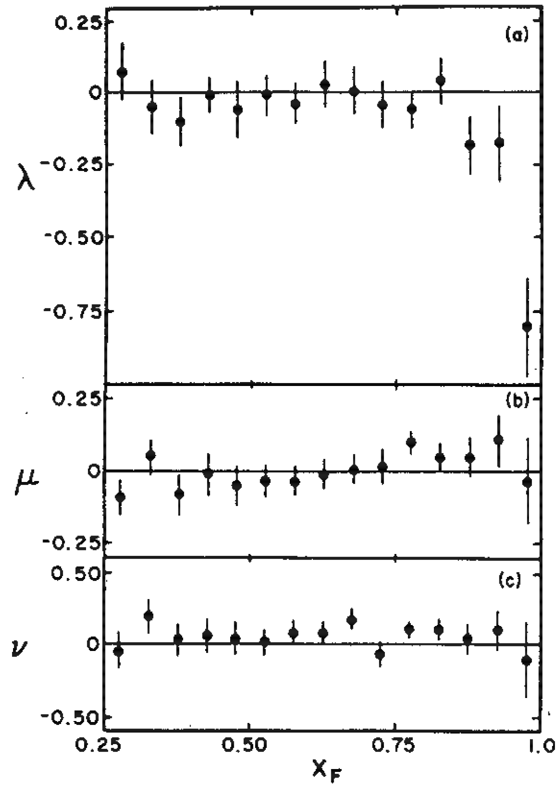

Figure 1.9: $\lambda(x_F)$ from CIP πN experiment. The parameters λ, μ, and ν were fitted to the J/ψ decay angular distribution in Equation 1.5. (Taken from [Bii 87])

plus an exponential of a first-order polynomial for the continuum background. The number of J/ψ's in the 375 bins of x_F, $\cos\theta$, and ϕ were then corrected for acceptance and for each of the fifteen regions of x_F the J/ψ angular distribution was fitted by the general form [Lam 78]

$$d^2\sigma/d\cos\theta d\phi \sim 1 + \lambda\cos^2\theta + \mu\sin 2\theta\cos\phi + \frac{1}{2}\nu\sin^2\theta\cos 2\phi \qquad (1.5)$$

The λ, μ, and ν are consistent with zero over a wide range of x_F. Note that λ approaches -1 at high x_F. This behavior was also observed in a Drell-Yan con-

Table 1.1: Summary of the experimental and theoretical results.

Experiment	reaction	$\sqrt{S}$	x_F range	λ
E537	$\overline{p}$ + W	15.3 GeV	$x_F > 0$	-0.115 ± 0.061
E537	π^- + W	15.3 GeV	$x_F > 0$	0.028 ± 0.004
E672/706	π^- + Be	31.5 GeV	$0.1 < x_F < 0.8$	-0.01 ± 0.08
E771	p + Si	38.8 GeV	$-0.05 < x_F < 0.25$	-0.09 ± 0.12
CIP	π + W	21.7 GeV	$0.25 < x_F < 1.0$	$\sim$0, $\rightarrow -1$ at large x_F

Theory	x_F range	λ
CSM	$x_F > 0$	~ 0.25
CEM	$x_F > 0$	0
NRQCD	$x_F > 0$	$0.31 < \lambda < 0.63$

tinuum production experiment [Ale 86]. Table 1.1 summarizes the experimental and theoretical results of J/ψ polarization.

1.4 Fermilab E866 Measurement

E866 at Fermilab was designed to measure the $\overline{u}/\overline{d}$ asymmetry in the nucleon sea. After the run ended in March, 1997, additional measurements were performed in the run extension period. Two major topics in the run extension were angular distribution of the J/ψ decay and nuclear dependence of J/ψ production. The work presented here is based on the data sample collected during a four week dedicated beam-dump run, from which the angular distribution of the J/ψ decay in the dilepton channel was studied. This angular-distribution measurement is unique since no high-statistics proton-induced data exists. Also, the J/ψ production diagrams are different for pN and πN interactions. A total of 10 million J/ψ's (with $\sim 1\%$ of unseparated ψ''s) were collected, and the kinematic coverage of the data extends over $x_F > 0.2$, $p_T < 5 GeV$, and $-0.95 < \cos\theta < 0.95$. The quantity of the data sample has allowed us to present the λ parameter in Equation 1.1 in seven regions of x_F and four regions of p_T. The results could provide a test of the color-octet mechanism, and hopefully will improve our understanding of the higher-twist effects.

2. EXPERIMENTAL APPARATUS

The experiment E866 was performed at the Meson-East experimental area of Fermi National Accelerator Laboratory. The spectrometer, shown in Figure 2.1, was a modified version of the E605/E772/E789 spectrometer. This spectrometer was designed to detect dimuon events with forward x_F, though certain combination of target position and analyzing magnet settings allows finite negative-x_F acceptance. The spectrometer primarily consisted of three dipole magnets, seven hodoscope planes, eighteen drift-chamber planes, and three proportional-tube planes. The hodoscope planes were used to provide the trigger information, the drift-chamber planes were used to find the trajectories, and the proportional-tube planes, which were also part of the trigger system, were used to identify muons. The SM3 magnet measured the momentum of the muon pairs while the SM0 and SM12 magnets allowed us to select the desired mass range. The charged particles produced in the target were split according to the sign of their charges while going through the set of three magnets.

A thick hadron absorber wall was installed in SM12 for the experiment so that the long-lived hadrons (mainly pions) can be stopped before hitting station 1. The absorber wall consisted of Cu, C, and $(CH_2)_n$ blocks, and gave a hadron attenuation factor of e^{-20}. Not shown in Figure 2.1 is the copper beam dump sitting in front of the hadron absorber wall. The beam dump was used to stop the 800 GeV proton beam. For the angular distribution measurement we used the beam dump

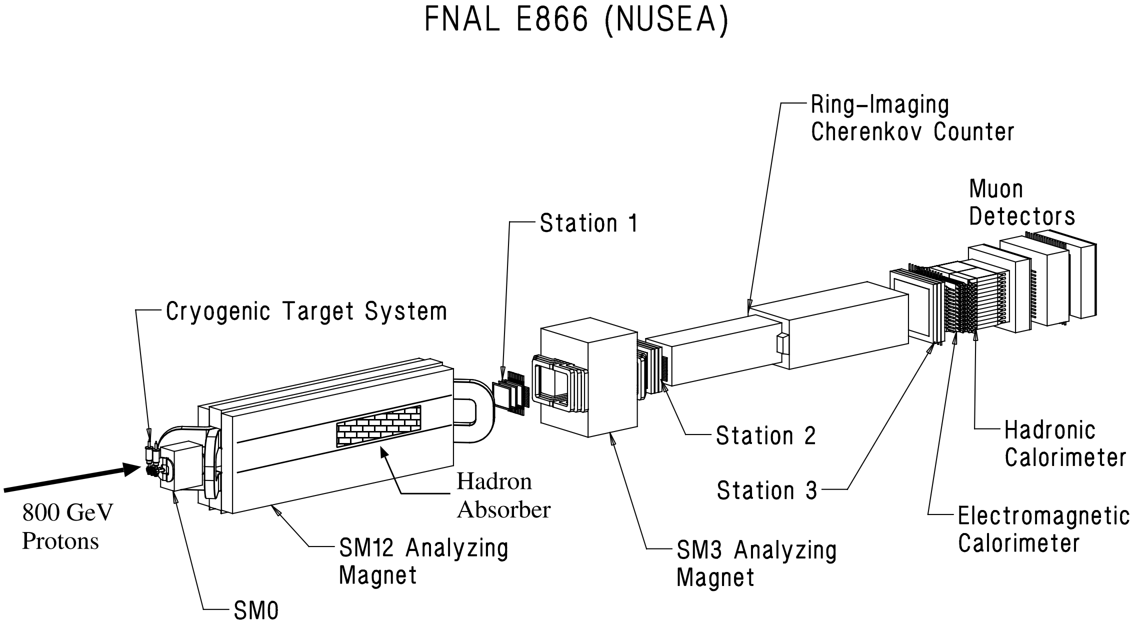

Figure 2.1: The E866 spectrometer.

as the target. There were also an electromagnetic and a hadronic calorimeter and a ring-imaging Cherenkov counter (RICH), which, however, were not operating during this experiment. The RICH counter was filled with helium bags to reduce multiple scattering. This chapter will discuss only these components that were needed for this study.

Throughout, we will make reference to the spectrometer-fixed coordinate system. The E866 coordinate system aligns the Z-axis horizontally with the accelerator proton beamline and the Y-axis with the vertical direction. The X-axis is then chosen to form a right-handed Cartesian system. The positive Z direction is chosen to be same as the beamline direction, which is also referred to as "downstream," and the positive Y direction is chosen to be up. The origin is located at the center of the upstream face of the SM12 spectrometer magnet.

2.1 Accelerator and Beam

The high-energy proton beam was produced in the Tevatron, which is a superconducting proton synchrotron. Protons were first accelerated by a pre-accelerator up to about 700 KeV. These protons were then accelerated in a linear accelerator to about 400 MeV. Subsequently, a Booster Ring boosted the proton energy to 8 GeV. Protons were then injected into the main ring, located in the same tunnel as the Tevatron but constructed from conventional magnets, in which protons could reach an energy of 400 GeV before being transferred into the superconducting ring, where the protons were accelerated to 800 GeV. After the proton beam was accelerated to 800 GeV, it was extracted and split by the switchyard for sending three streams of proton beams to the Meson, Neutrino, and Proton beam lines for the fixed-target experiments.

Protons in a spill were bunched into RF buckets separated from one another by 18.9 ns, with bucket length $\sim$ 1 ns. Each spill contained about 10^9 buckets. This small scale beam structure was due to the Tevatron accelerating radio frequency of 53 MHz. A square wave signal at this frequency, called the RF clock, was used to synchronize the E866 electronics with the Tevatron beam structure. It took $\sim$ 25 seconds to accelerate a fill of protons up to 800 GeV. These protons were then extracted from the accelerator for 20 seconds. After that, the superconducting magnets ramped down for 15 seconds. The entire cycle time was approximately one spill per minute. Typical proton intensities in the Tevatron were $1-2*10^{13}$ protons per spill.

Within the Meson area, a three-way split divided the proton beam between the Meson-East line and the rest of the Meson lines. To monitor the beam intensity, luminosity, position, and beam-spot size, several beamline detectors and monitors were used. During the beam-dump running mode the typical beam intensity was $6*10^{10}$ protons per spill. The beam intensity was monitored by an ion chamber located in the ME3 sector (IC3), a secondary-emission monitor located in the ME6 sector (SEM6), and a beam Cherenkov monitor. Both the size and the position of the beam were monitored by segmented wire ion chambers (SWICs) and the Beam-Position Monitor (BPM). The beam luminosity was monitored by the AMON and WMON scintillation counters, which were installed at about 85 degrees from the target position.

2.2 Beam-Dump Target

For this study the beam dump itself was the target. The dump was suspended from two of the central magnet inserts inside the SM12 magnet, beginning at Z = 68 inches, extending 168 inches downstream, and ending at Z = 236 inches. In Figure 2.2 a picture of the beam dump and absorber wall is shown. The beam dump was made of pure copper with cooling water tubes running through the sides. There was a 12-inch deep rectangular-shaped hole in the center of the upstream face of the dump to help contain backscattered particles, so actually the beam protons did not hit the dump until Z = 80 inches. This still left 156 inches thickness of copper, which is equivalent to 26.5 interaction lengths for p + Cu collisions, to stop the protons and secondary particles. The probability for a primary proton to punch through the entire dump was less than $4 * 10^{-12}$. Most primary protons would interact within the first few interaction lengths. Secondary particles from the primary interaction would further interact to form showers and eventually be stopped in the dump, but the high-energy muons produced would penetrate the entire dump with little interaction since muons are not strongly-interacting particles. However, these muons would still lose energy and suffer multiple scattering on their way through the dump, and thus added uncertainties to the reconstructed x_F and p_T.

2.3 Spectrometer Magnets and Absorber Wall

Two dipole magnets, SM12 and SM3 were used in this study (the current of SM0 was set to zero during the beam-dump data taking). The magnetic fields of these magnets were oriented horizontally. The field strengths of the dipole magnets could be configured to optimize the mass acceptance for J/ψ's. The bending magnet used for this study was SM12. The length of the SM12 magnet, made of iron, was 567 inches. The magnet produced an average horizontal field of up to 1.3 Tesla at a maximum current of 4000 Amperes. This corresponds to a 7-GeV transverse momentum kick to the charged particles which traveled through its entire length. In this study, SM12 was set to 2800 Amperes and 2040 Amperes during two separate data-taking periods, delivering a transverse-momentum kick of 4.2 GeV and 3.1 GeV, respectively.

The momenta of the muon tracks were measured by the analyzing magnet SM3. The location of the SM3 magnet was between Station 1 and Station 2, as shown in Figure 2.1. SM3 delivered a transverse momentum kick of 0.914 GeV to the charged particles traveling through when operated at its maximum current of 4260 Amperes. The field was uniform enough so that the reconstruction of a particle trajectory through the field volume can be described by a single bend-plane approximation.

The absorber wall was located inside the SM12 magnet directly behind the beam dump. It filled the SM12 magnet completely in the x and y direction. The absorber wall was constructed of one 24-inch section of copper, three 27-inch sections of carbon graphite, one 27-inch section of carbon-polyethelene compound, and two 36-inch sections of polyethelene.

Both magnets were filled with helium bags to minimize the multiple scatterings of the muons.

2.4 Detector Stations

There were four detector stations in the E866 spectrometer, denoted as Station 1 to 4. Station 1-3 each consisted of hodoscopes and drift chambers, while Station 4 consisted of hodoscopes and proportional tubes. Those stations record the passage of charged particles in space and time across their active area. Together with the information provided by the magnet field maps, this allowed the 4-momentum of the individual tracks to be reconstructed. Stations 1-3 were used for triggering and tracking, while Station 4 was used for muon identification and triggering.

2.4.1 Drift Chambers

Each one of Stations 1-3 consisted of 6 planes of drift chambers. The 6 planes were arranged in pairs with parallel wire orientation. The second plane of a pair had its wires offset by half the cell size of the drift chamber. The upstream plane of each pair was denoted as the "unprimed" plane, while the downstream plane was denoted as the "primed" plane. The Y-Y$'$ pair of each station held the wires horizontally to measure the Y-intercept of the tracks, while the V-V$'$ and U-U$'$ chambers had their wires tilted at -14 (a slope of -0.25) degrees and $+14$ (a slope of 0.25) degrees from the X-axis respectively. These planes determined the X-intercept of the track and also provided a check on the Y-intercept. The configuration of the drift chambers are given in Table 2.1.

The drift chambers were all operated with a gas mixture of 49.7% argon, 49.6% ethane, and 0.7% ethanol by volume, which was mixed at a constant 25 °F. The Station-1 anode wires were made of gold-plated tungsten wire, while Stations 2 and 3 used silver-coated beryllium-copper wires. All the anode wires were 25 μm in diameter. The cathode wires for all three stations were silver-coated beryllium-

Table 2.1: Drift chamber parameters. The unit length is one inch.

detector	Z-position	No.of wires	cell size	aperture(X×Y)	operating voltage
V1	724.69	200	0.25	48×40	+1700
V1′	724.94	200	0.25	48×40	+1700
Y1	740.81	160	0.25	48×40	+1700
Y1′	741.06	160	0.25	48×40	+1700
U1	755.48	200	0.25	48×40	+1700
U1′	755.73	200	0.25	48×40	+1700
V2	1083.40	160	0.388	66×51.2	−2000
V2′	1085.52	160	0.388	66×51.2	−2000
Y2	1093.21	128	0.40	66×51.2	−2000
Y2′	1095.33	128	0.40	66×51.2	−2000
U2	1103.25	160	0.388	66×51.2	−1950
U2′	1105.37	160	0.388	66×51.2	−1975
V3	1790.09	144	0.796	106×95.5	−2200
V3′	1792.84	144	0.796	106×95.5	−2150
Y3	1800.20	112	0.82	106×91.8	−2200
Y3′	1802.95	112	0.82	106×91.8	−2200
U3	1810.24	144	0.796	106×95.5	−2200
U3′	1812.99	144	0.796	106×95.5	−2200

copper wire with a diameter of 62.5 μm. The absolute operating voltages were between 1700 and 2200 volts, which gave a typical drift velocity about 50 μm/ns.

The signals of these chambers were read out by a fast amplifier and discriminator system. Single-hit TDCs (Time-to-Digital Converters), which only record the first hit on the wire during an event, were used to measure the drift time. The combination of good hits together with their associated drift times in all three views gave a "triplet" hit for a station. The bank of the triplets was saved to provide information for the track reconstruction.

2.4.2 Hodoscopes

Associated with the drift-chamber planes, there were also hodoscope planes in each tracking station. These hodoscopes provided fast tracking signals for use in triggering. In Stations 1, 3, and 4 there were two hodoscopes planes which measured the X and Y intercepts of the tracks, while in Station 2 there was only one hodoscope plane. Each hodoscope plane was arranged into two half-planes of parallel scintillator paddles, which were attached to photomultiplier tubes via plexiglass light guides. During operation, each paddle only gave a single bit of signal (one or zero).

The hodoscope planes were named according to the tracking station they belonged to, preceeded by X or Y depending on the orientation of the paddles. For example, "Y3 hodoscope" referred to the Station-3 hodoscope plane in which 2×13

Table 2.2: Hodoscope plane layout. Dimensions are in inches.

detector	Z-position	No. of counters	cell width	aperture X×Y
Y1	769.78	2×16	2.5	47.50×40.75
X1	770.72	12×2	4.0	47.53×40.78
Y2	1114.94	2×16	3.0	64.625×48.625
X3	1822.00	12×2	8.68	105.18×92.00
Y3	1832.00	2×13	7.5	104.00×92.00
Y4	2035.50	2×14	8.0	116.00×100.00
X4	2131.12	16×2	7.125	126.00×114.00

scintillator detectors was positioned horizontally and separated into left and right side. The parameters of the seven hodoscope planes are given in Table 2.2.

2.4.3 Proportional Tubes

Station 4 was also called the muon station. It was located downstream of the calorimeters and consisted of two hodoscope planes (Y4,X4) and three proportional tube planes(PTY1, PTX, PTY2). Each of the three proportional tube planes had two layers of 1×1-inch cells. These two layers were offset by a half-cell spacing to cover the dead region between the adjacent cells. The proportional tubes used the same argon/ethane/ethanol gas mixture as the drift chambers. To minimize the probability of hadron punch-through, an absorber wall (3 feet of zinc and 4 inches of lead) was placed between the calorimeter and the muon detector. Furthermore, 3-foot thick concrete walls were placed between PTY1 and X4, and between PTX and PTY2. This provided a total of 16.6 interaction lengths upstream of Y4. Thus the only charged particles which could reach Station 4

Table 2.3: Proportional tube parameters. All dimensions are in inches.

detector	Z-position	No.of wires	cell size	aperture X×Y
PTY1	2041.75	120	1.0	117×120
PTX	2135.875	135	1.0	135.4×121.5
PTY2	2200.75	143	1.0	141.5×143

detectors were the muons. Signals from the cell of the proportional tubes were amplified and shaped by the attached pre-amplifier/discriminator cards. Signals exceeding the threshold voltage were sent to the Coincidence Registers(CRs) to indicate the arrival of muons. The parameters of all proportional tube planes are given in Table 2.3.

2.5 Trigger System

2.5.1 Trigger-System Hardware

A new trigger system was implemented for E866 data taking [Haw 98]. A block diagram of most of the trigger system is shown in Fig. 2.3. The major components of the trigger system are described in this section.

2.5.1.a Trigger Matrix Module

Scintillator counters were used to provide input signals for the trigger system. Signals from the photomultiplier tubes attached to the scintillator counters were brought to LeCroy 4416 16-channel discriminators via coaxial cables. Each discriminator output was synchronized to the accelerator RF signal and shaped to a fixed width of 15 ns by pulse stretchers, and then fanned out to Coincidence Registers (CRs), Terminator/OR modules, and the Trigger Matrix (TM) modules.

The Trigger Matrix modules were the core of the trigger system. The pulse-stretcher outputs were grouped as a half-bank (right or left) of Y1, Y2, and Y4 hodoscope planes. These groups were sent as inputs to the Trigger Matrix to identify tracks of muons originating in the target. Only Y-view hodo-roads were used here, because events with different Z positions and momentum had different "roads" in the Y view under the deflection of the bending magnets. This Trigger Matrix was conceptually a lookup table loaded to a set of six 256×4-bit ECL SRAM chips. All tracks of interest defined a set of valid "roads" going through the hodoscope planes. These roads were identified using a Monte Carlo simulation for muon tracks coming from the target, and thus a "map" of these roads was produced. The "map" was then written into a disk file, which was loaded into the SRAMs by the Data Acquisition (DAQ) online program during the start-run stage. While taking data, the hits on Y2 and Y4 were combined to form an "address" whose content were the predictions on Y1, which were compared to the actual Y1 hit pattern. Any coincidence in the comparison generated the Trigger Matrix output.

There were four sets of Trigger Matrix modules called MUL, MUR, MDL, and MDR. They covered different types of valid muon tracks, namely, up-left, up-right, down-left, and down-right, respectively. For finding the target muon pairs, the coincident combination of an up and a down track was required. The output signals of the Trigger Matrix modules were then sent to the Track Correlator for further triggering determination.

2.5.1.b Track Correlator

The Track Correlator (TC) modules were designed by Texas A&M University [Gag 98]. These programmable modules were used to filter specific combinations of Trigger Matrix, Terminator/OR, and S4XY [42] outputs to trigger on an event. However, during beam-dump data taking only output signals from the TMs were of interest. Four 16-bit patterns, according to the desired trigger conditions, were preloaded into a $2^{16} \times 4$ bit SRAM chip inside a TC during the start-run stage. Whenever the output combination of the TM modules matched one of the preloaded bit patterns, the TC would, prescaled to the desired frequency and synchronized with the RF clock, send out a signal to the Master Trigger OR module to notify the arrival of an interesting event. Each SRAM chip could be programmed with up to four independent trigger conditions.

There were three main Track Correlators which were able to trigger on an event to start the DAQ. The first TC, called Physics TC A, was programmed to select two-tracks events, like-sign or unlike-sign. The second TC, named Physics TC B, was designated for left-right efficiency studies, which involved the use of X hodo planes and single muon events. The third module, which was used to

Table 2.4: Correspondence of the SRAM chip bit to various input sources. The sources were connected to the Physics TC A,B modules.

Signal Origin	TC SRAM bit
S4UL1	bit0
S4UL2	bit1
S4DL1	bit2
S4DL2	bit3
S4UR1	bit4
S4UR2	bit5
S4DR1	bit6
S4DR2	bit7
MUL	bit8
MDL	bit9
MUR	bit10
MDR	bit11
X134L	bit12
X134R	bit13
- unused -	bit14
- unused -	bit15

trigger on cosmic rays to diagnose the trigger and DAQ systems, was called the Diagnostic TC. It also provided the measurements for scintillator efficiencies.

If the inputs to the Track Correlator fulfilled the triggering criteria, a Trigger Generate Input (TGI) signal would then be sent to the Master Trigger OR by the TC. The Master Trigger OR would then synchronize this trigger signal and the drop of DAQ System Busy with the RF clock to send out a Trigger Generate Output (TGO). Triggers were thus inhibited during event readout; the difference of TGI and TGO counts would provide information on readout dead time.

Table 2.5: Prescale factors and trigger descriptions for Physics TC module. The "*" represents a logical AND and the "+" represents a logical OR.

Trigger name	prescaler factor	description
PhysA1	1	(MUL*MDR) + (MUR*MDL)
PhysA2	1	(MUL*MUR) + (MDL*MDR)
PhysA3	1	(MUL*MDL)
PhysA4	1	(MUR*MDR)
PhysB1	10	(X134L*X134R)
PhysB2	1000	MUL + MDL + MUR + MDR
PhysB3	0	–
PhysB4	0	–

2.5.2 Trigger Firing Criteria

2.5.2.a PhysA Trigger

From Table 2.5 the definitions of PhysA1,2,3,4 triggers are self-explanatory. PhysA1 trigger required that two tracks went through two diagonally-opposite quarters of the spectrometer, while the PhysA3 and PhysA4 required that two tracks went through the same side, left or right, of the spectrometer with one track going up and the other going down. These tracks were identified as unlike-sign muon pairs and were treated as possible candidates of target events. The PhysA2 trigger required that both tracks went up or down, and thus gave like-sign muon pairs. This information was especially important for rate-dependence studies in extracting cross sections.

2.5.2.b PhysB Trigger

The Physics TC B was used for recording events for studies. In the PhysB1 trigger, the symbol "X134L(R)" represented a track that went through the left(right) side of X1, X3, and X4 hodoscope planes. The signals fed into the TC B were outputs of some Terminator/OR modules, whose outputs represented the logical ORs of the signals of the X hodo scintillators. The trigger requirement, X134L*X134R, was designed to measure the random muon coincidences. The other trigger PhysB2 only required a single hit on any of the four quarters to fire. It had a prescale factor of 1000 and was used to measure the rate of single muons.

2.6 Data-Acquisition System

The Data-Acquisition System could be divided into three parts by functionality: event readout, data archiving, and online analysis. The first part was based on a Nevis Transport system, the second was a VME-based data-transferring and controlling system, and the third was built on the SGI workstations.

2.6.1 Readout System

The backbone of the E866 readout was a Nevis transport system [Kap 82]. All detector subsystems ultimately fed data into the Transport. The subsystems included Time-to-Digital Converter (TDC) readouts from drift chambers and Coincidence Registers (CRs) from hodoscopes and muon proportional tubes signals. Bus arbitration was maintained by a hard-wired daisy chain, with the bus mastership determined by the Carry signal. This scheme not only prevented multiple subsystems from attempting to place data on the Transport simultaneously, but also guaranteed that events appeared on the readout bus in a well-defined order. The data bus was 16-bit wide, and the system clock was set to 10 MHz. All the data fed into the Transport Bus were then transferred to a VME-based archiving system [Car 91].

Upon receipt of the TGO signal, the first module in the Transport Bus Carry chain, the Event Generator Source (EGS), would raise the System Busy signal to inhibit any further triggers and take control of the Carry signal. The EGS then put a special "first-word" into the Transport bus to indicate the beginning of a new event in the data stream. After a few more words from the EGS, the Carry signal was passed to the first branch of the readout subsystem to begin transferring event data into the Transport.

Upon receipt of the TGO signal, the EGS module also fanned out "START" signals to CRs and TDCs to begin digitizing the pulse signals. For each hit in the hodo or prop tube the CR would generate one word in the event output, containing the scintillator ID or wire number of the muon proportional-tube hit. Each event also contained a record of which trigger caused it to be readout via the Trigger Bit Latch (TBL). In addition to the CR's, each TDC would begin incrementing a Gray-code counter once every 4 ns upon receiving the START signal. The incrementing process would be stopped by the amplified signal from the drift chamber. Each hit in the drift chamber would also produce a one-word output, containing the wire number of the hit and the Gray-code value of the TDC timer. This measured the drift time. All the data were transferred into the Transport bus in the Carry chain order.

2.6.2 Data Archiving System

Events from the Transport bus streamed into the VME through a pair of "ping-ponging" triple-ported VME high-speed memory boards by way of a front-panel ECL interface. Interrupt-driven software would initiate DMA transfers of packets of events from the high-speed memories across the VME bus into a 128-megabyte ring buffer. This buffer was continuously being drained across the VME bus into a single-board computer by a concurrent task which performed all the data formatting. From there, formatted packets of events were queued in a small pool for distribution to the taping subsystem, where up to four Exabyte 8mm tape drives would record the data.

Unlike in E789, the communications to the readout system and the run-control capabilities were all built on the VME single-board computer in E866. In addition, the scaler data were injected into the data pipeline, from the CAMAC system, as regular logical records on a spill-by-spill basis. These scalers included target, beam, magnet parameters and counts from varieties of trigger conditions. A small fraction of event packets were fanned to the UNIX workstations for online data sampling and analysis. This provided the capability of online monitoring.

For the beam-dump running, the average data-taking rate was about 20000 events per spill. The average event size during the beam-dump run was 192 16-bit words.

2.6.3 Data Monitoring System

The E866 online database system was based upon the ADAMO library distributed by CERN, with a graphical interface package called "PinKy." The database for E866 recorded various data streams, including the beginning-of-run (BOR), end-of-spill (EOS) scalers, and beamline data (EPICURE). The online monitoring tools included 1) "runstatus," a graphical display of certain critical data (magnet settings, beam intensity, luminosity, live-time, and duty-factor calculations) updated at each EOS, 2) "scan," a graphical display of scalers refreshed at each EOS, 3) "plot," a plotting tool for monitoring any entity stored in the database, 4) "review," a tool for fetching data for series of runs for plotting or exporting to the CERN Physics Analysis Workstation software package (PAW) ntuple file, in which the interested quantities of an event were stored in an array, and 5) "dd," a tool to receive and distribute data to the backend. These advanced monitoring tools provided the capabilities for us to reconstruct and monitor a fraction of events online during the data taking. The shift taker could, for example, see the mass spectrum, hits and multiplicities on the drift chambers and hodoscope planes, and format errors due to transport readout problems while the data were being taken. Thus this capability helped us to diagnose the hardware problems and improved the quality of the data.

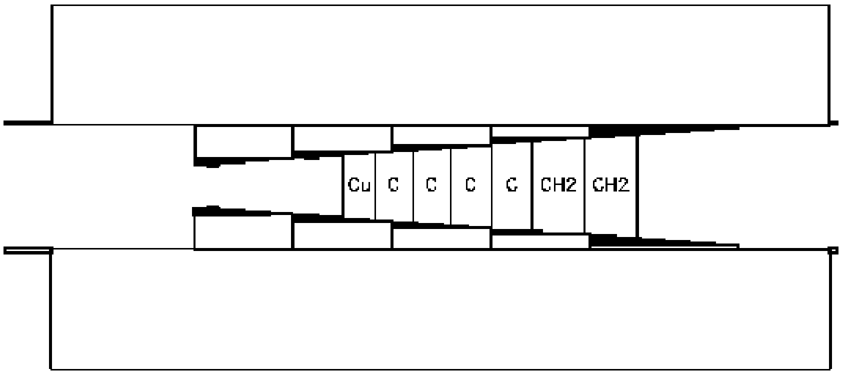

Plan View (X)

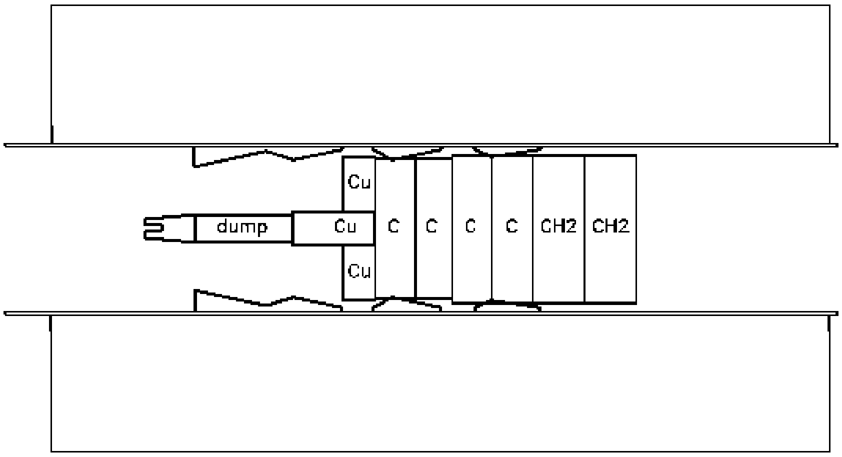

Elevation View (Y)

Figure 2.2: The SM12 acceptance defining magnet with the absorber wall. The magnet coils and iron return yoke are only partially shown. The beam dump is also not shown in the plan view.

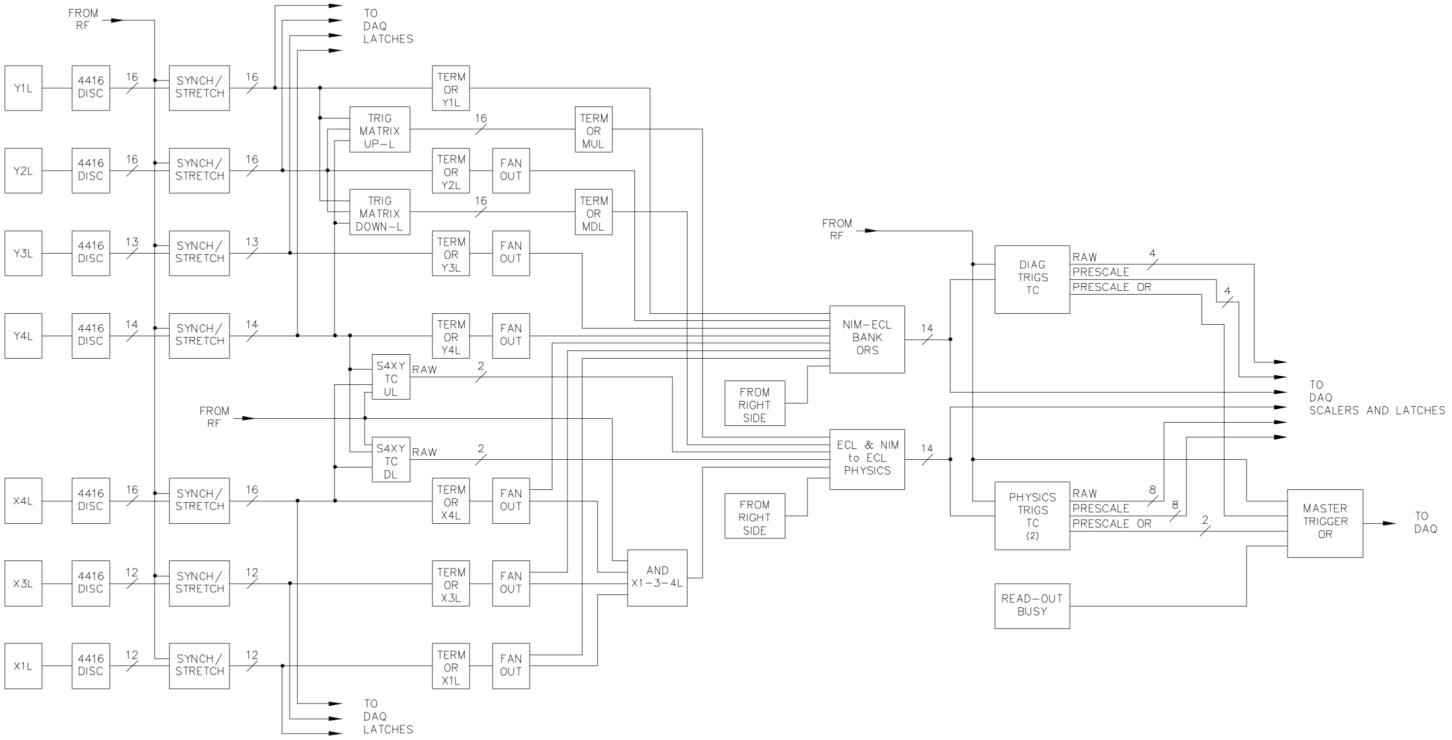

Figure 2.3: Block diagram of the E866 trigger system. Note only the inputs and associated electronics for the left half of the spectrometer are shown.

3. MUON-TRACK RECONSTRUCTION

The data recorded in 8mm tapes are logical records and have to be decoded before using. The decoding was accomplished by the analysis code developed for E866. The most important information stored in the data stream is actually the space-time marks of the electronic signals traveling through the detector stations. These marks in reality present the trajectories of the charged particles. From the trajectories the kinematic quantities of the particles can then be determined if the mass of the charged particle and the strength of the magnetic field is known.

In this chapter we will first summarize the data taken in April of 1997 for this study, and then describe in detail the method of track reconstruction in this experiment.

3.1 Data-Set Summary

During beam-dump data taking the typical beam intensity request was 6E10, $6 * 10^{10}$ protons per spill. The average triggering rate was about 20000 triggers per spill and the average event size was 192 16-bit words, as mentioned in the last chapter. A total of 82 magnetic tapes of raw data were used, with an average of 1.8 Gb of raw data written onto one tape. About 400M events in total were recoded during the beam-dump run.

One data set was distinguished from another by changing magnet-setting configurations or trigger-matrix configurations. There were four data sets in the beam-dump data sample. The specifications are given in Table 3.1.

Table 3.1: Magnet currents and trigger-matrix of different data sets. The magnet currents are in Amperes. SM0 was off during the beam-dump run.

data sets	SM12 current	SM3 current	trigger matrix
12	-2800	-4230	trigmat.psidump, trigmat.psi2800
13	-2040	-4230	trigmat.psi2000
14	$+2040$	$+4230$	trigmat.psi2000
15	$+2800$	$+4230$	trigmat.psi2800

The data were taken under two different SM12 settings and two polarities in order to reduce possible systematic errors. It was known that the incident beam was not perfectly lined-up with the Z-axis of the spectrometer, so the data show an up-down asymmetry in the event distribution with respect to the $\mathrm{Y} = 0$ plane. The flipping of the magnet polarity thus provided crucial information on the measurement of this asymmetry. The changing of SM12 current also changed the acceptance of the spectrometer. The consistency on the results obtained from the two magnet settings would provide a test, since the physics should be acceptance-independent. Each of the four data sets contained about equal amount of data.

Data set 12 was further divided into data set 12a, 12b, and 12c, and data set 15 was divided into 15a and 15b, according to the incident beam angle and trigger matrix file. However the beam angle was only determined after the data were analyzed, so not till the later chapters will such division be used.

3.2 Track Reconstruction

In this section the methodology of track reconstruction applied in the E866 analysis is described. For each event, the procedure can be considered as two main steps. The first step involved track finding, which was based on the drift-chamber hits and muon identification from the proportional-tube signals, and track fitting, in which the possible candidates of track segments between Stations 2 and 3 were found. In the second step a trace-back procedure was applied to the track candidates, so that the complete trajectories through the SM12 and SM0 to the target position were reconstructed.

3.2.1 Identifying Drift Chamber Hits

Each drift chamber station consisted of six planes: Y, U, V, and their associated prime planes Y′,U′,V′. When a charged particle traveled through the drift-chamber array in one station, correlated signals from different planes were produced. The subroutine DCTRIPS searched station 3 and station 2 for the correlated hit patterns. Only the patterns that consisted of at least 4 crossed hits whose cross-intersections were very close to a space point were registered. A triplet pattern was defined as having hits in all three views, while a doublet pattern was defined as having hits in two views only. An associated hit was defined as a particle that hits both the prime and unprimed planes.

3.2.2 Fitting the Tracks

Once all the valid hit patterns were registered, the next step was to link the registered hits from Station 3 and Station 2. The subroutine DCTRAX looped over the triplets and doublets in Stations 2 and 3 to construct the track candidates, called DC track segments. Several constrains were imposed on the track candidates: 1) if a doublet in one station was found, it was only allowed to connect to a triplet from another station; 2) at least 3 associated hits from Stations 2 and 3 were required to construct the track segment; 3) the segment was extrapolated to Station 4 and was required to fire at least 3 out of 5 planes in the desired location; 4) the segment was approximately pointing to the target location. For this study, very loose cuts were made to confine the segment vectors, and muon identification was done in DCTRAX.

The next step was to link the track segments with the identified hits in Station 1. The subroutine WCTRAX required each of the track segments to be lined up with a valid hit of Station 1 in the X-Z view (non-bend plane) within a vertical band. Only hits within this Station-1 window were further considered. A single bend-plane approximation was used to account for the SM3 momentum kick. Once a valid hit was identified in station 1, the entire track was refit into two straight-line segments joint at the bend plane. The fitting routine, FITTIME, using all 18 planes of drift chambers to fit the track, and routine SM3 calculated the momentum kick and the Z-coordinate of the bend plane. The result of this final fit gave the coordinate of the track at the SM3 bend plane, the Y-slopes before and after the bend plane, and the X-slope at the intersection point. With the knowledge of the SM3 field map, together with the slope information, the track momentum at Station 1 was determined.

3.2.3 Tracing Back through SM12

3.2.3.a Energy-Loss Correction

From the SM3 bend plane to the target position, the track was reconstructed in a routine called PBSWIM. Given the field map of SM12, the coordinates and the momentum of the track were reconstructed in the field-map grid step by the routine TRACER. During the procedure of tracing back, the effect of energy loss in the absorber wall and in the beam dump material was taken into account. The lost energy, calculated by an empirical formula

$$E_{loss} = a + b * \log(P_{in}) + c * \log(P_{in})^2 \tag{3.1}$$

for each layer of the absorber materials, was added back to the track after TRACER had traced through that layer. The coefficients in the formula were determined from dedicated Monte Carlo studies. The total energy loss in the beam dump was estimated in the same way. For each step inside the dump, a fraction of the total estimated energy loss, proportional to the step size, was added back to the track.

3.2.3.b Multiple Scattering

Due to multiple scattering, it was impossible to trace back to the exact event-producing location. So it was assumed that all the events came from a point located at one interaction length into the dump. In this case Z_{target} was set to 86 inches in the E866 coordinate frame. To correct for the effects of multiple scattering, a scattering bend-plane approximation was used. After the initial traceback, the intercepts of the track at Z_{target} were compared with the beam centroid,

$$dX = X_{target} - X_{centroid}, \tag{3.2}$$

$$dY = Y_{target} - Y_{centroid}. \tag{3.3}$$

Based on these differences, an angular correction to the track direction at the scattering bend plane (located at $\mathrm{Z}_{scatter}$) was calculated:

$$d\theta_x = dX/(Z_{target} - Z_{scatter}), \tag{3.4}$$

$$d\theta_y = dY/(Z_{target} - Z_{scatter}). \tag{3.5}$$

After the angular correction was applied, the track was traced again to Z_{target} starting from $Z_{scatter}$. The iteration procedure was repeated until the intercept errors became negligible. The value of $Z_{scatter}$ was determined by optimizing the angular resolution at the target point.

3.2.3.c Additional Angle Corrections

Further Monte Carlo study had shown that the single scattering bend-plane approximation actually over-calculated the reconstructed angle, as shown in Figure 3.1.

In order to reconstruct the opening angle correctly, an empirical formula, the angle deviation expressed as a polynomial function of the reconstructed angle, was used to adjust the angle that came out of the initial scattering-plane approximation. The formula was purely empirical and relied completely on Monte Carlo studies, so it was important to test whether these corrections gave back the thrown angular distribution for Monte Carlo events after the events were analyzed, even though this self-consistency check is only necessary but not sufficient. Figure 3.2 shows the reconstructed $\cos\theta$ distributions for both magnet settings. Those plots were obtained from the thrown-reconstructed events divided by the unsmeared acceptances. The function $p1 \times (1 + p2 * \cos^2\theta)$ was used to fit the plots to test whether there is any systematic bias while reconstructing the $\cos\theta$ distributions. As a result, a nearly flat distribution of $\cos\theta$ ($\lambda = -0.02 \pm 0.017$) is recovered for the 2040Amp data set, and $\lambda = 0.02 \pm 0.018$ for the 2800Amp data set.

It was also important to test with Drell-Yan data, where we believe we know the angular distribution, to search for additional systematic problems not revealed from Monte Carlo studies alone. The angular distribution study of Drell-Yan events as a confidence check will be presented in Chapter 5.

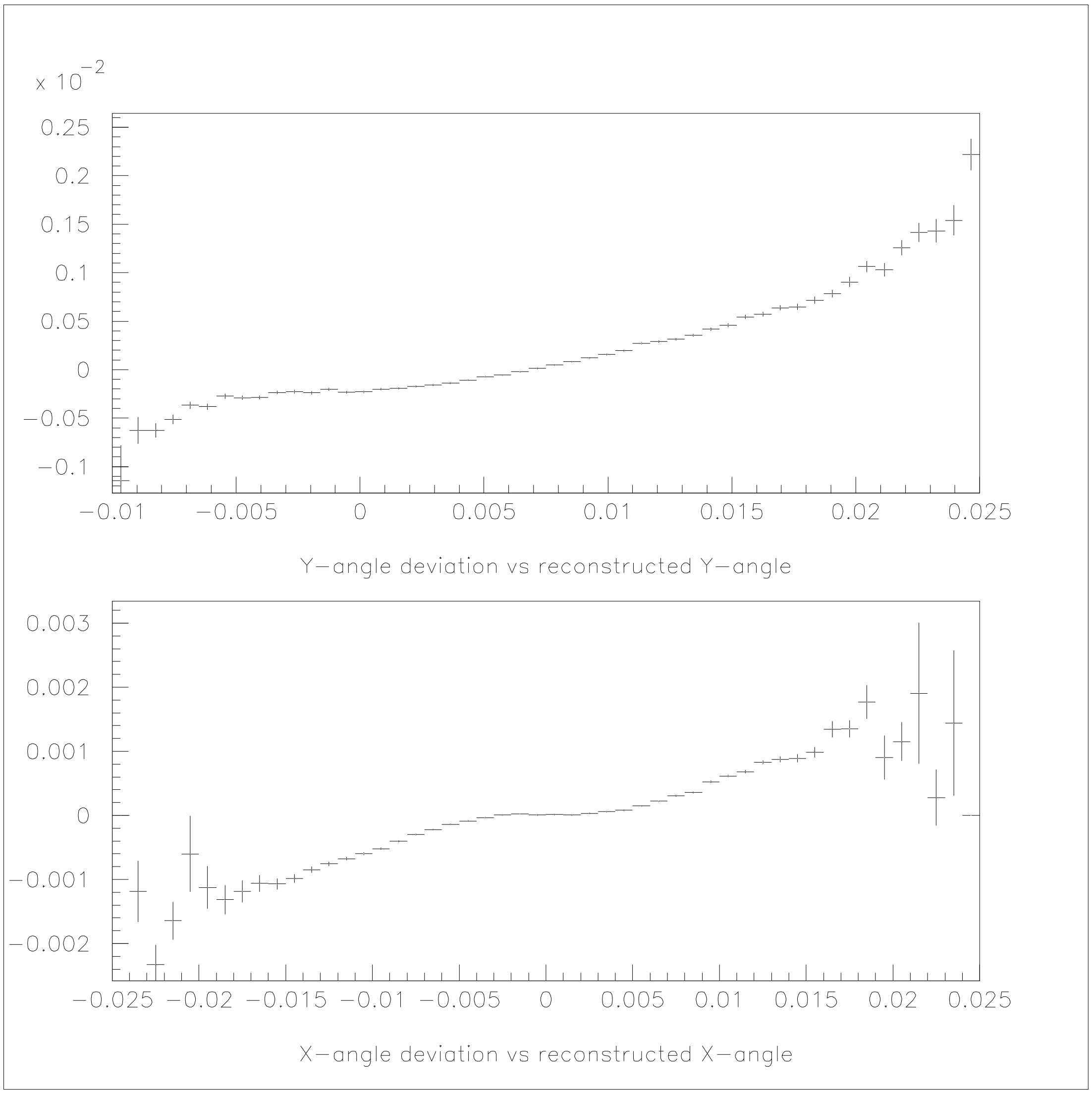

Figure 3.1: Angle corrections from single scattering-plane approximation. The single scattering-plane approximation fails at large angles. The reconstructed angles are greater than the thrown angles by about 10% at large angles. The figures shown here are taken from the up-going muon tracks.

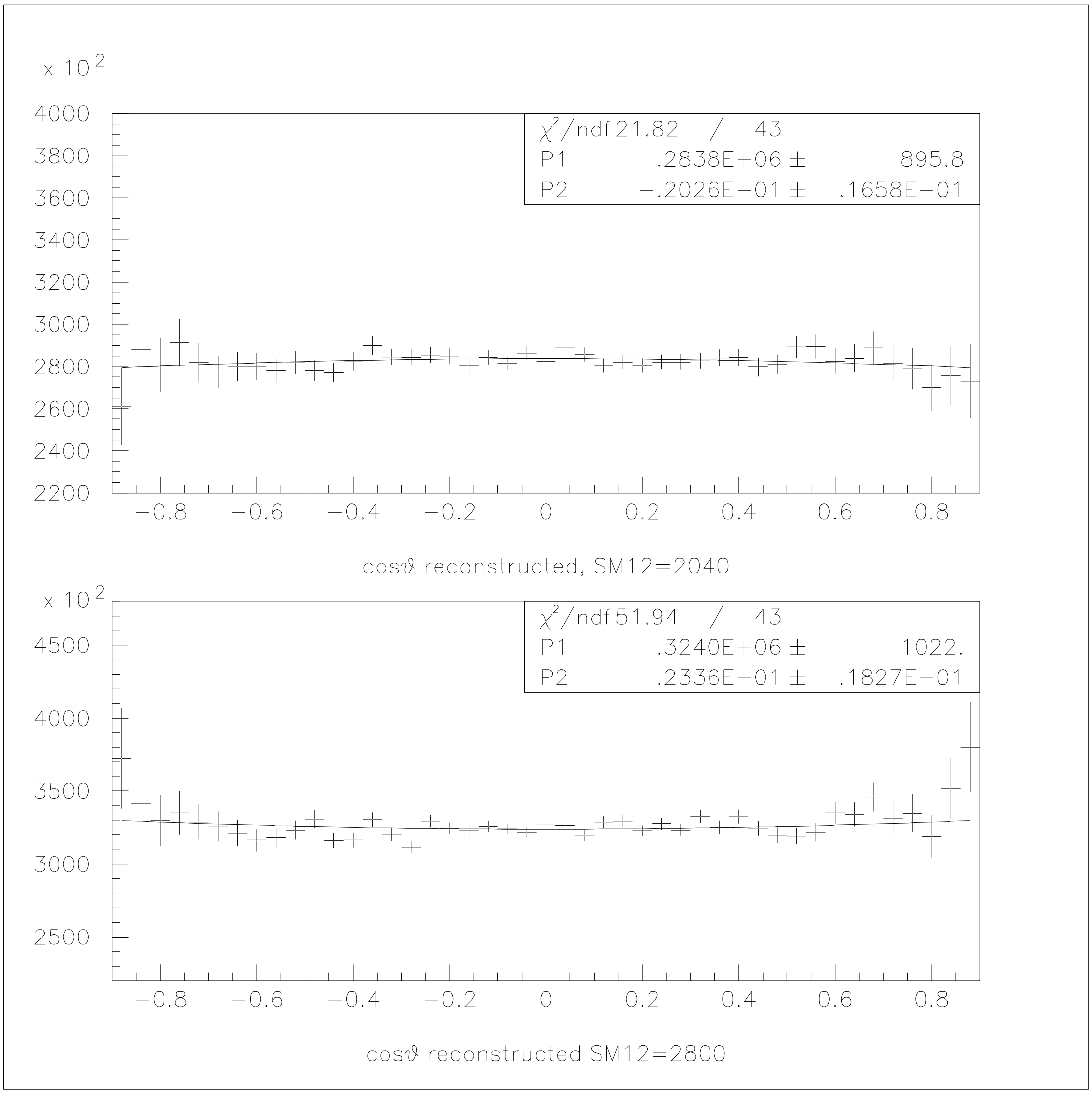

Figure 3.2: Reconstructed $\cos\theta$ distributions for both magnet settings. The reconstructed distributions recover the thrown (flat) distributions.

4. DATA ANALYSIS

From the raw-data tapes to the final physics results, several types of computing hardware and software were used. The whole procedure can be divided into three passes in the analysis, which will be described in this chapter.

4.1 Pass-1: Fermilab IBM Farm

The first pass of data analysis was performed on the Fermilab parallel computing farms. The computing farm system is a cluster of IBM workstations which can distribute the raw data into all the computing nodes and analyze the data simultaneously. The events passing the first-pass analysis were then written on to Data Summary Tapes (DSTs) for the second-pass analysis.

The tasks of the first-pass analysis were mainly to find dimuon events originating in the beam dump within the desired mass range. An 18-inch grid SM12 magnet map was used to trace the tracks in this pass, and very loose aperture and target cuts were applied. However it required the events to have two muon tracks and the mass of the muon pair has to be greater than 2 GeV. As a consequence only about 5% of the events passed the cuts and were written onto DSTs.

4.2 Pass-2: Hewlett-Packard Workstation

The second pass of the data analysis was performed on the Hewlett-Packard Workstation located in New Mexico State University. The inputs of this phase were DSTs, and the outputs were the ntuple files. The main task of this phase of analysis was to reconstruct the kinematics of the DST events as accurately as possible. A 2-inch grid SM12 magnet map as well as a Y-field map were used to reconstruct the events instead of the 18-inch map. No other tighter cuts were applied, but many fine-tuning tasks were done in this pass of analysis.

4.2.1 Determining Tweeks

The "tweek" is an overall correction factor for the magnetic field strength provided by the field map. The field maps provided by the ANL (Argonne National Lab) group assumed that the magnets were operated at the preset currents, SM3 at 4260 Amperes and SM12 at 2800 Amperes, for example. But in reality the operating currents were not precisely equal to the desired currents, and there were uncertainties in the mapping, therefore it was necessary to apply the corrections to the magnet maps for analyzing the events or to generate Monte Carlo events.

Since the actual currents were not known, this whole subject relied on careful Monte Carlo studies. There were two unknown quantities to be determined: the tweek of SM12 and the tweek of SM3. The two conditions used to determine these two quantities were 1) reconstructed J/ψ mass and 2) the uniterated Z-vertex (ZUNIN). By adjusting the magnet map in the MC event-generating phase, it was required that the reconstructed experimental data have the same mass and ZUNIN location as the MC reconstructed events; the tweeks used in the data event reconstruction were the same as in the MC event generation and reconstruction. Figures 4.1 and 4.2 show the ZUNIN and mass peaks of the real

Table 4.1: The tweek values of SM12 and SM3 for all the data sets.

Data Set	SM12(Amp)	SM3(Amp)	TWEEK12	TWEEK3
12	-2800	-4260	1.006	0.986
13	-2040	-4260	1.019	1.002
14	$+2040$	$+4260$	1.019	1.002
15	$+2800$	$+4260$	1.006	0.986

events and MC events from both magnet settings. The shape of the ZUNIN peaks is not symmetric around its central value because of energy loss and multiple scattering of the muon tracks. The peaks were fitted to a Gaussian using asymmetric boundaries, -10 inches to 33 inches, in order to locate the peak centroids without being affected by the non-Gaussian tails. The mass peaks of the data distributions were fitted to a second-order polynomial plus a Gaussian function, while the mass distributions from Monte Carlo were fitted to Gaussians since the Monte Carlo did not include any background events. As one can see from Figures 4.1 and 4.2, the agreement between Monte Carlo and the experimental data is satisfactory. The tweek values are given in Table 4.1.

4.2.2 Determining Beam Positions

During the course of analyzing the raw data, it was found that the beam centroid was not steadily fixed at a single location over the entire period of running. The moving range of the centroid is greater than three sigma of the beam profile, which is 0.14 inches in X and 0.07 inches in Y at the target position, so this was

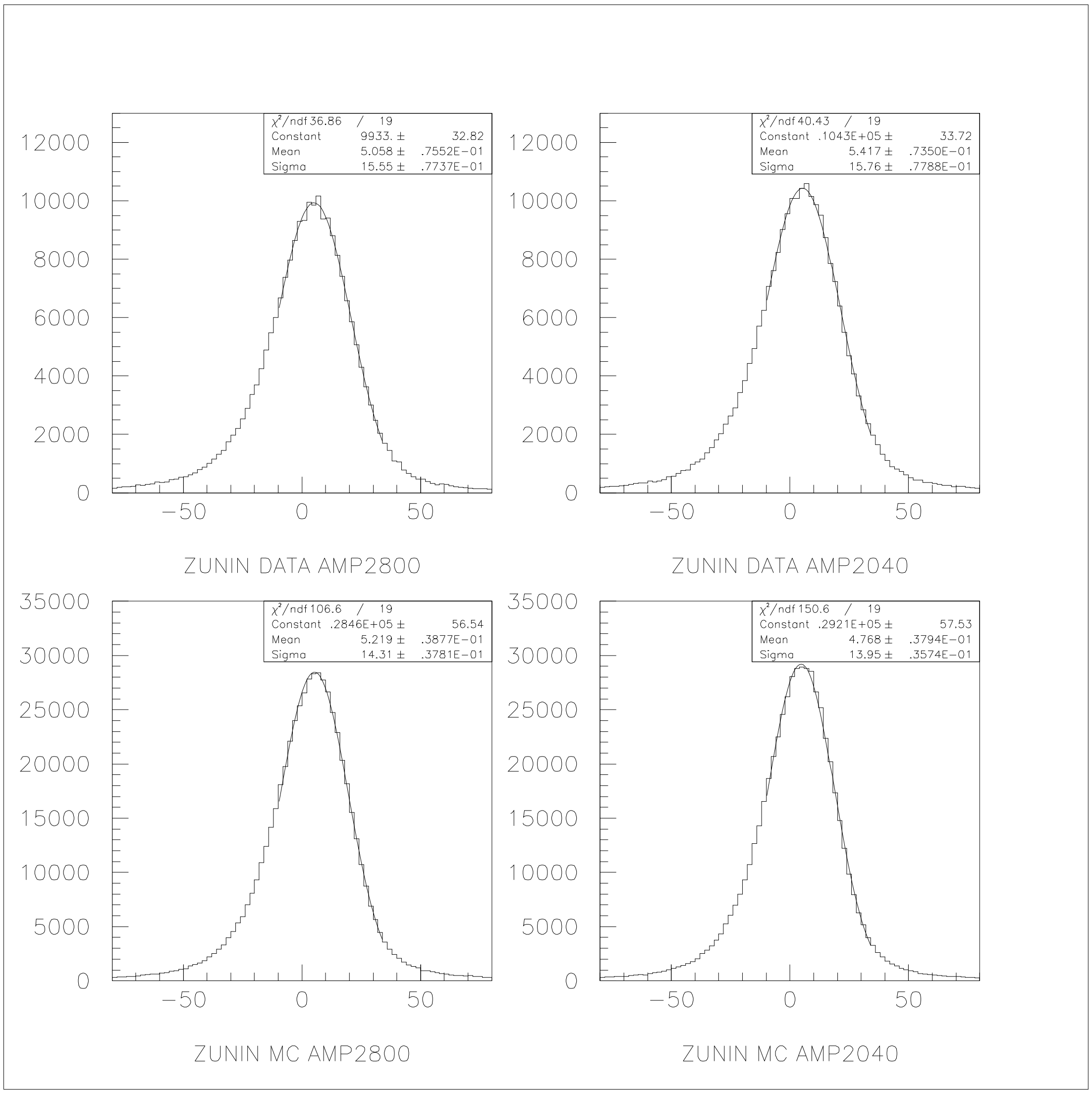

Figure 4.1: ZUNIN peaks of Data and MC from both magnet settings.

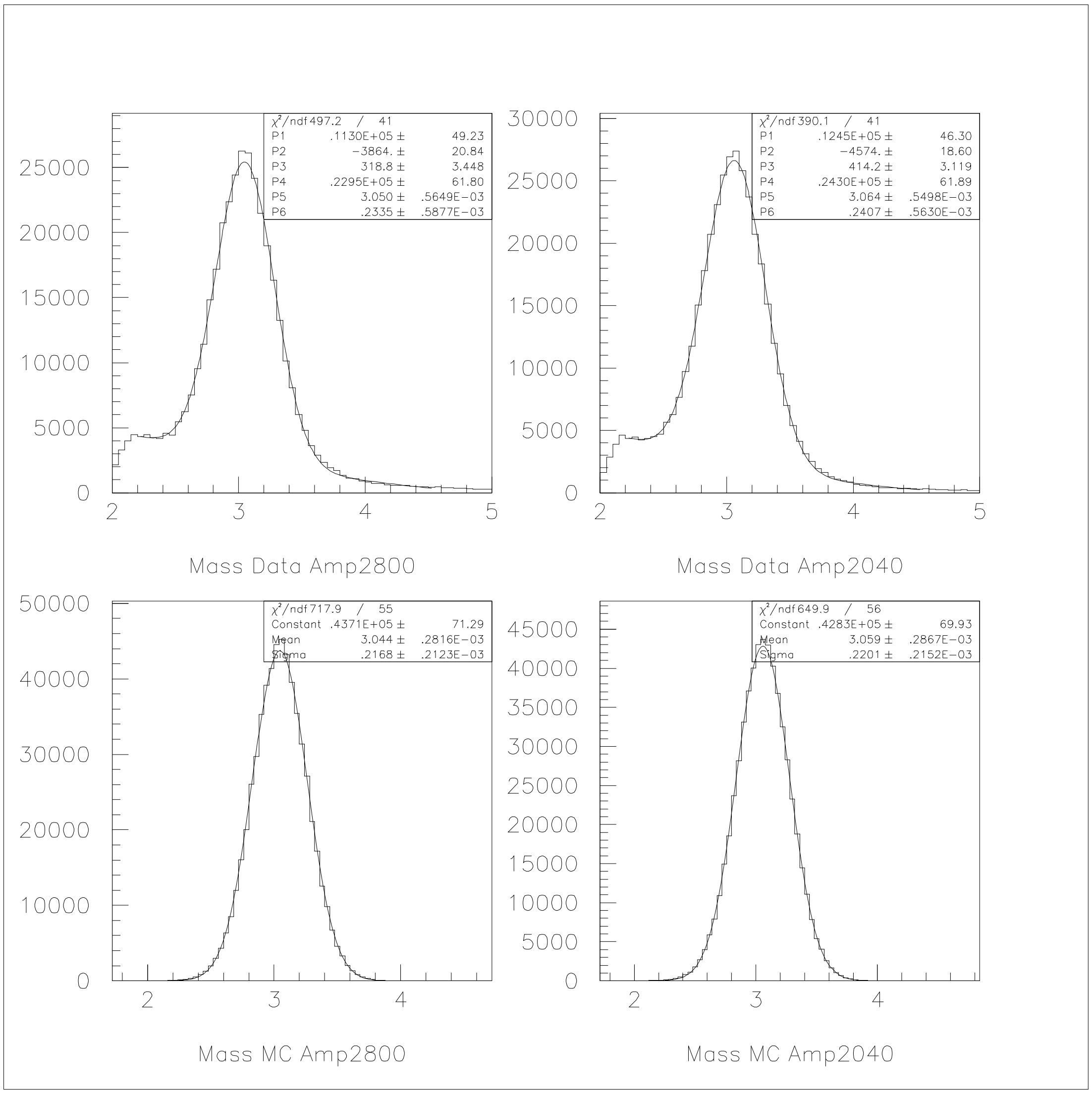

Figure 4.2: Mass peaks of Data and MC from both magnet settings.

due to the beam-line magnet-current fluctuations. A typical reconstructed beam centroid distribution during one run is shown in Figure 4.3.

Since the angular distribution was affected by the beam angle (a slight offset of the beam angle will generate a linear term of $\cos\theta$ in the final λ extraction) and a single fixed target point in the analysis was not able to account for the angle fluctuations due to the beam-line movement, the beam centroids at the target were determined in a spill-by-spill basis by fitting the beam profile of the raw data at the target position. In the first second-pass analysis, the beam centroid of each event in each spill was determined by averaging the X and Y coordinates of the two muon tracks at the Z = 86 inches plane and then saved the centroid distributions (one for X and one for Y) in a temporary histogram. Then these distributions were fitted using Gaussian functions to determine the central values. These central values were tagged with the run number and the spill number and were saved in a 2-D lookup table. This procedure was applied to every spill of the raw data. If there were not enough events (the threshold number of events to perform the fitting was set to 50) in a spill to perform the fit, the centroid value was taken from the previous spill. If the first spill in a run did not have enough statistics, the centroid value was set to some default value depending on the data set. Then a second second-pass analysis was performed, using the centroid values stored in the lookup table, for each spill of data. The beam angles reconstructed in this procedure, on a run-by-run basis, were approximately constant within a

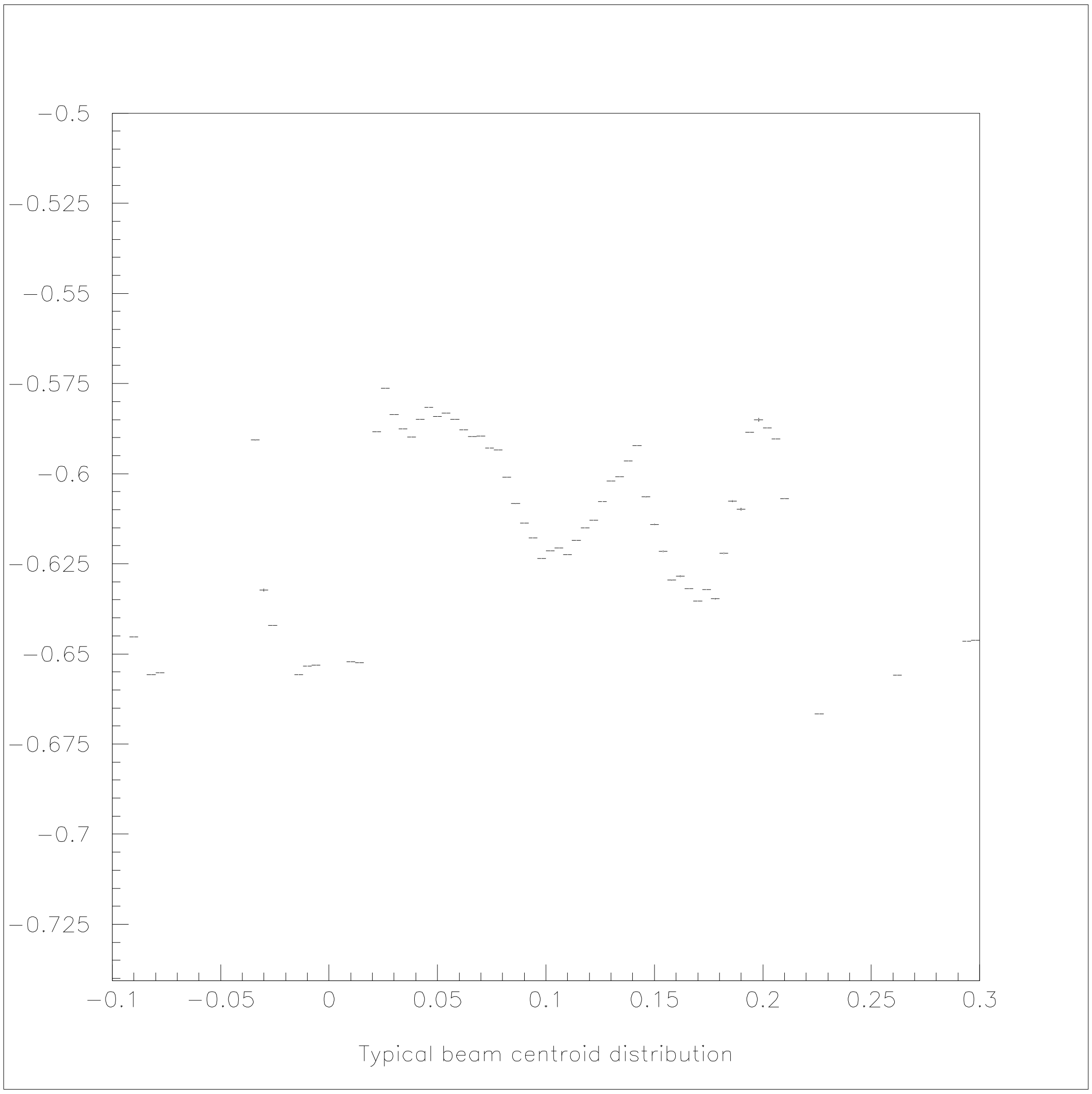

Figure 4.3: Beam-centroids positions during data taking. The vertical scale gives the Y-position and the horizontal scale gives the X-position in inches in the lab frame.

Table 4.2: Beam angles of each data set.

Data set	X angle(1E-3)	Y angle(1E-3)
12a	0.12	−1.09
12b	0.11	−1.05
12c	0.11	−0.94
13	0.00	−0.76
14	−0.02	0.11
15a	0.10	0.12
15b	0.05	0.31

data set. Some runs within a data set had very different angles and had to be treated separately. Data set 12 was broken into 12a, 12b, and 12c, and data set 15 was broken into 15a and 15b. The reconstructed beam angle for each data set is shown in Table 4.2.

4.2.3 Determining Beam Angle

The determination of the beam angle for each data set involved two phases. In the first step we obtained the initial value of the angle recovered by plotting the momentum vector from the ntuple. Note that the beam-centroid-fitting procedure described in the previous section had to be applied first. Then the second-pass analysis was done again using the initial angle. It was found that after one iteration the reconstructed angles converged within 0.03 mrad. Thus a second iteration was not necessary. Figure 4.4 shows the beam angle reconstructed from the experimental data set 15b as an example.

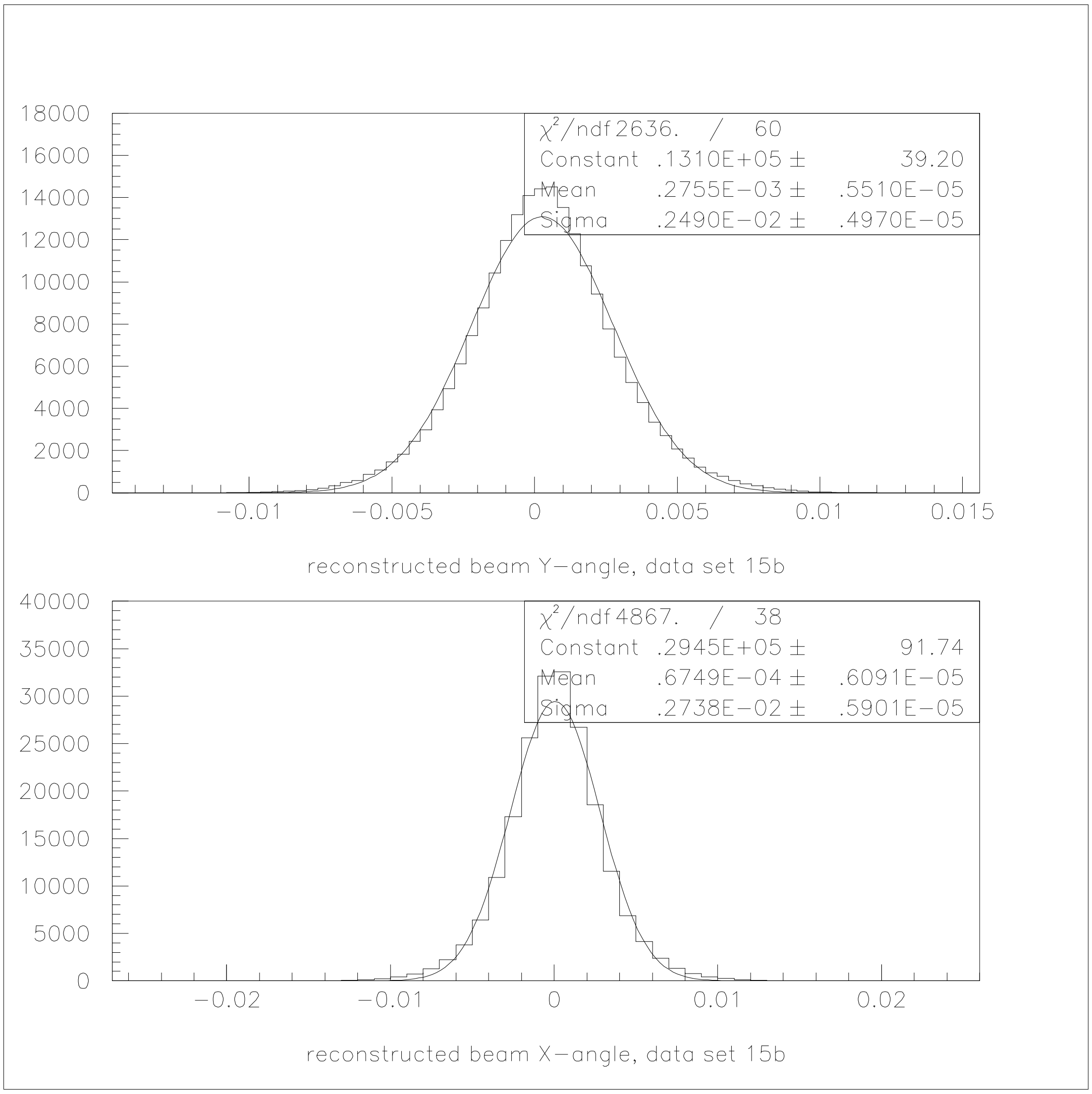

Figure 4.4: Beam angle reconstruction plots. These plots use data set 15b as an example. The peaks are fitted to a Gaussian function to determine the central values.

The second step in determining the beam angle was to look at the production-ϕ distribution. The production-ϕ (PPHI) distribution was very sensitive to the input beam angle. Monte Carlo events were generated to compare with the PPHI plots of the real data. The ϕ distribution of the real data is expected to be isotropical because both the beam and target were not polarized, and in the Monte Carlo the PPHI distribution was thrown isotropically. It was required that the ratio of the PPHI plots be flat, so there was no ϕ-term contribution in extracting the angular distribution. Usually small changes in the beam angle had to be added to the Monte Carlo in the generation phase to obtain good PPHI agreement. However those changes were small compared to the beam angle variation of 0.3 mrad, so it was not necessary to repeat the second-pass analysis. The ratio of real-data PPHI over MC data PPHI is given in Figure 4.5. The plot was fitted to $p1 \times \sin(p2 + \theta) + p3$. The amplitude shows that the uncertainty of the beam angle values used in Monte Carlo is about 2%.

4.3 Pass-3: PAW

The third and final pass of the analysis was performed with the Physics Analysis Workstation (PAW) program. This program provided a way to present a graphical output of the analysis. The input of this program can either be an existing histogram file, which is simply a vector, or an ntuple file, which consists of columns of vectors. When filtering the final candidates, some additional cuts

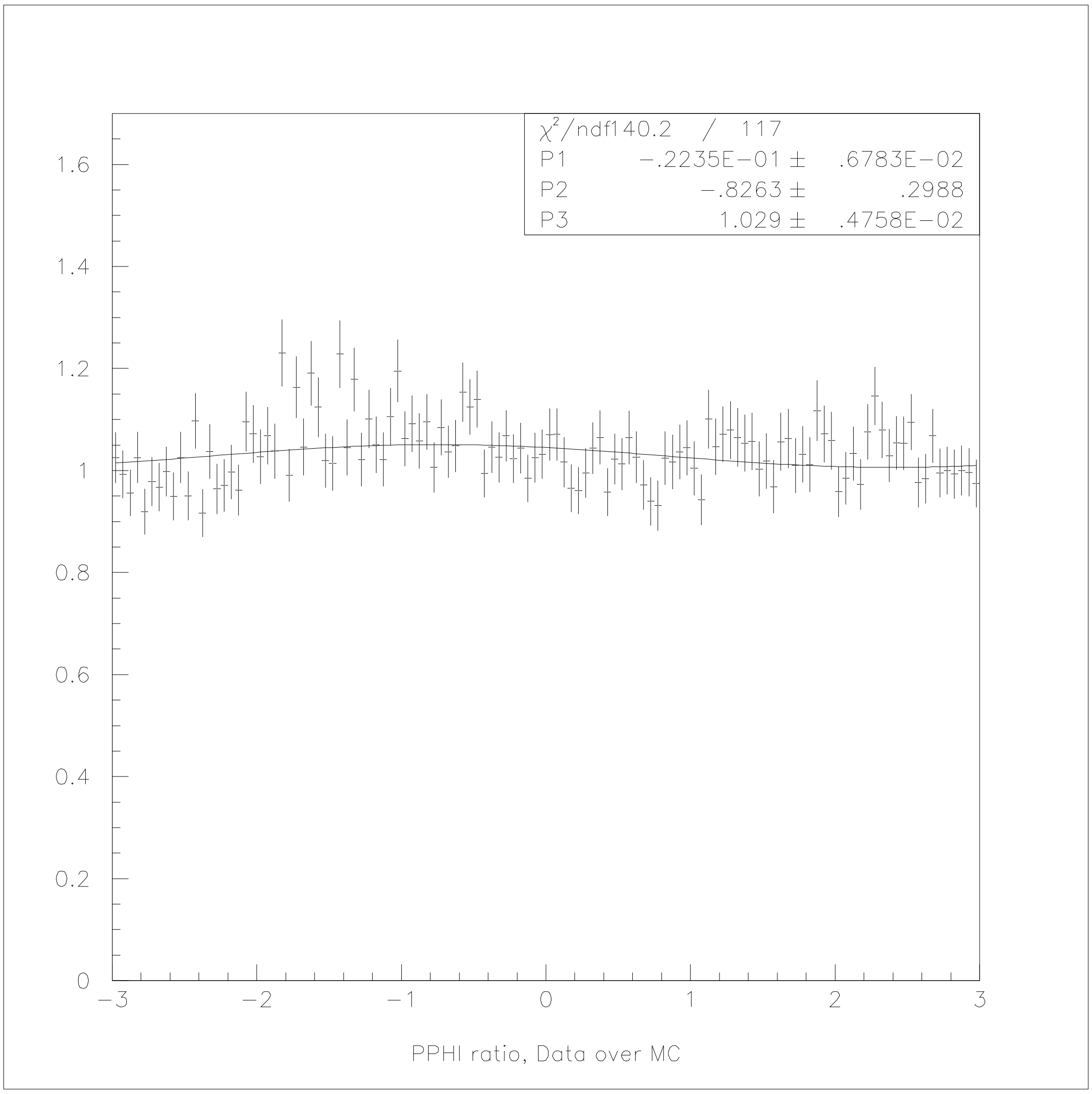

Figure 4.5: Production-ϕ distribution ratio. The ratio is experimental data divided by Monte Carlo. The plot is fitted to a sine function. The result shows a 2% uncertainty in the incident angle.

were applied to the events. Target vertex cuts and trigger-bit cuts were imposed. Events originating outside a $2''(\mathrm{X})\times 2''(\mathrm{Y})\times 200''(\mathrm{Z})$ range centered at the nominal target position were discared. The trigger-bit information TBRAW_CK of each event was checked to assure that it satisfied the physics-trigger requirements (satisfies Physics Trigger A 1, 2 or 4, see section 2.5.2). Like-sign pairs were discarded by the trigger cut at this point. As a result, about 94% of events survived the vertex cut and 91% of events survived both vertex and trigger cuts.

Those events left were then distributed according to their p_T and x_F values. The x_F range in this study was from 0.25 to 1.0 binned in intervals of 0.1; p_T was binned in intervals of 1 GeV. The last bin of x_F combined all the data above 0.85, and the last bin of p_T included the data having $p_T > 3.0$ GeV. The mass spectrum, from 2.0 GeV to 7.0 GeV plotted in 50-MeV bins, for each x_F and p_T bin was then fitted to a Gaussian plus some background function. The J/ψ peak was described by the Gaussian function, but the background shape varied as the kinematic range changed. Listed below are the functional forms used to do the background fitting in this study:

$$f(x) = exp(p1 + p2 * x), \tag{4.1}$$

$$f(x) = p1 + p2 * x + p3 * x^2, \tag{4.2}$$

$$f(x) = p1/(1 + (x/p2)^{p3}). \tag{4.3}$$

The uncertainties caused by the background function forms are discussed in section 4.6. The counts of J/ψ's in each bin of x_F and p_T were then determined by the formula

$$COUNTS = N * (bin\ width/\sqrt{2\pi}\sigma) * exp(-(x - centroid)^2/2\sigma^2) \tag{4.4}$$

where N, centroid, and σ are free parameters to fit. The value $N + \Delta N$ returned from the PAW fitting program provided the population of J/ψ's and the statistical uncertainty in that bin. Tables 4.3 to 4.6 give the approximate number of J/ψs in each bin for each data set.

Figure 4.6 shows the reconstructed spectra of some kinematic variables. The mass spectrum, on the upper-left, presents all the dimuon pairs recorded during the beam-dump run with masses up to 7.0 GeV. The other three variables, namely x_F, p_T, and $\cos\theta$, are plotted for the events that satisfied the vertex cuts and the trigger cuts and have a mass in the range between 2.5 GeV and 4.0 GeV. The purpose of the mass cut was to reduce the contributions from non-J/ψ events in these variables. One can see from the figure that this data sample contains a large collection of J/ψ's that extend over a wide kinematic range.

4.4 Monte Carlo

To extract J/ψ angular distributions correctly we rely on good knowledge of the angular acceptance. Monte Carlo simulation is the standard technique to ob-

Table 4.3: Number of J/ψ's in each bin of data set 12.

x_F / p_T(GeV)	0 - 1	1 - 2	2 - 3	> 3
0.3	322000	292000	78800	16600
0.4	531000	497000	137000	28000
0.5	323000	310000	84800	16900
0.6	142000	139000	36500	6900
0.7	43100	42000	10700	1900
0.8	8800	7800	2200	300
> 0.85	900	900	-	-

Table 4.4: Number of J/ψ's in each bin of data set 13.

x_F / p_T(GeV)	0 - 1	1 - 2	2 - 3	> 3
0.3	363000	336000	91800	17800
0.4	244000	232000	66400	14000
0.5	119000	116000	32400	7100
0.6	47500	45900	13100	2600
0.7	13400	13100	3600	700
0.8	2500	2800	700	100
> 0.85	300	300	-	-

Table 4.5: Number of J/ψ's in each bin of data set 14.

x_F / p_T(GeV)	0 - 1	1 - 2	2 - 3	> 3
0.3	372000	355000	99300	19100
0.4	244000	243000	71000	15200
0.5	120000	120000	34200	7300
0.6	47600	47300	13200	2800
0.7	13300	13600	3800	700
0.8	2600	2700	800	100
> 0.85	400	300	-	-

Table 4.6: Number of J/ψ's in each bin of data set 15.

x_F / p_T(GeV)	0 - 1	1 - 2	2 - 3	> 3
0.3	260000	235000	62300	13200
0.4	413000	387000	107000	22800
0.5	250000	240000	65200	13400
0.6	109000	106000	27700	5400
0.7	33100	32100	8400	1500
0.8	6400	6300	1500	300
> 0.85	700	600	-	-

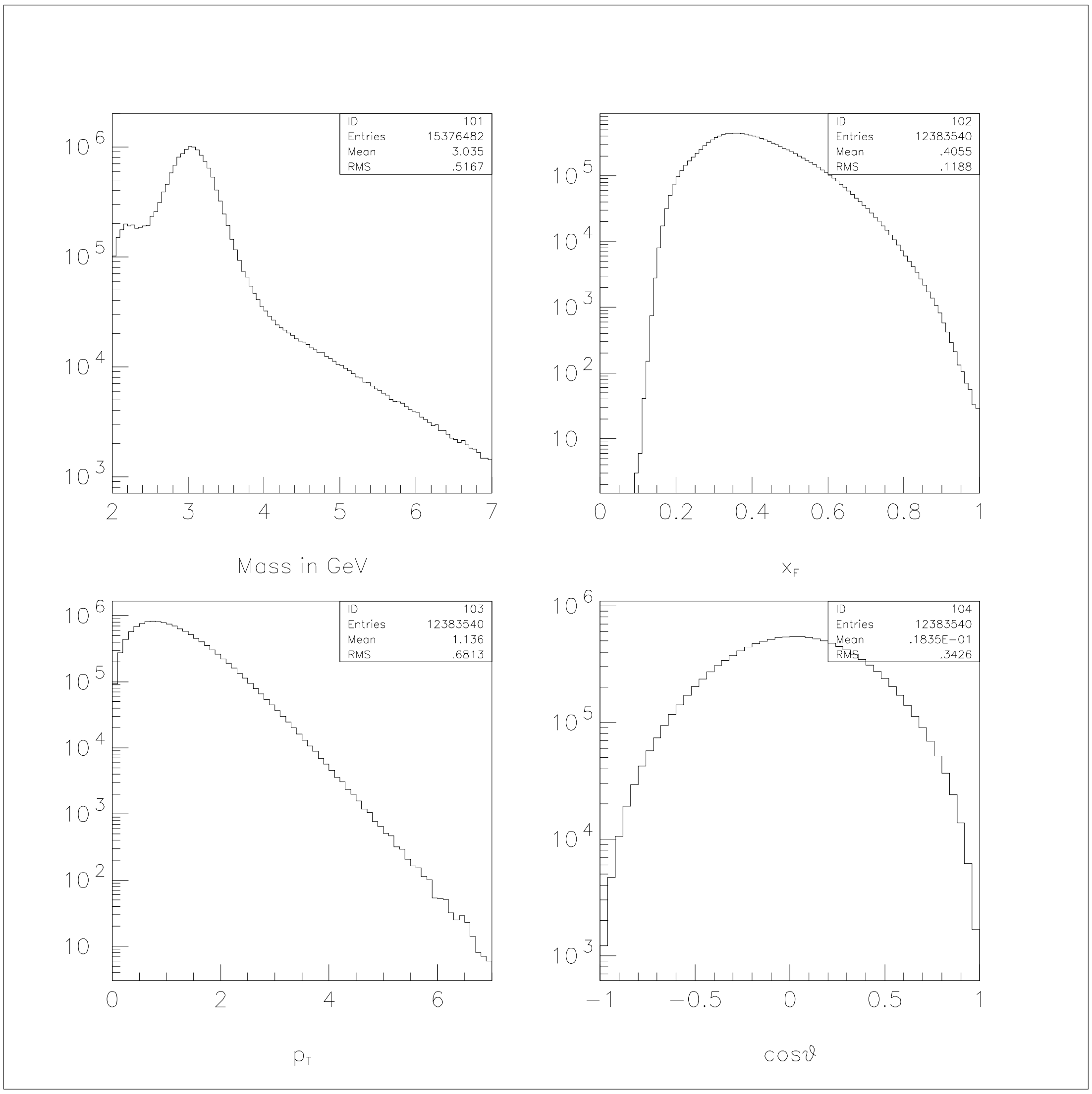

Figure 4.6: Reconstructed spectra of some kinematic variables. Mass (2.5-4.0 GeV), vertex, and trigger cuts have been applied to the x_F, p_T and $\cos\theta$ plots.

tain the acceptance. In the Monte Carlo study the experimental apparatus setup was programmed as close as possible to the real experiment, and all the apparatus input parameters, some of which were physically measurable, were tuned according to the best of our knowledge. However the physics part of the Monte Carlo generation, which is the part of real interest, was unknown and relied completely on theoretical model calculations. The output of the Monte Carlo was then compared with the experimental data, assuming that the simulation of the apparatus part was reliable and trustworthy. The difference between the Monte Carlo results and the experimental measurements was then used to improve the various thrown physics kinematic quantities. The whole procedure was an iterative process since the acceptance depended on the thrown distributions, and the thrown distributions, usually taken from the experimental data distributions, relied on the knowledge of the acceptance. The accepted Monte Carlo events were stored in the same format as the raw data, and then were analyzed as the experimental data. The final output was stored in the form of ntuple files, like the real data. The acceptance correction of a physical variable to be applied to the experimental data was given by the reconstructed MC distribution divided by the thrown distribution.

In this section we will describe the thrown functions of the physical variables and compare them with the experimental data.

4.4.1 x_F Distribution

x_F can be understood as the J/ψ longitudinal momentum P_L divided by its maximum kinematically allowed value $P_{L,Max}$, which is approximately equal to half of the square root of the center-of-mass energy S, in the beam-target center-of-mass frame. Theoretically the x_F differential cross section is of interest because it can be calculated based on the knowledge of the parton distributions and some phenomenological models. In this study we used an empirical formula for the thrown x_F distribution for J/ψ within the range $0.25 < x_F < 1.0$:

$$x_F \equiv \frac{P_L}{P_{L,Max}} \approx \frac{P_L}{\sqrt{S}/2} , \tag{4.5}$$

$$d\sigma/dx_F = P3(1-0.82x_F)^{8.7} , \tag{4.6}$$

$$P3 = 2.784 - 10.14x_F + 17.81x_F^2 - 9.585x_F^3 . \tag{4.7}$$

The third-order polynomial was used to describe better the high-x_F part. The comparison of the Monte Carlo and the real data is shown in Figure 4.7. At each bin of x_F the counts of J/ψ's for the real data were obtained by fitting the mass spectrum to a Gaussian plus a exponential background. The agreement is good to about 3% for $x_F < 0.7$, which includes 98.2% of all the data. The largest discrepancy, however, about 20%, for $x_F > 0.7$ comes from the thrown shape in the Monte Carlo and the background uncertainty in the data. This has no effect on our results of $d\sigma/d\cos\theta dx_F$ and $d\sigma/d\cos\theta dx_F dp_T$ since these are differential quantities. The effects on $d\sigma/d\cos\theta$ are also expected to be very small because only a few events are at that high x_F.

4.4.2 p_T Distribution

p_T is the transverse momentum of the dimuon pair. The origin of p_T is understood as a combination of intrinsic transverse motions of the partons inside the hadrons and higher-order QCD processes. Naively p_T was expected to be an independent variable from x_F, which accounts for the longitudinal part of the dimuon pair momentum, except at some extreme kinematic ranges where the maximum available energy becomes a constraint. However experimentally it was found that $< p_T >$ was correlated with x_F beyond pure acceptance effects. In our Monte Carlo code we have the following form for the p_T thrown function:

$$d\sigma/dp_T = p_T/(1 + (p_T/p0(x_F))^2)^6, \tag{4.8}$$

$$p0 = 1.43 + 8.28x_F - 15.3x_F^2 + 2.66x_F^3 + 13.9x_F^4 - 9.23x_F^5. \tag{4.9}$$

p0 was expressed in a polynomial form of x_F. This form attemped to fold in the real physical correlations between x_F and $< p_T >$ as well as possible residual acceptance effects. Figure 4.8 shows $< p_T >$ as a function of x_F for the experimental data and Monte Carlo data. The overall integrated p_T distribution from MC was then compared to the integrated p_T distribution of the data; this is shown in Figure 4.9. For each bin of p_T, the mass spectrum of the data was fitted to

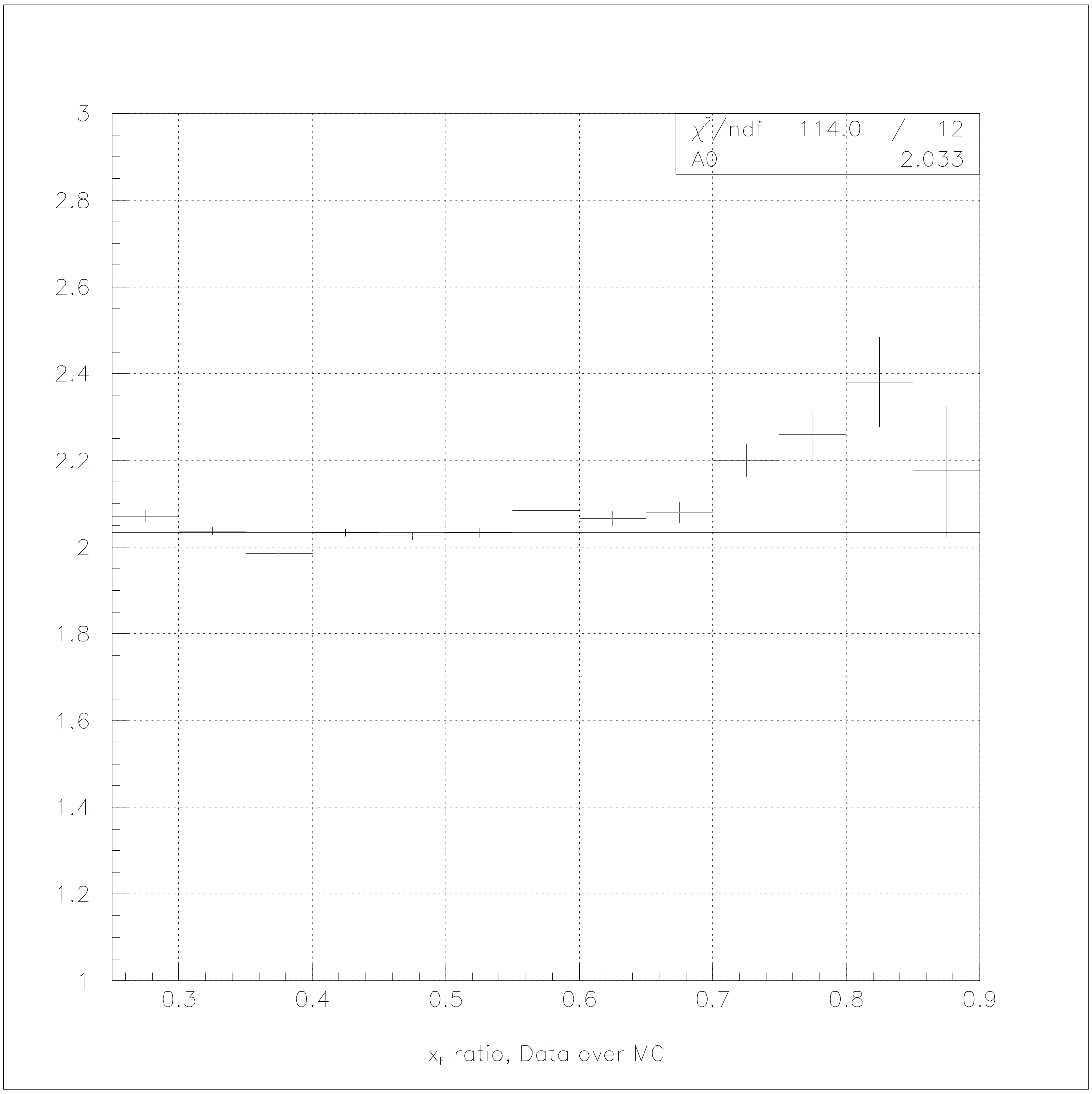

Figure 4.7: $d\sigma/dx_F$ of data over $d\sigma/dx_F$ of Monte Carlo. The agreement is good within 3% for $x_F < 0.7$, in which contains 98.2% of the data.

a Gaussian plus a second-order polynomial as the background. The number of J/ψ's was then calculated from the Gaussian parameters. The Monte Carlo $\cos\theta$ distribution was weighted according to the normalized ratio of Figure 4.9.

4.4.3 Angular Thrown Distributions

There are three independent angles used to specify the dilepton pair production: decay-θ (DTHETA), decay-ϕ (DPHI), and production-ϕ (PPHI). The DTHETA variable was defined as the polar angle in the Collin-Soper frame, and the DPHI variable was defined by the azimuthal angle with DPHI $= 0$ pointing up with respect to the Z axis in the C-S frame. The PPHI gave the azimuthal angle of the virtual photon around the lab Z-axis. PPHI $= 0$ was chosen to be the positive X direction of the lab coordinate system and it is a lab-frame variable. All three angles in this MC code were thrown as flat distributions. The angular distributions obtained from the final ntuple thus gave the angular-acceptance shape directly.

4.5 Extracting Angular Distributions

In this section the technique for obtaining the polarization parameter λ is described.

4.5.1 General Procedure

$d\sigma/d\cos\theta dp_T dx_F$ of J/ψ was determined by taking the accepted events divided by the acceptance, which was obtained by taking the Monte Carlo $\cos\theta$

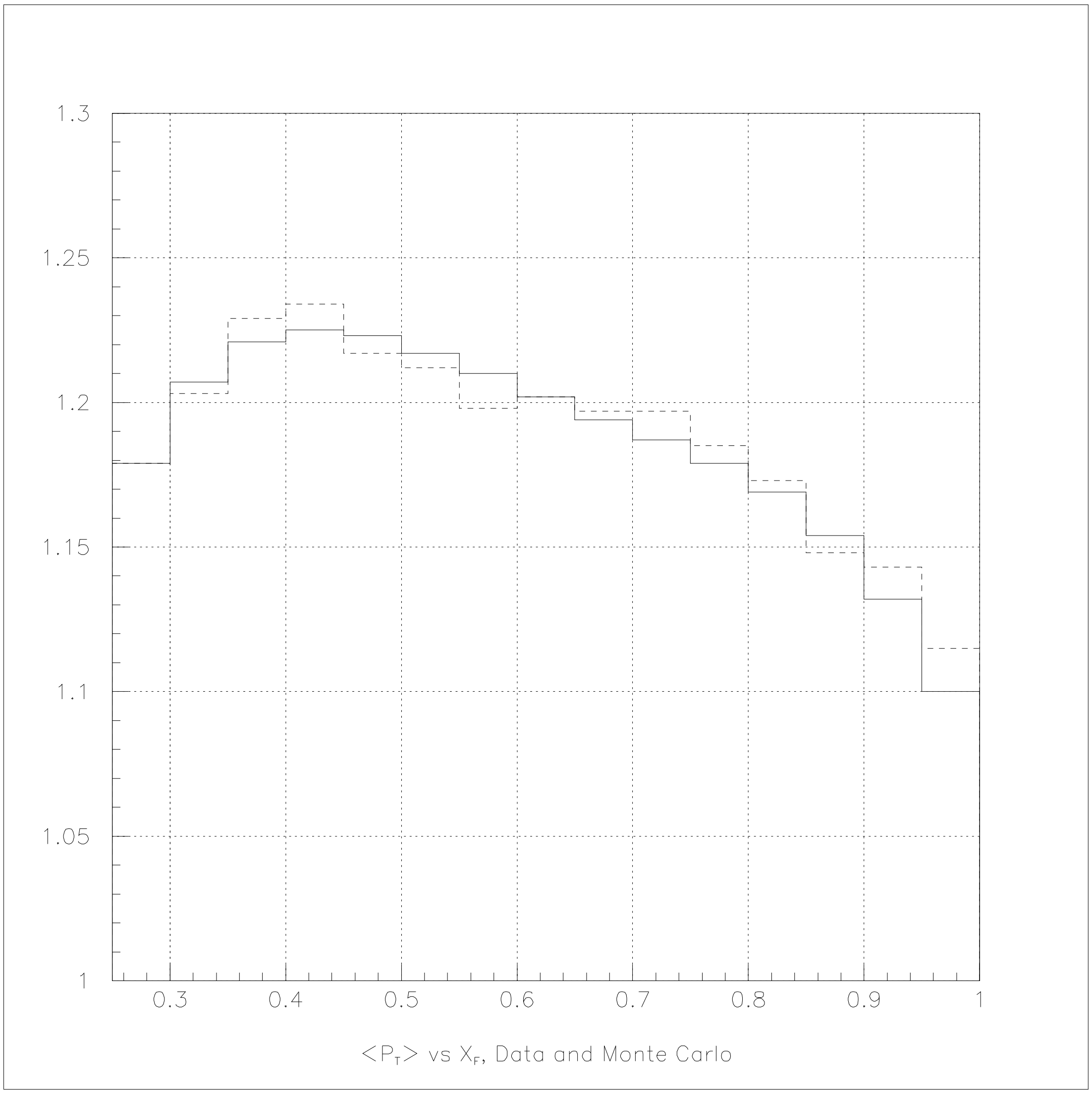

Figure 4.8: $< p_T >$ vs x_F. Solid line: Data. Dashed line: Monte Carlo.

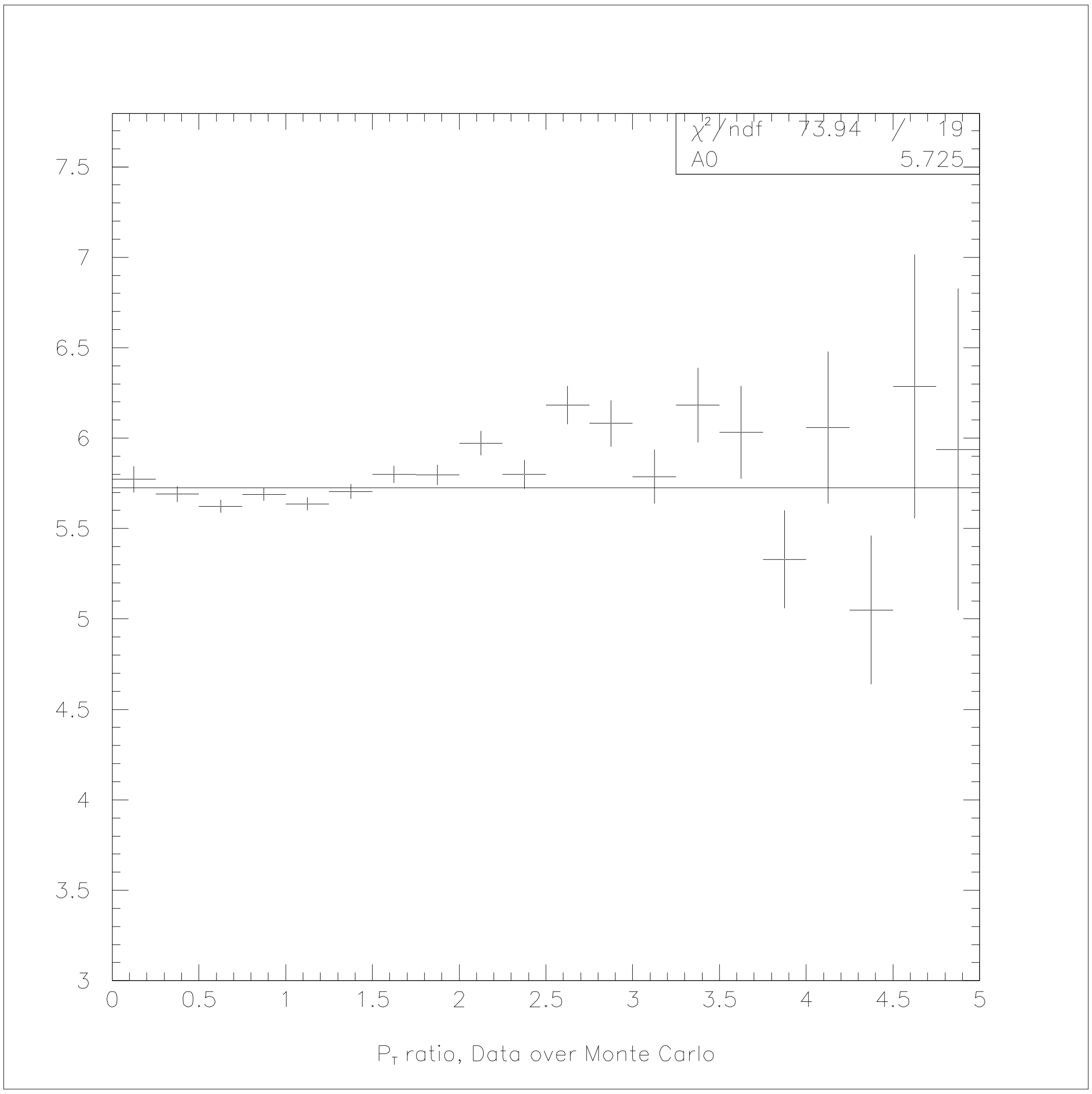

Figure 4.9: $d\sigma/dp_T$ of data over $d\sigma/dp_T$ of Monte Carlo. The plot is fitted to a zeroth-order polynomial. The result of the fit is the normalization constant used in the $\cos\theta$ weighting.

distribution divided by the flat thrown distribution. The statistical uncertainty of the acceptance was small compared to the statistical uncertainty of the data. Before being applied to the data, the acceptance curves were weighted by the p_T distribution of the real data. The uncertainties associated with the p_T thrown function were thus expected to be minimized. In addition, since the $\cos\theta$ acceptances in this study were calculated in small x_F and p_T bins, the uncertainties due to the shape of the thrown x_F and p_T distributions should be reduced. The acceptance of J/ψ as a function of $\cos\theta$ for each bin of x_F and p_T of the Monte Carlo simulation is given in Appendix A.

To extract the counts of J/ψ, the fitting procedure described in section 4.3 was applied to each bin of x_F, p_T, and $\cos\theta$, with bin width being 0.1, 1.0 GeV, and 0.1, respectively. At large x_F and p_T bins, the bin width of $\cos\theta$ was increased to 0.2 to give better statistics. The fitting of each histogram is shown in Appendix B. The number of counts, calculated according to Equation 4.4, in each bin of $\cos\theta$ was plotted to obtain the accepted $\cos\theta$ distribution. Each accepted $\cos\theta$ distribution was then divided by the corresponding acceptance, and the shape of $d\sigma/d\cos\theta dp_T dx_F$ of J/ψ was thus obtained. The $\cos\theta$ distribution for each bin of x_F and p_T was then fitted according to $d\sigma/d\cos\theta \sim 1 + \lambda\cos^2\theta$. The fitting plots of $d\sigma/d\cos\theta dp_T dx_F$ are shown in Appendix C.

4.5.2 Combined Data Set

As mentioned in section 4.2, there were seven data sets differing by the incident beam angle, the trigger matrix, or the magnet settings. To obtain the final results, those sets were combined according to the SM12 currents. Data sets 12a, 12b, 12c, 15a, and 15b together formed the "SM12 = 2800" set and data sets 13 and 14 formed the "SM12 = 2040" set. The events from different experimental data sets were directly added together, and the average $\cos\theta$ acceptance was calculated by

$$< Acceptance >= \sum_i f_i \times a_i(\cos\theta)/N_i(\cos\theta) \tag{4.10}$$

with

$$\sum_i f_i = 1, \tag{4.11}$$

where f_i is the fraction of the accepted events of data set i among all accepted events, and $a_i(\cos\theta)/N_i(\cos\theta)$ is the $\cos\theta$ acceptance distribution of data set i. The combined results were obtained by dividing the sum of the accepted events by the average acceptance. The results for the two different magnet settings were obtained separately.

In the next chapter and throughout Appendix A to C, the results are presented for the two magnet settings. The agreement between the two sets of results provides an important check that our results are not affected by apparatus effects. Combined results from the two magnet settings are derived to compare with results from other fixed-target experiments.

4.6 Uncertainties

In this section two types of errors are discussed: statistical uncertainties and systematic uncertainties. These different sources of errors are summarized in tables.

4.6.1 Statistical Uncertainty

Statistical errors in determining λ are the direct results of statistical uncertainties in the counts of J/ψ. The statistical errors of the acceptance are supressed by outnumbering Monte Carlo events over the experimental data. The statistical errors of λ were obtained by including only the statistical uncertainties of the J/ψ counting in the λ fitting. The λ's and the statistical errors are shown in Table 5.1 and Table 5.2.

4.6.2 Systematical Errors from Analysis and MC Inputs

To estimate the errors caused by the uncertainties of the magnetic fields, the tweek values used in the analysis were varied by 1% in the analysis and Monte Carlo. The 1% uncertainty is a reasonable upper limit for the magnetic-field strength because the tweek values were tightly constrained by the reconstructed J/ψ mass and the uniterated Z-vertex position. It was found that the λ values changed by ±0.01 as the field strength of SM12 was adjusted, and varied by ±0.01 as SM3 was changed.

The incident beam angle has a strong effect on the $\cos\theta$ distribution. Although the value of the beam angle was tuned to remove any asymmetry in the ratio plots of decay θ and production ϕ between experimental data and Monte Carlo, the precise incident angle is actually unknown. To study the effect of this uncertainty, the beam angle used in the analysis and Monte Carlo was varied by ± 0.0002, which is twice the beam angle-spread sigma. The results showed that the λ values were changed by ± 0.02 for large x_F and by ± 0.04 for small x_F.

The target position in the X-Y plane used in the Monte Carlo was an average value determined from the data. In data reconstruction the beam center was calculated for each spill. To study this uncertainty, the beam centroid of Monte Carlo events was moved by ± 0.1 inch in both the X and Y direction. The circle of the 0.1 inch confinement was determined by the data distribution. The net effect on the λ values is ± 0.02.

The p_T dependence of the $\cos\theta$ distribution and the impact of the p_T thrown function on the $\cos\theta$ acceptance was also studied. The $\cos\theta$ acceptance was calculated by weighting the p_T distribution according to the real data. Another calculation was performed without weighting to the real data. The $< p_T >$ with and without weighting differed by 5%, which is compatible with the uncertainties in extracting the p0 parameter in the p_T thrown formula. It was then found that within this variation, the λ values moved by ± 0.06.

Table 4.7: Summary of the systematic errors from all the sources.

x_F	SM12	SM3	angle	centroid	$< p_T >$	fit limit	background	overall
0.3	0.01	0.01	0.04	0.02	0.06	0.05	0.06	0.109
0.4	0.01	0.01	0.04	0.02	0.06	0.04	0.05	0.099
0.5	0.01	0.01	0.02	0.02	0.06	0.04	0.03	0.084
0.6	0.01	0.01	0.02	0.02	0.06	0.03	0.02	0.077
0.7	0.01	0.01	0.02	0.02	0.06	0.03	0.02	0.077
0.8	0.01	0.01	0.02	0.02	0.06	0.03	0.02	0.077
0.9	0.01	0.01	0.02	0.02	0.06	0.03	0.02	0.077

4.6.3 Systematical Errors from Peak Fitting

Other contributions to the systematic errors come from the J/ψ peak fitting process. The λ values were found to change slightly with different choices of the fitting limits. With the same background function, changing the fitting limit was equivalent to changing the continuum shape within the uncertainties. It was found that this contributed a ± 0.03 uncertainty to the systematic errors.

The selection of the background function form also produced systematic errors. Three different functions, equations 4.1, 4.2, 4.3, were used to fit the continuum distribution. The uncertainty from different background functions on λ is ± 0.02 for large x_F and is about ± 0.05 for small x_F. Table 4.7 gives a summary of the systematic errors from all the contributions.

5. RESULTS

The angular distributions of the J/ψ decay in the dimuon channel have been measured for the process $p + Cu \rightarrow J/\psi + X$ using an 800 GeV proton beam. In this chapter the results are presented, along with comparison to the theoretical predictions and the results from other experiments.

5.1 Drell-Yan Angular Distribution

In the same data sample used in this study, about 200K dimuon pairs with mass ranging from 4.0 GeV to 7.5 GeV were also recovered, of which most are Drell-Yan events. This data sample is of interest because the target was copper and no angular-distribution measurements had ever been published for the proton-induced Drell-Yan process in this mass range. Though the amount of data sample was not enough to study the polarization as a function of x_F, it was still useful to examine the overall polarization parameter λ, which was expected to be equal to unity based on the standard Drell-Yan production mechanism, as a cross check for the J/ψ angular distribution results. Below the procedures are described in more detail, and the results are presented

5.1.1 Random Background

Random muon pairs were the most significant background contamination in the mass range of interest. The definition of a random pair is that two opposite-sign muons, which were produced independently by pion decay or other processes, coincidentally fired the trigger system and appeared to be a valid target dimuon event. The random pair distribution could not be measured directly, because the pairs were indistinguishable from the real Drell-Yan dimuons in the spectrometer; they were however simulated from the like-sign event distribution by changing the sign of the Y-momentum of one of the like-sign tracks to calculate other kinematic variables of the pair, based on the assumption that the probability to form a random pair is the same as to form a like-sign pair given the first muon track. Single-muon trigger rates were used to normalize the ratio of like-sign pairs and the randoms; the like-sign pairs were expected to have the same single-muon trigger rate as the random pair would have. Figure 5.1 shows some kinematic-variable distributions of the random pairs.

5.1.2 Random Subtraction and Results

From Figure 5.2 it was understood that the random subtraction was important in order to extract the Drell-Yan angular distribution, even for pairs of mass greater than 5.0 GeV. The normalization factor for the random events was determined by matching the number of like-sign pairs from the random ntuple file and from the data, since the random events were generated according to the amount of like-sign pairs of the data. Then the angular acceptance of the Drell-Yan events was obtained by a dedicated Monte Carlo run. The $\cos\theta$ distribution of the Drell-Yan data, after subtracting out the randoms, was corrected for acceptance and the angular distribution was obtained. The angular distribution of Drell-Yan events

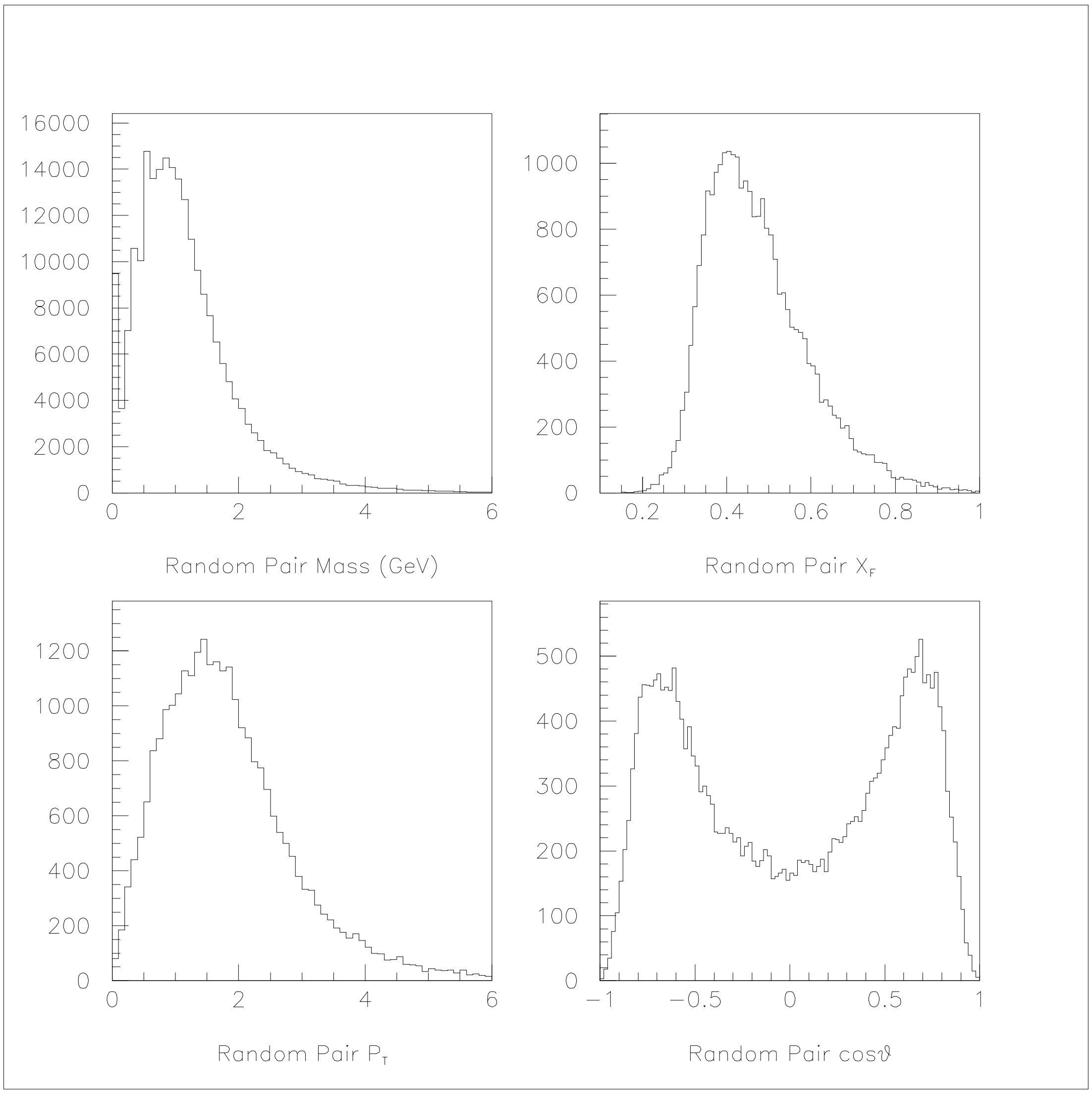

Figure 5.1: Some kinematic variables of the random pairs. The mass range of the x_F, p_T, and $\cos\theta$ plots is above 2 GeV.

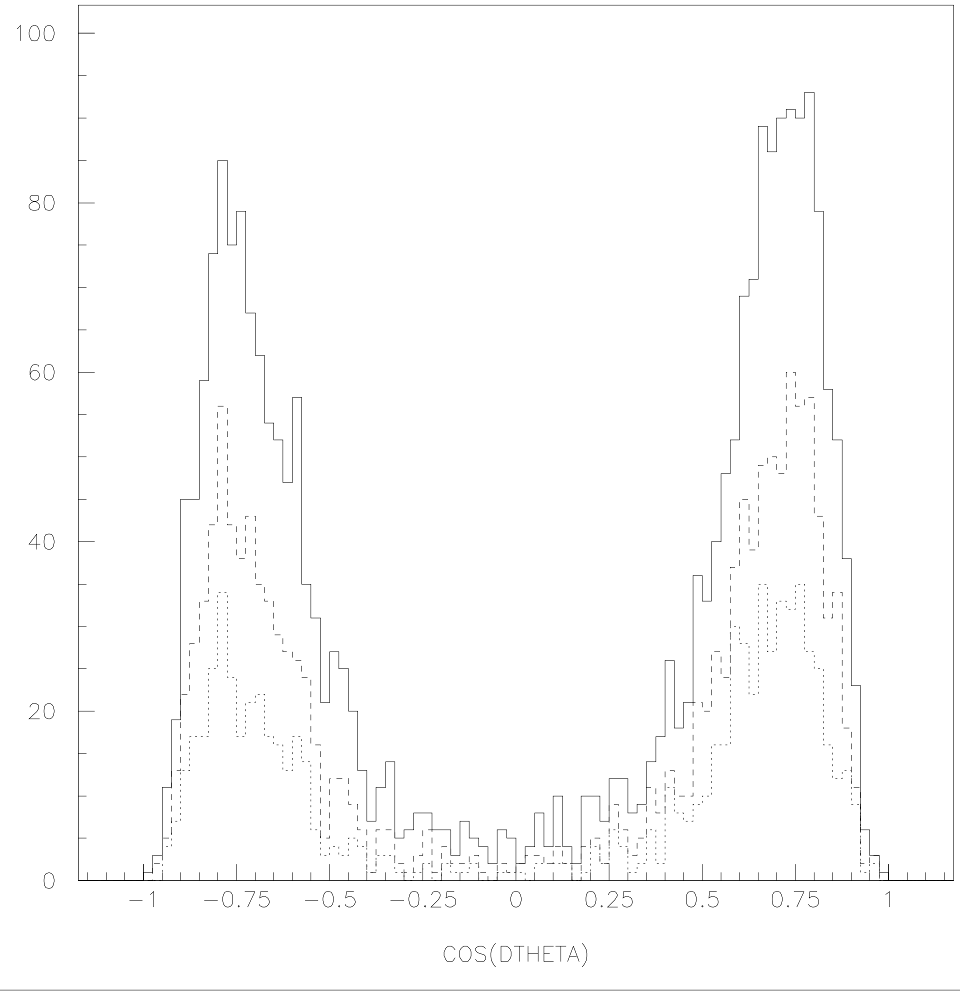

Figure 5.2: $\cos\theta$ of the random pairs. Solid line: pair mass $>$ 4 GeV. Dashed line: pair mass $>$ 4.5 GeV. Dotted line: pair mass $>$ 5 GeV.

in the mass range of 4.0 GeV to 7.0 GeV is shown in Figure 5.3. The rise at the edges is understood as a resolution problem and the same effect has been reproduced by broadening the $\cos\theta$ resolution. Also, the random pairs show a very strong rise at large $\cos\theta$; a slight mismatch in the normalization can result in the same effect. For these reasons, for the Drell-Yan data the angular distribution was fitted in the range of $-0.7 < \cos\theta < 0.7$ in which the systematic uncertainties are best handled. A result of $\lambda = 0.98 \pm 0.04$ was obtained. This is consistent with 1.0 as predicted. This provided a confidence check for the J/ψ angular distribution presented in next section.

5.2 J/ψ Angular Distribution Results

In this section the J/ψ angular distribution results are presented. The measurements were performed under two different magnet configurations, therefore different acceptances, in order to minimize the systematic bias. They are effectively two independent measurements. The polarization parameter λ in bins of p_T and x_F is presented in Tables 5.1 and 5.2, and plotted in Figure 5.4. In the figures only the statistical errors are shown. The results from the two measurements are in agreement with each other. This provides a confirmation that the results are not affected by the specific apparatus settings.

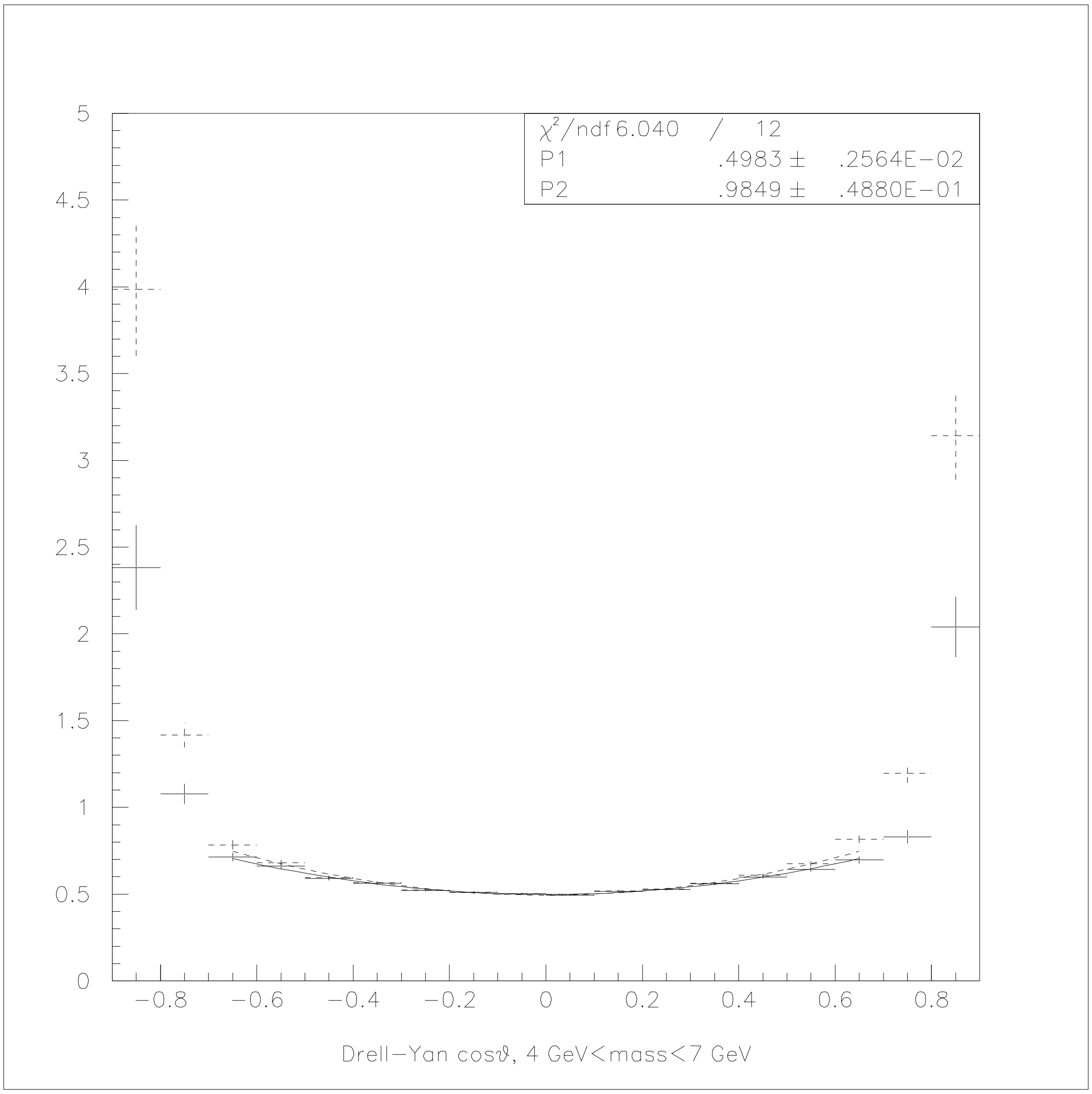

Figure 5.3: $\cos\theta$ of the Drell-Yan pairs. The pairs have mass ranging from 4 GeV to 7 GeV. Solid line: After random subtraction. Dashed line: Before random subtraction. A λ value of 0.98 ± 0.04 is obtained after correcting for the random pairs. The rise at the edges is due to resolution effects.

Table 5.1: λ in x_F and p_T bins for the "SM12 = 2040" data. The errors are statistical only.

x_F	$0 < p_T < 1$	$1 < p_T < 2$	$2 < p_T < 3$	$3 < p_T$
0.25 - 0.35	0.153 ± 0.037	0.057 ± 0.024	0.093 ± 0.026	0.124 ± 0.049
0.35 - 0.45	0.218 ± 0.031	0.015 ± 0.019	0.095 ± 0.026	0.141 ± 0.056
0.45 - 0.55	0.146 ± 0.023	0.035 ± 0.017	0.101 ± 0.025	-0.052 ± 0.049
0.55 - 0.65	0.151 ± 0.039	-0.013 ± 0.027	0.072 ± 0.041	-0.06 ± 0.08
0.65 - 0.75	0.111 ± 0.070	-0.211 ± 0.046	0.023 ± 0.093	-0.43 ± 0.13
0.75 - 0.85	-0.17 ± 0.15	-0.22 ± 0.09	-0.14 ± 0.30	-
> 0.85	-0.44 ± 0.42	-	-	-

Table 5.2: λ in x_F and p_T bins for the "SM12 = 2800" data. The errors are statistical only.

x_F	$0 < p_T < 1$	$1 < p_T < 2$	$2 < p_T < 3$	$3 < p_T$
0.25 - 0.35	0.189 ± 0.044	0.135 ± 0.023	0.120 ± 0.034	0.060 ± 0.064
0.35 - 0.45	0.162 ± 0.029	0.095 ± 0.015	0.170 ± 0.021	0.170 ± 0.045
0.45 - 0.55	0.115 ± 0.022	0.051 ± 0.013	0.153 ± 0.020	0.057 ± 0.040
0.55 - 0.65	0.018 ± 0.028	-0.053 ± 0.020	-0.026 ± 0.028	0.01 ± 0.06
0.65 - 0.75	-0.032 ± 0.049	-0.174 ± 0.033	-0.167 ± 0.059	-0.09 ± 0.12
0.75 - 0.85	-0.25 ± 0.10	-0.09 ± 0.10	-0.21 ± 0.19	-
> 0.85	-0.51 ± 0.54	-	-	-

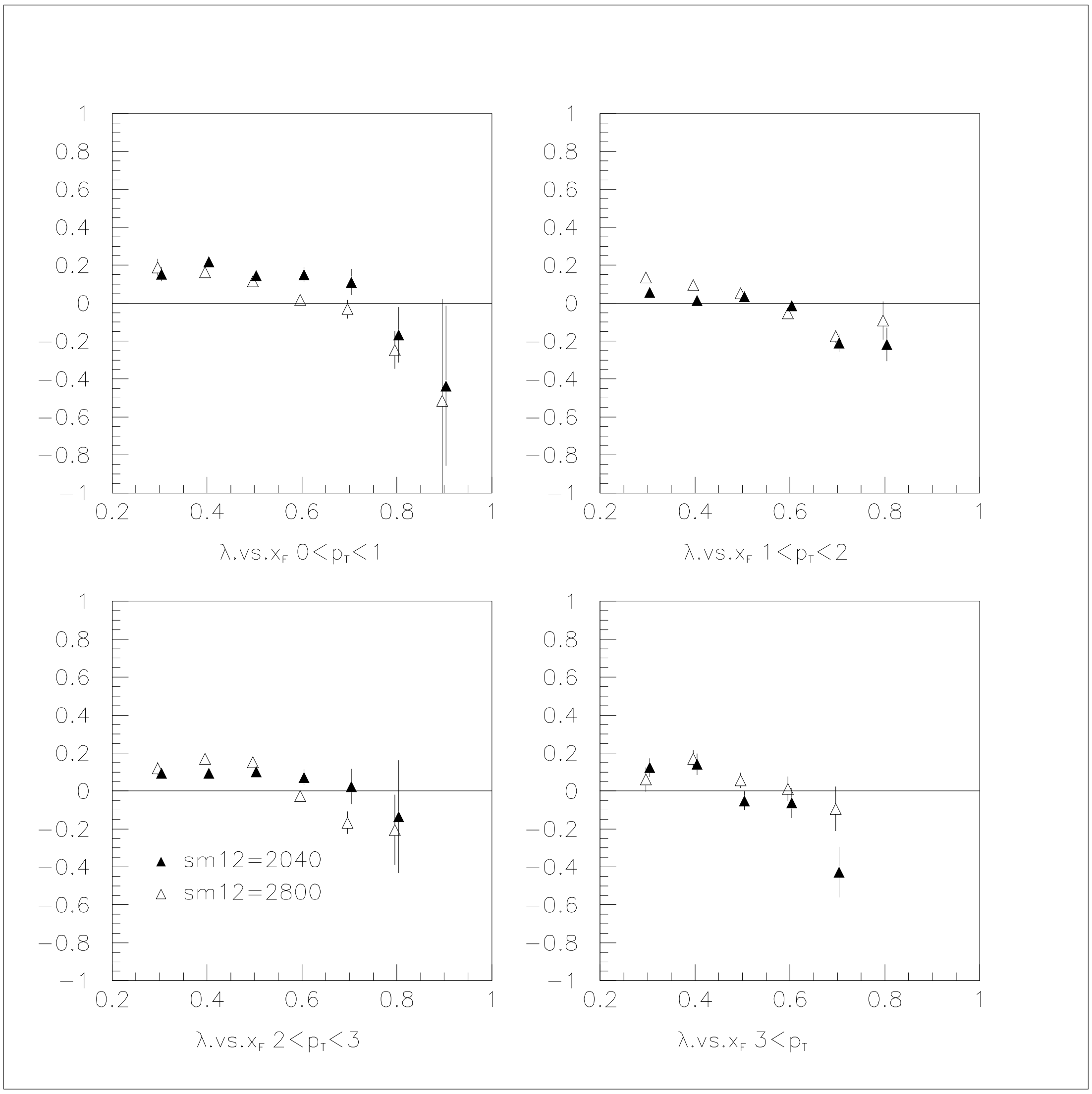

Figure 5.4: J/ψ polarization parameter λ in x_F and p_T bins. The errors shown here are statistical only.

Table 5.3: λ in x_F bins with statistical errors only.

x_F	$\lambda(x_F)(\mathrm{SM12} = 2040)$	$\lambda(x_F)(\mathrm{SM12} = 2800)$	Combined
0.25 - 0.35	0.092 ± 0.015	0.134 ± 0.017	0.110 ± 0.011
0.35 - 0.45	0.081 ± 0.013	0.129 ± 0.011	0.109 ± 0.008
0.45 - 0.55	0.073 ± 0.012	0.086 ± 0.009	0.081 ± 0.007
0.55 - 0.65	0.041 ± 0.019	-0.026 ± 0.014	-0.002 ± 0.011
0.65 - 0.75	-0.116 ± 0.034	-0.134 ± 0.024	-0.128 ± 0.020
0.75 - 0.85	-0.200 ± 0.073	-0.174 ± 0.066	-0.186 ± 0.049
> 0.85	-0.44 ± 0.42	-0.51 ± 0.54	-0.47 ± 0.33
All data	0.065 ± 0.007	0.070 ± 0.005	0.069 ± 0.004

5.3 Comparison

In order to compare with other experiments, λ values in x_F and p_T bins from E866 measurements were combined to obtain λ in x_F bins and the overall integrated λ using the following the relations:

$$\bar{A} = \frac{\sum_i w_i A_i}{\sum_i w_i} \tag{5.1}$$

$$w_i = 1/\sigma_i^2 \tag{5.2}$$

where σ_i is the statistical error of some measurement A_i, and $\bar{A}$ is the average value of A_i. The results are shown in Table 5.3. One can see from the table that the J/ψ starts slightly transversely polarized at small x_F, then eventually becomes partially longitudinally polarized as x_F increases toward unity. The λ values from both magnet settings versus x_F are plotted in Figure 5.5.

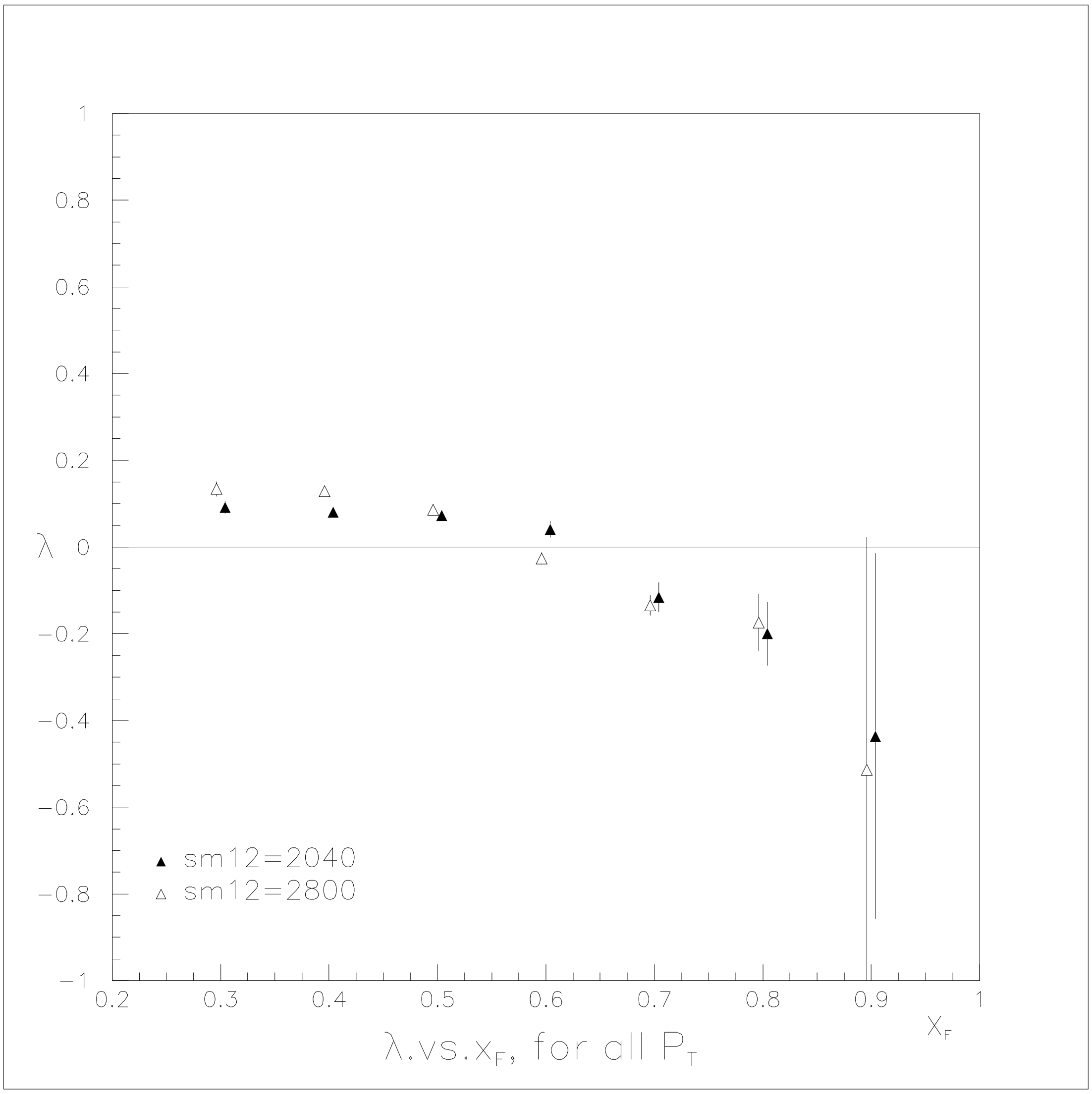

Figure 5.5: J/ψ polarization parameter λ in x_F bins. The errors are statistical only.

The E866 results are compared with the results of CIP data [Bii 87]. Figure 5.6 shows the E866 results and data published by the CIP group. Recall that the CIP experiment was fixed-target πN collisions. At large x_F, both experiments observe longitudinal polarizations. At smaller x_F, E866 sees small transverse polarization while the CIP group saw no polarization. Since the dominant Feynman diagrams are different for pN (mainly g-g fusion) and πN (it has significant $q\bar{q}$ contributions) at small x_F, the differences in the polarization are not unexpected. However if the 0.1 systematic errors are included, the E866 results at $x_F < 0.5$ are marginally in agreement with no polarization.

The integrated polarization parameter λ obtained by E866 and other previous experiments are presented in Table 5.4 for comparison. Recall that E866 uses the Collin-Soper frame and the other experiments have used the Gottfried-Jackson frame as their reference frame. However the p_T in fixed-target experiments is low enough that the direct comparison is still sensible. E866 gives $\lambda = 0.069 \pm 0.004$ integrated over all available data. If the systematic error is included, the E866 result shows no polarization. The transverse polarization at small x_F is partially cancelled by the longitudinal polarization at large x_F. The overall result is in agreement with other experiments, and in contrast to the non-relativistic QCD calculation.

The λ's were also integrated in 1-GeV p_T bins for $x_F < 0.45$ and $x_F > 0.45$ to study the p_T dependence, as shown in Figure 5.7. No p_T dependence was

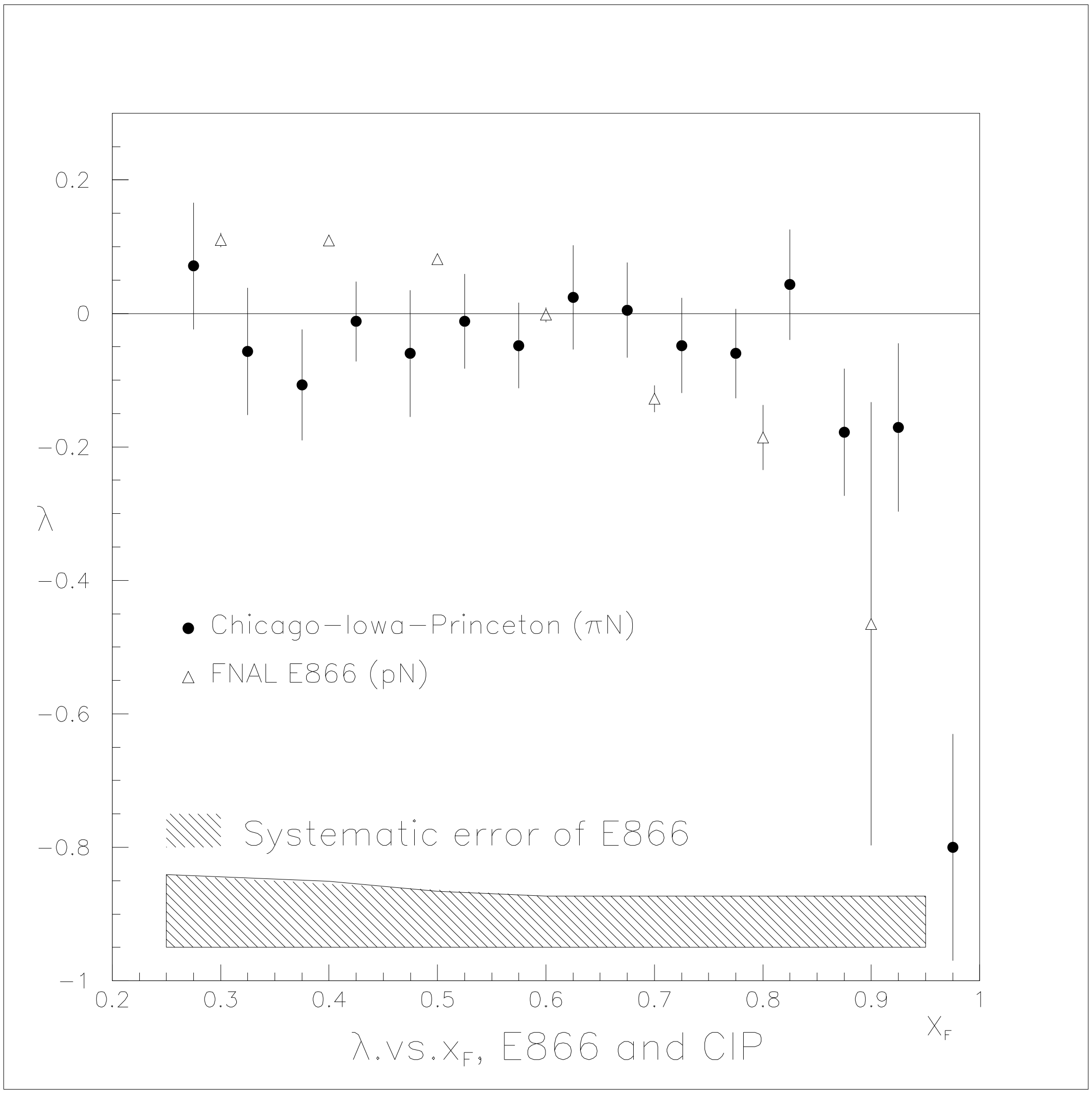

Figure 5.6: $\lambda(x_F)$ from FNAL E866 and from CIP group. The error bars on E866 data are statistical only; the systematic error is shown in the shadowed band below.

Table 5.4: Overall λ values from other fixed-target experiments and E866.

Experiment	reaction	$\sqrt{S}$	x_F range	λ
E537	$\overline{p}$ + W	15.3 GeV	$x_F > 0$	-0.115 ± 0.061
E537	π^- + W	15.3 GeV	$x_F > 0$	0.028 ± 0.004
E672/706	π^- + Be	31.5 GeV	$0.1 < x_F < 0.8$	-0.01 ± 0.08
E771	p + Si	38.8 GeV	$-0.05 < x_F < 0.25$	-0.09 ± 0.12
E866	p + Cu	38.8 GeV	$0.25 < x_F < 1.0$	$0.069 \pm 0.004 \pm syst.$

identified for either x_F region. This suggests that nuclear effects are probably not responsible for the polarization observed, since one important cause of the broadening in the p_T distribution in nuclear targets is the multiple scattering of the incoming and outgoing partons with the nuclear media. If some of the nuclear effects, e.g. energy loss inside nucleus, are important, one would expect to see significant p_T dependence on the polarization.

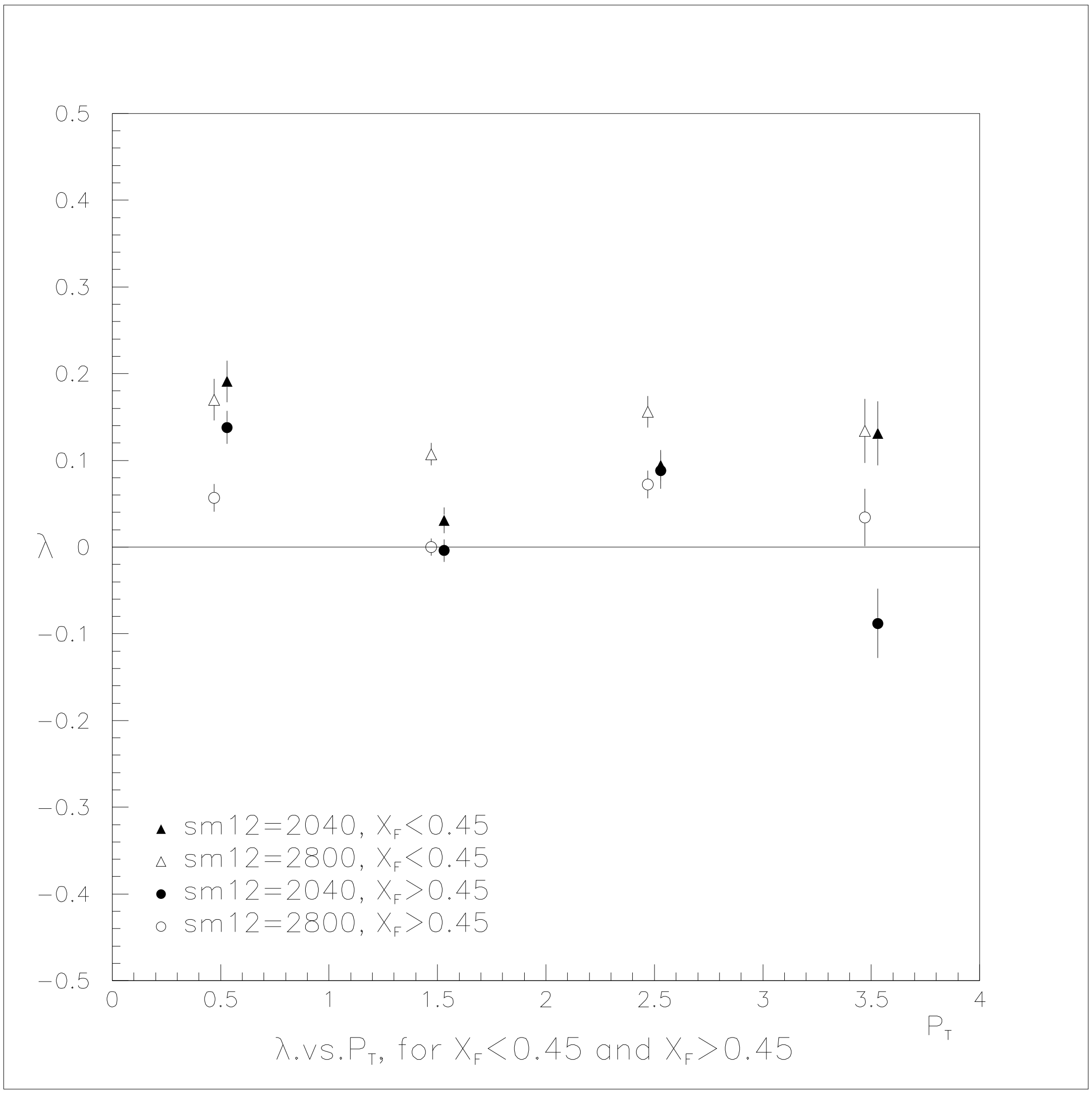

Figure 5.7: J/ψ polarization parameter λ in 1-GeV p_T bins. The plot shows λ in two regions of x_F: $x_F < 0.45$ and $x_F > 0.45$. The errors are statistical only.

6. CONCLUSIONS AND FUTURE PROSPECTS

The angular distribution of J/ψ decays in the $\mu^+\mu^-$ channel produced in 800 GeV proton-copper collisions has been measured for $x_F > 0.25$. The polarization parameter λ is extracted in p_T and x_F bins for two magnet configurations with different acceptances. The data indicate that the J/ψ's are produced with a slight transverse polarization at $x_F < 0.6$, which turns to longitudinal at $x_F > 0.6$. This suggests that gluon-gluon fusion, which dominates at small x_F, and quark-antiquark annihilation, which dominates at large x_F, leave J/ψ's in different polarization states. Another fixed-target experiment [Bii 87], using pion beams, also showed longitudinal polarization at $x_F \rightarrow 1$. However at smaller x_F the uncertainties are large and no evidence of polarization is seen in Biino's paper. The difference of the results from E866 will provide interesting information on how the production mechanism affects the polarization, because in πN interactions the production is dominated by quark-antiquark annihilation while in the pN case the production is dominated by gluon-gluon fusion in the range of $x_F < 0.6$.

It should be mentioned that the J/ψ samples collected in this study do not purely come from pN interactions. A significant amount of pions were generated at the dump by hadronic interactions, and those pions can further interact with the beam dump to produce J/ψ's. A calculation [Mue 99] shows that about 10% of the J/ψ's come from pion interactions at small x_F. This has to be taken into account when comparing with the theoretical calculations. Table 6.1 shows the

Table 6.1: Ratio of primary proton and secondary pion induced-J/ψ [Mue 99]. At small x_F, about 10 % of the J/ψ's were produced by pions generated from the primary proton beam interacting with the dump.

x_F	ratio(%)
0.2	15.1
0.3	9.3
0.4	6.2
0.5	4.4
0.6	3.4
0.7	3.0
0.8	2.9

estimate of the ratios of the J/ψ's produced by the secondary pions to those produced by the primary proton beam in various x_F ranges.

It is also important to keep in mind that a substantial fraction of J/ψ's come from decays of the χ_c states and ψ' decays in addition to direct J/ψ's. All the processes contribute different amounts of polarization to J/ψ. Thus one needs to know the relative production cross sections of the various charmonium states to interpret the results properly. So far, only production ratios for pion-produced charmonium states are available. It is also necessary to know the polarization of J/ψ's from each process to extract the polarization of direct J/ψ decays. A theoretical calculation has been done for πN collisions using the Color-Singlet Model [Van 95], but the results do not agree with the pion data. It would be interesting to see the predictions of similar calculations for pN collisions. A measurement of ψ' polarization would be very interesting since the χ_c state contribution is absent.

In this experiment the mass resolution was sacrificed to gain the yield rate and angular coverage; the data sample contains only about 1 % of ψ''s and they are not resolved from the J/ψ peak.

It is interesting to notice that if the J/ψ's are integrated over the entire x_F range, the transverse polarization at small x_F partially cancels the longitudinal polarization at large x_F, and the overall effect appears to be no polarization if the systematic uncertainty is included. Unpolarized J/ψ's were also observed in other fixed-target experiments, using either proton or pion beams.

Nuclear effects may also affect the J/ψ polarization, since the J/ψ may collide with other nucleons before it can escape the nucleus. The original polarization may thus be supressed or smeared out. To eliminate such an effect, a hydrogen target is preferable, at the price of smaller production rate however. It would also be interesting to study the nuclear dependence of λ to understand the nuclear effects on the polarization patterns.

The large-x_F behavior is of interest and yet remains mysterious. The polarization is changed to longitudinal. Similar behavior was observed also in the pion data and a possible explanation is higher-twist effects [Van 95]. It is not clear however how this mechanism applies to proton-induced data. In this study the x_F coverage is only up to 0.95. The statistics are too poor to produce sensible results for $x_F > 0.95$. Even for the $0.85 < x_F < 0.95$ bin it is desirable to reduce the statistical uncertainty. It would be interesting to know whether λ actually drops to -1 when x_F approaches 1.0 in pN interactions. This might give us better understandings of the higher-twist effects.

A. $\cos\theta$ Acceptance in x_F and p_T Bins

The $\cos\theta$ acceptance in x_F and p_T bins for both magnet settings is presented in this appendix. In Figures A1 to A6 the $\cos\theta$ acceptance for the "SM12=2040" data is plotted, and from Figure A7 to A12 the $\cos\theta$ acceptance for the "SM12=2800" data is plotted.

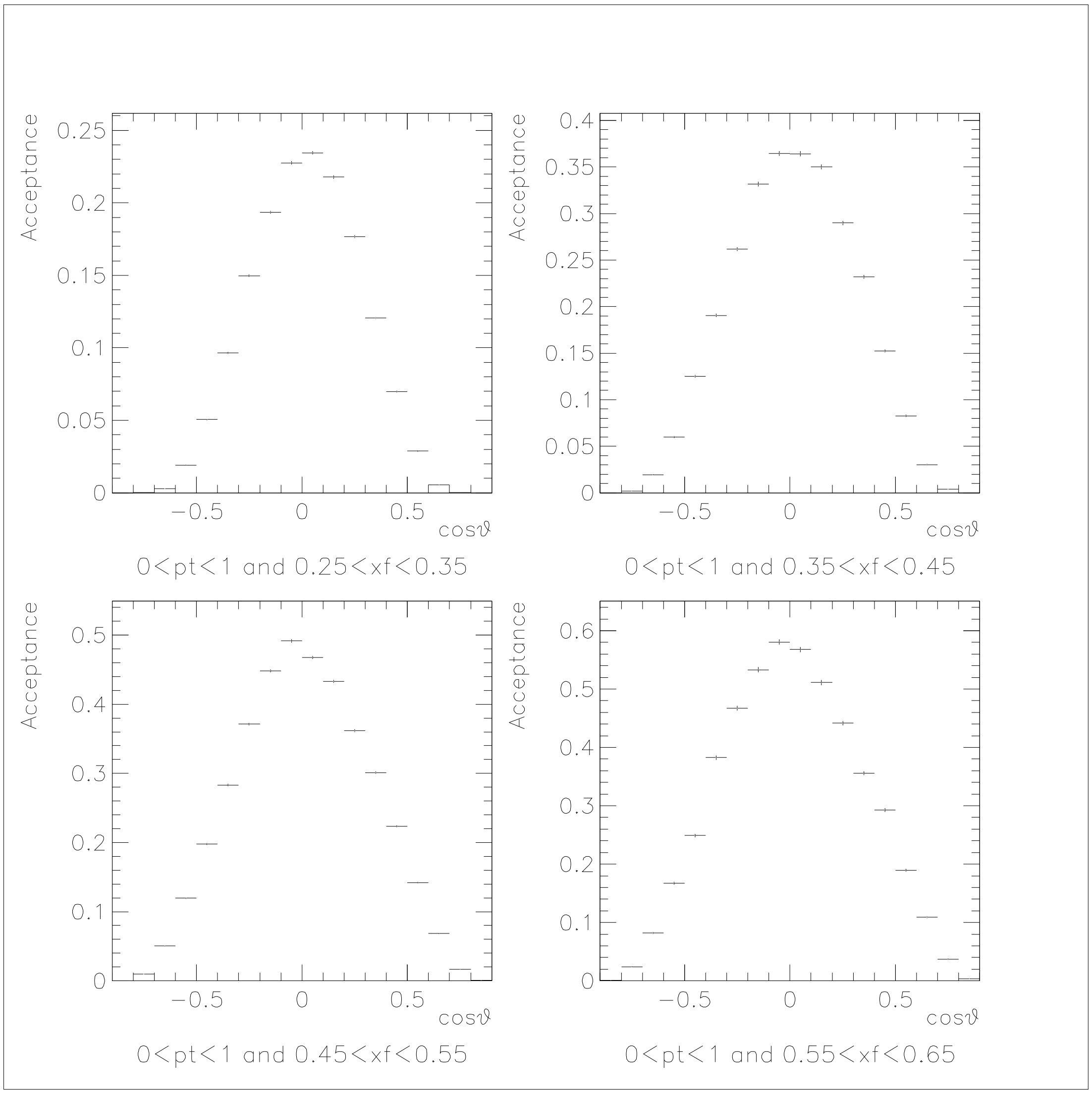

Figure A.1: $\cos\theta$ acceptance in x_F and p_T bins of the 2040Amp data.

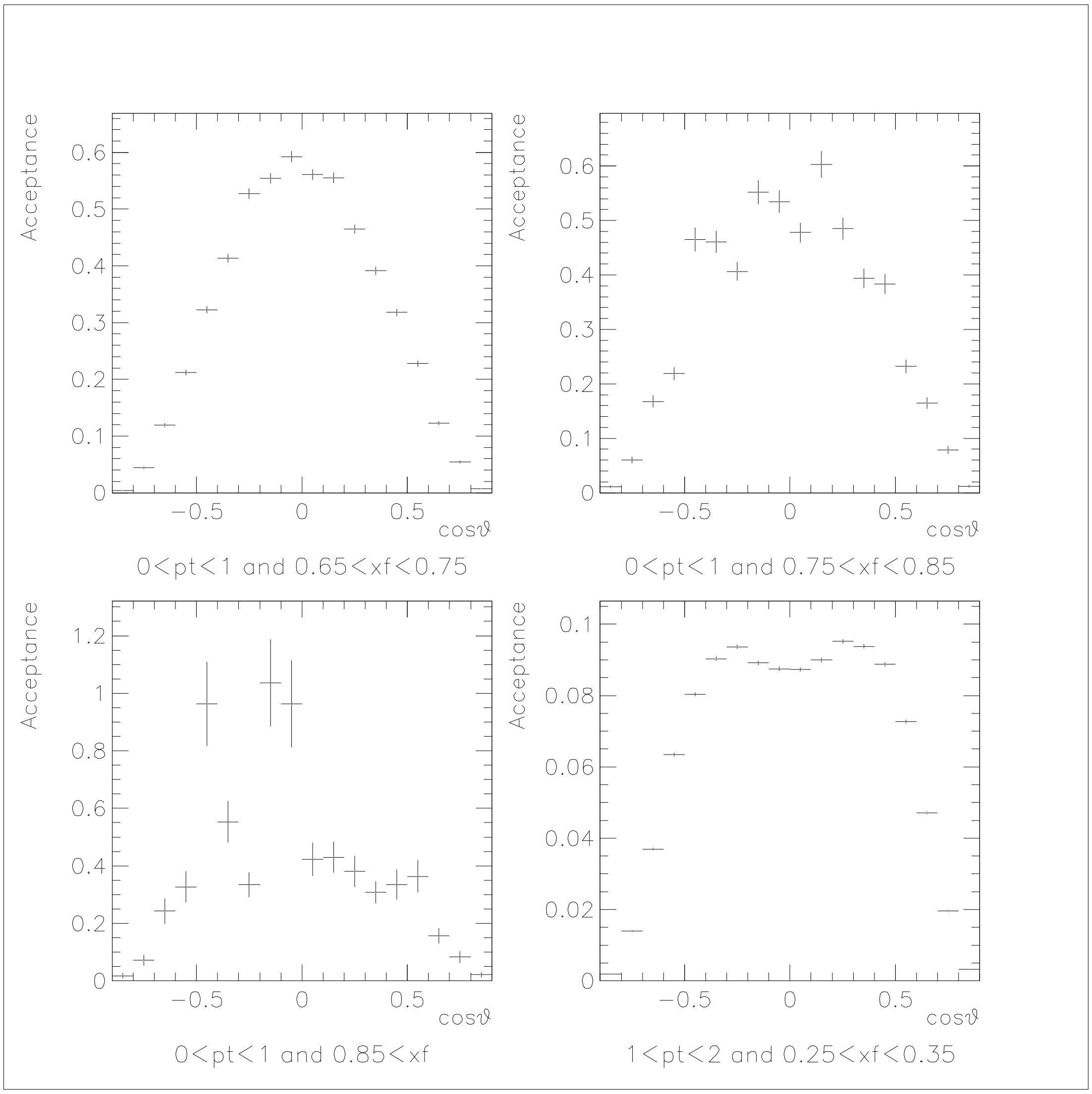

Figure A.2: $\cos\theta$ acceptance in x_F and p_T bins of the 2040Amp data.

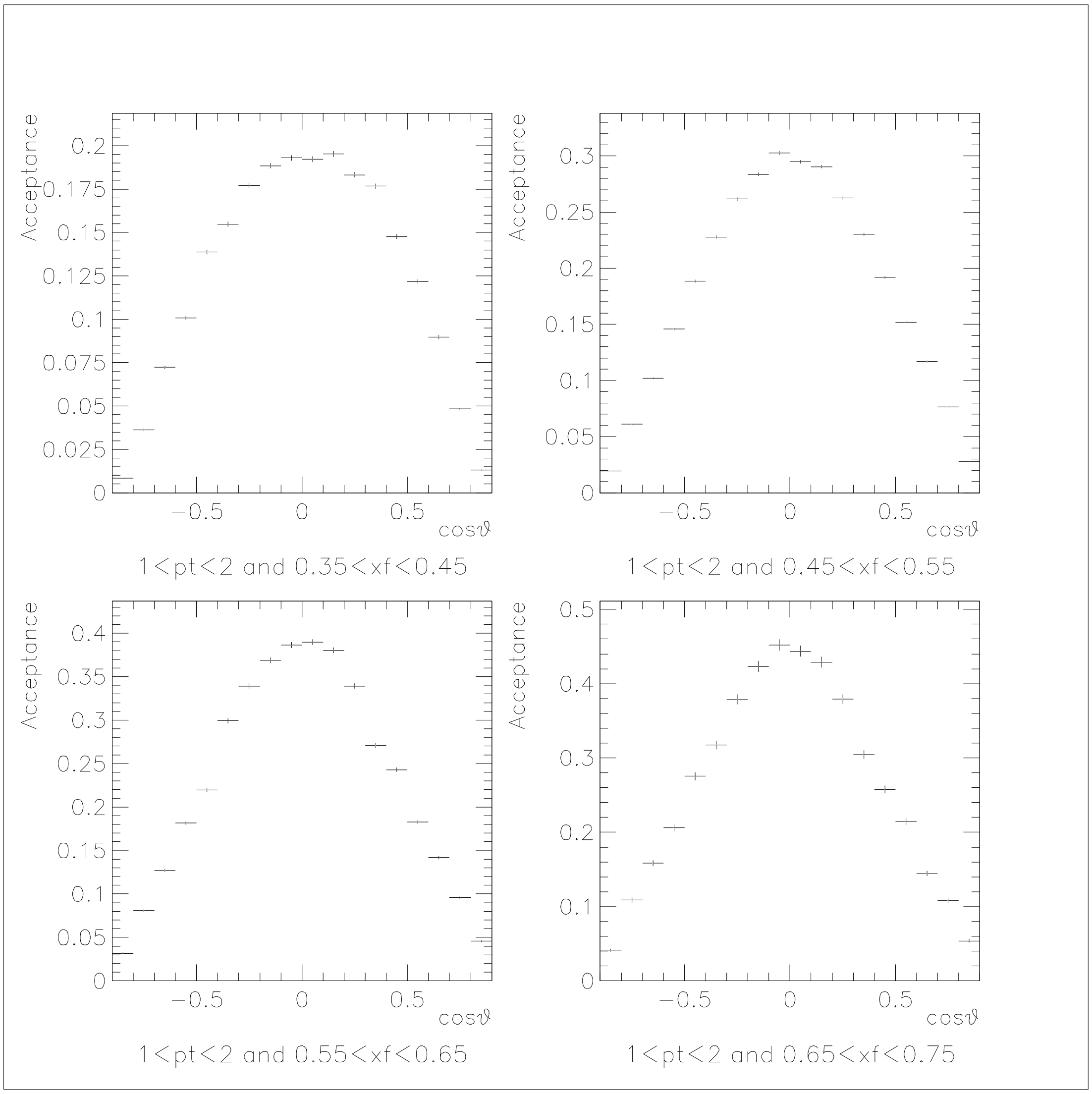

Figure A.3: $\cos\theta$ acceptance in x_F and p_T bins of the 2040Amp data.

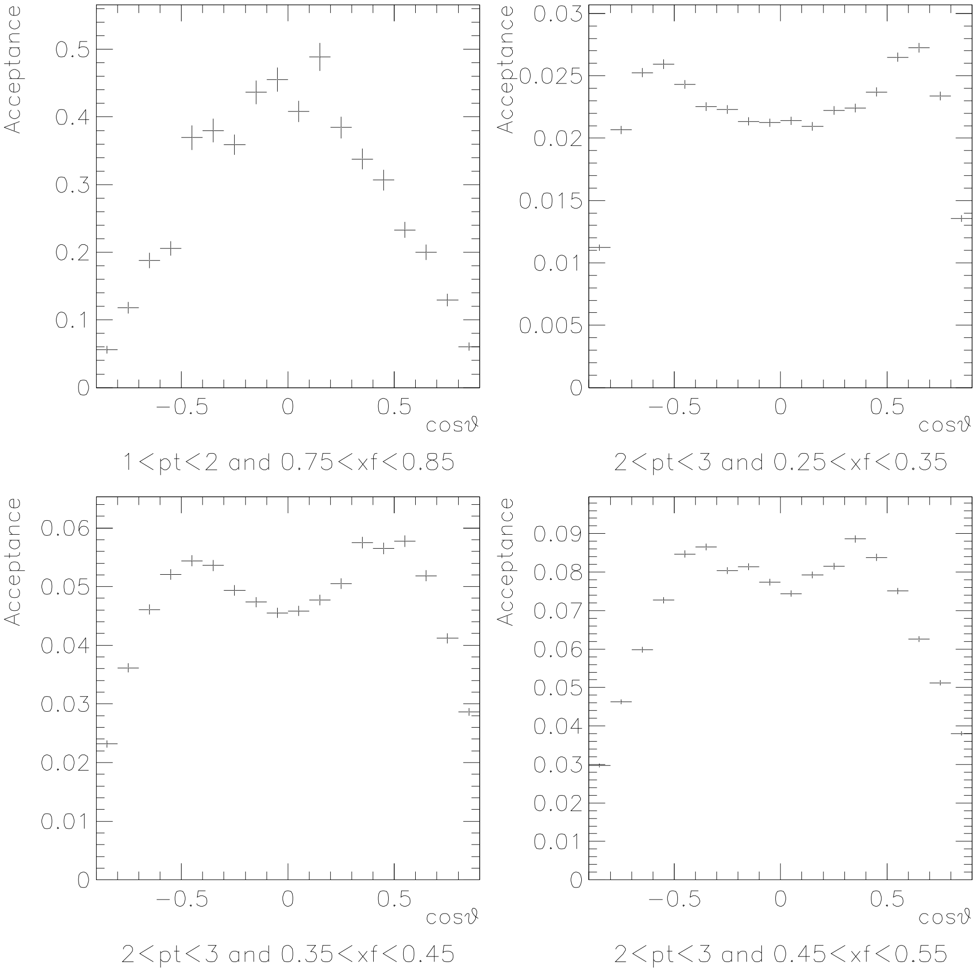

Figure A.4: $\cos\theta$ acceptance in x_F and p_T bins of the 2040Amp data.

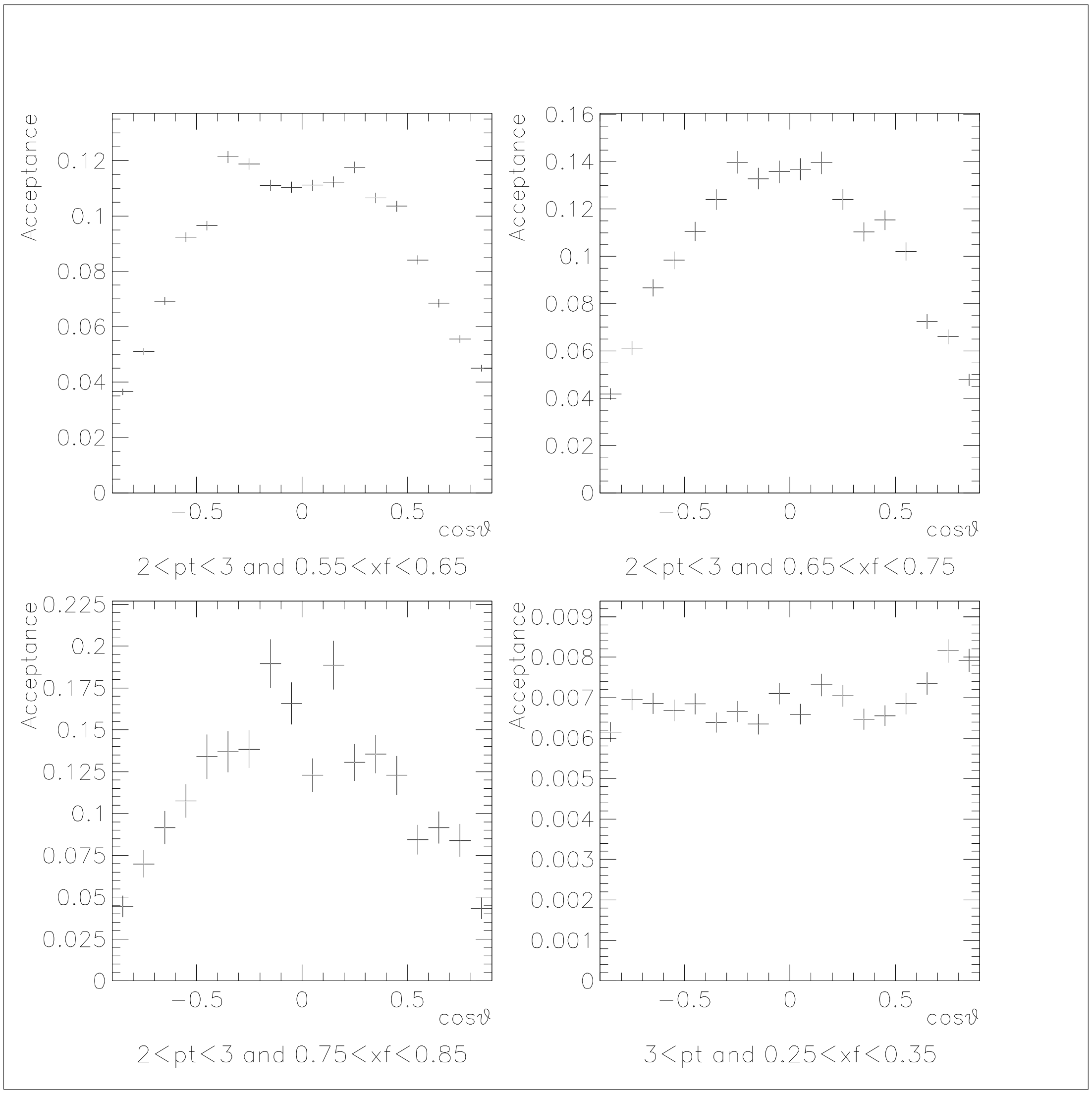

2<pt<3 and 0.55<xf<0.65

2<pt<3 and 0.65<xf<0.75

2<pt<3 and 0.75<xf<0.85

3<pt and 0.25<xf<0.35

Figure A.5: $\cos\theta$ acceptance in x_F and p_T bins of the 2040Amp data.

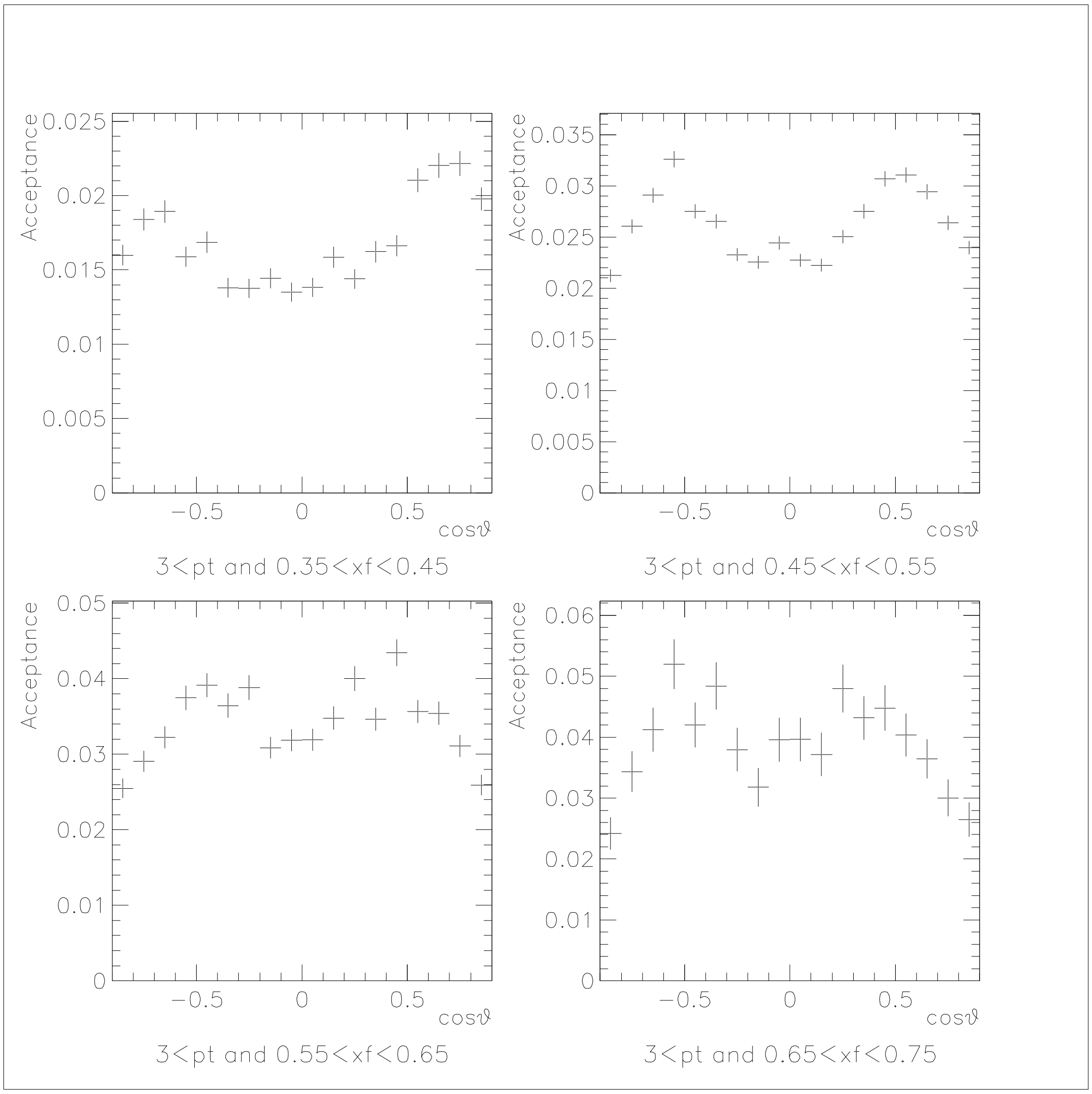

Figure A.6: $\cos\theta$ acceptance in x_F and p_T bins of the 2040Amp data.

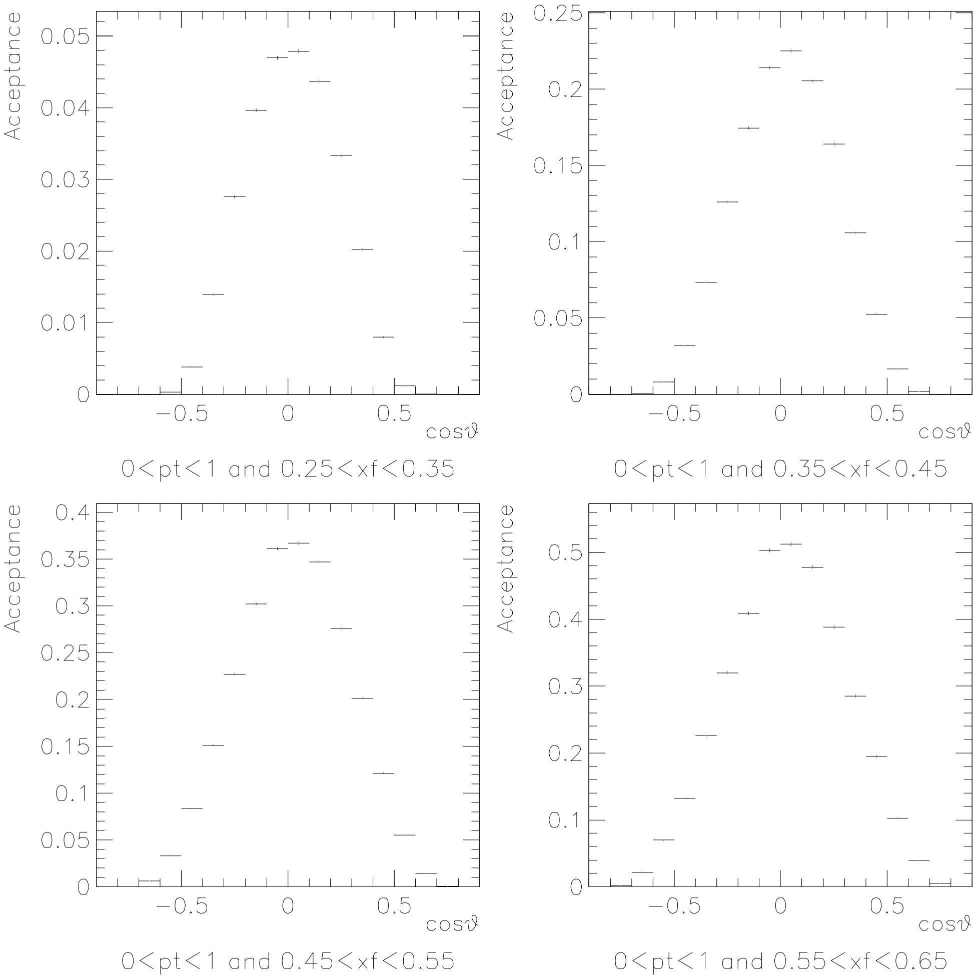

Figure A.7: $\cos\theta$ acceptance in x_F and p_T bins of the 2800Amp data.

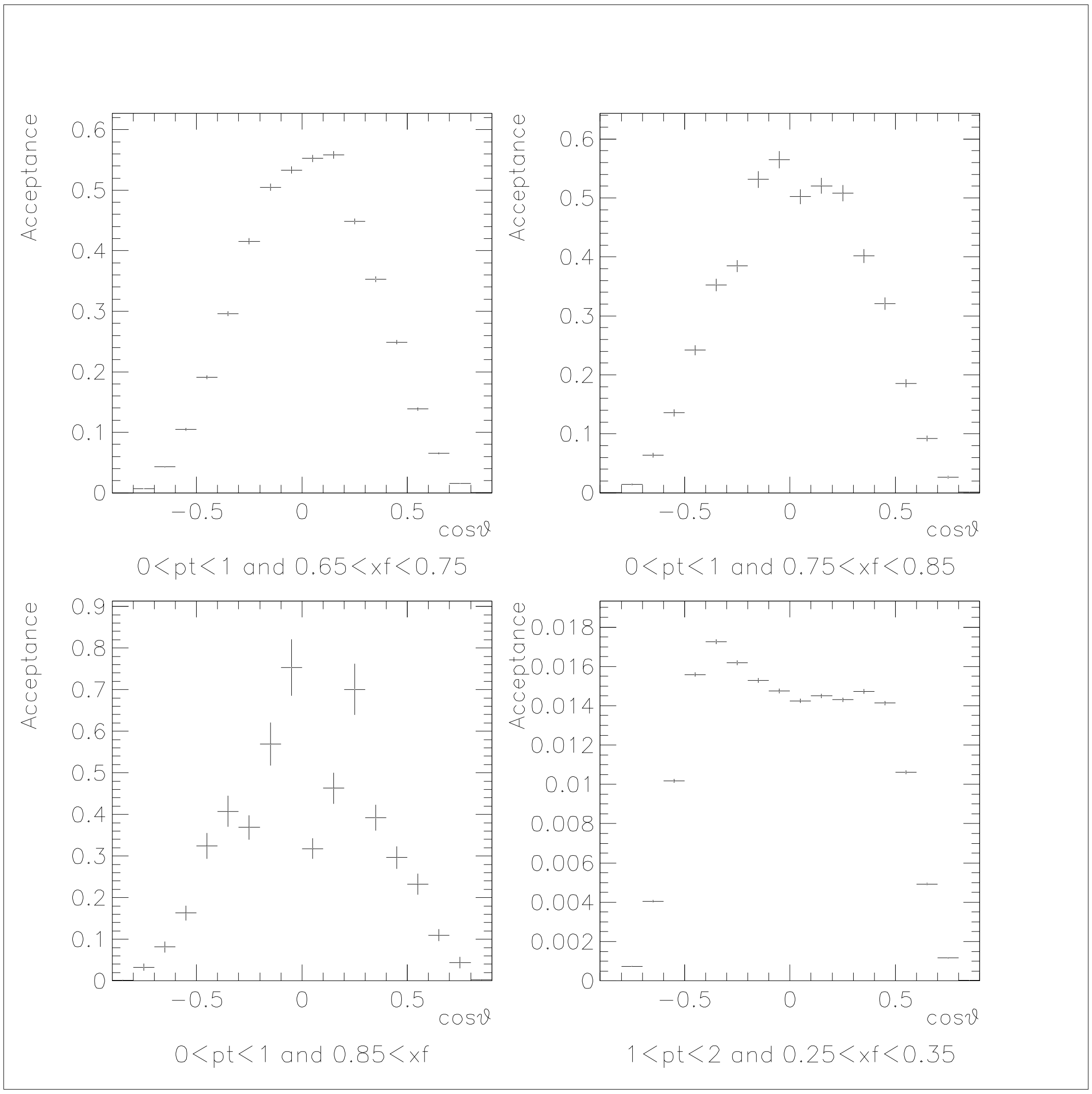

Figure A.8: $\cos\theta$ acceptance in x_F and p_T bins of the 2800Amp data.

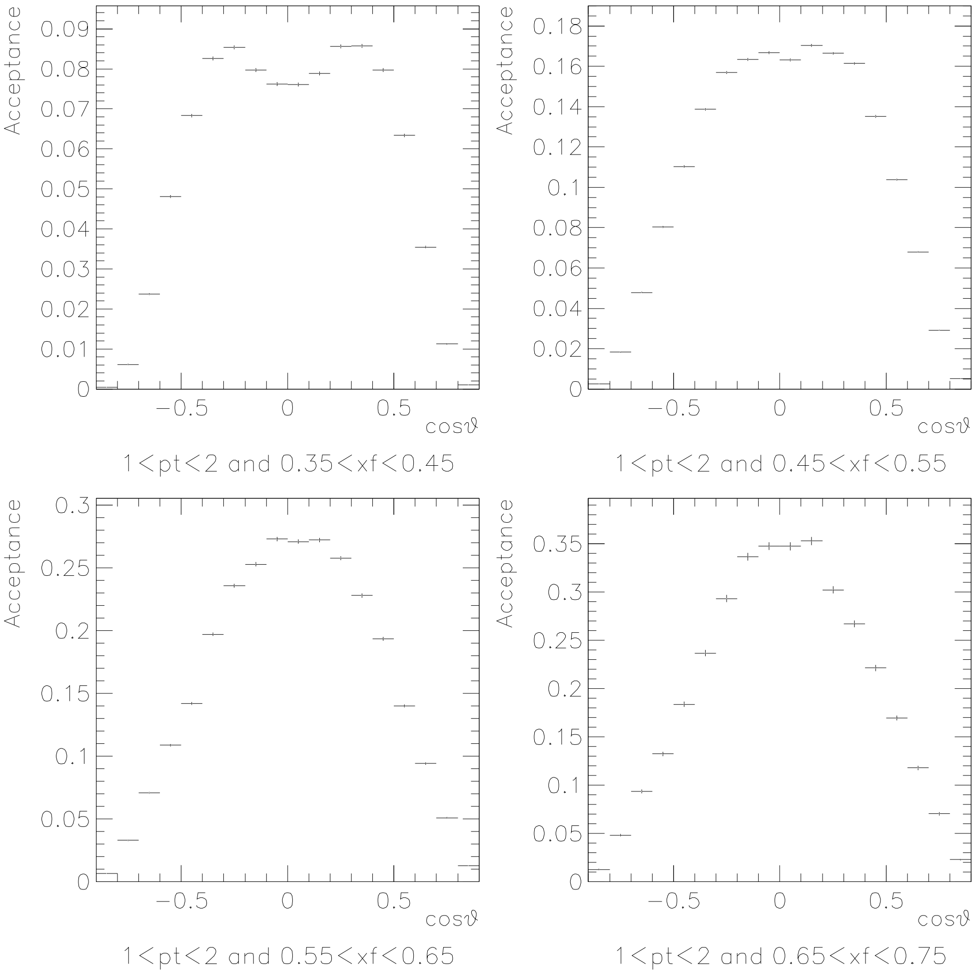

1<pt<2 and 0.35<xf<0.45

1<pt<2 and 0.45<xf<0.55

1<pt<2 and 0.55<xf<0.65

1<pt<2 and 0.65<xf<0.75

Figure A.9: $\cos\theta$ acceptance in x_F and p_T bins of the 2800Amp data.

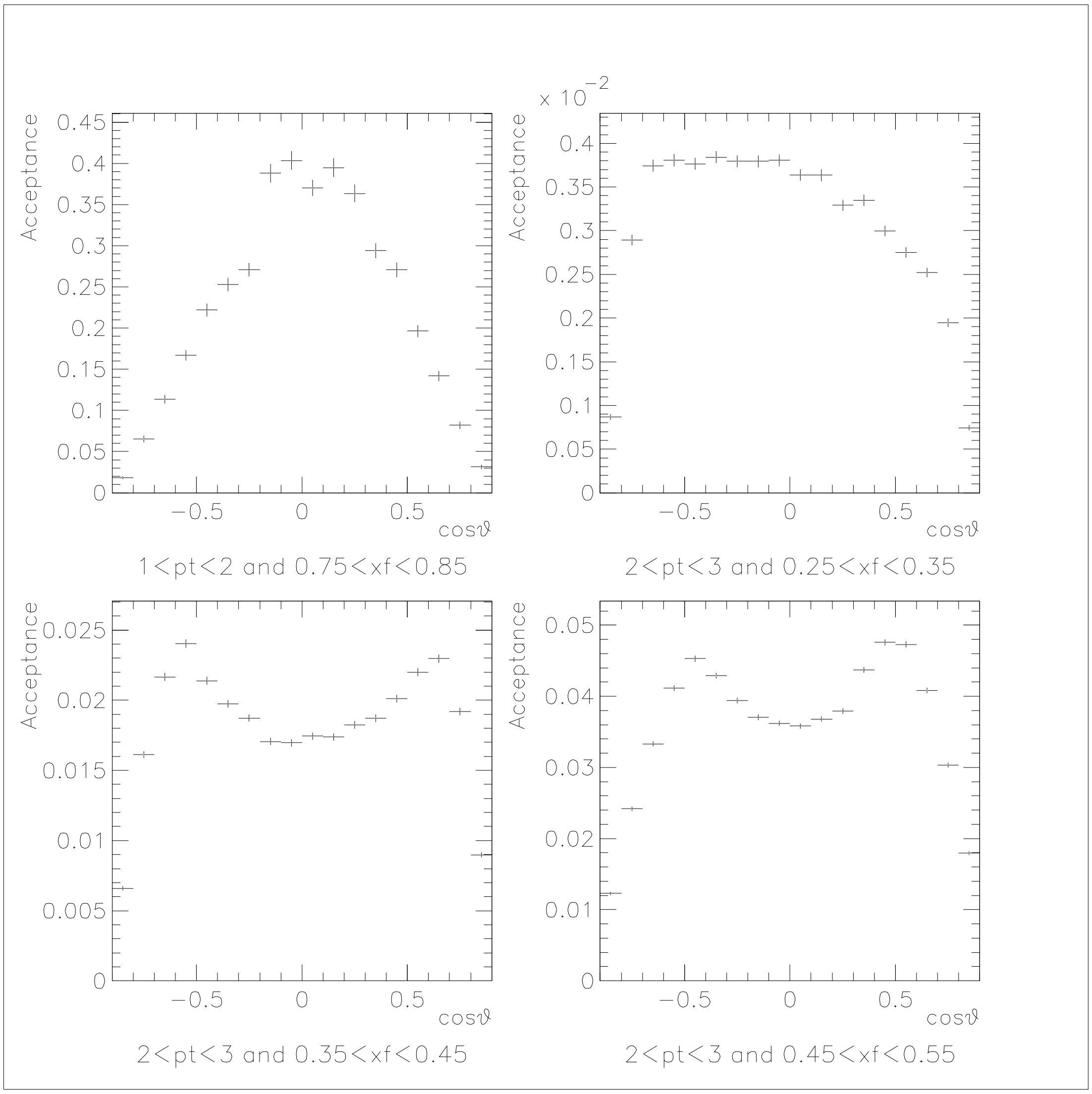

Figure A.10: $\cos\theta$ acceptance in x_F and p_T bins of the 2800Amp data.

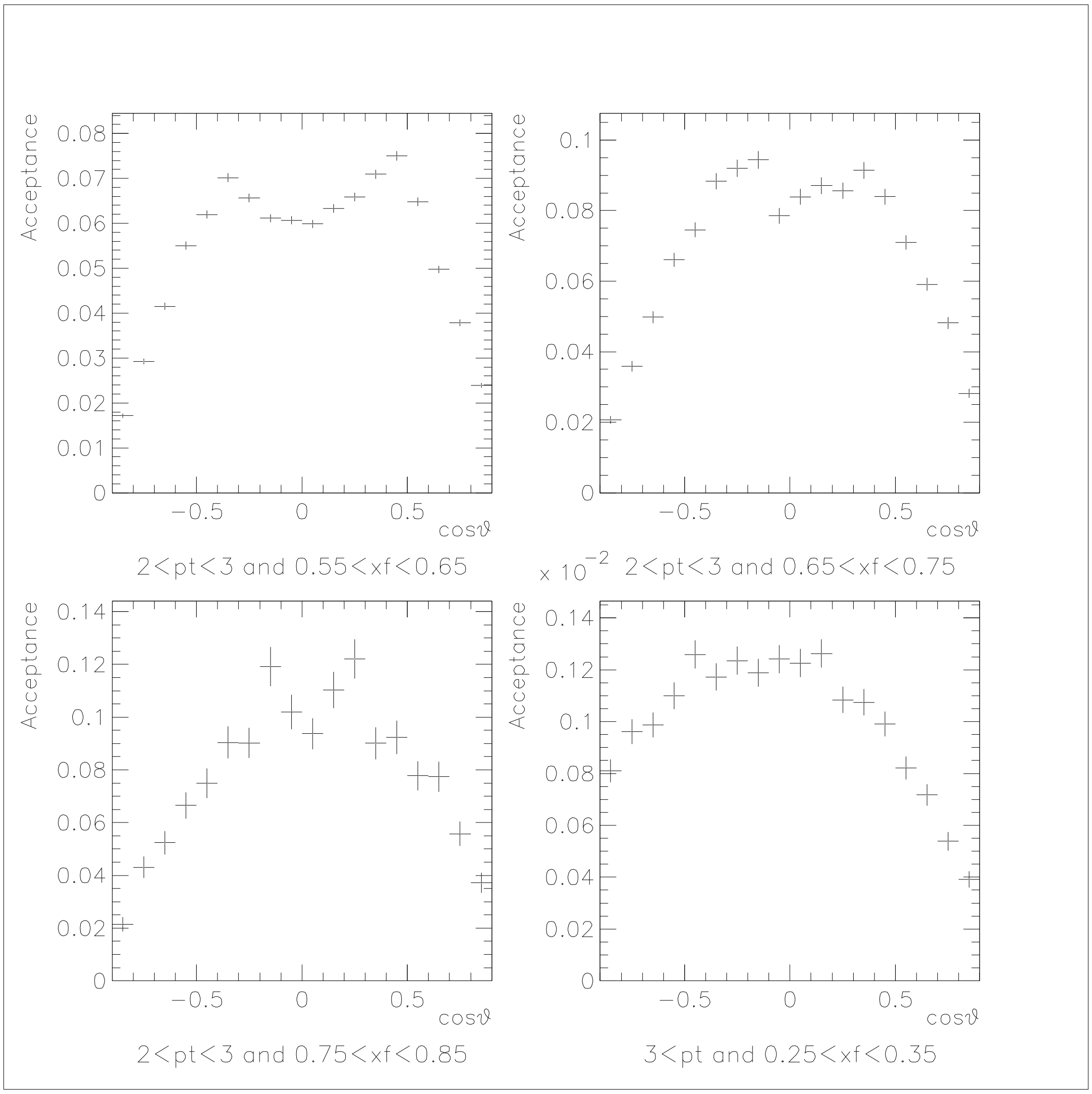

Figure A.11: $\cos\theta$ acceptance in x_F and p_T bins of the 2800Amp data.

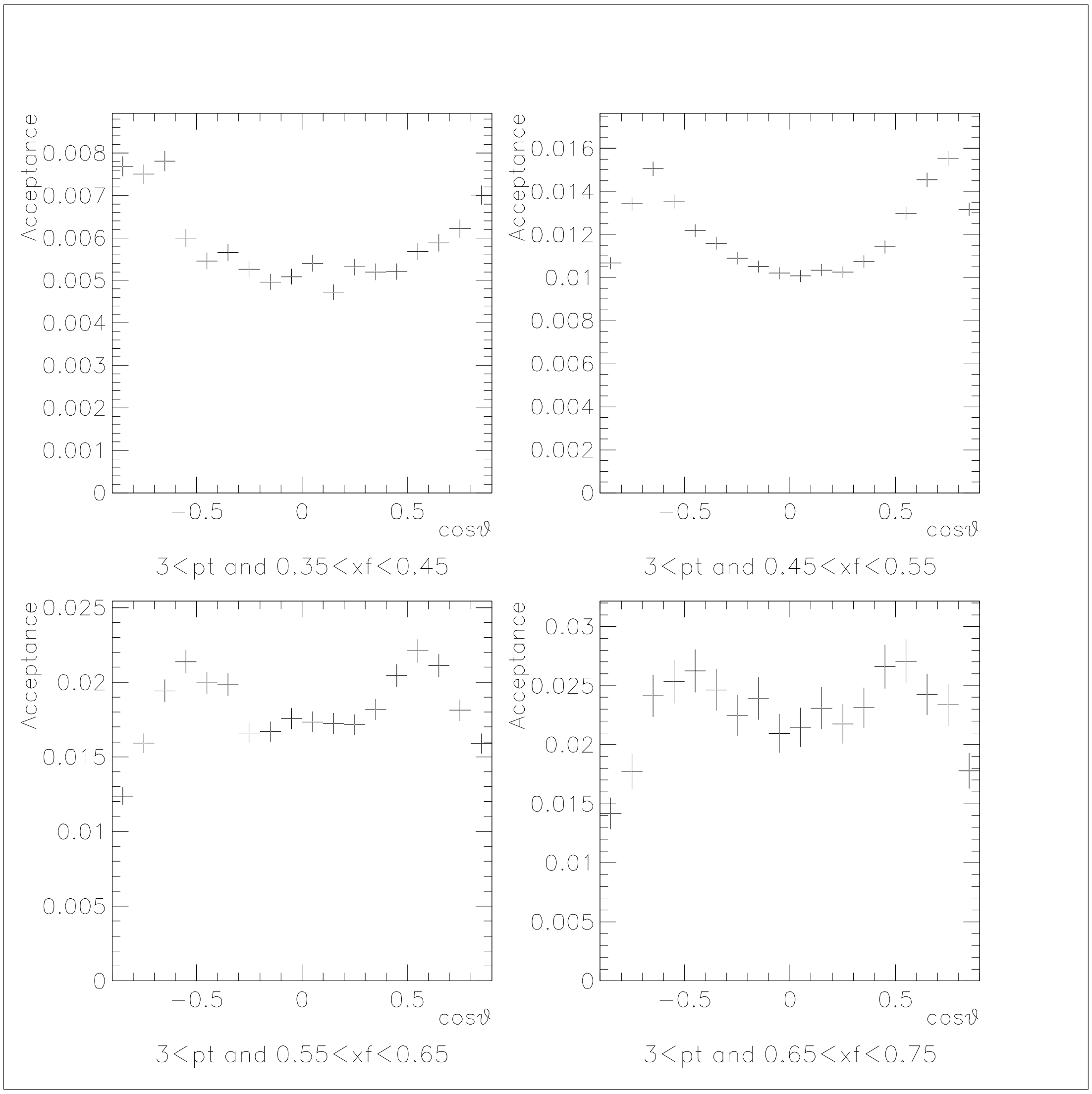

Figure A.12: $\cos\theta$ acceptance in x_F and p_T bins of the 2800Amp data.

B. Fitting the J/ψ Peaks

In this appendix the fitting of the J/ψ peaks is presented. The di-muon mass spectrum from each bin of $\cos\theta$, p_T, and x_F, are fitted to a Gaussian plus a background function with J/ψ's fitted to a Gaussian shape. The count of J/ψ's in each bin was then calculated according to the output parameters of the Gaussian fit. Figure B1 to B42 show the fittings from the "SM12 = 2040 Amp" data set, and Figure B43 to B84 show the fittings from the "SM12 = 2800 Amp" data set.

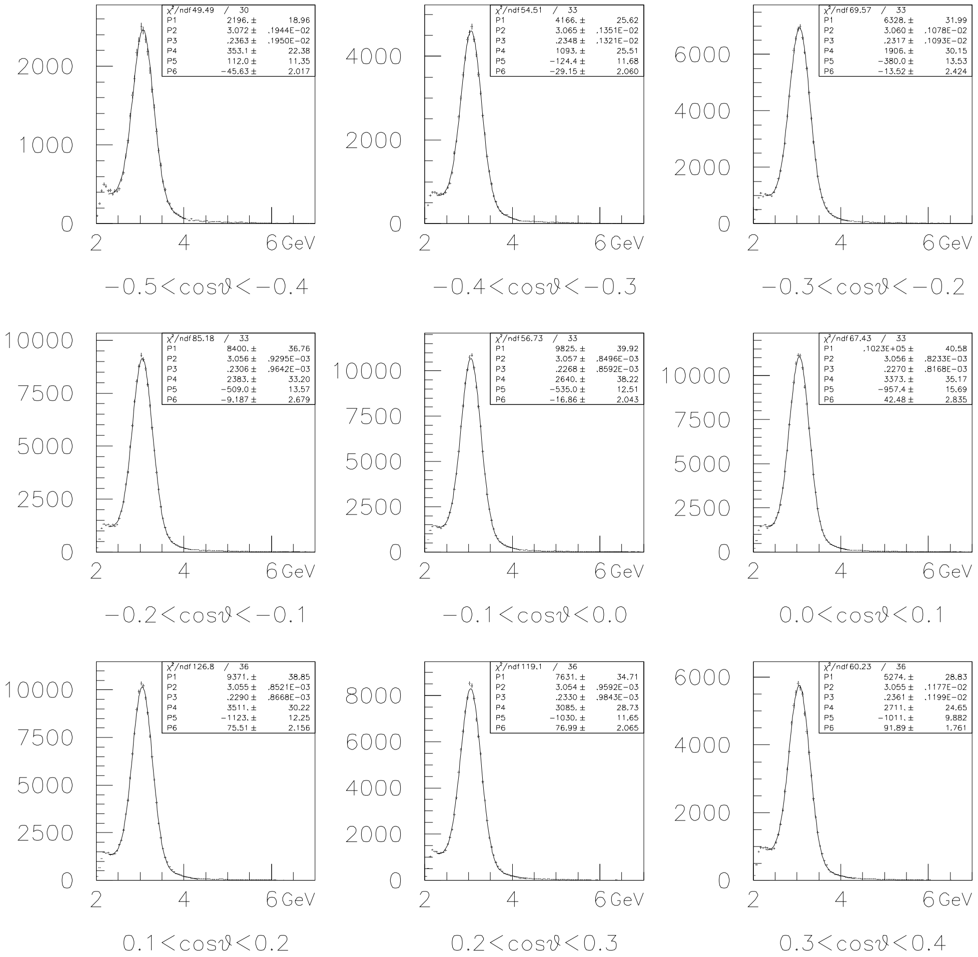

$-0.5<\cos\vartheta<-0.4$ $-0.4<\cos\vartheta<-0.3$ $-0.3<\cos\vartheta<-0.2$

$-0.2<\cos\vartheta<-0.1$ $-0.1<\cos\vartheta<0.0$ $0.0<\cos\vartheta<0.1$

$0.1<\cos\vartheta<0.2$ $0.2<\cos\vartheta<0.3$ $0.3<\cos\vartheta<0.4$

Figure B.1: Fitting of the mass spectrum: $0 < p_t < 1$ and $0.25 < x_F < 0.35$. The backgrounds were fitted to second-order polynomials, and the J/ψ's were fitted to Gaussians. The $\cos\theta$ ranges are indicated under each spectrum. The current of SM12 magnet was 2040 Ampere.

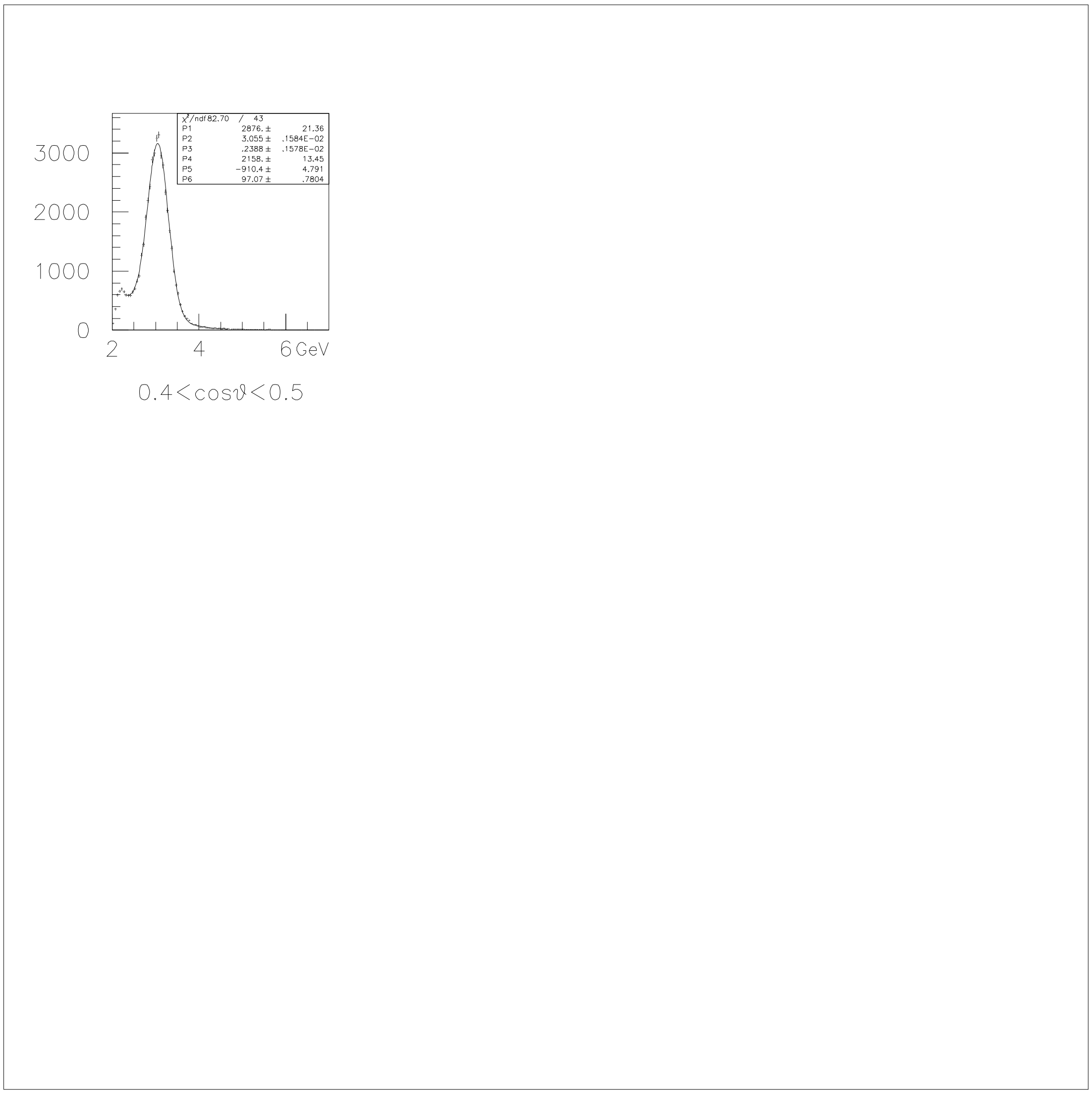

Figure B.2: Fitting of the mass spectrum: $0 < p_t < 1$ and $0.25 < x_F < 0.35$. The backgrounds were fitted to second-order polynomials, and the J/ψ's were fitted to Gaussians. The $\cos\theta$ ranges are indicated under each spectrum. The current of SM12 magnet was 2040 Ampere.

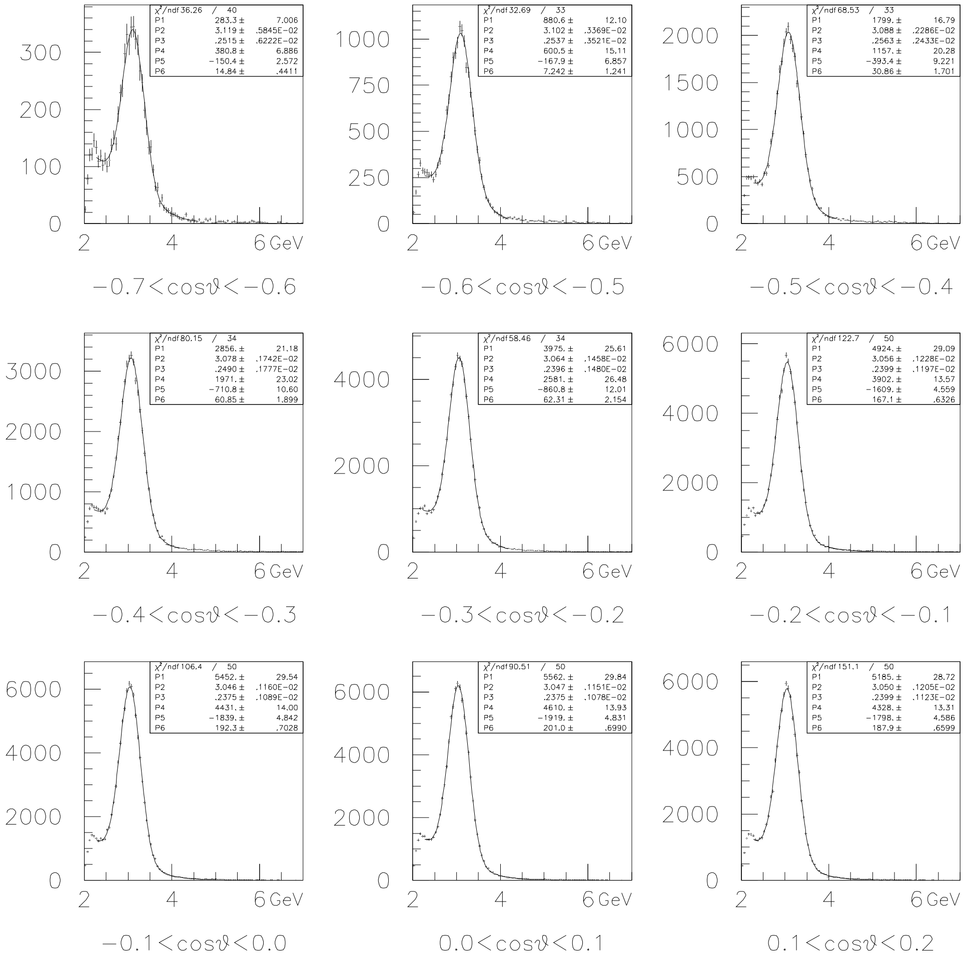

Figure B.3: Fitting of the mass spectrum: $0 < p_t < 1$ and $0.35 < x_F < 0.45$. The backgrounds were fitted to second-order polynomials, and the J/ψ's were fitted to Gaussians. The $\cos\theta$ ranges are indicated under each spectrum. The current of SM12 magnet was 2040 Ampere.

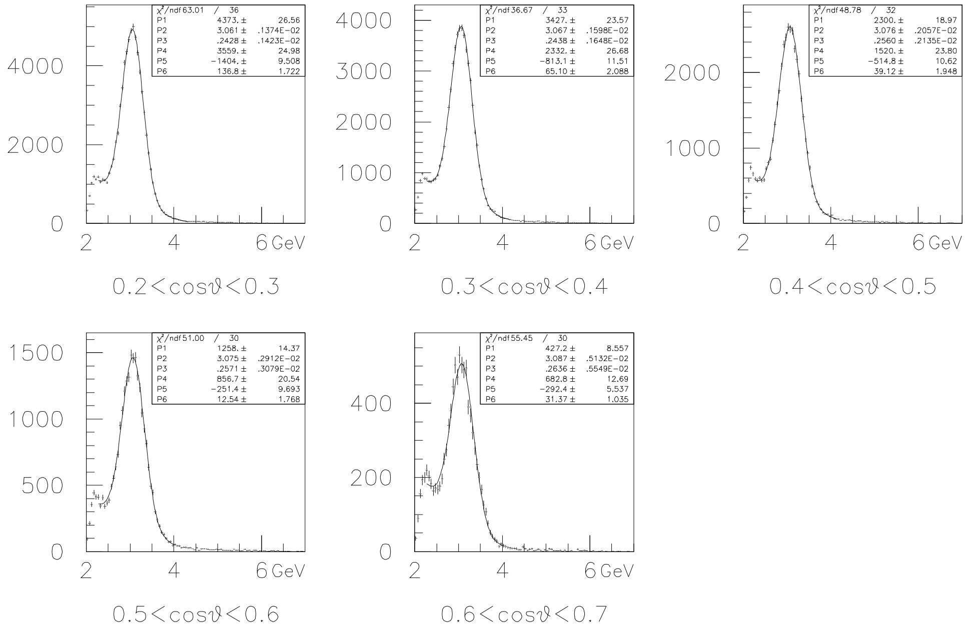

$0.2<\cos\vartheta<0.3$ $0.3<\cos\vartheta<0.4$ $0.4<\cos\vartheta<0.5$

$0.5<\cos\vartheta<0.6$ $0.6<\cos\vartheta<0.7$

Figure B.4: Fitting of the mass spectrum: $0 < p_t < 1$ and $0.35 < x_F < 0.45$. The backgrounds were fitted to second-order polynomials, and the J/ψ's were fitted to Gaussians. The $\cos\theta$ ranges are indicated under each spectrum. The current of SM12 magnet was 2040 Ampere.

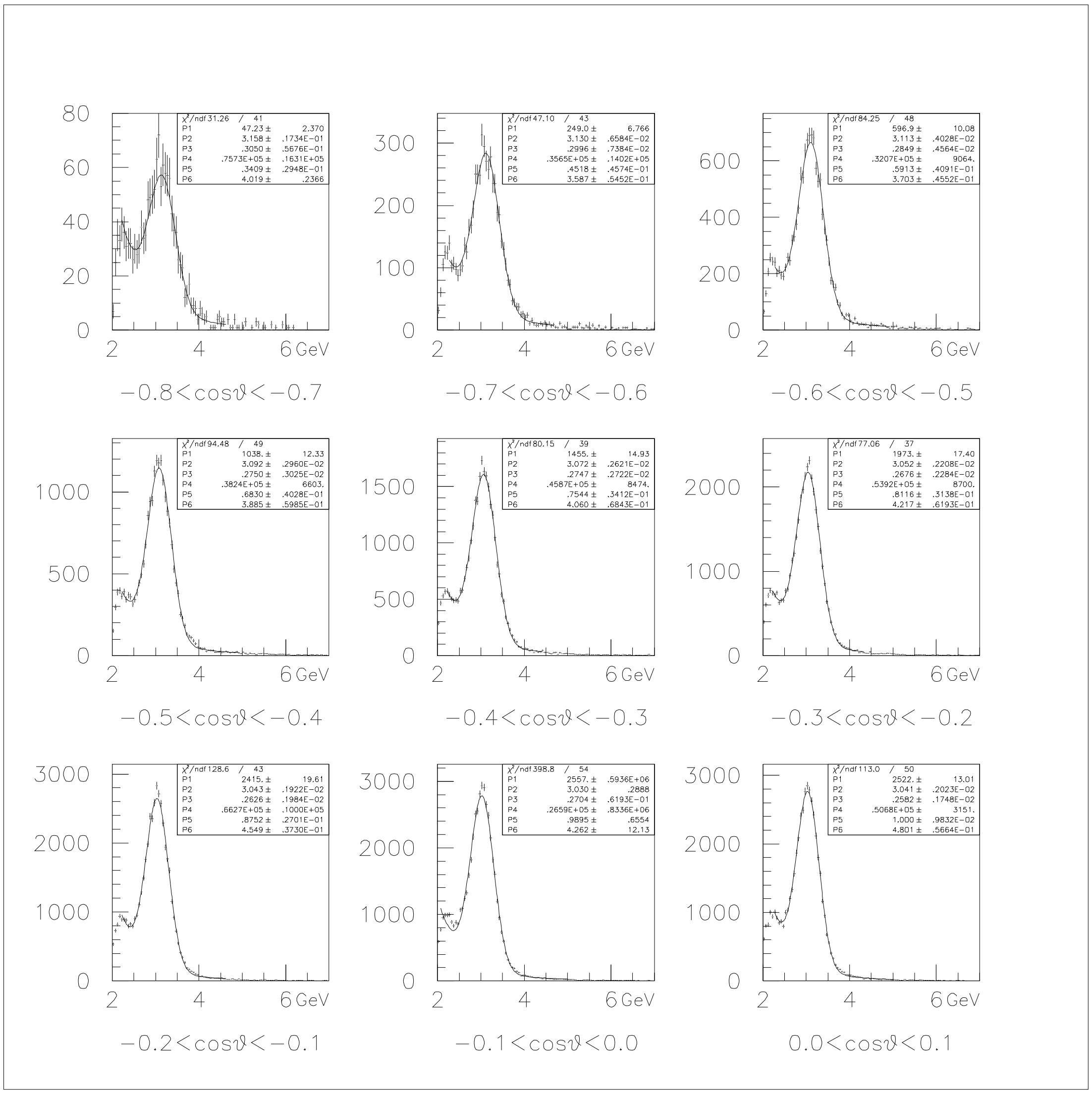

$-0.8 < \cos\vartheta < -0.7$ $-0.7 < \cos\vartheta < -0.6$ $-0.6 < \cos\vartheta < -0.5$

$-0.5 < \cos\vartheta < -0.4$ $-0.4 < \cos\vartheta < -0.3$ $-0.3 < \cos\vartheta < -0.2$

$-0.2 < \cos\vartheta < -0.1$ $-0.1 < \cos\vartheta < 0.0$ $0.0 < \cos\vartheta < 0.1$

Figure B.5: Fitting of the mass spectrum: $0 < p_t < 1$ and $0.45 < x_F < 0.55$. The backgrounds were fitted to Kaplan functions, and the J/ψ's were fitted to Gaussians. The $\cos\theta$ ranges are indicated under each spectrum. The current of SM12 magnet was 2040 Ampere.

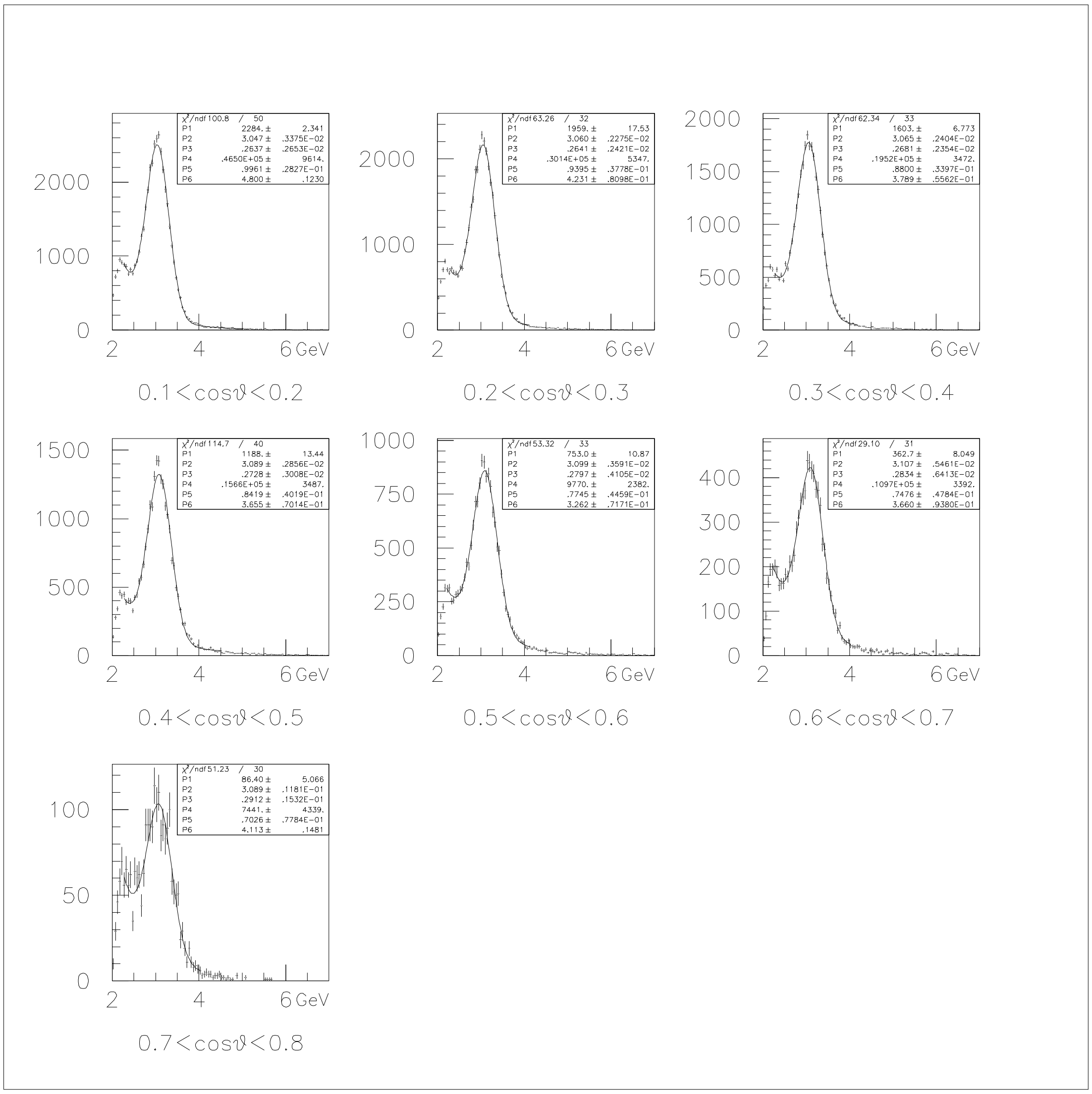

Figure B.6: Fitting of the mass spectrum: $0 < p_t < 1$ and $0.45 < x_F < 0.55$. The backgrounds were fitted to Kaplan functions, and the J/ψ's were fitted to Gaussians. The $\cos\theta$ ranges are indicated under each spectrum. The current of SM12 magnet was 2040 Ampere.

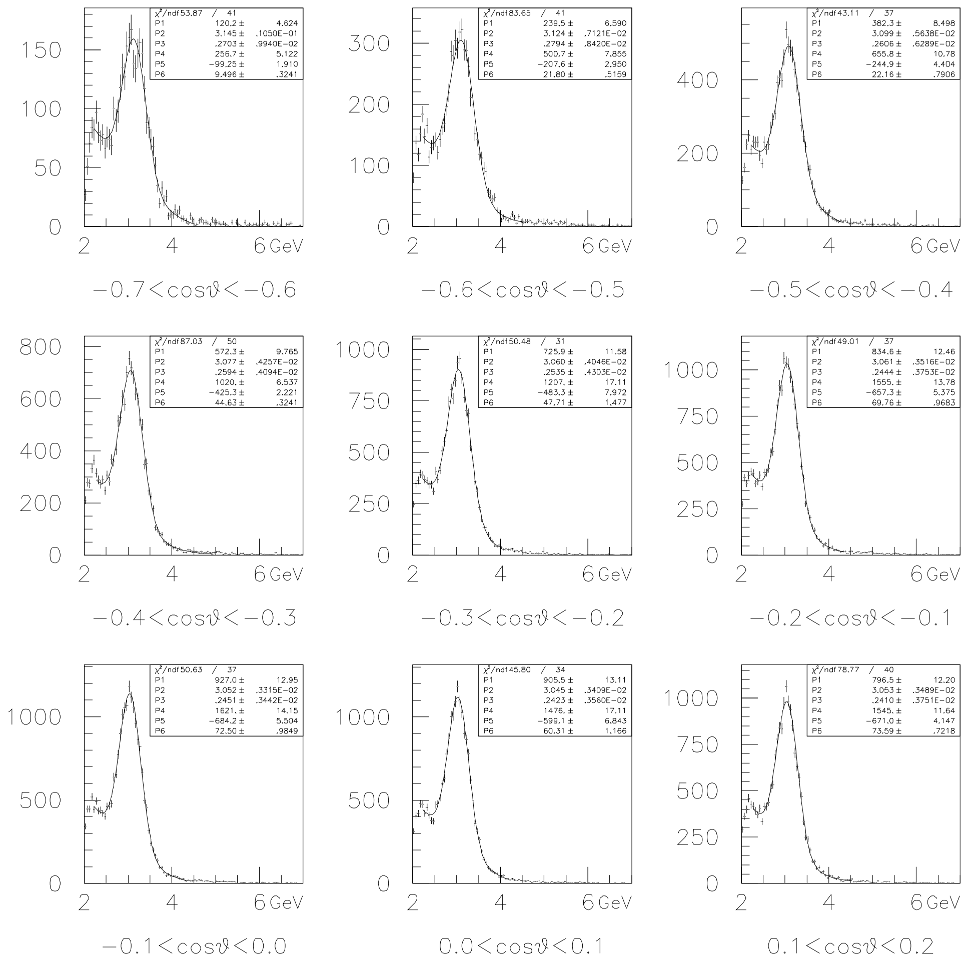

Figure B.7: Fitting of the mass spectrum: $0 < p_t < 1$ and $0.55 < x_F < 0.65$. The backgrounds were fitted to second-order polynomials, and the J/ψ's were fitted to Gaussians. The $\cos\theta$ ranges are indicated under each spectrum. The current of SM12 magnet was 2040 Ampere.

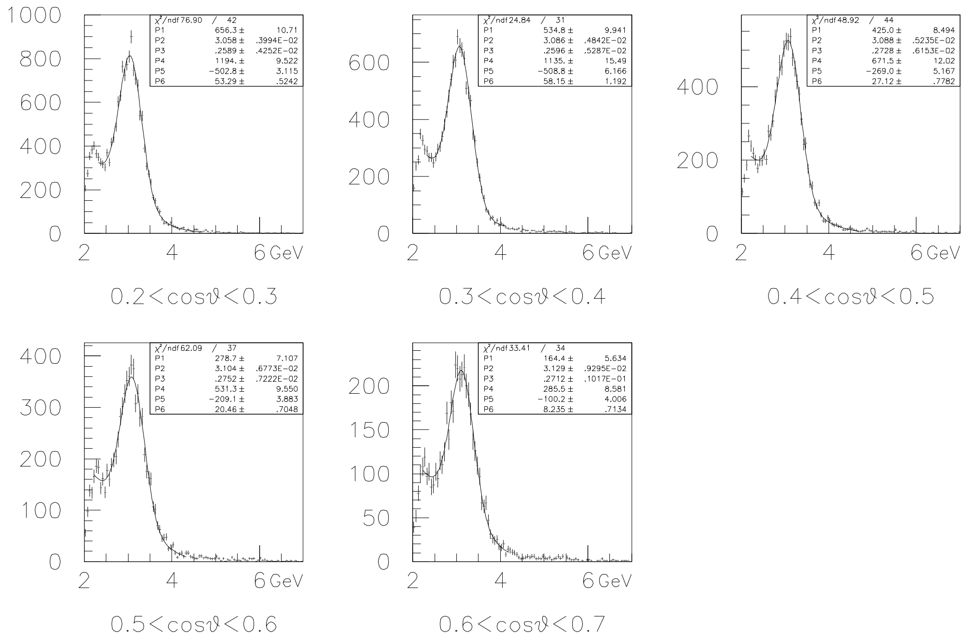

Figure B.8: Fitting of the mass spectrum: $0 < p_t < 1$ and $0.55 < x_F < 0.65$. The backgrounds were fitted to second-order polynomials, and the J/ψ's were fitted to Gaussians. The $\cos\theta$ ranges are indicated under each spectrum. The current of SM12 magnet was 2040 Ampere.

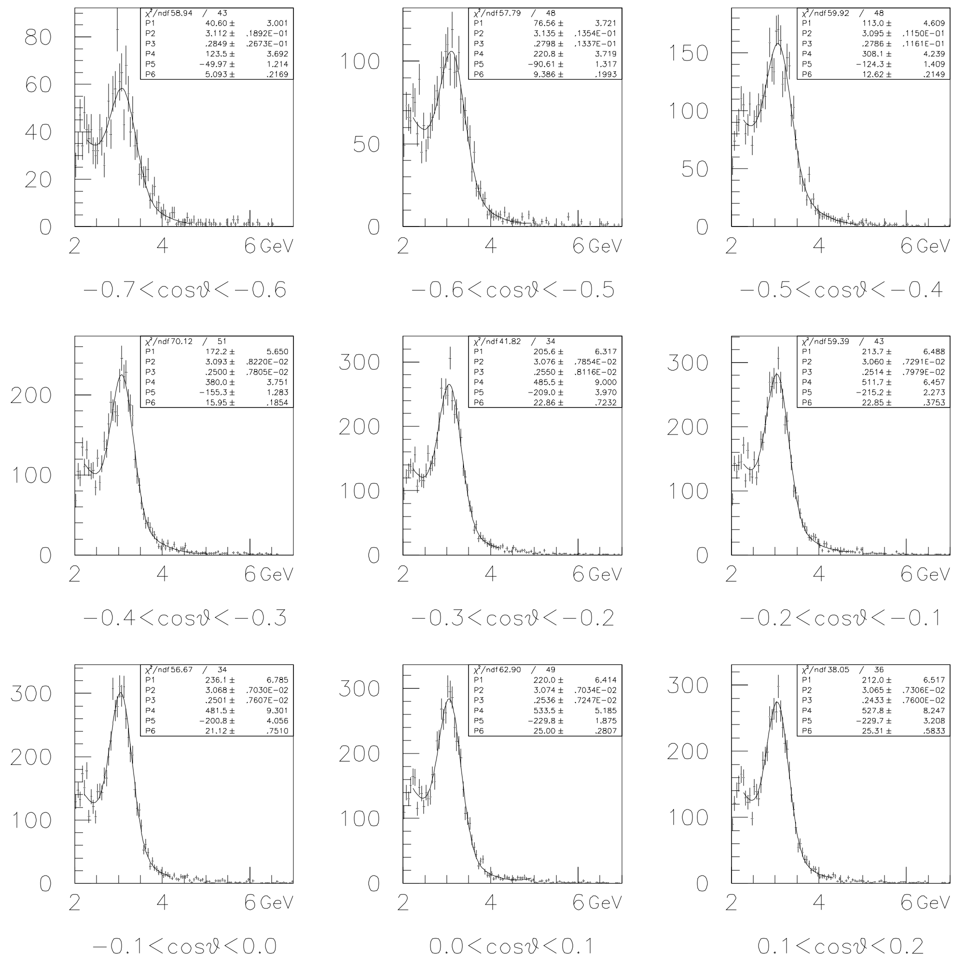

Figure B.9: Fitting of the mass spectrum: $0 < p_t < 1$ and $0.65 < x_F < 0.75$. The backgrounds were fitted to second-order polynomials, and the J/ψ's were fitted to Gaussians. The $\cos\theta$ ranges are indicated under each spectrum. The current of SM12 magnet was 2040 Ampere.

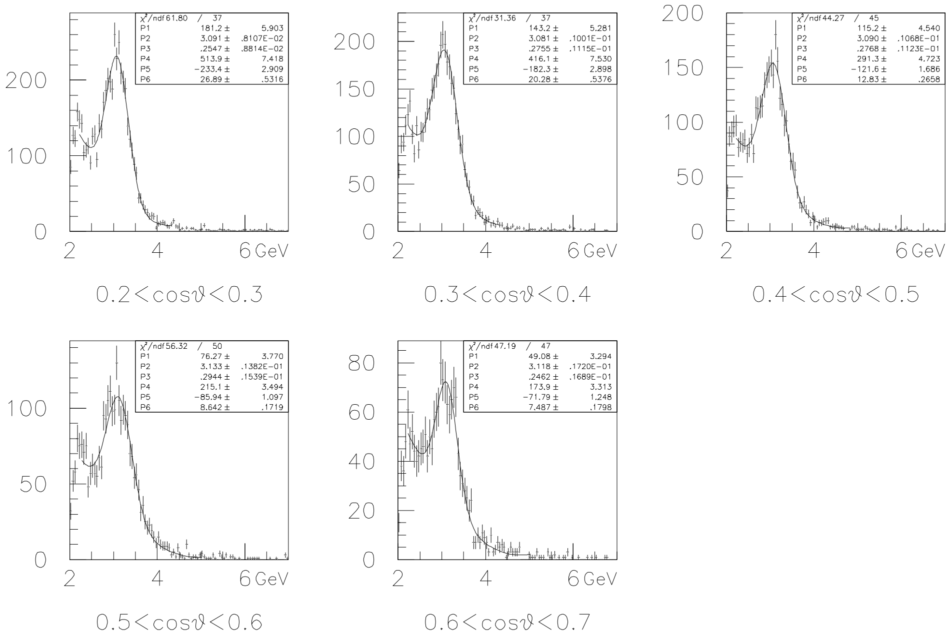

$0.2<\cos\vartheta<0.3$ $0.3<\cos\vartheta<0.4$ $0.4<\cos\vartheta<0.5$

$0.5<\cos\vartheta<0.6$ $0.6<\cos\vartheta<0.7$

Figure B.10: Fitting of the mass spectrum: $0 < p_t < 1$ and $0.65 < x_F < 0.75$. The backgrounds were fitted to second-order polynomials, and the J/ψ's were fitted to Gaussians. The $\cos\theta$ ranges are indicated under each spectrum. The current of SM12 magnet was 2040 Ampere.

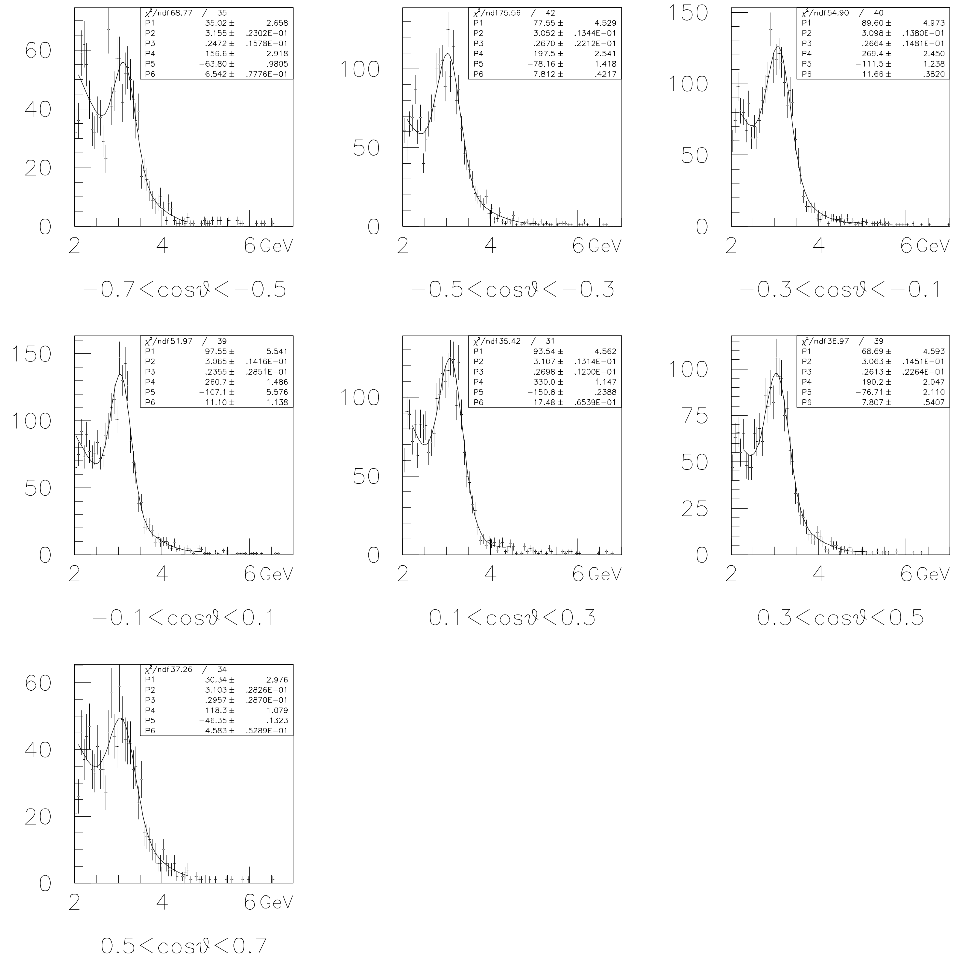

$-0.7<\cos\vartheta<-0.5$

$-0.5<\cos\vartheta<-0.3$

$-0.3<\cos\vartheta<-0.1$

$-0.1<\cos\vartheta<0.1$

$0.1<\cos\vartheta<0.3$

$0.3<\cos\vartheta<0.5$

$0.5<\cos\vartheta<0.7$

Figure B.11: Fitting of the mass spectrum: $0 < p_t < 1$ and $0.75 < x_F < 0.85$. The backgrounds were fitted to second-order polynomials, and the J/ψ's were fitted to Gaussians. The $\cos\theta$ ranges are indicated under each spectrum. The current of SM12 magnet was 2040 Ampere.

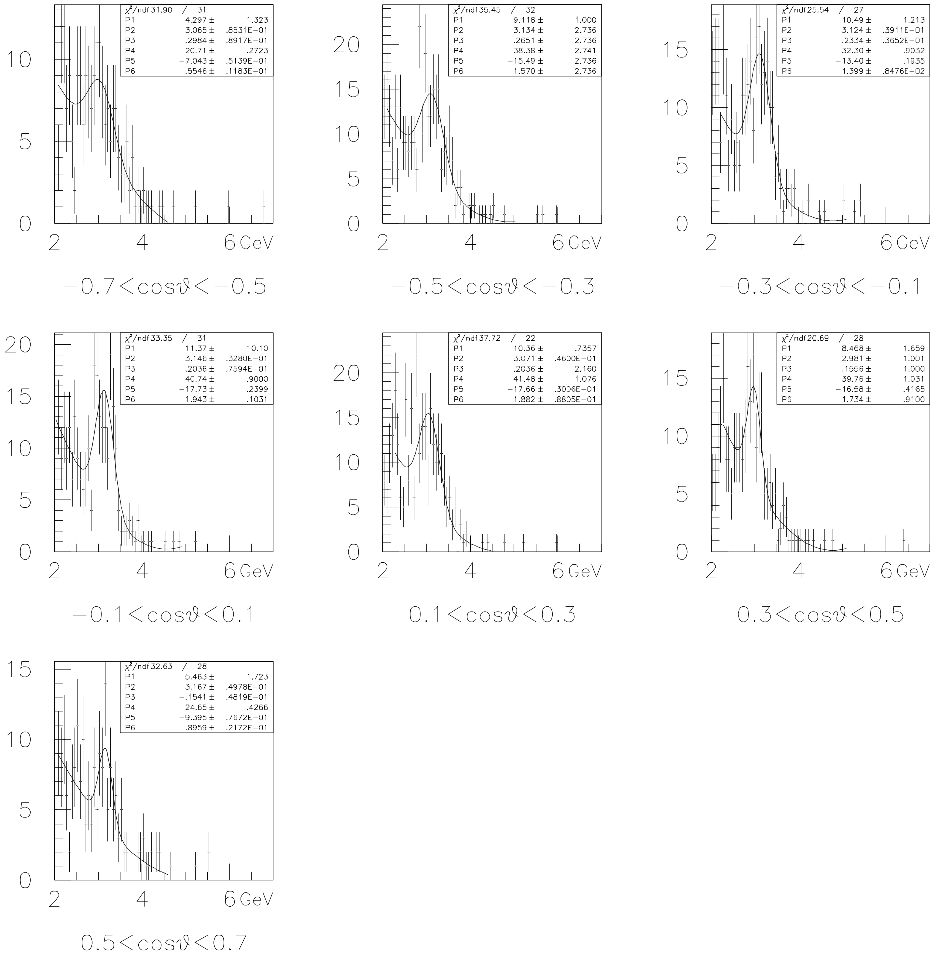

Figure B.12: Fitting of the mass spectrum: $0 < p_t < 1$ and $0.85 < x_F$. The backgrounds were fitted to second-order polynomials, and the J/ψ's were fitted to Gaussians. The $\cos\theta$ ranges are indicated under each spectrum. The current of SM12 magnet was 2040 Ampere.

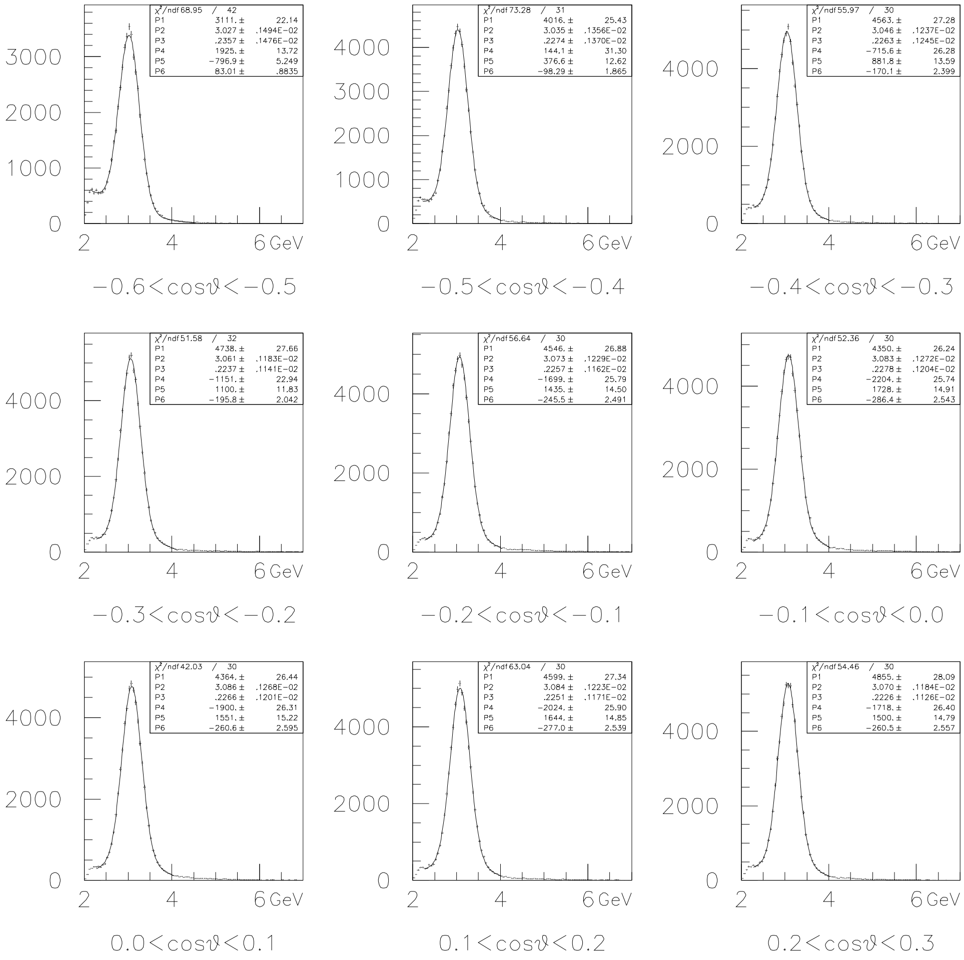

Figure B.13: Fitting of the mass spectrum: $1 < p_t < 2$ and $0.25 < x_F < 0.35$. The backgrounds were fitted to second-order polynomials, and the J/ψ's were fitted to Gaussians. The $\cos\theta$ ranges are indicated under each spectrum. The current of SM12 magnet was 2040 Ampere.

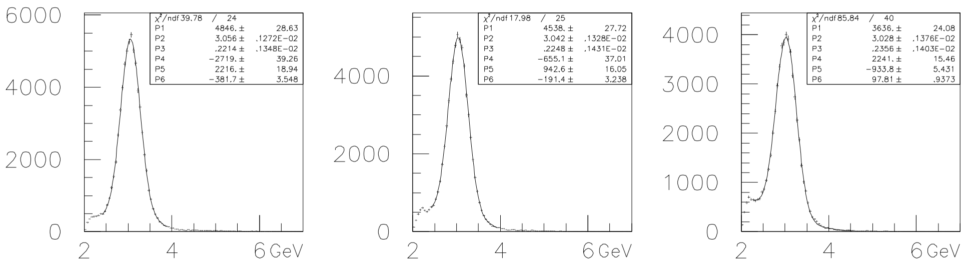

$0.3<\cos\vartheta<0.4$ $0.4<\cos\vartheta<0.5$ $0.5<\cos\vartheta<0.6$

Figure B.14: Fitting of the mass spectrum: $1 < p_t < 2$ and $0.25 < x_F < 0.35$. The backgrounds were fitted to second-order polynomials, and the J/ψ's were fitted to Gaussians. The $\cos\theta$ ranges are indicated under each spectrum. The current of SM12 magnet was 2040 Ampere.

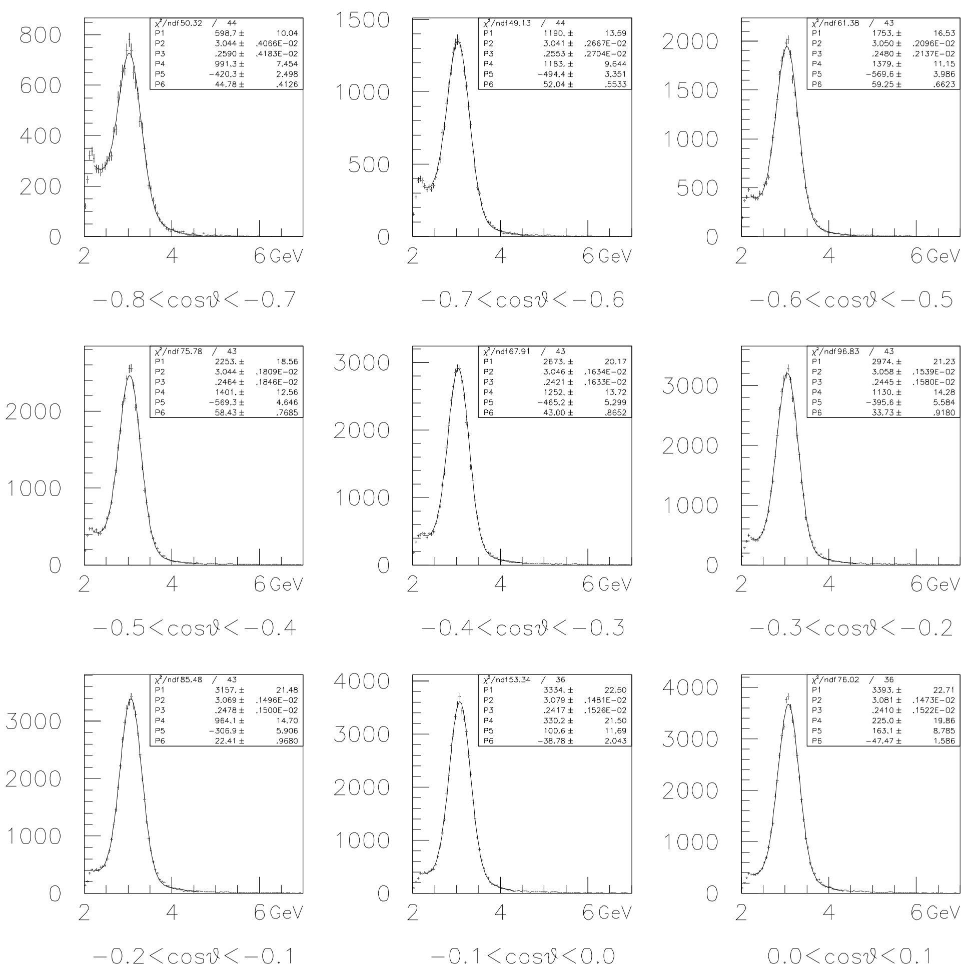

Figure B.15: Fitting of the mass spectrum: $1 < p_t < 2$ and $0.35 < x_F < 0.45$. The backgrounds were fitted to second-order polynomials, and the J/ψ's were fitted to Gaussians. The $\cos\theta$ ranges are indicated under each spectrum. The current of SM12 magnet was 2040 Ampere.

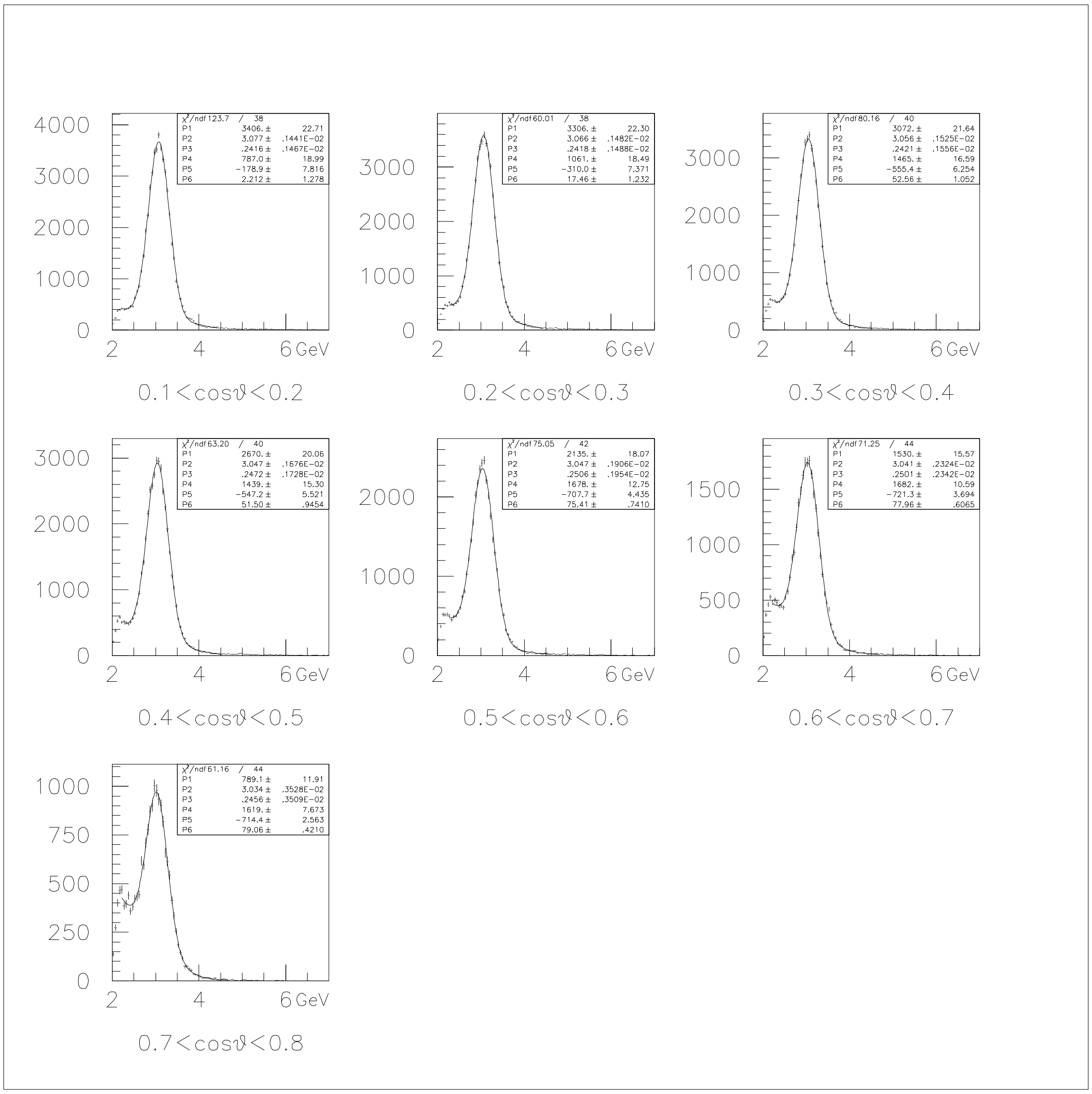

$0.1 < \cos\vartheta < 0.2$

$0.2 < \cos\vartheta < 0.3$

$0.3 < \cos\vartheta < 0.4$

$0.4 < \cos\vartheta < 0.5$

$0.5 < \cos\vartheta < 0.6$

$0.6 < \cos\vartheta < 0.7$

$0.7 < \cos\vartheta < 0.8$

Figure B.16: Fitting of the mass spectrum: $1 < p_t < 2$ and $0.35 < x_F < 0.45$. The backgrounds were fitted to second-order polynomials, and the J/ψ's were fitted to Gaussians. The $\cos\theta$ ranges are indicated under each spectrum. The current of SM12 magnet was 2040 Ampere.

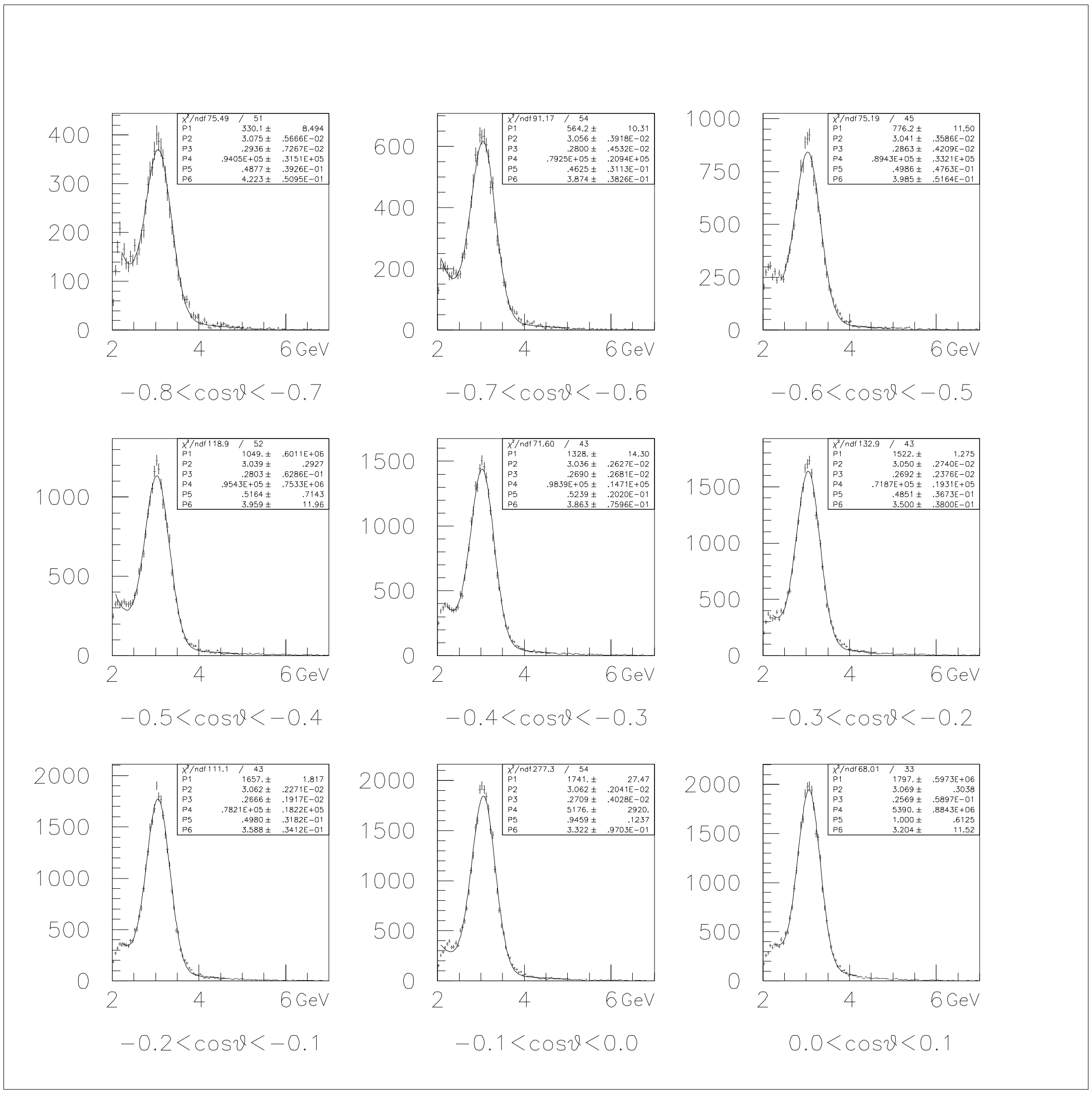

Figure B.17: Fitting of the mass spectrum: $1 < p_t < 2$ and $0.45 < x_F < 0.55$. The backgrounds were fitted to Kaplan functions, and the J/ψ's were fitted to Gaussians. The $\cos\theta$ ranges are indicated under each spectrum. The current of SM12 magnet was 2040 Ampere.

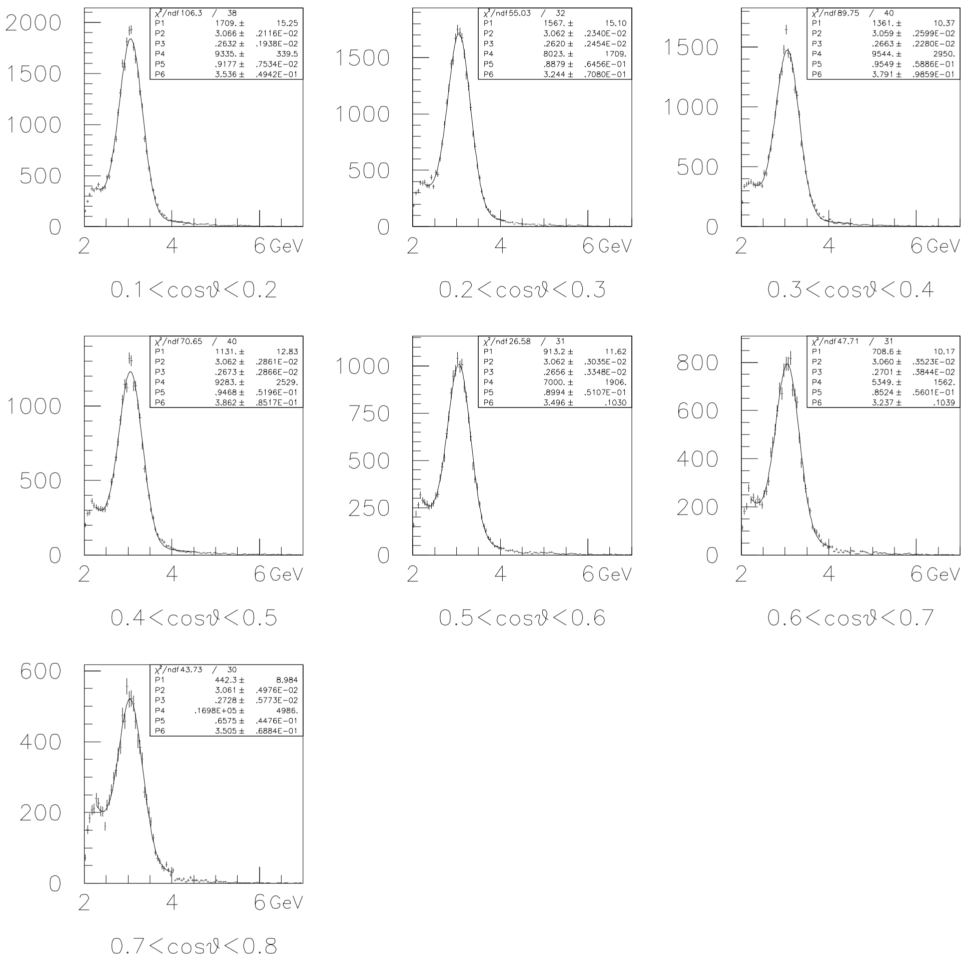

0.1<cosϑ<0.2

0.2<cosϑ<0.3

0.3<cosϑ<0.4

0.4<cosϑ<0.5

0.5<cosϑ<0.6

0.6<cosϑ<0.7

0.7<cosϑ<0.8

Figure B.18: Fitting of the mass spectrum: $1 < p_t < 2$ and $0.45 < x_F < 0.55$. The backgrounds were fitted to Kaplan functions, and the J/ψ's were fitted to Gaussians. The $\cos\theta$ ranges are indicated under each spectrum. The current of SM12 magnet was 2040 Ampere.

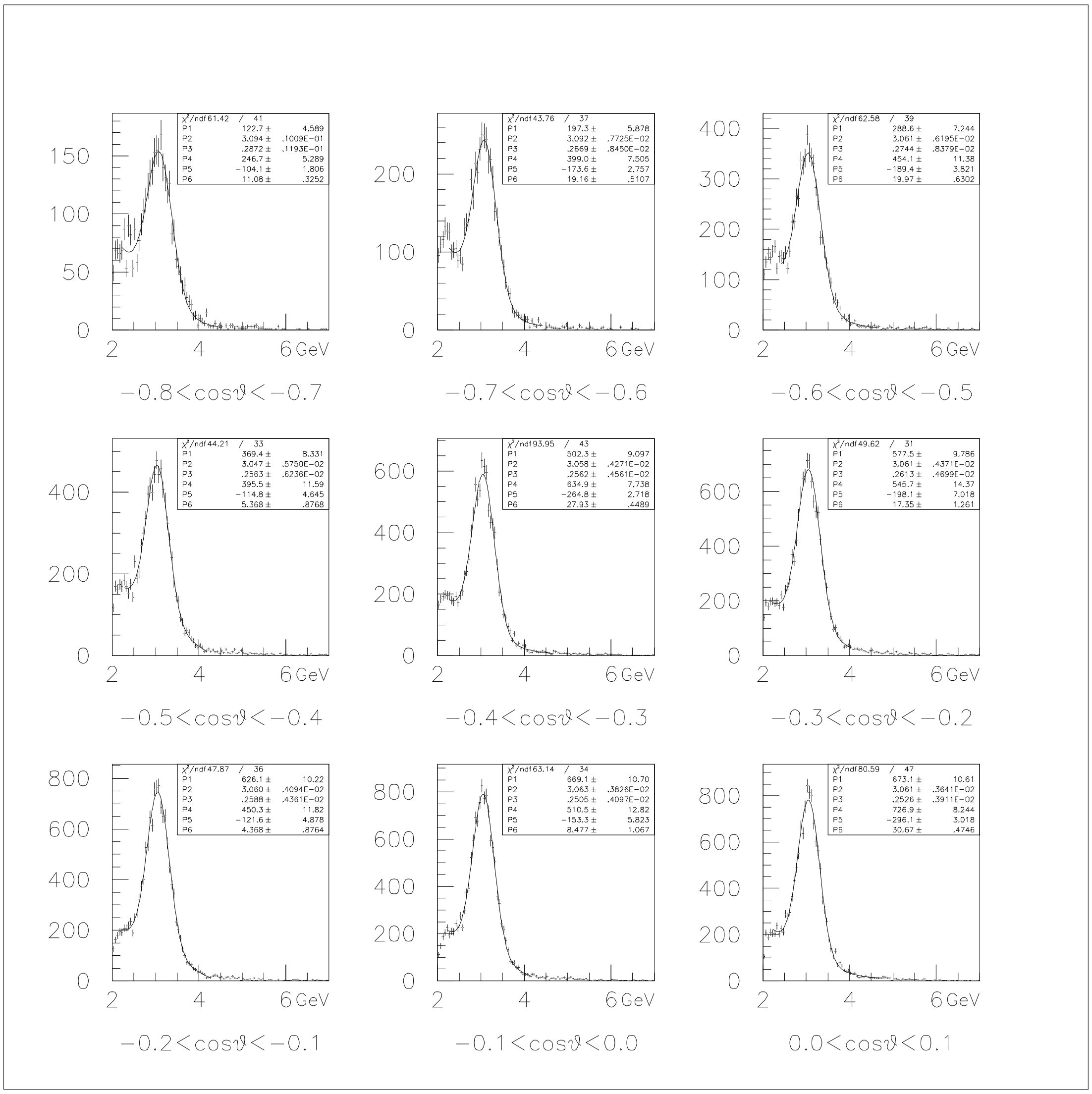

$-0.8<\cos\vartheta<-0.7$ $-0.7<\cos\vartheta<-0.6$ $-0.6<\cos\vartheta<-0.5$

$-0.5<\cos\vartheta<-0.4$ $-0.4<\cos\vartheta<-0.3$ $-0.3<\cos\vartheta<-0.2$

$-0.2<\cos\vartheta<-0.1$ $-0.1<\cos\vartheta<0.0$ $0.0<\cos\vartheta<0.1$

Figure B.19: Fitting of the mass spectrum: $1 < p_t < 2$ and $0.55 < x_F < 0.65$. The backgrounds were fitted to second-order polynomials, and the J/ψ's were fitted to Gaussians. The $\cos\theta$ ranges are indicated under each spectrum. The current of SM12 magnet was 2040 Ampere.

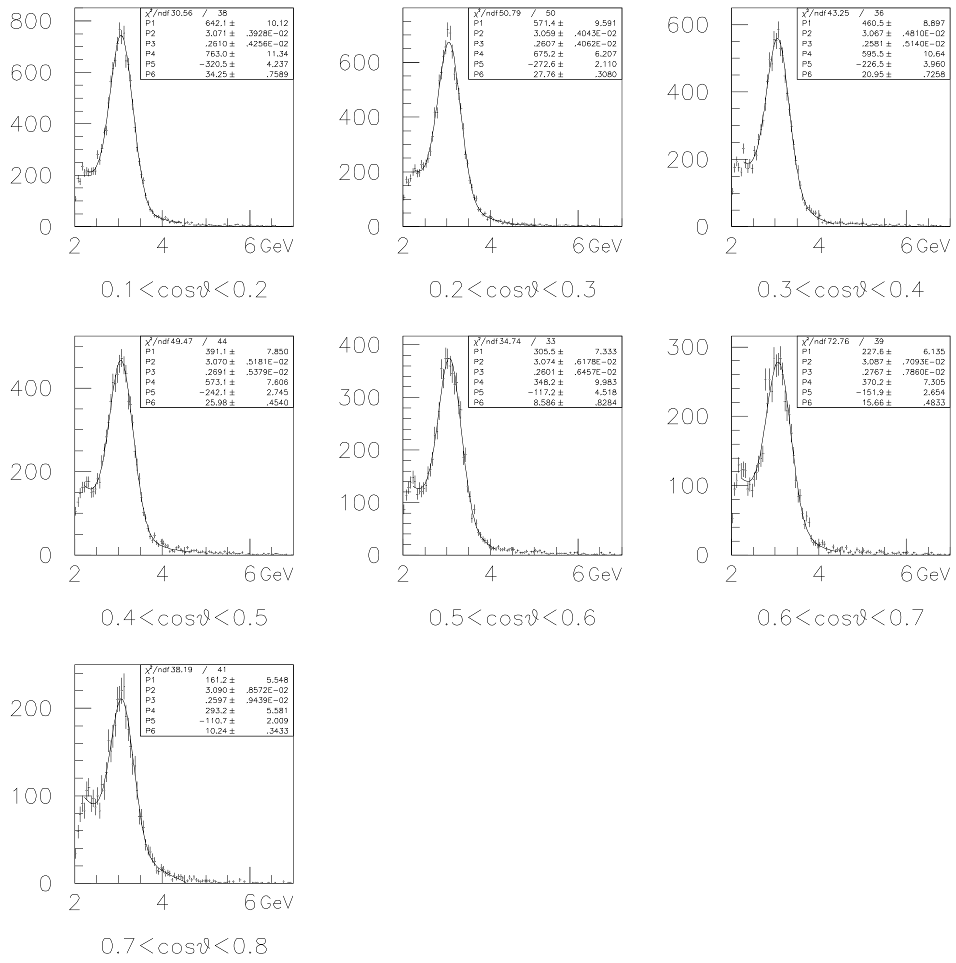

$0.1<\cos\vartheta<0.2$

$0.2<\cos\vartheta<0.3$

$0.3<\cos\vartheta<0.4$

$0.4<\cos\vartheta<0.5$

$0.5<\cos\vartheta<0.6$

$0.6<\cos\vartheta<0.7$

$0.7<\cos\vartheta<0.8$

Figure B.20: Fitting of the mass spectrum: $1 < p_t < 2$ and $0.55 < x_F < 0.65$. The backgrounds were fitted to second-order polynomials, and the J/ψ's were fitted to Gaussians. The $\cos\theta$ ranges are indicated under each spectrum. The current of SM12 magnet was 2040 Ampere.

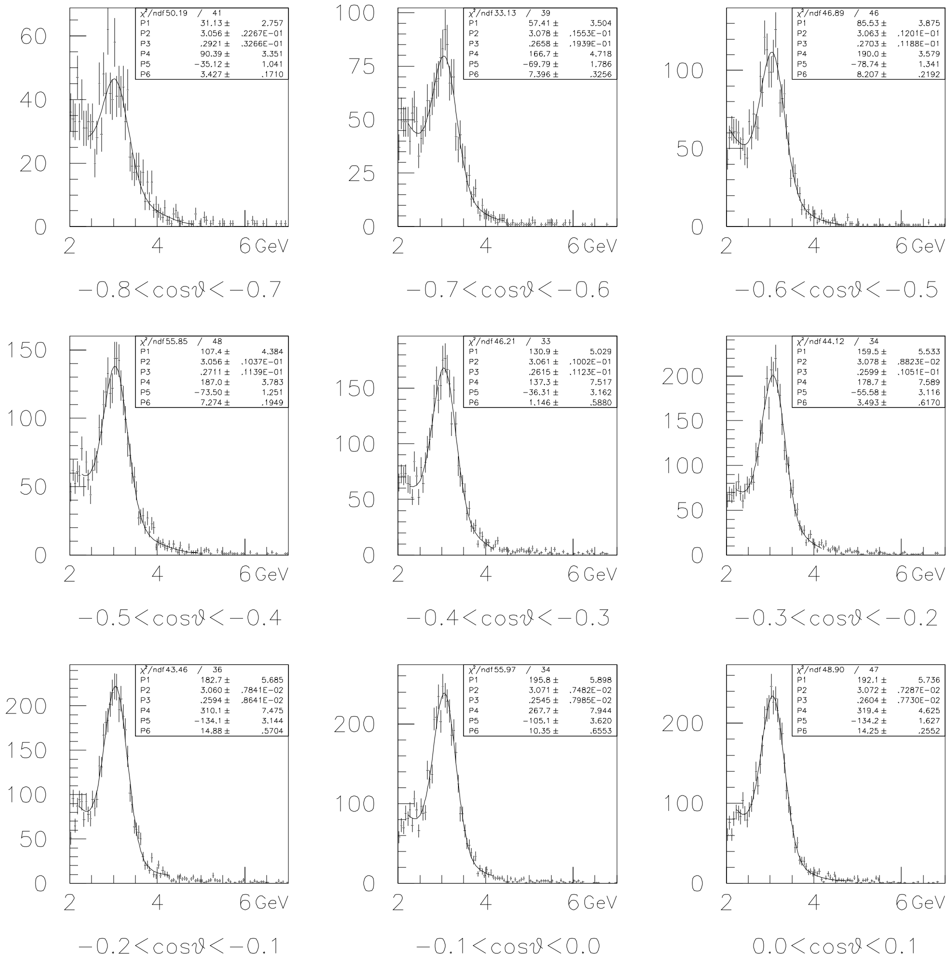

$-0.8<\cos\vartheta<-0.7$ $-0.7<\cos\vartheta<-0.6$ $-0.6<\cos\vartheta<-0.5$

$-0.5<\cos\vartheta<-0.4$ $-0.4<\cos\vartheta<-0.3$ $-0.3<\cos\vartheta<-0.2$

$-0.2<\cos\vartheta<-0.1$ $-0.1<\cos\vartheta<0.0$ $0.0<\cos\vartheta<0.1$

Figure B.21: Fitting of the mass spectrum: $1 < p_t < 2$ and $0.65 < x_F < 0.75$. The backgrounds were fitted to second-order polynomials, and the J/ψ's were fitted to Gaussians. The $\cos\theta$ ranges are indicated under each spectrum. The current of SM12 magnet was 2040 Ampere.

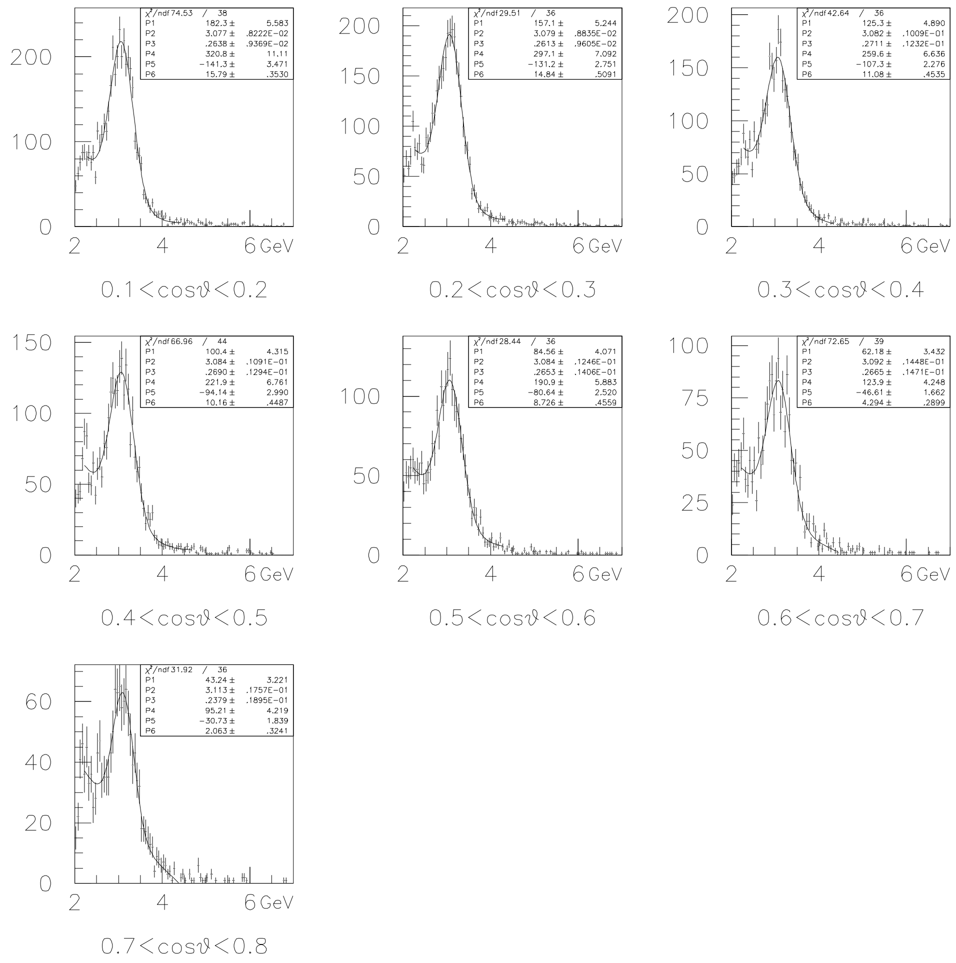

0.1<cosϑ<0.2

0.2<cosϑ<0.3

0.3<cosϑ<0.4

0.4<cosϑ<0.5

0.5<cosϑ<0.6

0.6<cosϑ<0.7

0.7<cosϑ<0.8

Figure B.22: Fitting of the mass spectrum: $1 < p_t < 2$ and $0.65 < x_F < 0.75$. The backgrounds were fitted to second-order polynomials, and the J/ψ's were fitted to Gaussians. The $\cos\theta$ ranges are indicated under each spectrum. The current of SM12 magnet was 2040 Ampere.

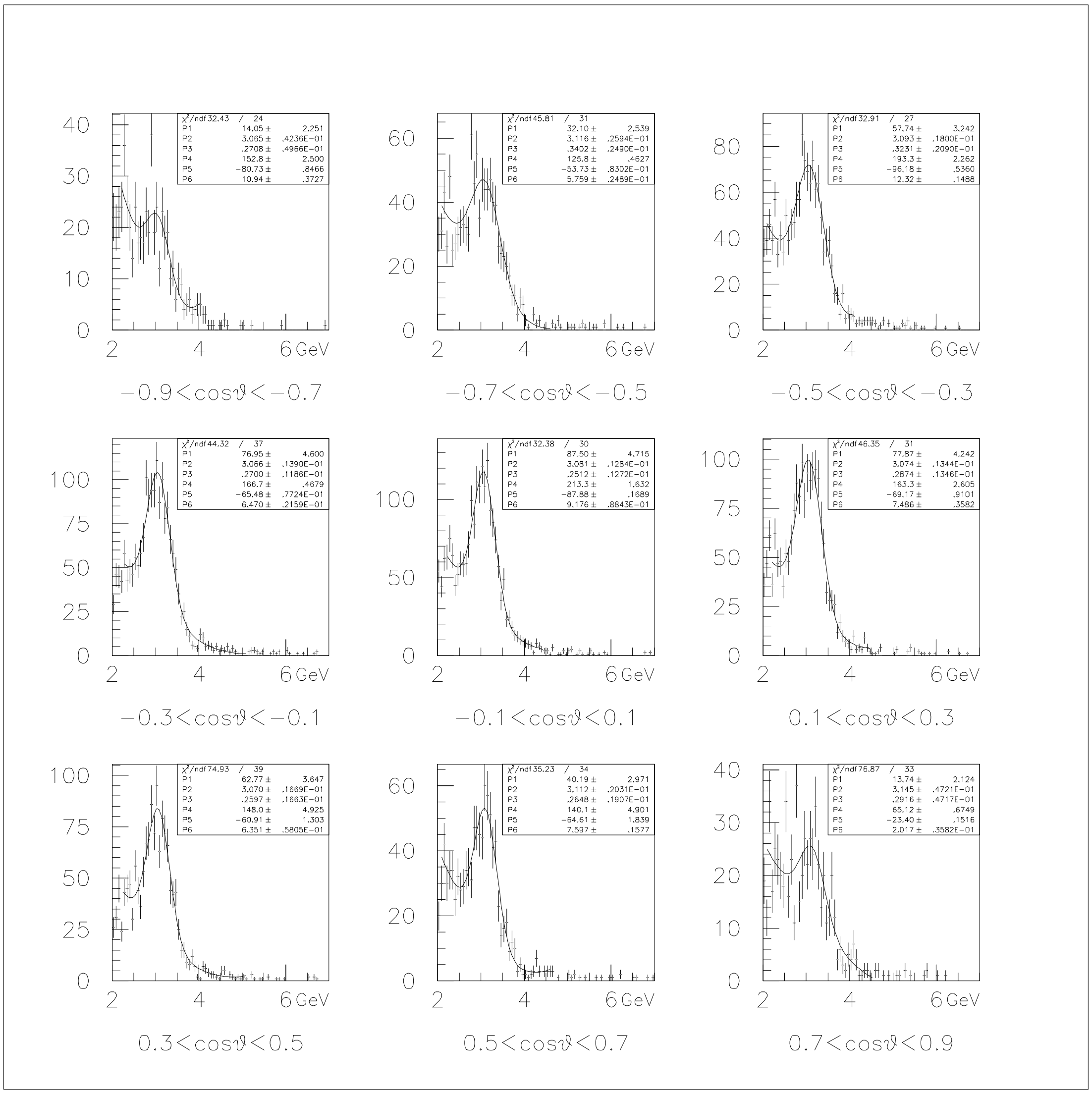

Figure B.23: Fitting of the mass spectrum: $1 < p_t < 2$ and $0.75 < x_F < 0.85$. The backgrounds were fitted to second-order polynomials, and the J/ψ's were fitted to Gaussians. The $\cos\theta$ ranges are indicated under each spectrum. The current of SM12 magnet was 2040 Ampere.

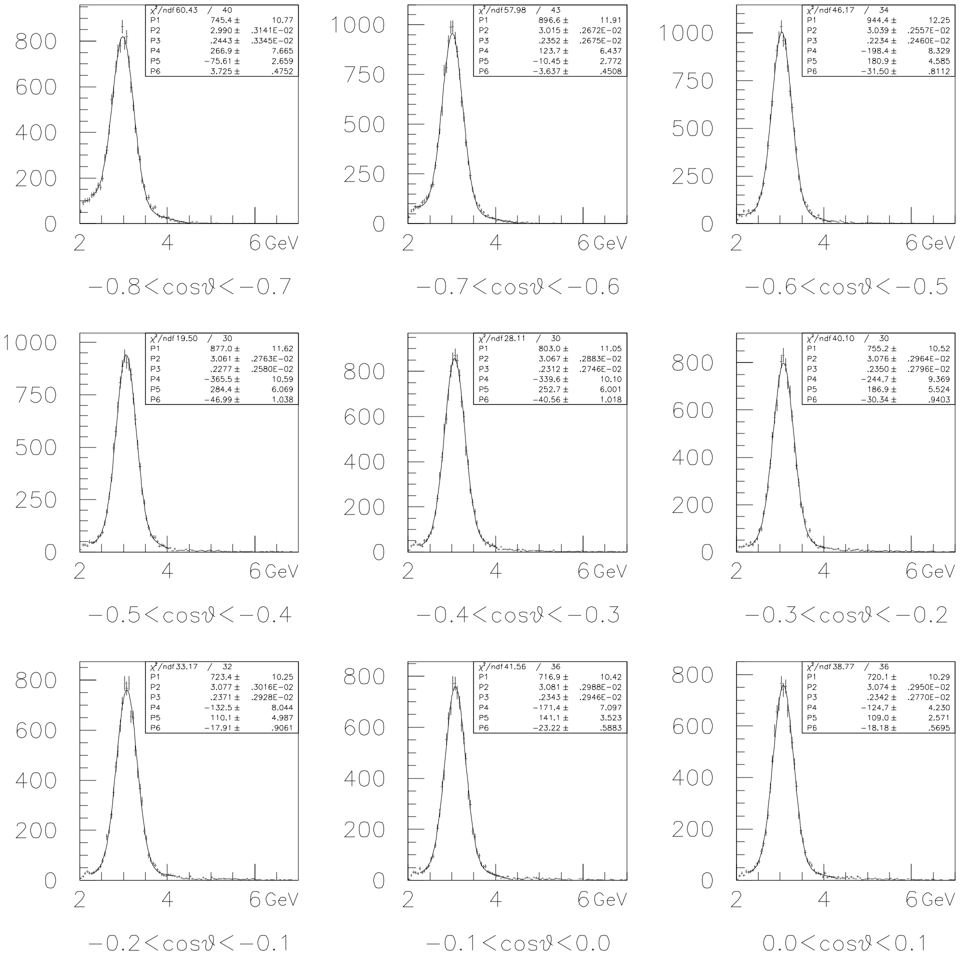

Figure B.24: Fitting of the mass spectrum: $2 < p_t < 3$ and $0.25 < x_F < 0.35$. The backgrounds were fitted to second-order polynomials, and the J/ψ's were fitted to Gaussians. The $\cos\theta$ ranges are indicated under each spectrum. The current of SM12 magnet was 2040 Ampere.

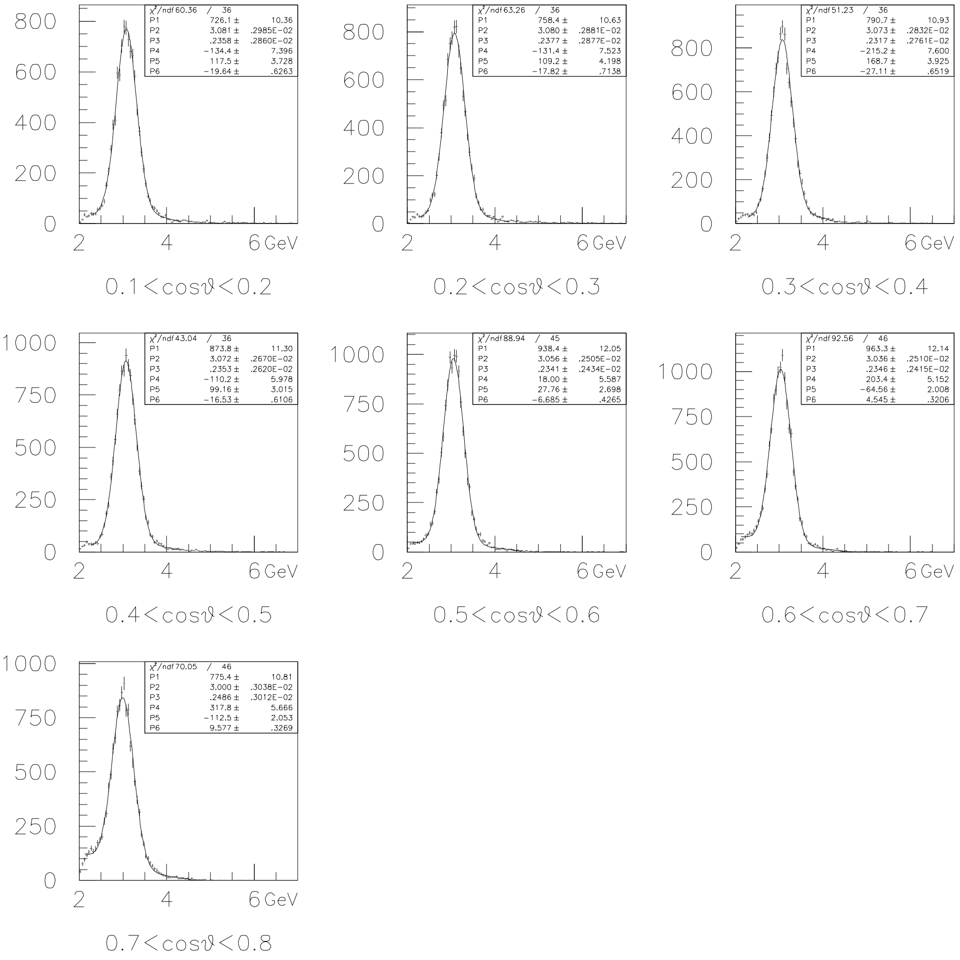

0.1<cosϑ<0.2

0.2<cosϑ<0.3

0.3<cosϑ<0.4

0.4<cosϑ<0.5

0.5<cosϑ<0.6

0.6<cosϑ<0.7

0.7<cosϑ<0.8

Figure B.25: Fitting of the mass spectrum: $2 < p_t < 3$ and $0.25 < x_F < 0.35$. The backgrounds were fitted to second-order polynomials, and the J/ψ's were fitted to Gaussians. The $\cos\theta$ ranges are indicated under each spectrum. The current of SM12 magnet was 2040 Ampere.

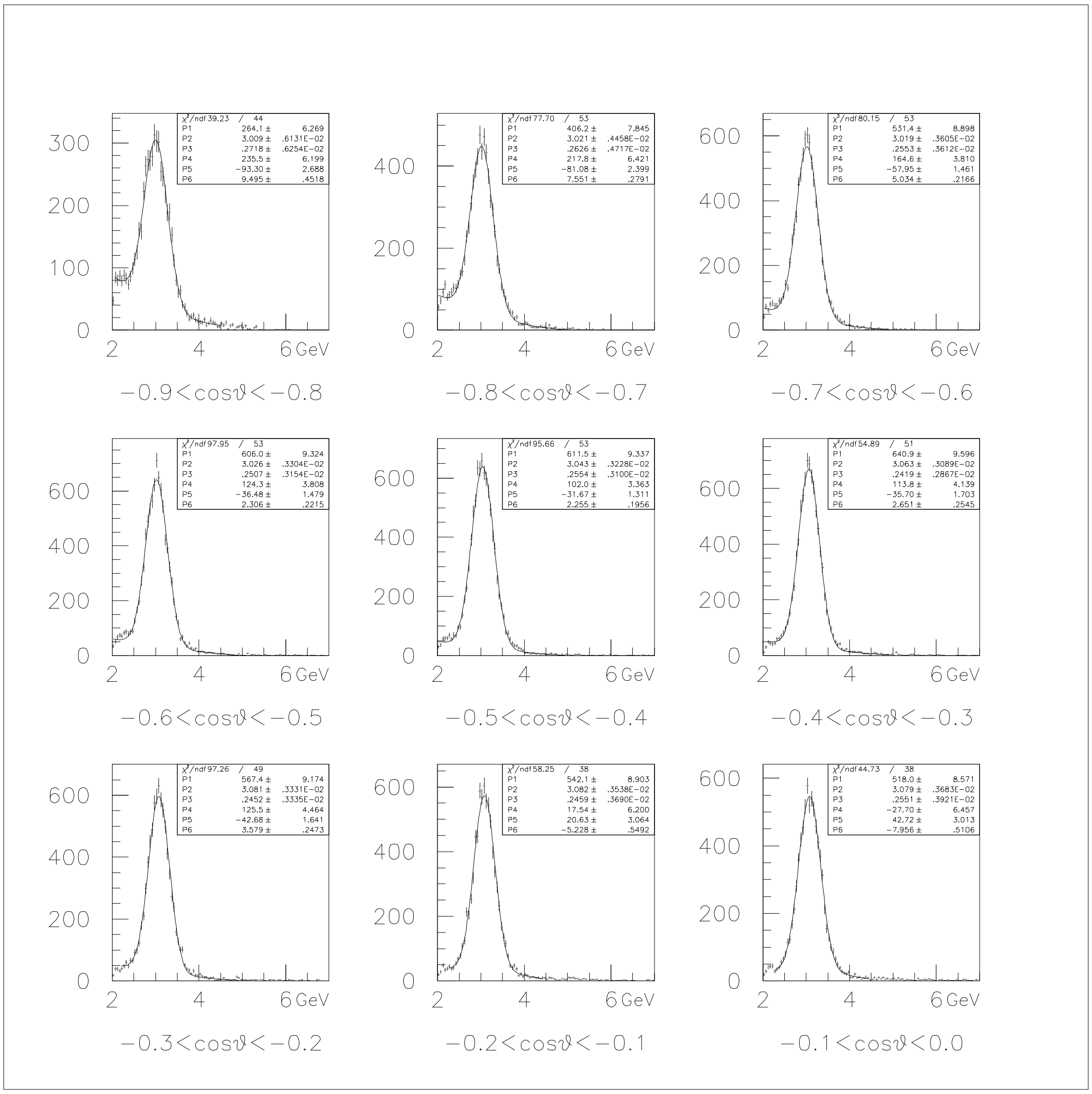

$-0.9<\cos\vartheta<-0.8$

$-0.8<\cos\vartheta<-0.7$

$-0.7<\cos\vartheta<-0.6$

$-0.6<\cos\vartheta<-0.5$

$-0.5<\cos\vartheta<-0.4$

$-0.4<\cos\vartheta<-0.3$

$-0.3<\cos\vartheta<-0.2$

$-0.2<\cos\vartheta<-0.1$

$-0.1<\cos\vartheta<0.0$

Figure B.26: Fitting of the mass spectrum: $2 < p_t < 3$ and $0.35 < x_F < 0.45$. The backgrounds were fitted to second-order polynomials, and the J/ψ's were fitted to Gaussians. The $\cos\theta$ ranges are indicated under each spectrum. The current of SM12 magnet was 2040 Ampere.

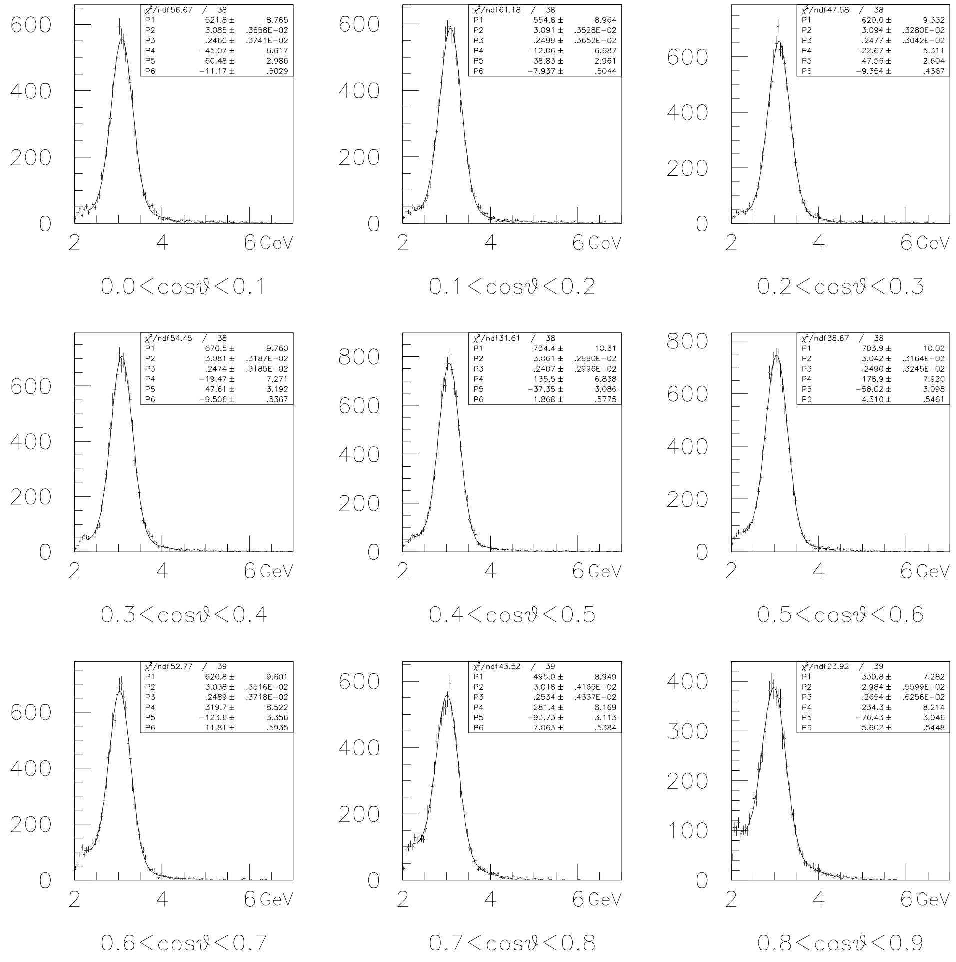

Figure B.27: Fitting of the mass spectrum: $2 < p_t < 3$ and $0.35 < x_F < 0.45$. The backgrounds were fitted to second-order polynomials, and the J/ψ's were fitted to Gaussians. The $\cos\theta$ ranges are indicated under each spectrum. The current of SM12 magnet was 2040 Ampere.

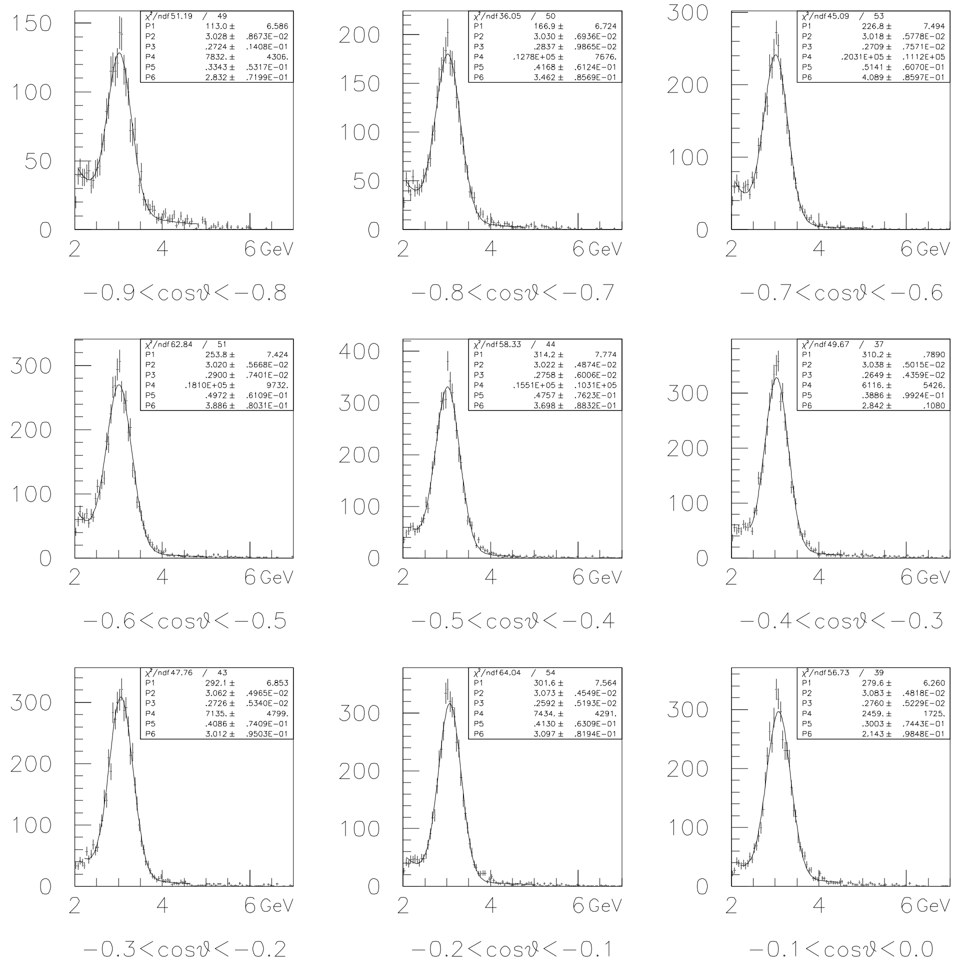

$-0.9<\cos\vartheta<-0.8$ $-0.8<\cos\vartheta<-0.7$ $-0.7<\cos\vartheta<-0.6$

$-0.6<\cos\vartheta<-0.5$ $-0.5<\cos\vartheta<-0.4$ $-0.4<\cos\vartheta<-0.3$

$-0.3<\cos\vartheta<-0.2$ $-0.2<\cos\vartheta<-0.1$ $-0.1<\cos\vartheta<0.0$

Figure B.28: Fitting of the mass spectrum: $2 < p_t < 3$ and $0.45 < x_F < 0.55$. The backgrounds were fitted to Kaplan functions, and the J/ψ's were fitted to Gaussians. The $\cos\theta$ ranges are indicated under each spectrum. The current of SM12 magnet was 2040 Ampere.

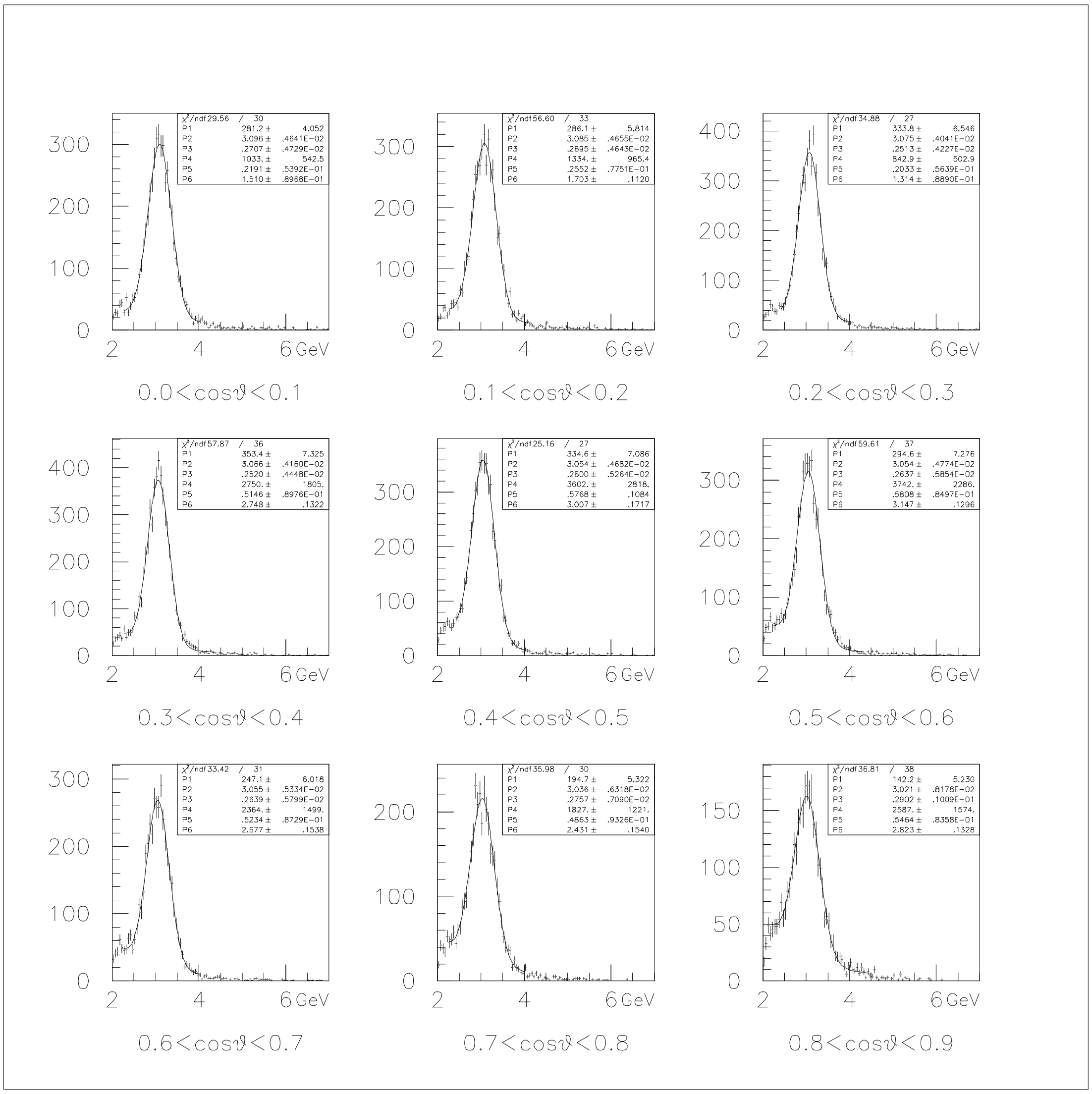

Figure B.29: Fitting of the mass spectrum: $2 < p_t < 3$ and $0.45 < x_F < 0.55$. The backgrounds were fitted to Kaplan functions, and the J/ψ's were fitted to Gaussians. The $\cos\theta$ ranges are indicated under each spectrum. The current of SM12 magnet was 2040 Ampere.

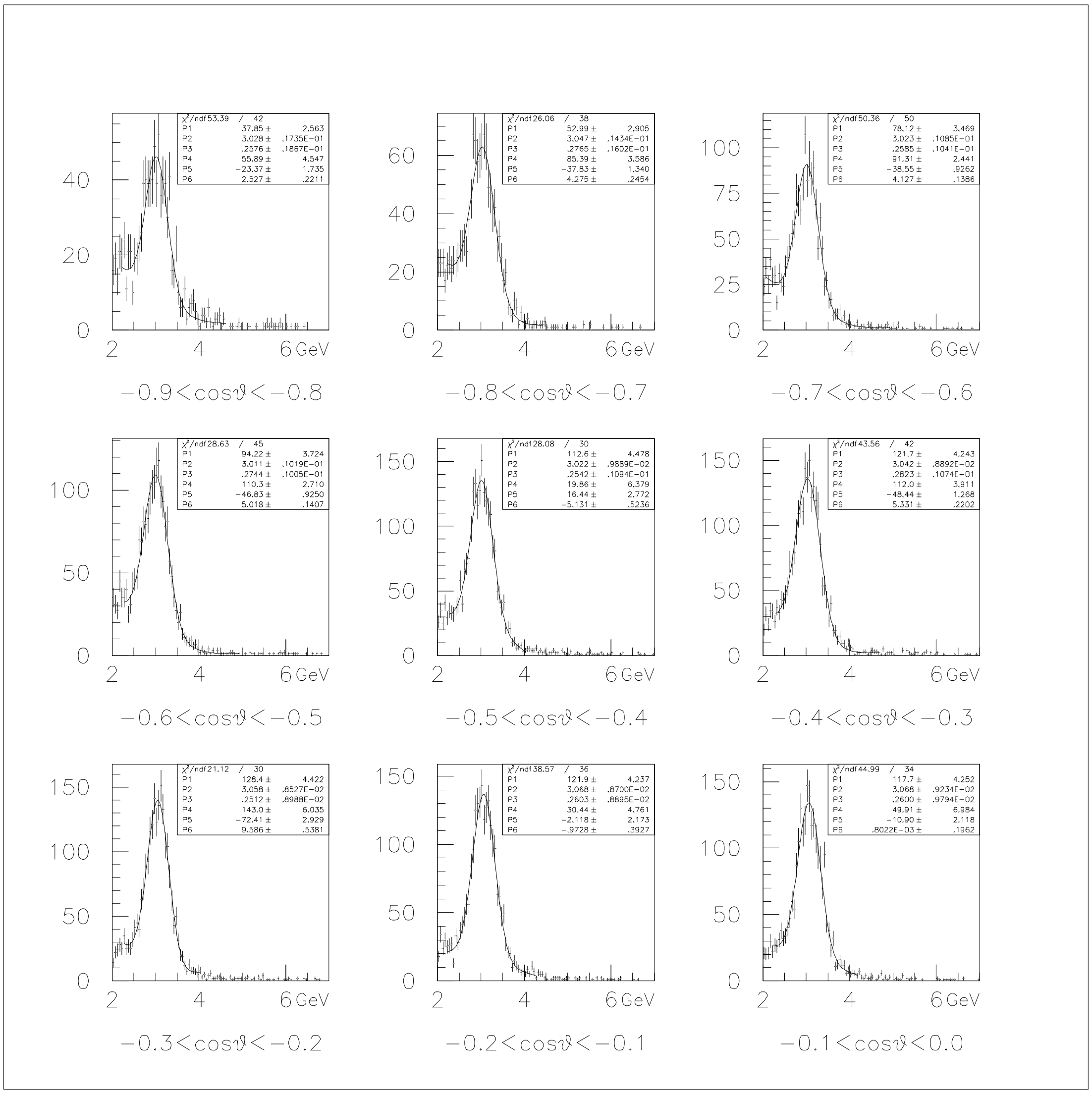

$-0.9<\cos\vartheta<-0.8$ $-0.8<\cos\vartheta<-0.7$ $-0.7<\cos\vartheta<-0.6$

$-0.6<\cos\vartheta<-0.5$ $-0.5<\cos\vartheta<-0.4$ $-0.4<\cos\vartheta<-0.3$

$-0.3<\cos\vartheta<-0.2$ $-0.2<\cos\vartheta<-0.1$ $-0.1<\cos\vartheta<0.0$

Figure B.30: Fitting of the mass spectrum: $2 < p_t < 3$ and $0.55 < x_F < 0.65$. The backgrounds were fitted to second-order polynomials, and the J/ψ's were fitted to Gaussians. The $\cos\theta$ ranges are indicated under each spectrum. The current of SM12 magnet was 2040 Ampere.

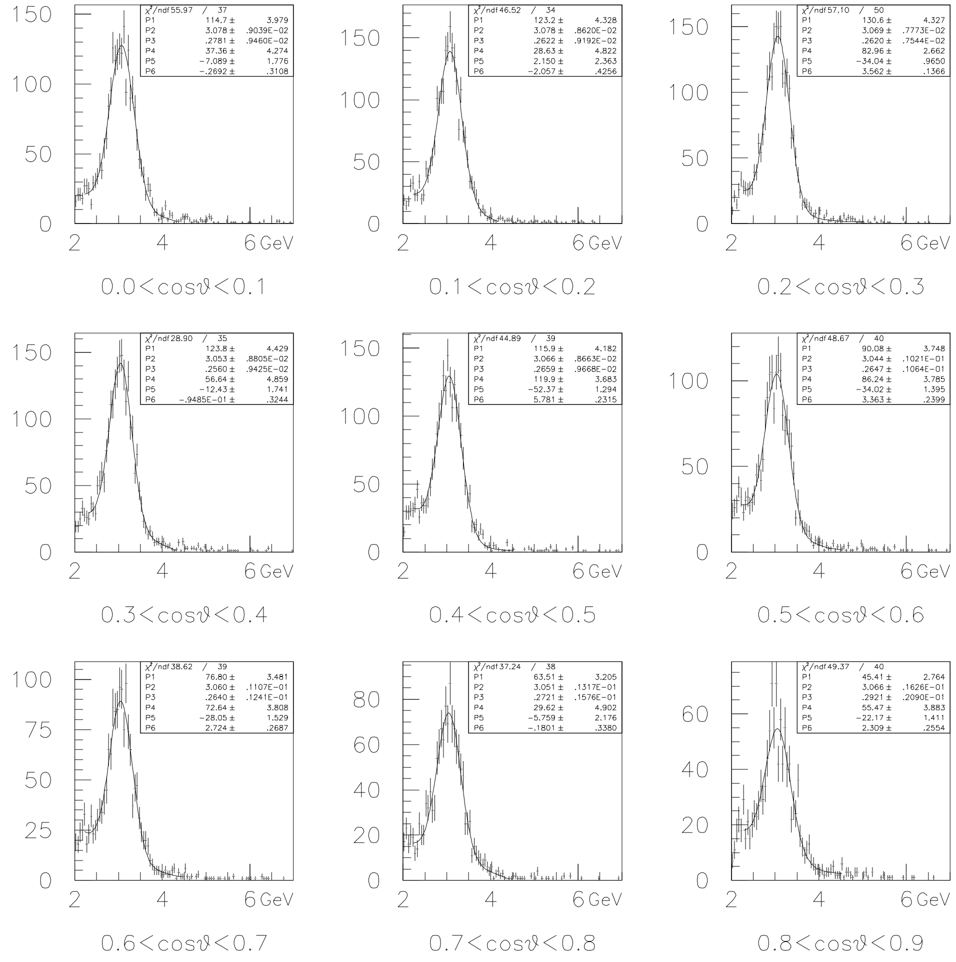

Figure B.31: Fitting of the mass spectrum: $2 < p_t < 3$ and $0.55 < x_F < 0.65$. The backgrounds were fitted to second-order polynomials, and the J/ψ's were fitted to Gaussians. The $\cos\theta$ ranges are indicated under each spectrum. The current of SM12 magnet was 2040 Ampere.

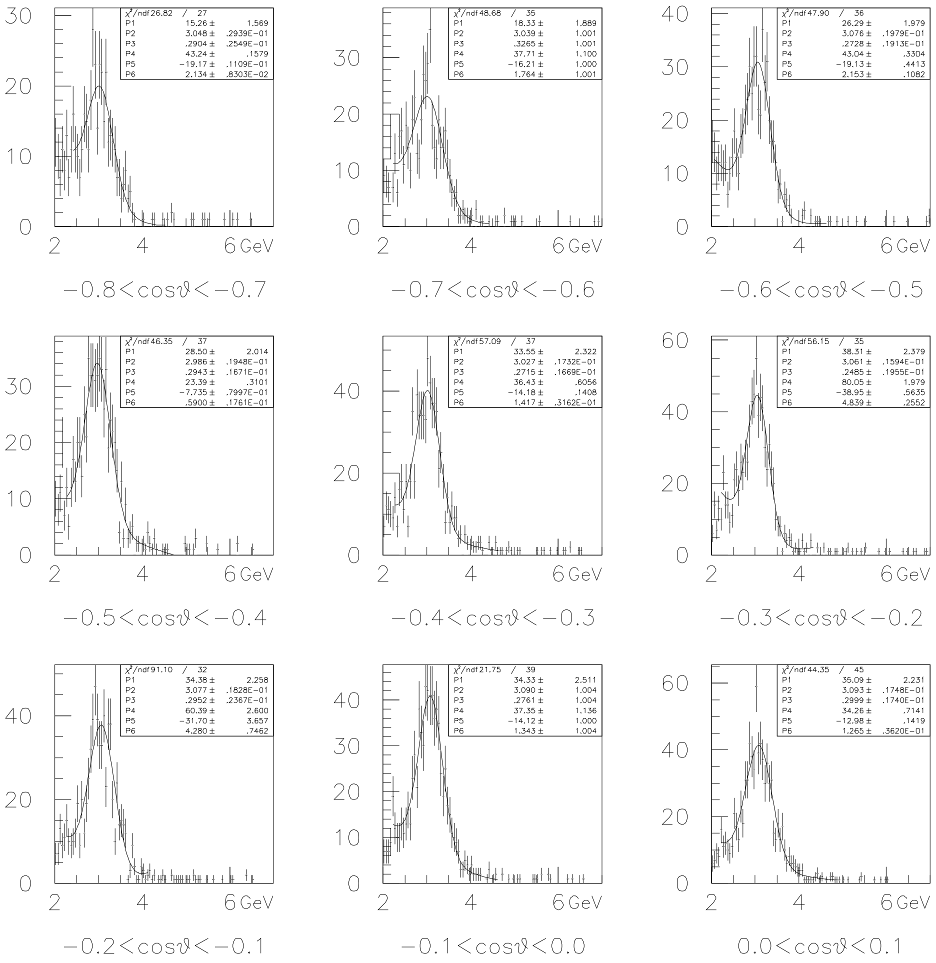

Figure B.32: Fitting of the mass spectrum: $2 < p_t < 3$ and $0.65 < x_F < 0.75$. The backgrounds were fitted to second-order polynomials, and the J/ψ's were fitted to Gaussians. The $\cos\theta$ ranges are indicated under each spectrum. The current of SM12 magnet was 2040 Ampere.

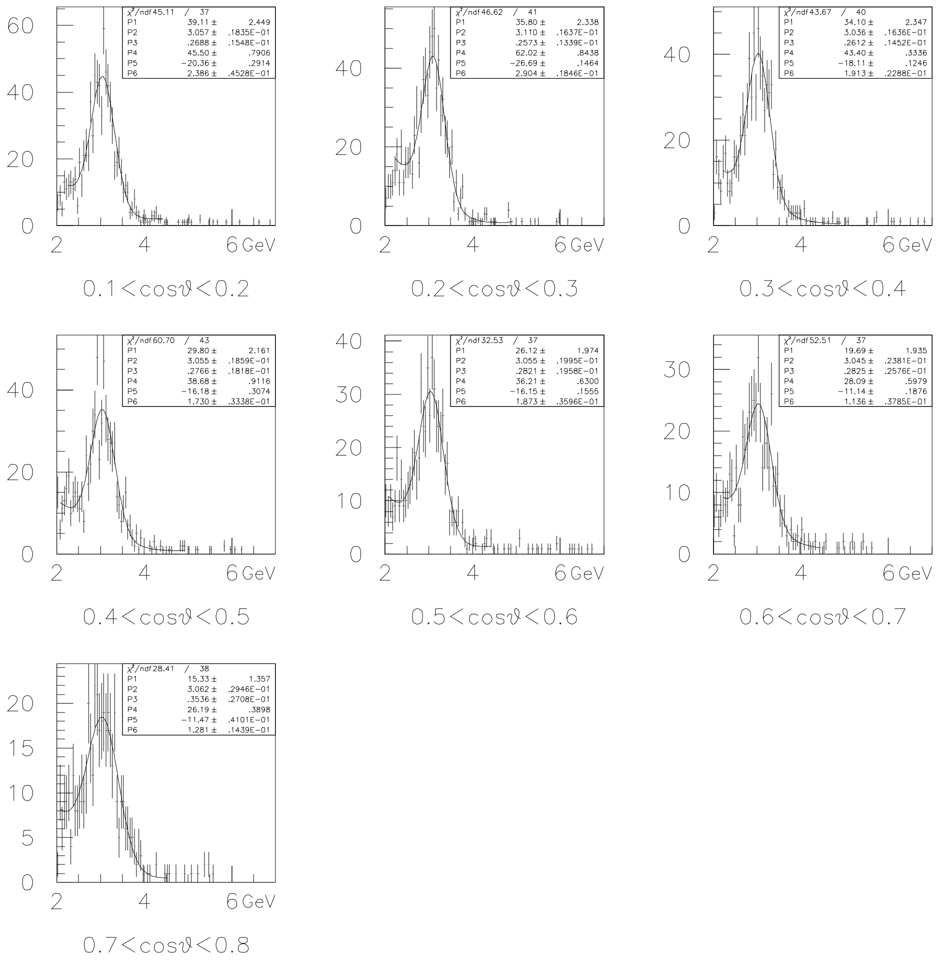

Figure B.33: Fitting of the mass spectrum: $2 < p_t < 3$ and $0.65 < x_F < 0.75$. The backgrounds were fitted to second-order polynomials, and the J/ψ's were fitted to Gaussians. The $\cos\theta$ ranges are indicated under each spectrum. The current of SM12 magnet was 2040 Ampere.

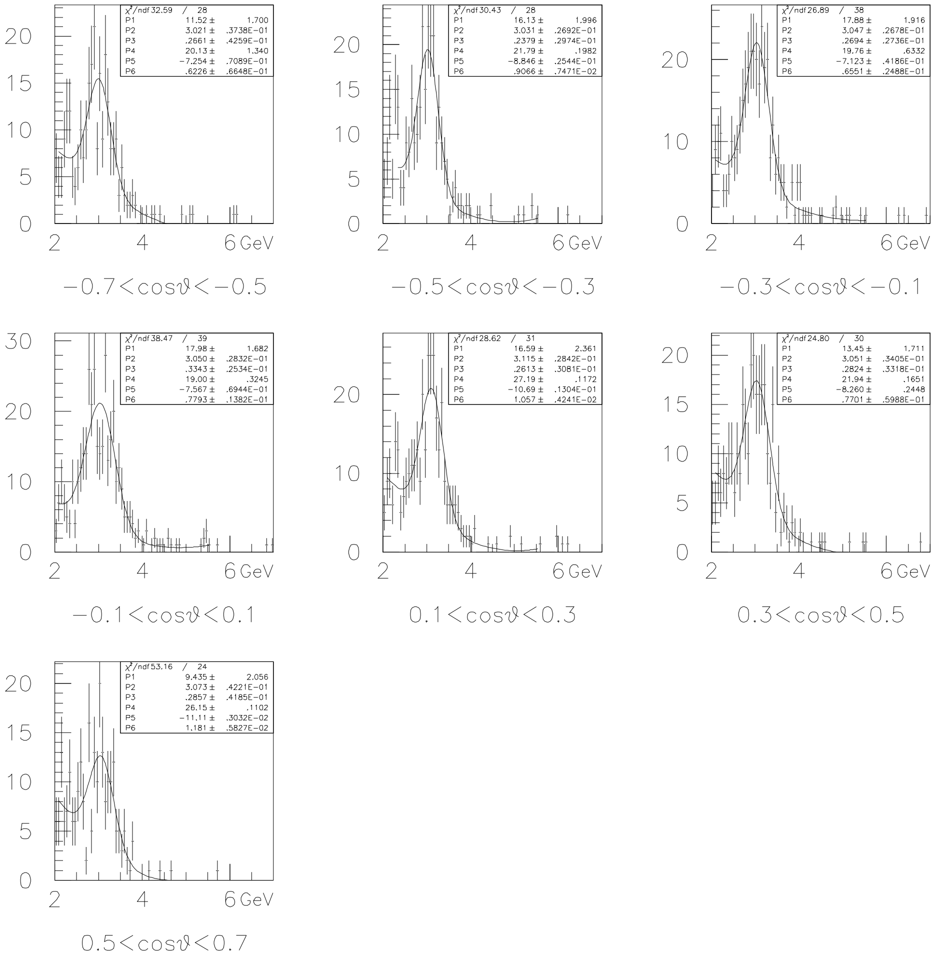

Figure B.34: Fitting of the mass spectrum: $2 < p_t < 3$ and $0.65 < x_F < 0.75$. The backgrounds were fitted to second-order polynomials, and the J/ψ's were fitted to Gaussians. The $\cos\theta$ ranges are indicated under each spectrum. The current of SM12 magnet was 2040 Ampere.

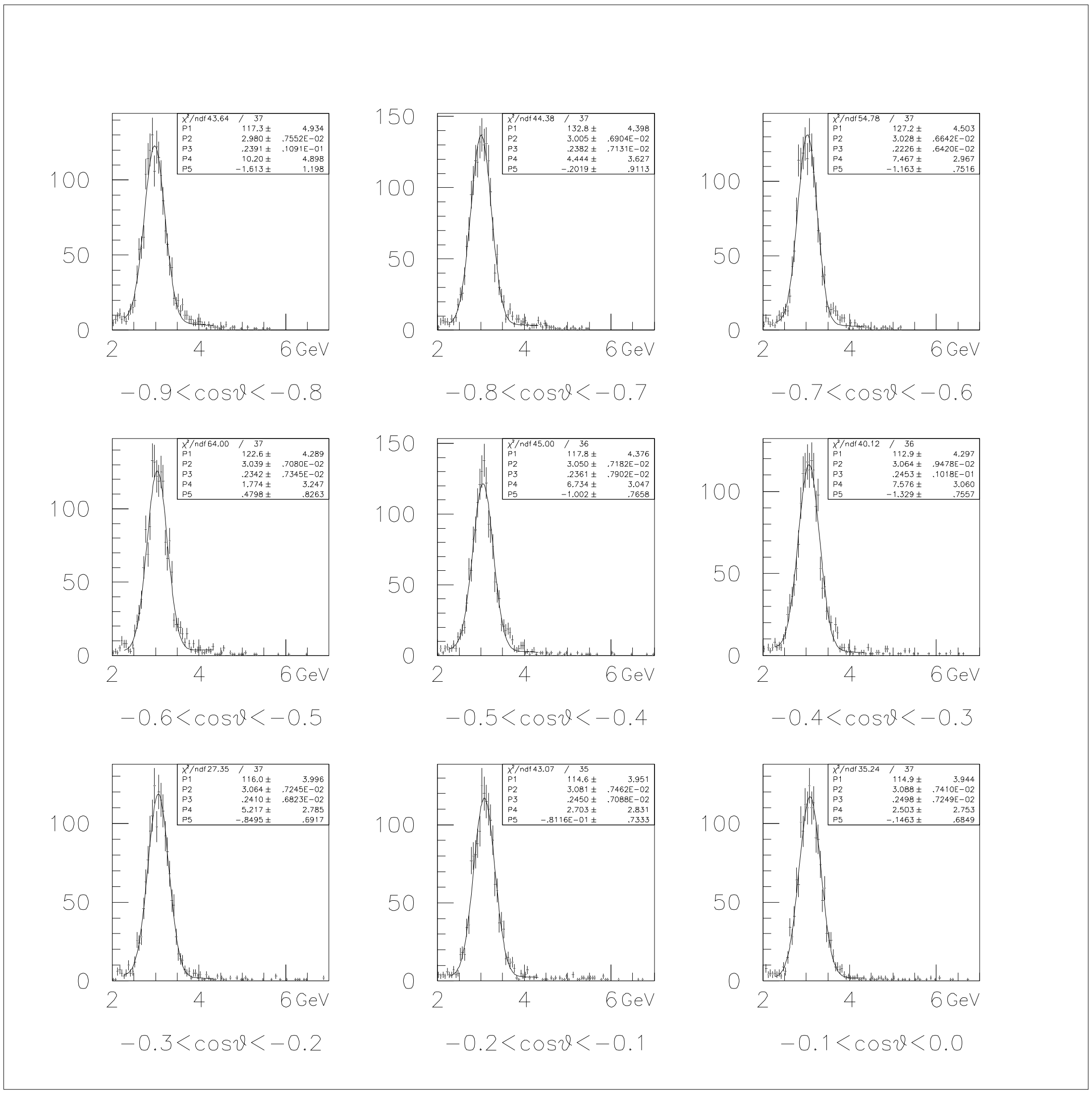

Figure B.35: Fitting of the mass spectrum: $3 < p_t$ and $0.25 < x_F < 0.35$. The backgrounds were fitted to exponential functions, and the J/ψ's were fitted to Gaussians. The $\cos\theta$ ranges are indicated under each spectrum. The current of SM12 magnet was 2040 Ampere.

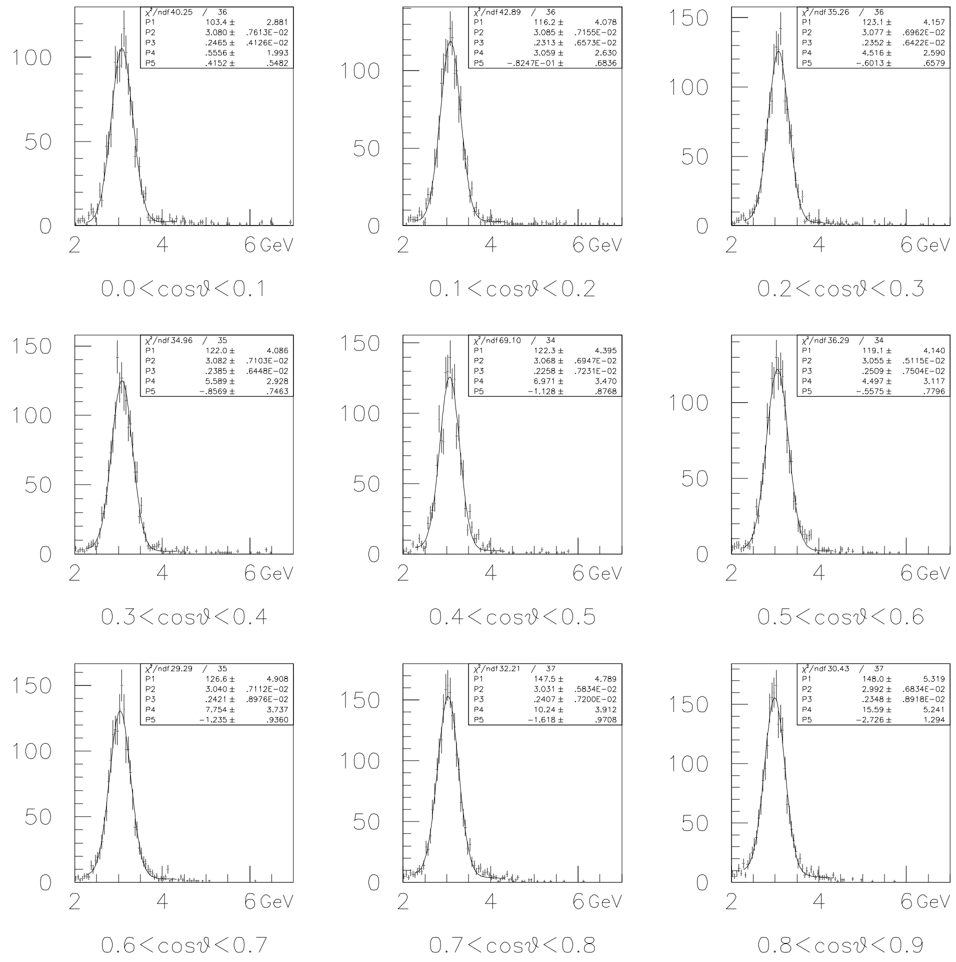

Figure B.36: Fitting of the mass spectrum: $3 < p_t$ and $0.25 < x_F < 0.35$. The backgrounds were fitted to exponential functions, and the J/ψ's were fitted to Gaussians. The $\cos\theta$ ranges are indicated under each spectrum. The current of SM12 magnet was 2040 Ampere.

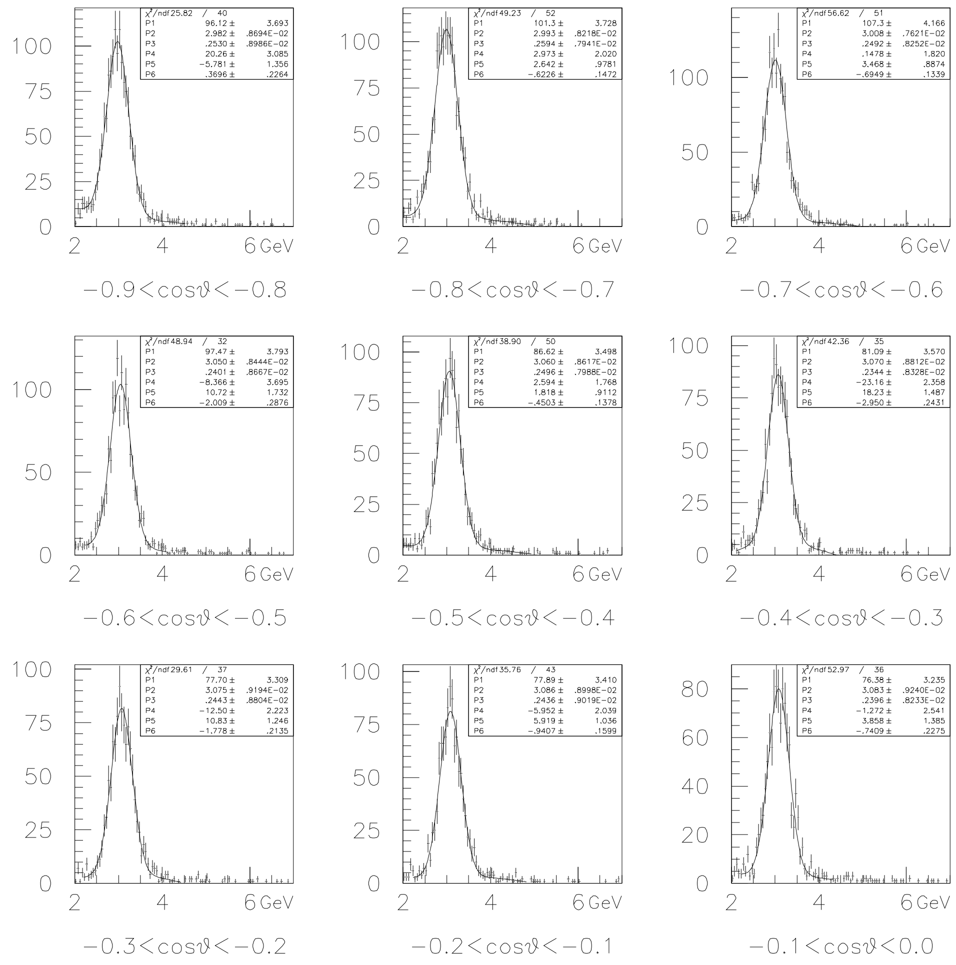

Figure B.37: Fitting of the mass spectrum: $3 < p_t$ and $0.35 < x_F < 0.45$. The backgrounds were fitted to second-order polynomials, and the J/ψ's were fitted to Gaussians. The $\cos\theta$ ranges are indicated under each spectrum. The current of SM12 magnet was 2040 Ampere.

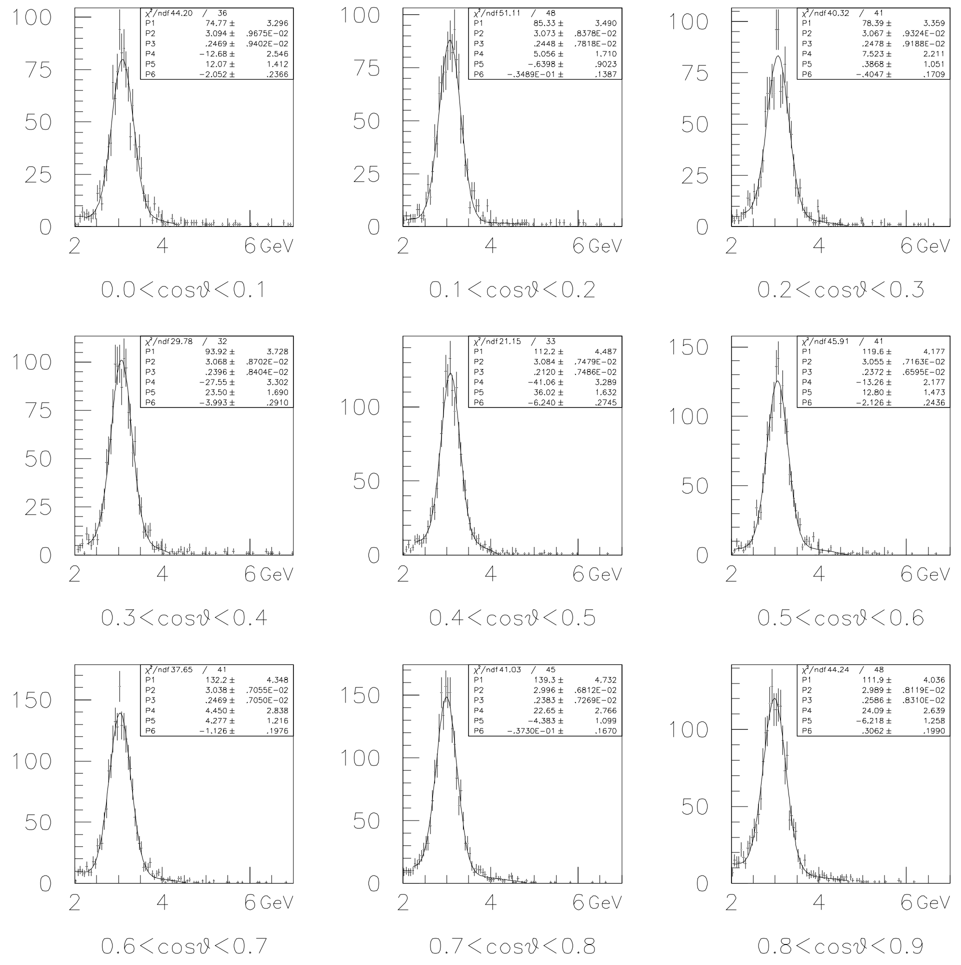

0.0<cosϑ<0.1 0.1<cosϑ<0.2 0.2<cosϑ<0.3

0.3<cosϑ<0.4 0.4<cosϑ<0.5 0.5<cosϑ<0.6

0.6<cosϑ<0.7 0.7<cosϑ<0.8 0.8<cosϑ<0.9

Figure B.38: Fitting of the mass spectrum: $3 < p_t$ and $0.35 < x_F < 0.45$. The backgrounds were fitted to second-order polynomials, and the J/ψ's were fitted to Gaussians. The $\cos\theta$ ranges are indicated under each spectrum. The current of SM12 magnet was 2040 Ampere.

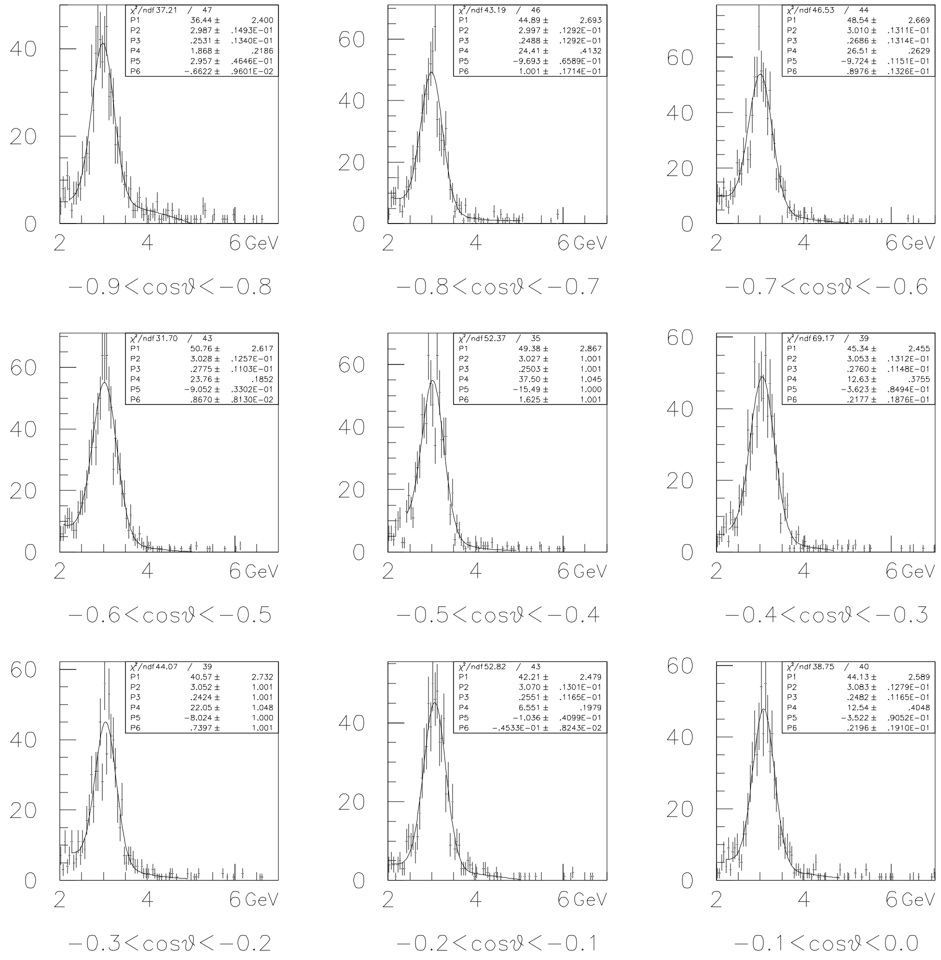

Figure B.39: Fitting of the mass spectrum: $3 < p_t$ and $0.45 < x_F < 0.55$. The backgrounds were fitted to second-order polynomials, and the J/ψ's were fitted to Gaussians. The $\cos\theta$ ranges are indicated under each spectrum. The current of SM12 magnet was 2040 Ampere.

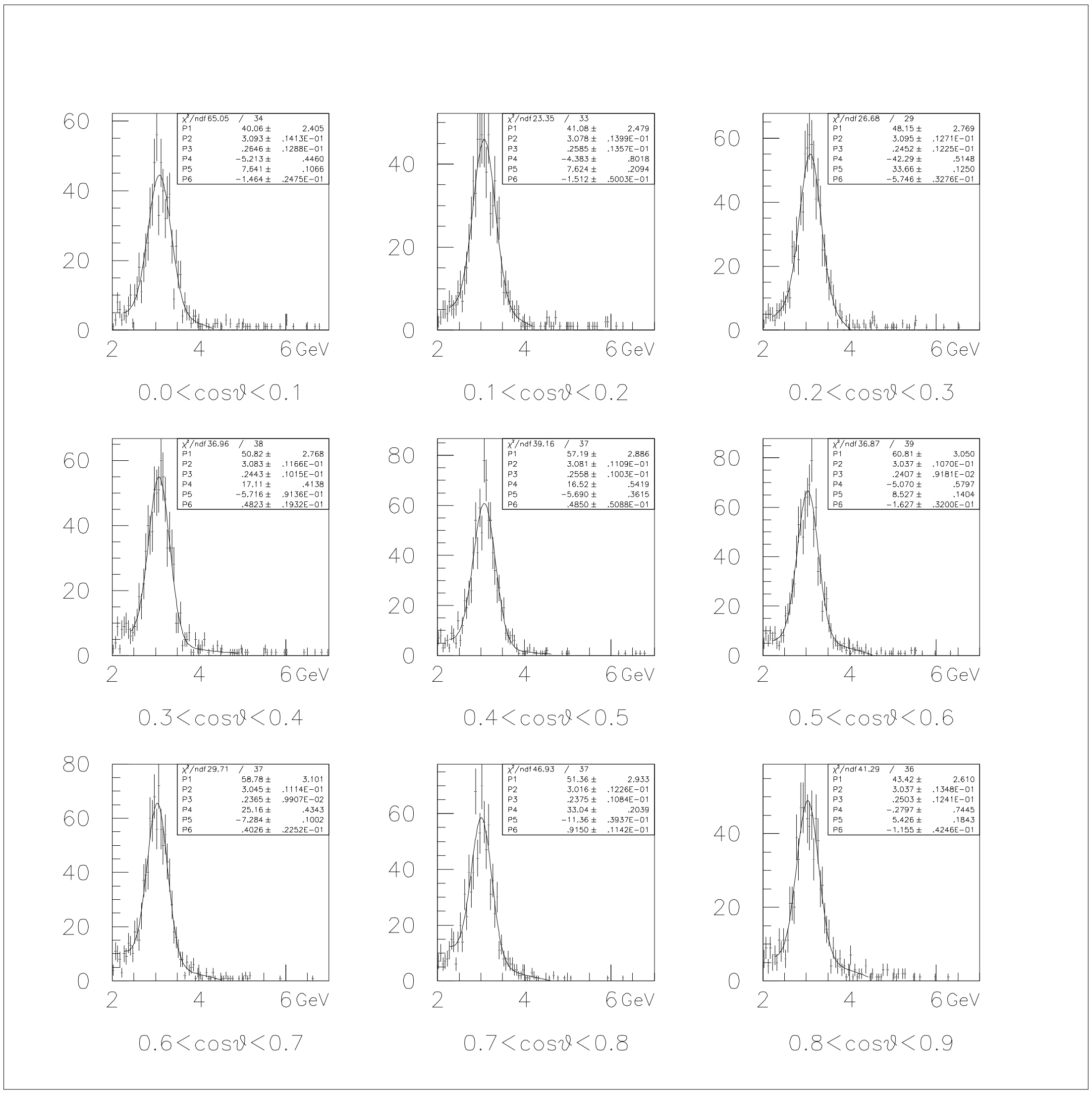

Figure B.40: Fitting of the mass spectrum: $3 < p_t$ and $0.45 < x_F < 0.55$. The backgrounds were fitted to second-order polynomials, and the J/ψ's were fitted to Gaussians. The $\cos\theta$ ranges are indicated under each spectrum. The current of SM12 magnet was 2040 Ampere.

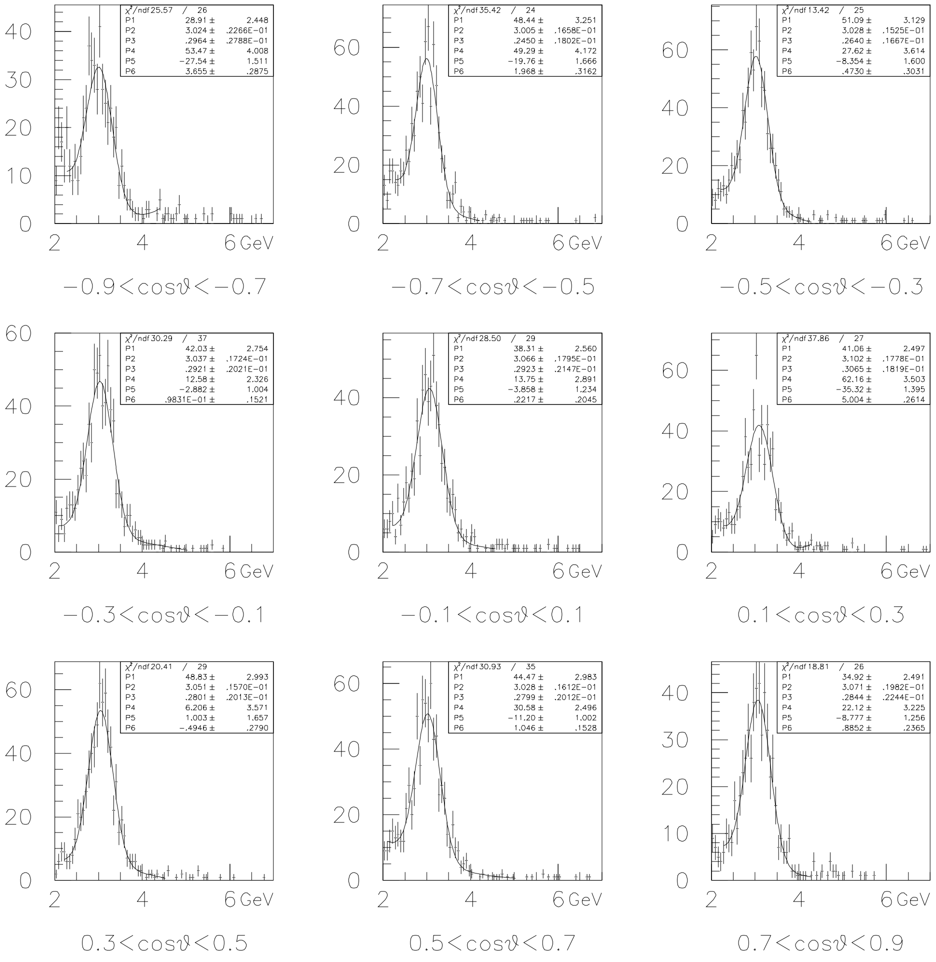

$-0.9<\cos\vartheta<-0.7$ $-0.7<\cos\vartheta<-0.5$ $-0.5<\cos\vartheta<-0.3$

$-0.3<\cos\vartheta<-0.1$ $-0.1<\cos\vartheta<0.1$ $0.1<\cos\vartheta<0.3$

$0.3<\cos\vartheta<0.5$ $0.5<\cos\vartheta<0.7$ $0.7<\cos\vartheta<0.9$

Figure B.41: Fitting of the mass spectrum: $3 < p_t$ and $0.55 < x_F < 0.65$. The backgrounds were fitted to second-order polynomials, and the J/ψ's were fitted to Gaussians. The $\cos\theta$ ranges are indicated under each spectrum. The current of SM12 magnet was 2040 Ampere.

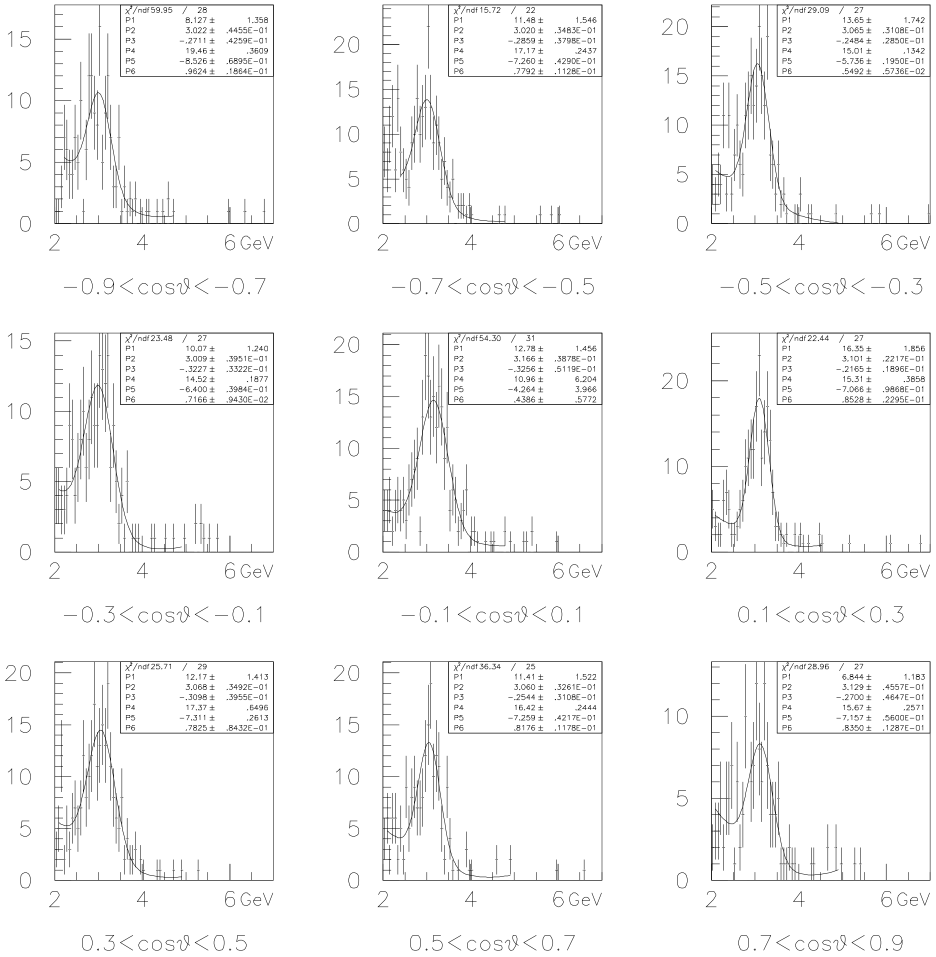

$-0.9<\cos\vartheta<-0.7$ $-0.7<\cos\vartheta<-0.5$ $-0.5<\cos\vartheta<-0.3$

$-0.3<\cos\vartheta<-0.1$ $-0.1<\cos\vartheta<0.1$ $0.1<\cos\vartheta<0.3$

$0.3<\cos\vartheta<0.5$ $0.5<\cos\vartheta<0.7$ $0.7<\cos\vartheta<0.9$

Figure B.42: Fitting of the mass spectrum: $3 < p_t$ and $0.65 < x_F < 0.75$. The backgrounds were fitted to second-order polynomials, and the J/ψ's were fitted to Gaussians. The $\cos\theta$ ranges are indicated under each spectrum. The current of SM12 magnet was 2040 Ampere.

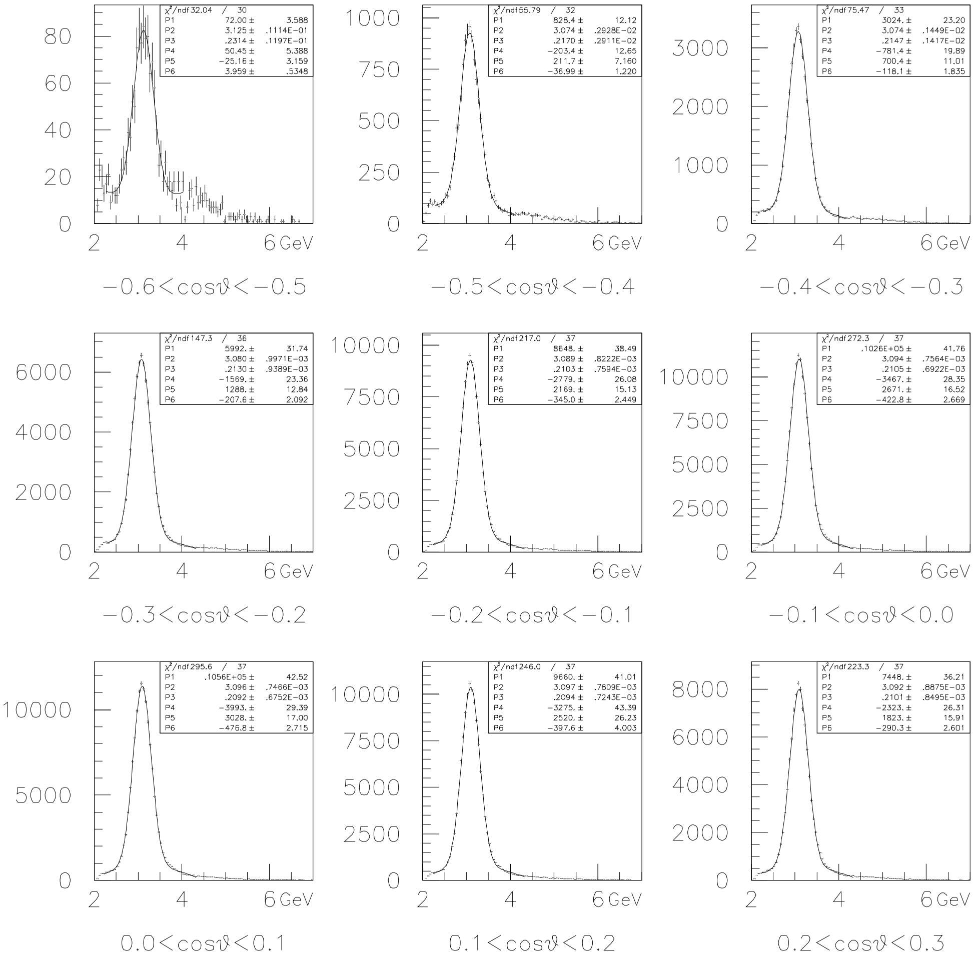

Figure B.43: Fitting of the mass spectrum: $0 < p_t < 1$ and $0.25 < x_F < 0.35$. The backgrounds were fitted to second-order polynomials, and the J/ψ's were fitted to Gaussians. The $\cos\theta$ ranges are indicated under each spectrum. The current of SM12 magnet was 2800 Ampere.

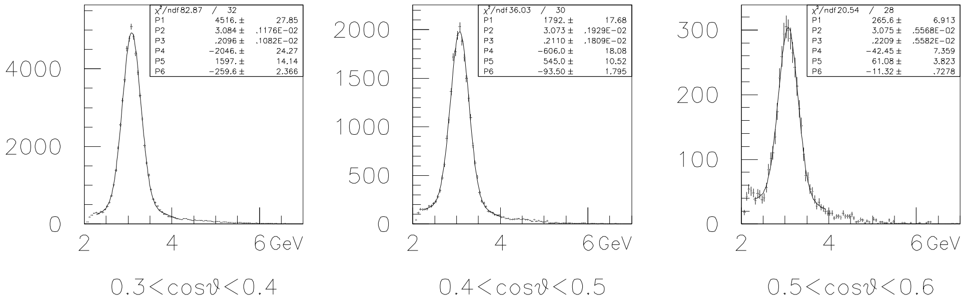

$0.3<\cos\vartheta<0.4$ $0.4<\cos\vartheta<0.5$ $0.5<\cos\vartheta<0.6$

Figure B.44: Fitting of the mass spectrum: $0 < p_t < 1$ and $0.25 < x_F < 0.35$. The backgrounds were fitted to second-order polynomials, and the J/ψ's were fitted to Gaussians. The $\cos\theta$ ranges are indicated under each spectrum. The current of SM12 magnet was 2800 Ampere.

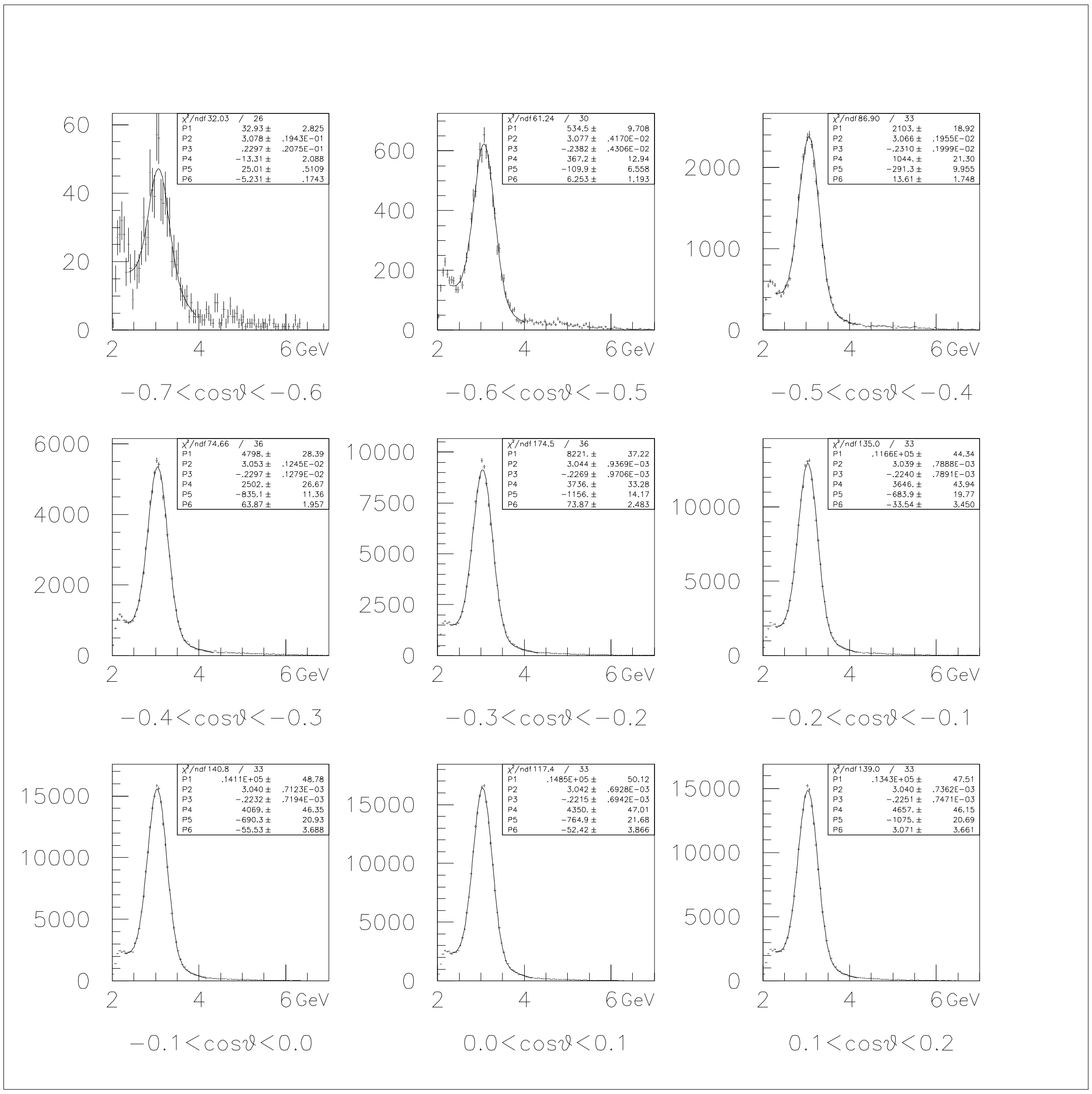

Figure B.45: Fitting of the mass spectrum: $0 < p_t < 1$ and $0.35 < x_F < 0.45$. The backgrounds were fitted to second-order polynomials, and the J/ψ's were fitted to Gaussians. The $\cos\theta$ ranges are indicated under each spectrum. The current of SM12 magnet was 2800 Ampere.

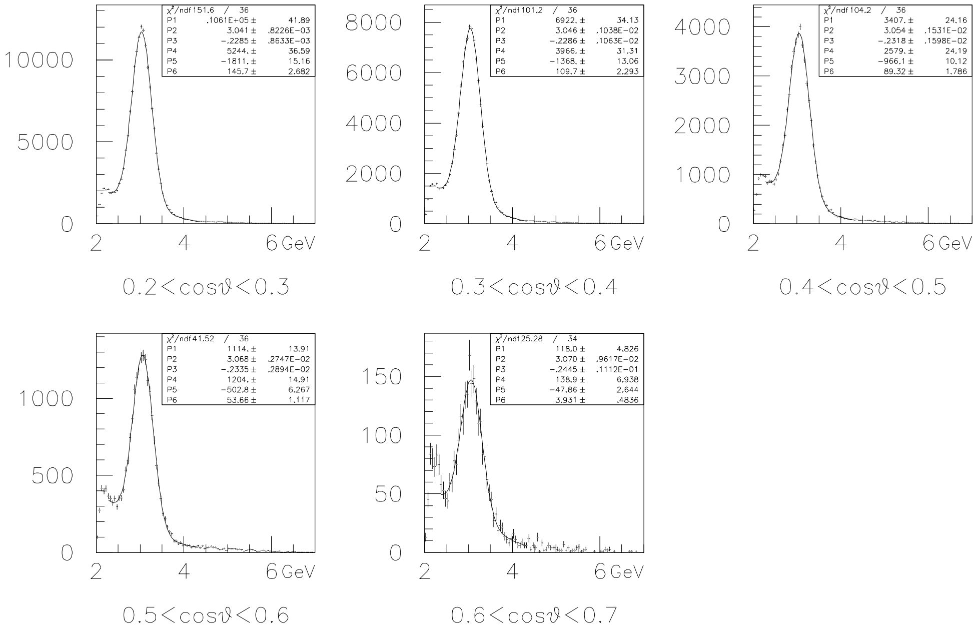

Figure B.46: Fitting of the mass spectrum: $0 < p_t < 1$ and $0.35 < x_F < 0.45$. The backgrounds were fitted to second-order polynomials, and the J/ψ's were fitted to Gaussians. The $\cos\theta$ ranges are indicated under each spectrum. The current of SM12 magnet was 2800 Ampere.

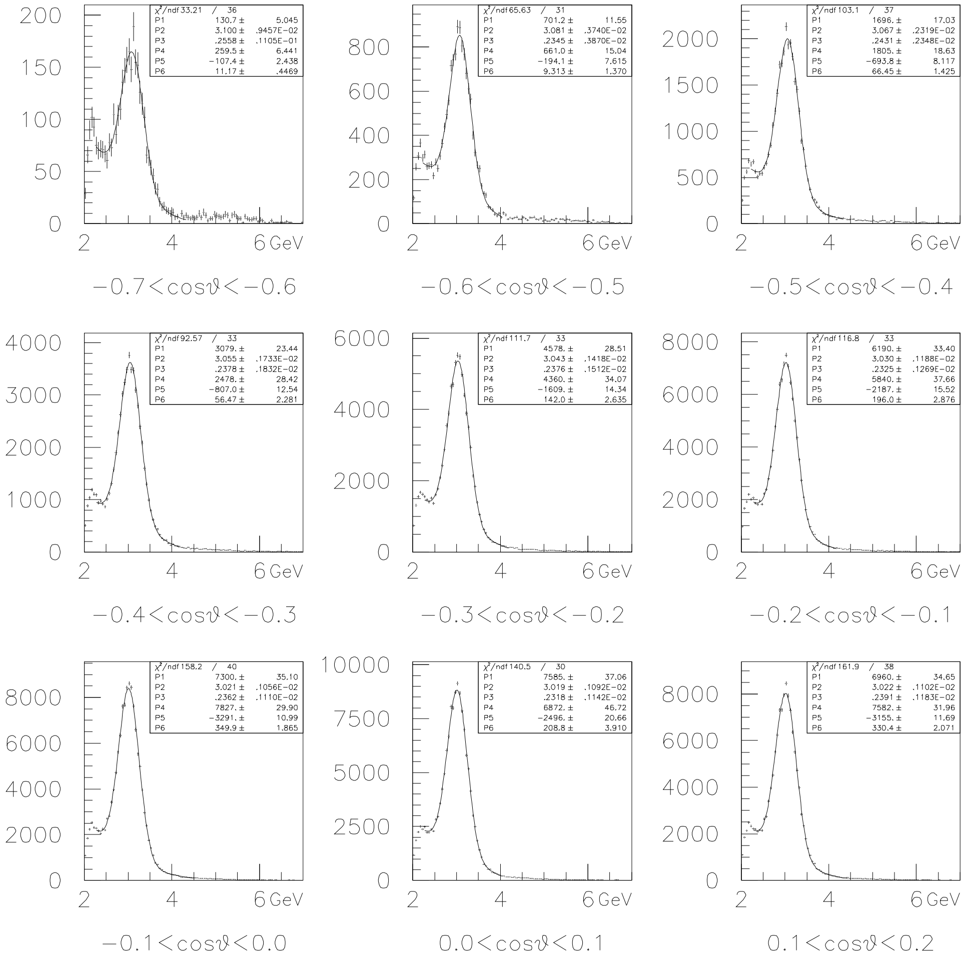

Figure B.47: Fitting of the mass spectrum: $0 < p_t < 1$ and $0.45 < x_F < 0.55$. The backgrounds were fitted to second-order polynomials, and the J/ψ's were fitted to Gaussians. The $\cos\theta$ ranges are indicated under each spectrum. The current of SM12 magnet was 2800 Ampere.

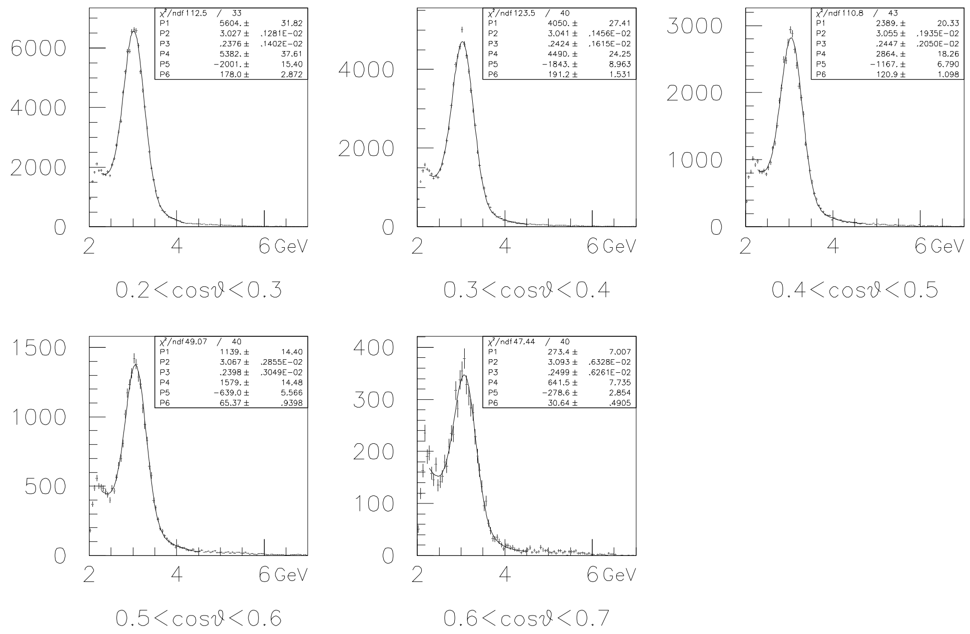

0.2<cosϑ<0.3

0.3<cosϑ<0.4

0.4<cosϑ<0.5

0.5<cosϑ<0.6

0.6<cosϑ<0.7

Figure B.48: Fitting of the mass spectrum: $0 < p_t < 1$ and $0.45 < x_F < 0.55$. The backgrounds were fitted to second-order polynomials, and the J/ψ's were fitted to Gaussians. The $\cos\theta$ ranges are indicated under each spectrum. The current of SM12 magnet was 2800 Ampere.

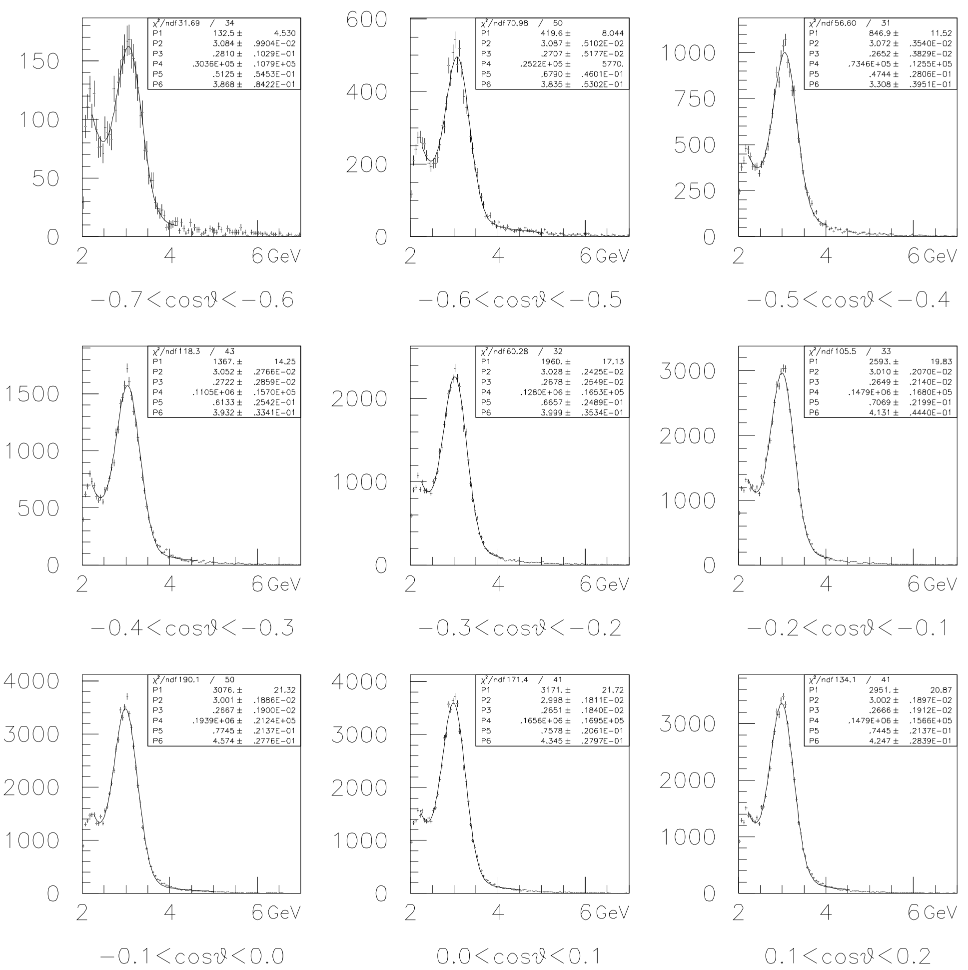

Figure B.49: Fitting of the mass spectrum: $0 < p_t < 1$ and $0.55 < x_F < 0.65$. The backgrounds were fitted to Kaplan functions, and the J/ψ's were fitted to Gaussians. The $\cos\theta$ ranges are indicated under each spectrum. The current of SM12 magnet was 2800 Ampere.

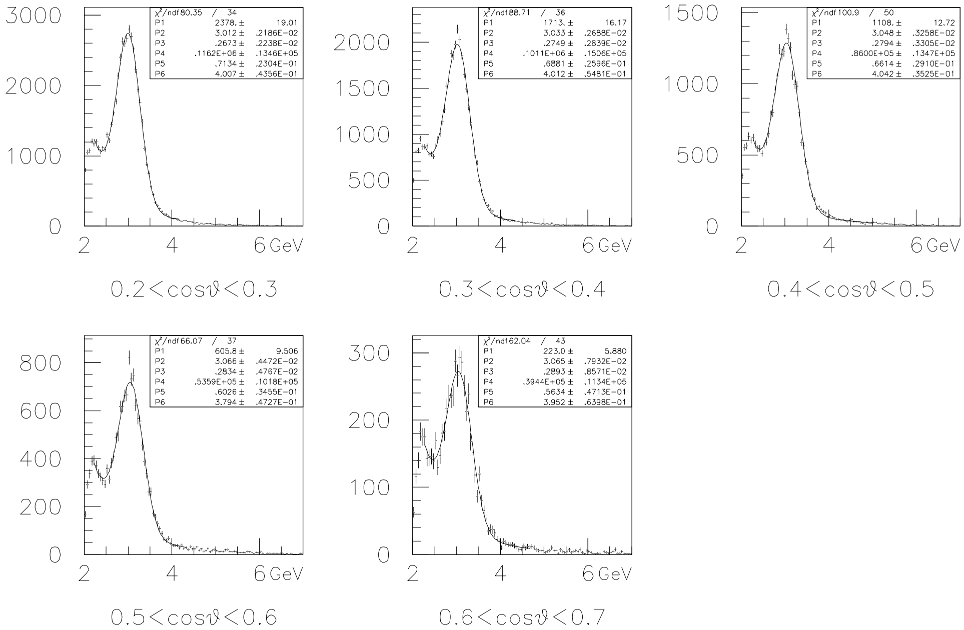

Figure B.50: Fitting of the mass spectrum: $0 < p_t < 1$ and $0.55 < x_F < 0.65$. The backgrounds were fitted to Kaplan functions, and the J/ψ's were fitted to Gaussians. The $\cos\theta$ ranges are indicated under each spectrum. The current of SM12 magnet was 2800 Ampere.

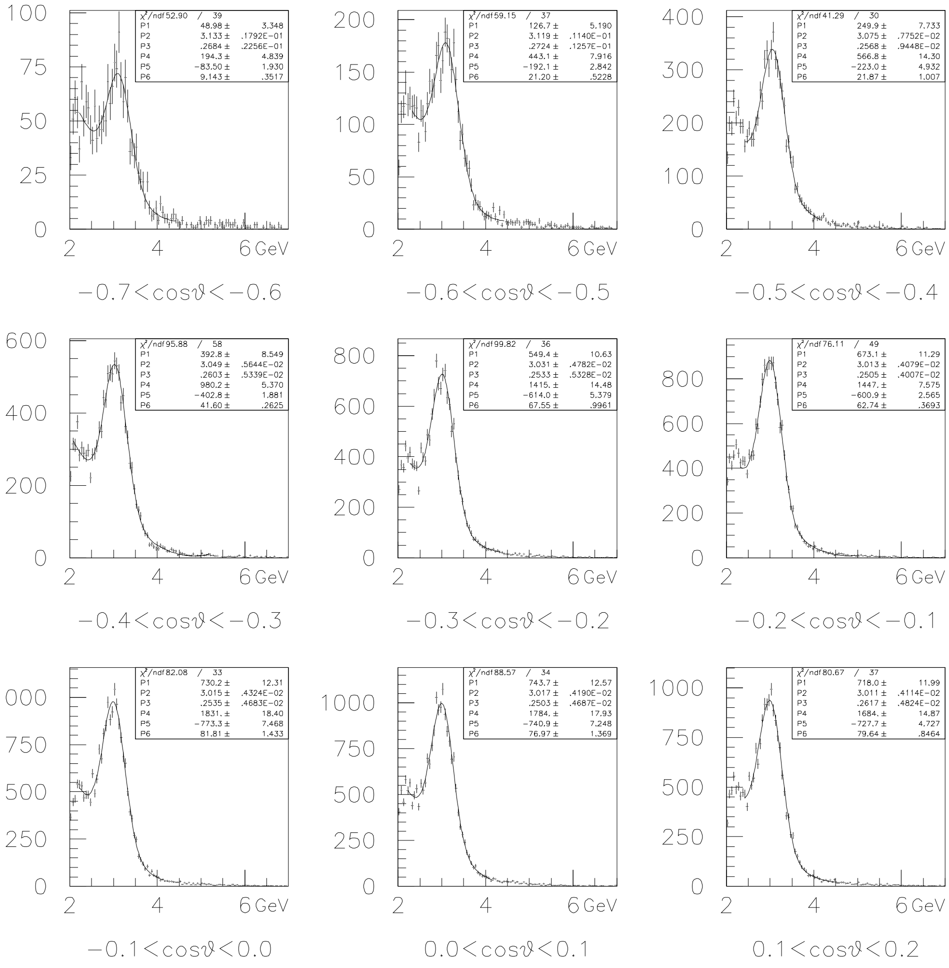

$-0.7 < \cos\vartheta < -0.6$ $-0.6 < \cos\vartheta < -0.5$ $-0.5 < \cos\vartheta < -0.4$

$-0.4 < \cos\vartheta < -0.3$ $-0.3 < \cos\vartheta < -0.2$ $-0.2 < \cos\vartheta < -0.1$

$-0.1 < \cos\vartheta < 0.0$ $0.0 < \cos\vartheta < 0.1$ $0.1 < \cos\vartheta < 0.2$

Figure B.51: Fitting of the mass spectrum: $0 < p_t < 1$ and $0.65 < x_F < 0.75$. The backgrounds were fitted to second-order polynomials, and the J/ψ's were fitted to Gaussians. The $\cos\theta$ ranges are indicated under each spectrum. The current of SM12 magnet was 2800 Ampere.

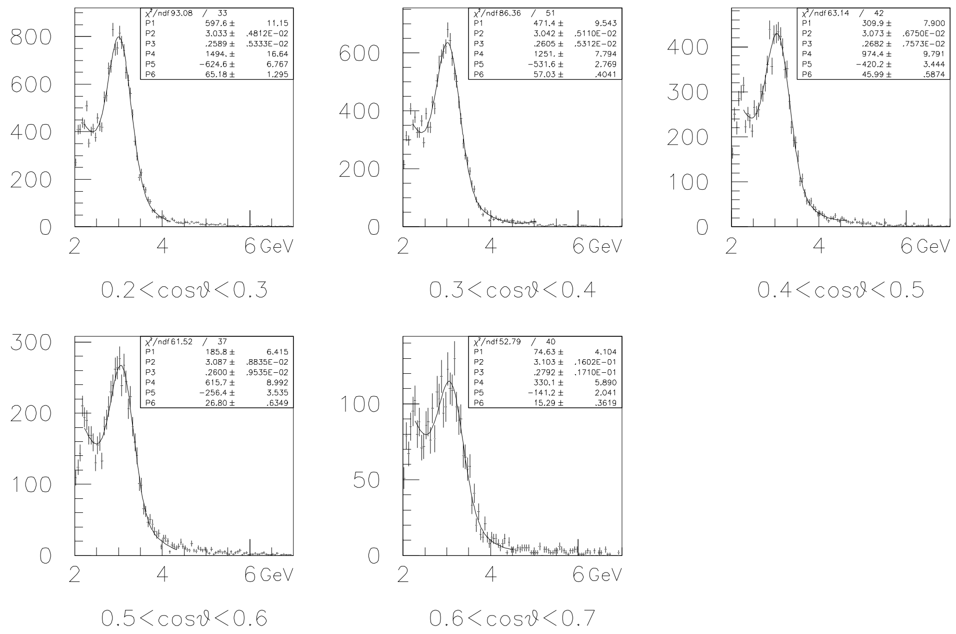

$0.2 < \cos\vartheta < 0.3$

$0.3 < \cos\vartheta < 0.4$

$0.4 < \cos\vartheta < 0.5$

$0.5 < \cos\vartheta < 0.6$

$0.6 < \cos\vartheta < 0.7$

Figure B.52: Fitting of the mass spectrum: $0 < p_t < 1$ and $0.65 < x_F < 0.75$. The backgrounds were fitted to second-order polynomials, and the J/ψ's were fitted to Gaussians. The $\cos\theta$ ranges are indicated under each spectrum. The current of SM12 magnet was 2800 Ampere.

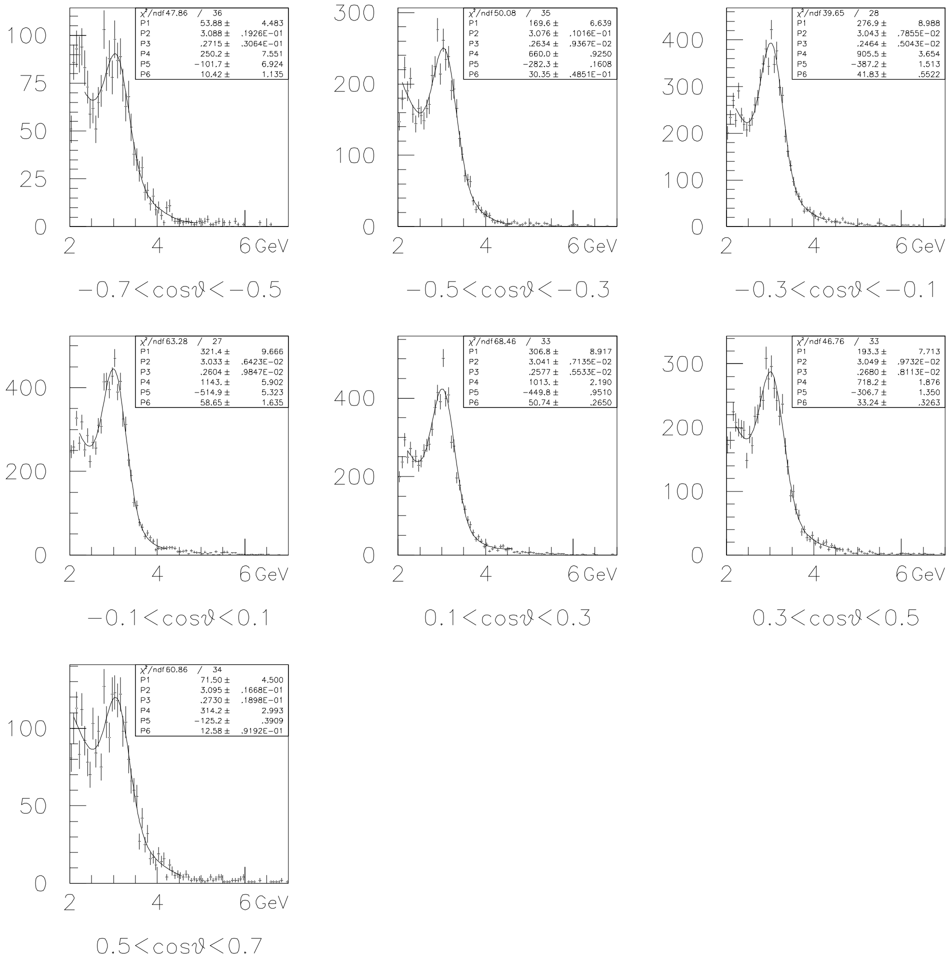

$-0.7 < \cos\vartheta < -0.5$

$-0.5 < \cos\vartheta < -0.3$

$-0.3 < \cos\vartheta < -0.1$

$-0.1 < \cos\vartheta < 0.1$

$0.1 < \cos\vartheta < 0.3$

$0.3 < \cos\vartheta < 0.5$

$0.5 < \cos\vartheta < 0.7$

Figure B.53: Fitting of the mass spectrum: $0 < p_t < 1$ and $0.75 < x_F < 0.85$. The backgrounds were fitted to second-order polynomials, and the J/ψ's were fitted to Gaussians. The $\cos\theta$ ranges are indicated under each spectrum. The current of SM12 magnet was 2800 Ampere.

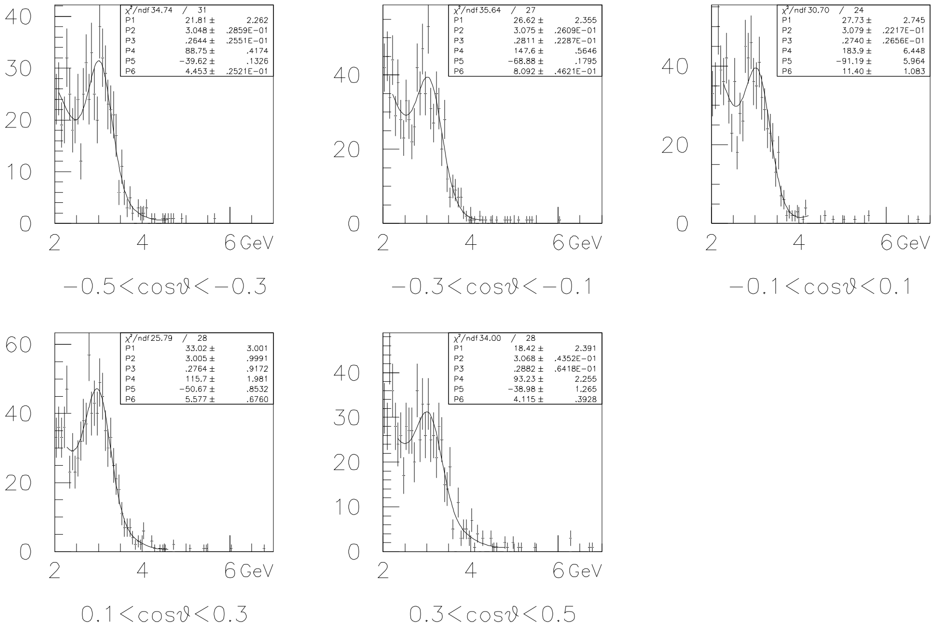

Figure B.54: Fitting of the mass spectrum: $0 < p_t < 1$ and $0.85 < x_F$. The backgrounds were fitted to second-order polynomials, and the J/ψ's were fitted to Gaussians. The $\cos\theta$ ranges are indicated under each spectrum. The current of SM12 magnet was 2800 Ampere.

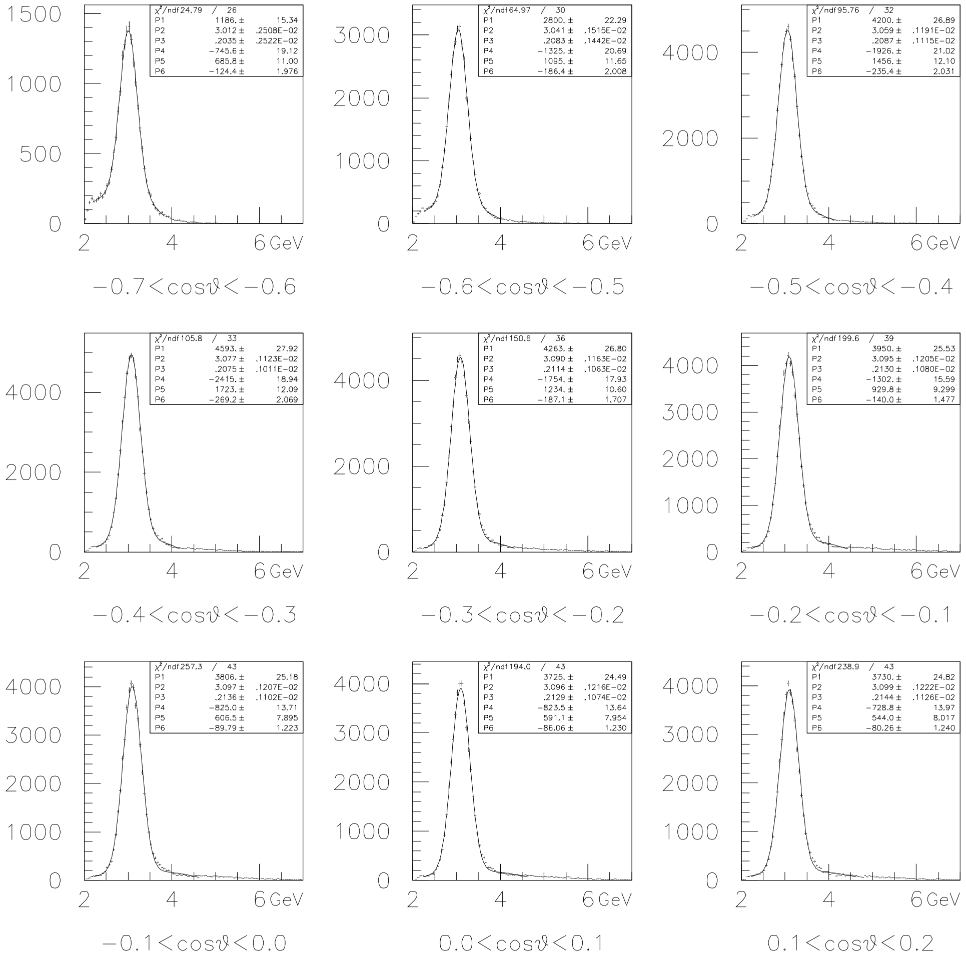

$-0.7 < \cos\vartheta < -0.6$ $-0.6 < \cos\vartheta < -0.5$ $-0.5 < \cos\vartheta < -0.4$

$-0.4 < \cos\vartheta < -0.3$ $-0.3 < \cos\vartheta < -0.2$ $-0.2 < \cos\vartheta < -0.1$

$-0.1 < \cos\vartheta < 0.0$ $0.0 < \cos\vartheta < 0.1$ $0.1 < \cos\vartheta < 0.2$

Figure B.55: Fitting of the mass spectrum: $1 < p_t < 2$ and $0.25 < x_F < 0.35$. The backgrounds were fitted to second-order polynomials, and the J/ψ's were fitted to Gaussians. The $\cos\theta$ ranges are indicated under each spectrum. The current of SM12 magnet was 2800 Ampere.

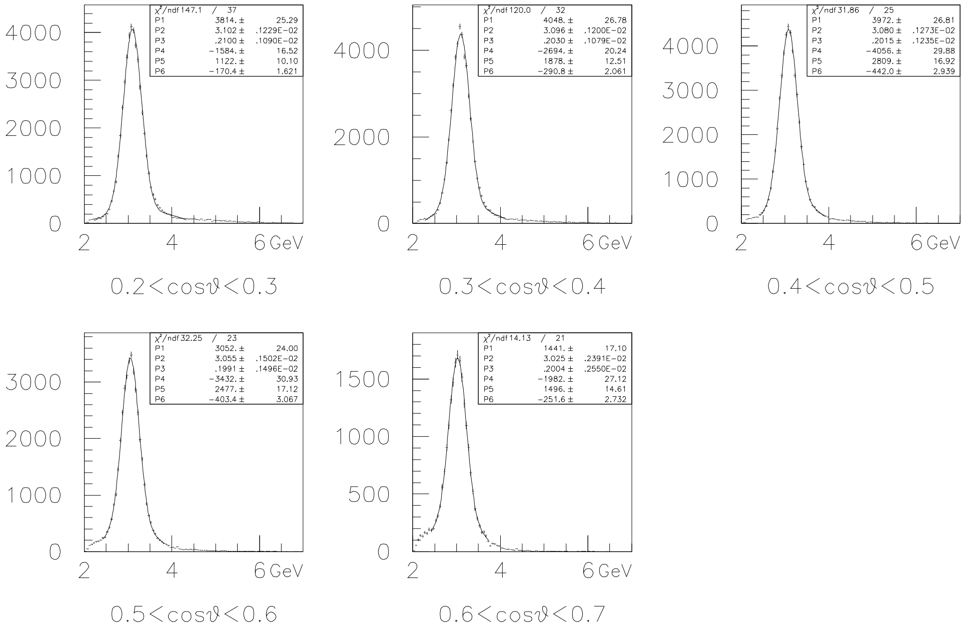

$0.2 < \cos\vartheta < 0.3$ $0.3 < \cos\vartheta < 0.4$ $0.4 < \cos\vartheta < 0.5$

$0.5 < \cos\vartheta < 0.6$ $0.6 < \cos\vartheta < 0.7$

Figure B.56: Fitting of the mass spectrum: $1 < p_t < 2$ and $0.25 < x_F < 0.35$. The backgrounds were fitted to second-order polynomials, and the J/ψ's were fitted to Gaussians. The $\cos\theta$ ranges are indicated under each spectrum. The current of SM12 magnet was 2800 Ampere.

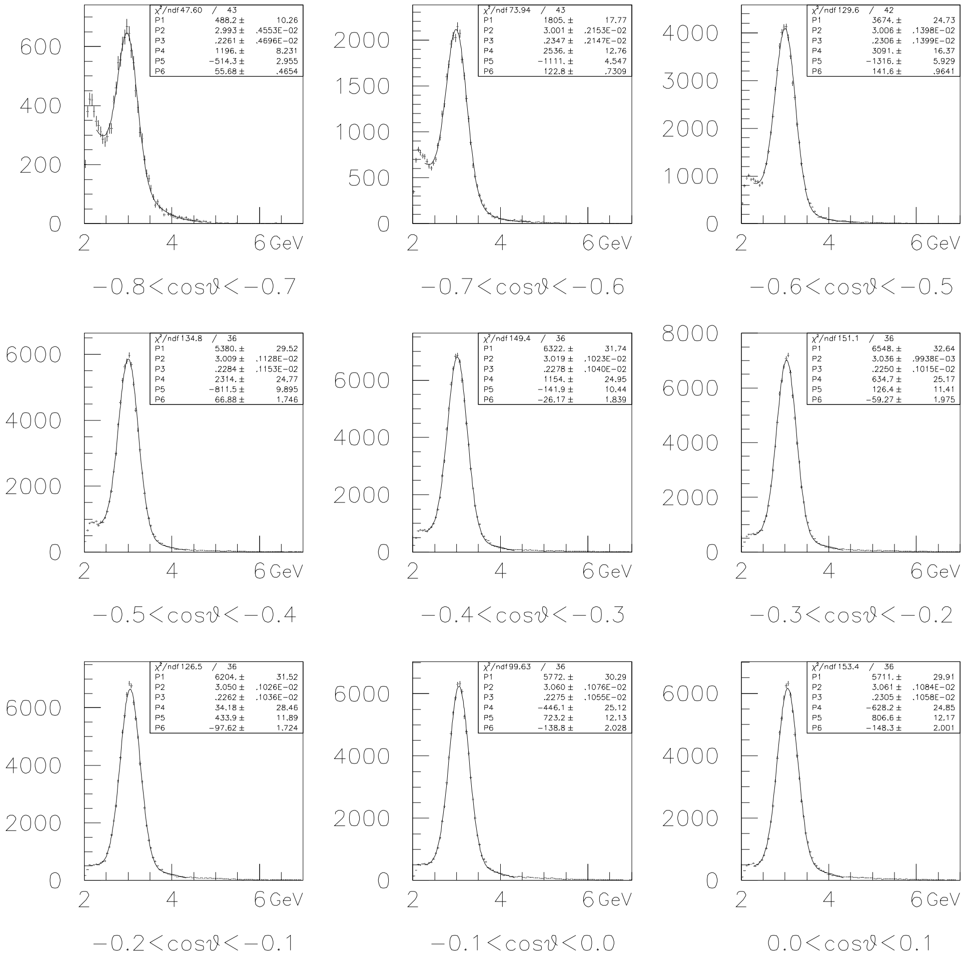

$-0.8<\cos\vartheta<-0.7$ $-0.7<\cos\vartheta<-0.6$ $-0.6<\cos\vartheta<-0.5$

$-0.5<\cos\vartheta<-0.4$ $-0.4<\cos\vartheta<-0.3$ $-0.3<\cos\vartheta<-0.2$

$-0.2<\cos\vartheta<-0.1$ $-0.1<\cos\vartheta<0.0$ $0.0<\cos\vartheta<0.1$

Figure B.57: Fitting of the mass spectrum: $1 < p_t < 2$ and $0.35 < x_F < 0.45$. The backgrounds were fitted to second-order polynomials, and the J/ψ's were fitted to Gaussians. The $\cos\theta$ ranges are indicated under each spectrum. The current of SM12 magnet was 2800 Ampere.

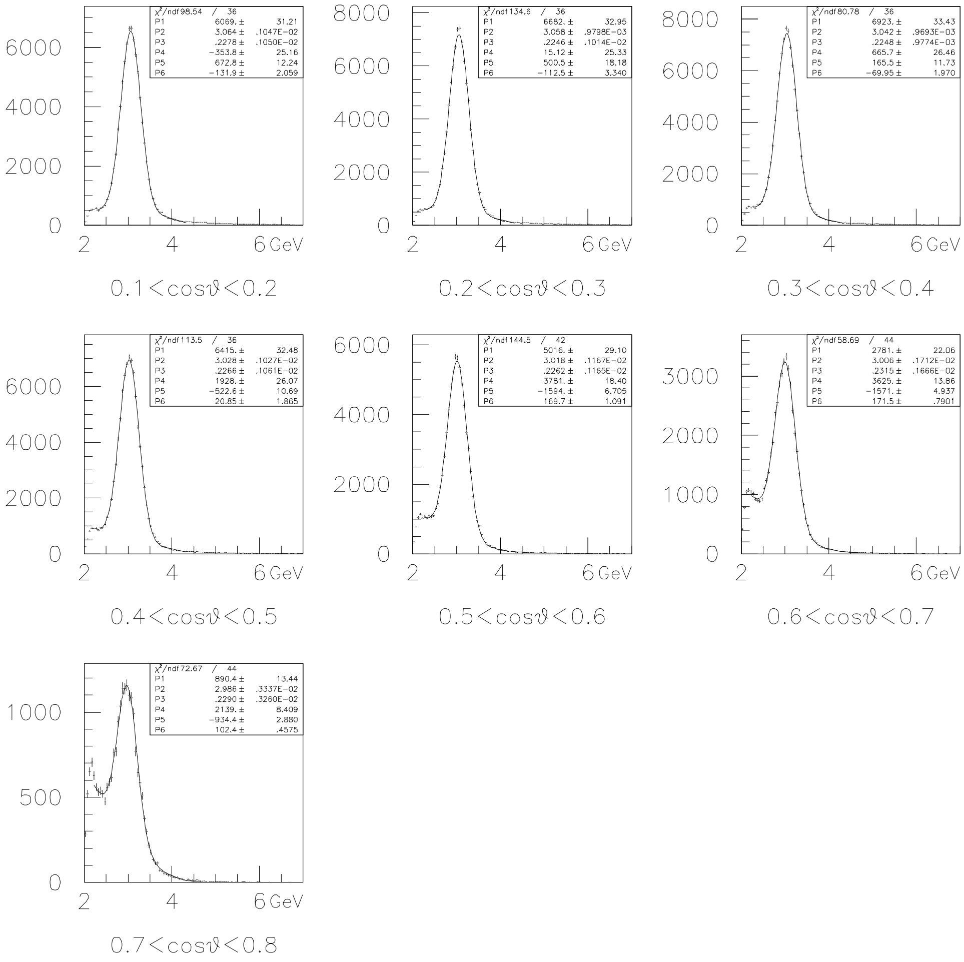

$0.1<\cos\vartheta<0.2$

$0.2<\cos\vartheta<0.3$

$0.3<\cos\vartheta<0.4$

$0.4<\cos\vartheta<0.5$

$0.5<\cos\vartheta<0.6$

$0.6<\cos\vartheta<0.7$

$0.7<\cos\vartheta<0.8$

Figure B.58: Fitting of the mass spectrum: $1 < p_t < 2$ and $0.35 < x_F < 0.45$. The backgrounds were fitted to second-order polynomials, and the J/ψ's were fitted to Gaussians. The $\cos\theta$ ranges are indicated under each spectrum. The current of SM12 magnet was 2800 Ampere.

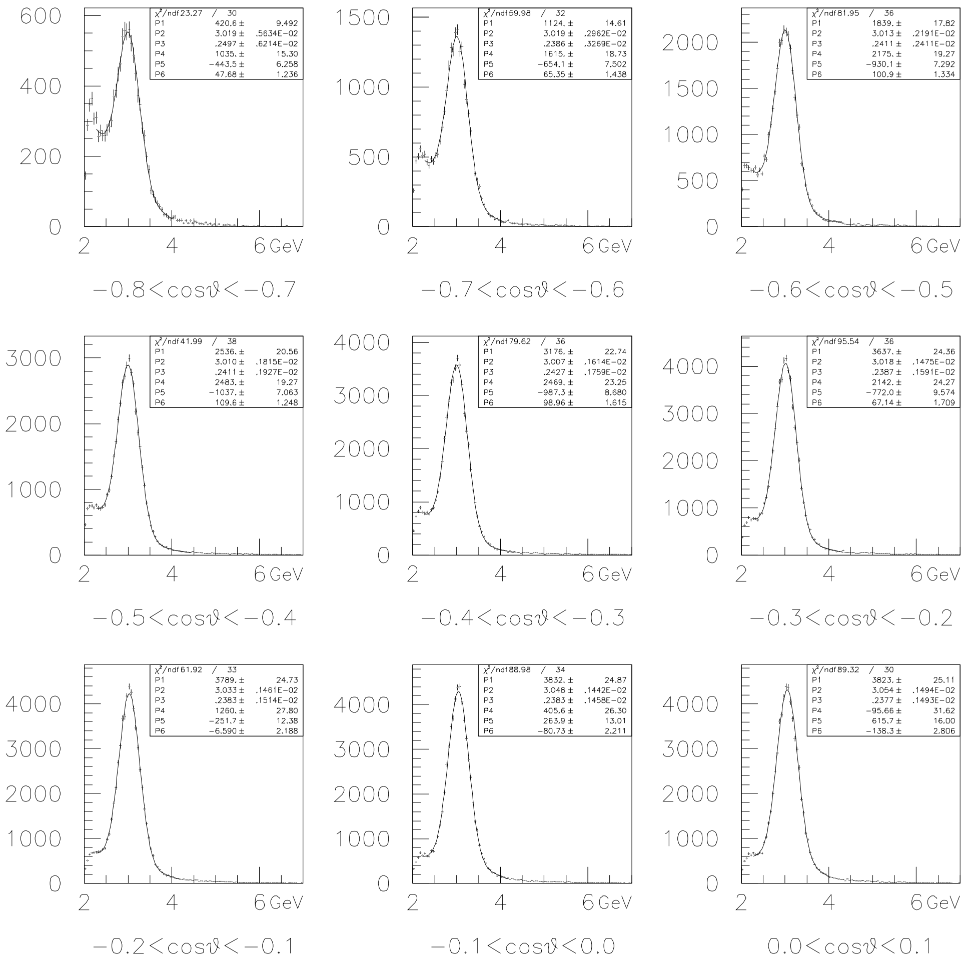

Figure B.59: Fitting of the mass spectrum: $1 < p_t < 2$ and $0.45 < x_F < 0.55$. The backgrounds were fitted to second-order polynomials, and the J/ψ's were fitted to Gaussians. The $\cos\theta$ ranges are indicated under each spectrum. The current of SM12 magnet was 2800 Ampere.

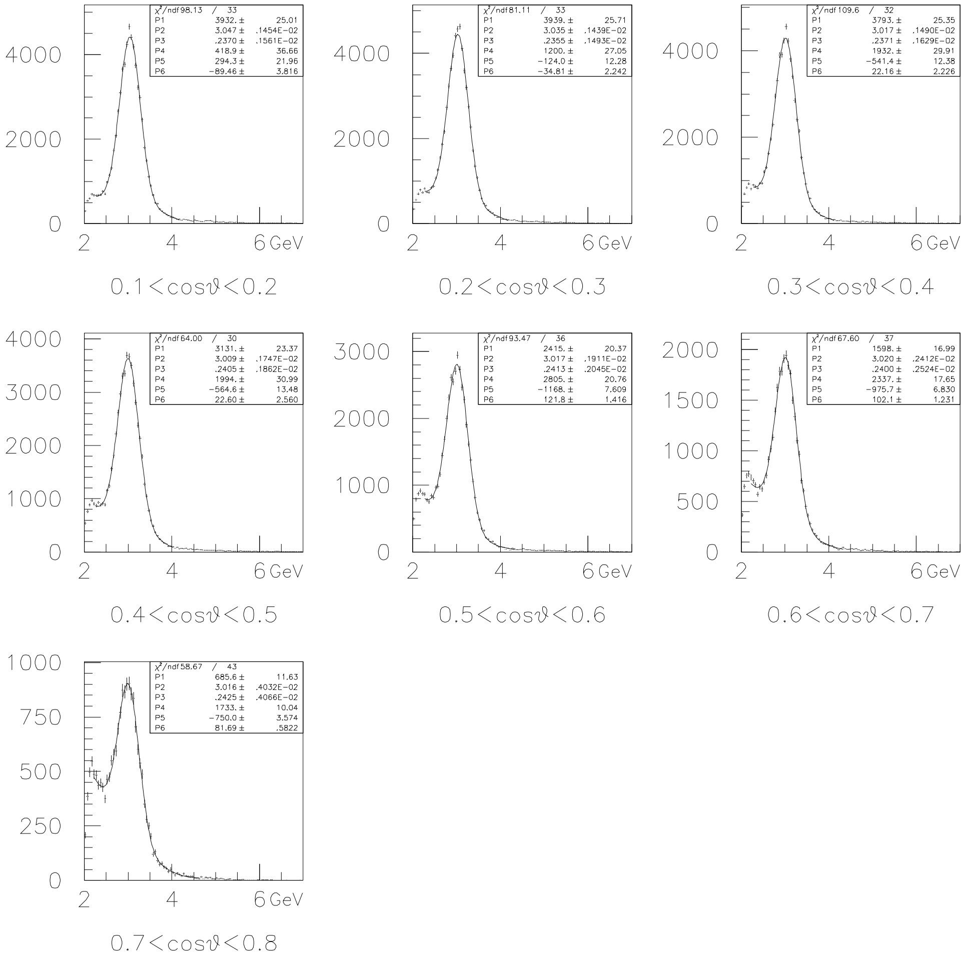

Figure B.60: Fitting of the mass spectrum: $1 < p_t < 2$ and $0.45 < x_F < 0.55$. The backgrounds were fitted to second-order polynomials, and the J/ψ's were fitted to Gaussians. The $\cos\theta$ ranges are indicated under each spectrum. The current of SM12 magnet was 2800 Ampere.

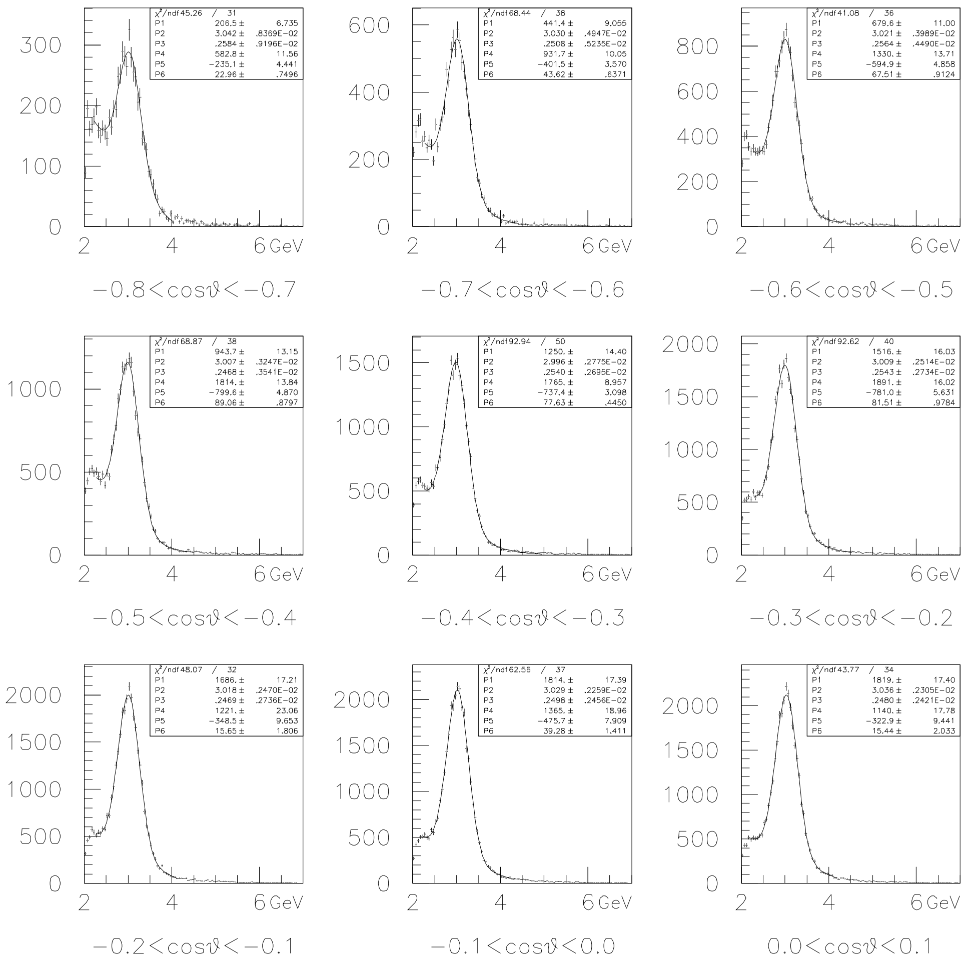

Figure B.61: Fitting of the mass spectrum: $1 < p_t < 2$ and $0.55 < x_F < 0.65$. The backgrounds were fitted to second-order polynomials, and the J/ψ's were fitted to Gaussians. The $\cos\theta$ ranges are indicated under each spectrum. The current of SM12 magnet was 2800 Ampere.

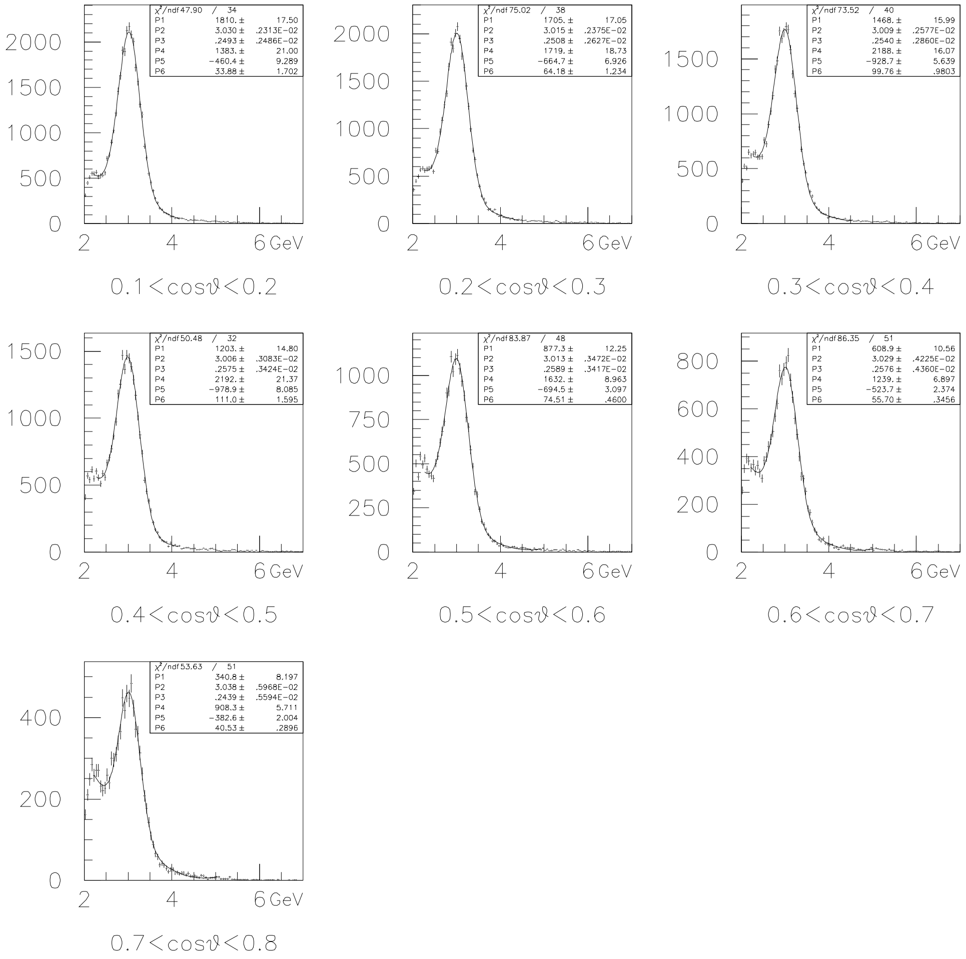

Figure B.62: Fitting of the mass spectrum: $1 < p_t < 2$ and $0.55 < x_F < 0.65$. The backgrounds were fitted to second-order polynomials, and the J/ψ's were fitted to Gaussians. The $\cos\theta$ ranges are indicated under each spectrum. The current of SM12 magnet was 2800 Ampere.

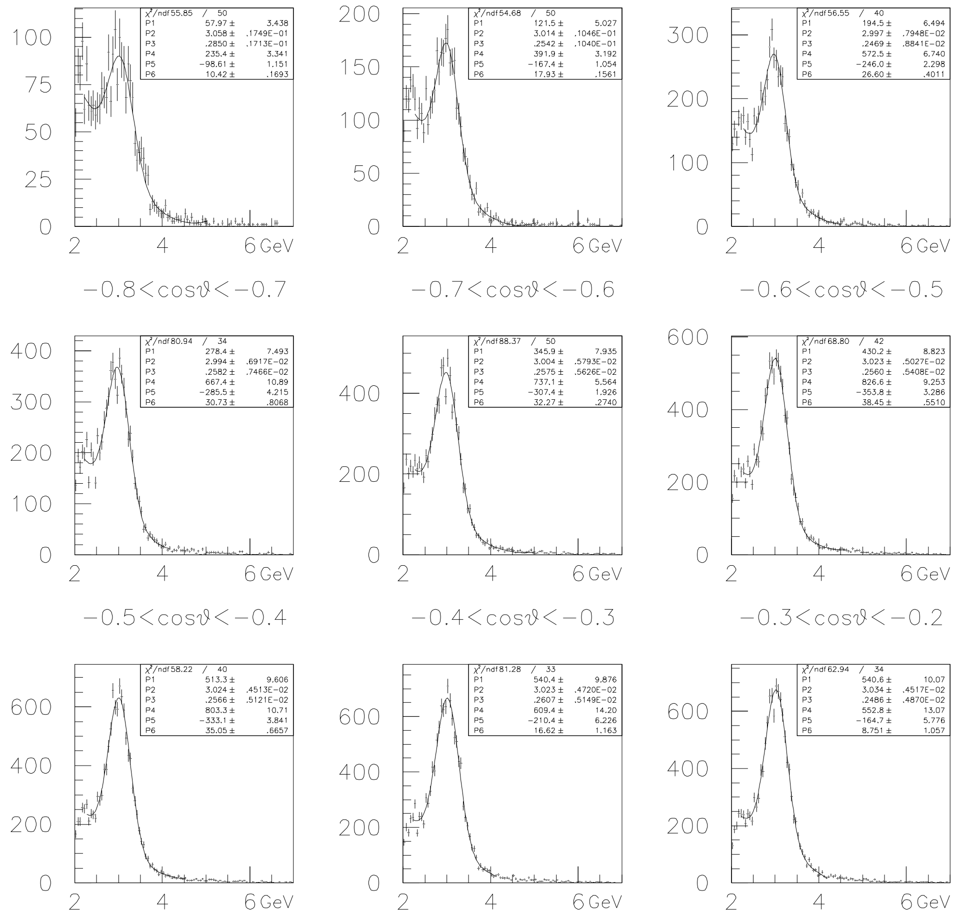

Figure B.63: Fitting of the mass spectrum: $1 < p_t < 2$ and $0.65 < x_F < 0.75$. The backgrounds were fitted to second-order polynomials, and the J/ψ's were fitted to Gaussians. The $\cos\theta$ ranges are indicated under each spectrum. The current of SM12 magnet was 2800 Ampere.

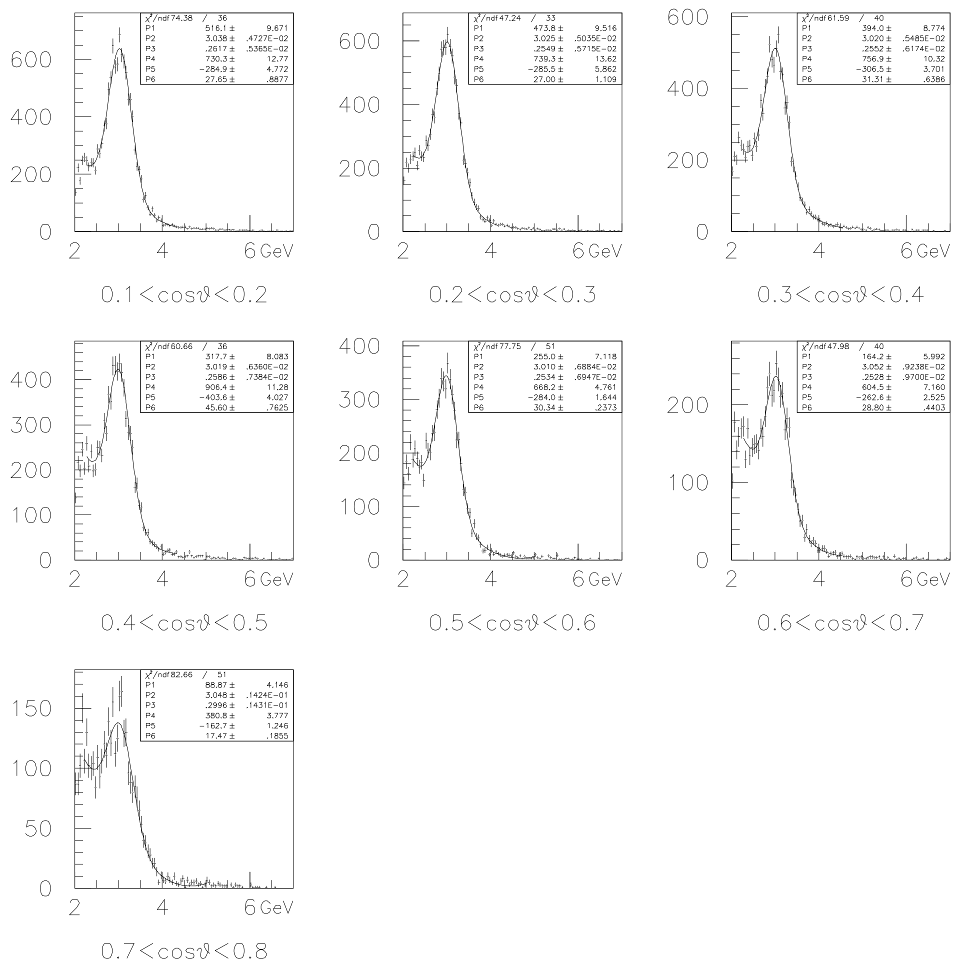

Figure B.64: Fitting of the mass spectrum: $1 < p_t < 2$ and $0.65 < x_F < 0.75$. The backgrounds were fitted to second-order polynomials, and the J/ψ's were fitted to Gaussians. The $\cos\theta$ ranges are indicated under each spectrum. The current of SM12 magnet was 2800 Ampere.

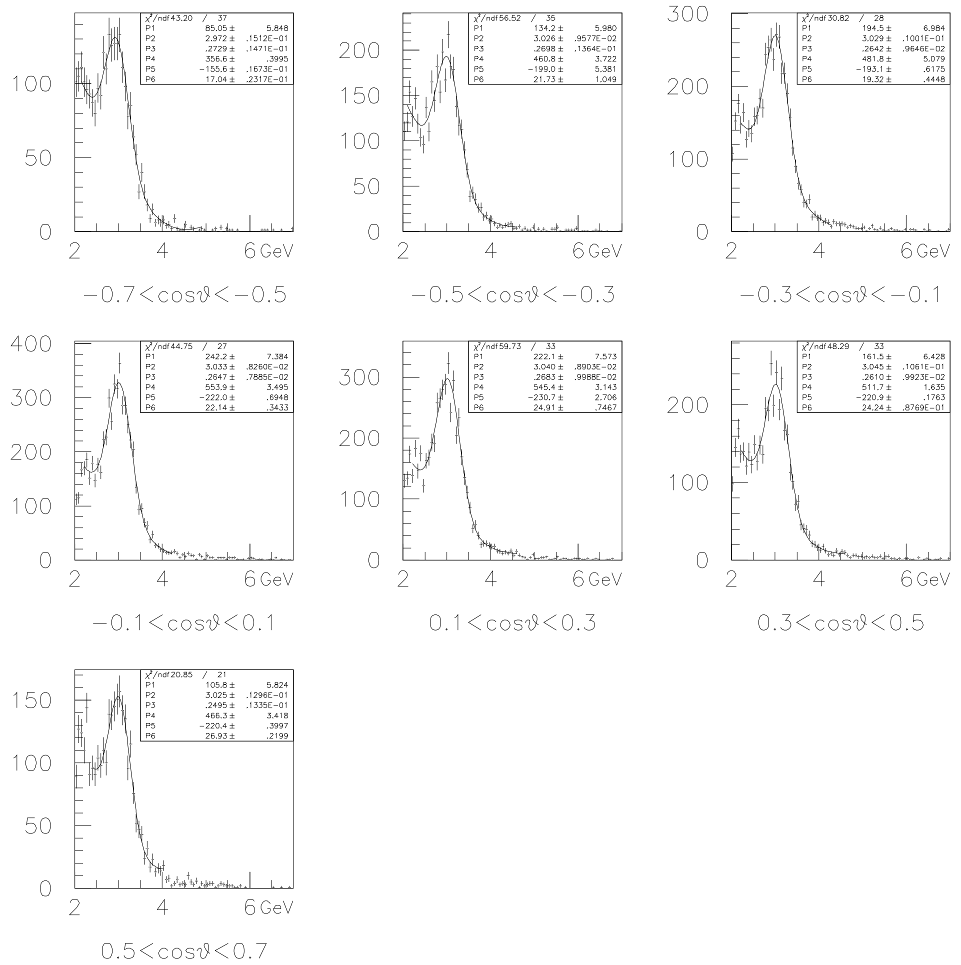

Figure B.65: Fitting of the mass spectrum: $1 < p_t < 2$ and $0.75 < x_F < 0.85$. The backgrounds were fitted to second-order polynomials, and the J/ψ's were fitted to Gaussians. The $\cos\theta$ ranges are indicated under each spectrum. The current of SM12 magnet was 2800 Ampere.

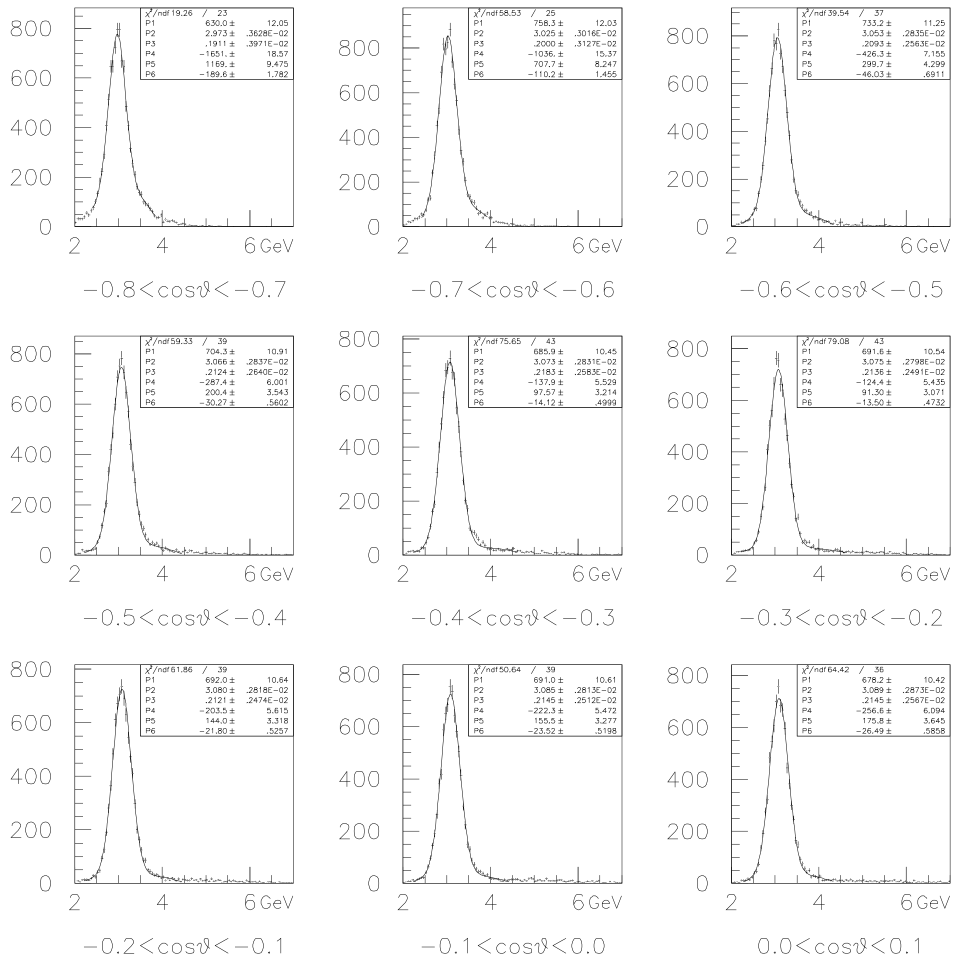

$-0.8<\cos\vartheta<-0.7$ $-0.7<\cos\vartheta<-0.6$ $-0.6<\cos\vartheta<-0.5$

$-0.5<\cos\vartheta<-0.4$ $-0.4<\cos\vartheta<-0.3$ $-0.3<\cos\vartheta<-0.2$

$-0.2<\cos\vartheta<-0.1$ $-0.1<\cos\vartheta<0.0$ $0.0<\cos\vartheta<0.1$

Figure B.66: Fitting of the mass spectrum: $2 < p_t < 3$ and $0.25 < x_F < 0.35$. The backgrounds were fitted to second-order polynomials, and the J/ψ's were fitted to Gaussians. The $\cos\theta$ ranges are indicated under each spectrum. The current of SM12 magnet was 2800 Ampere.

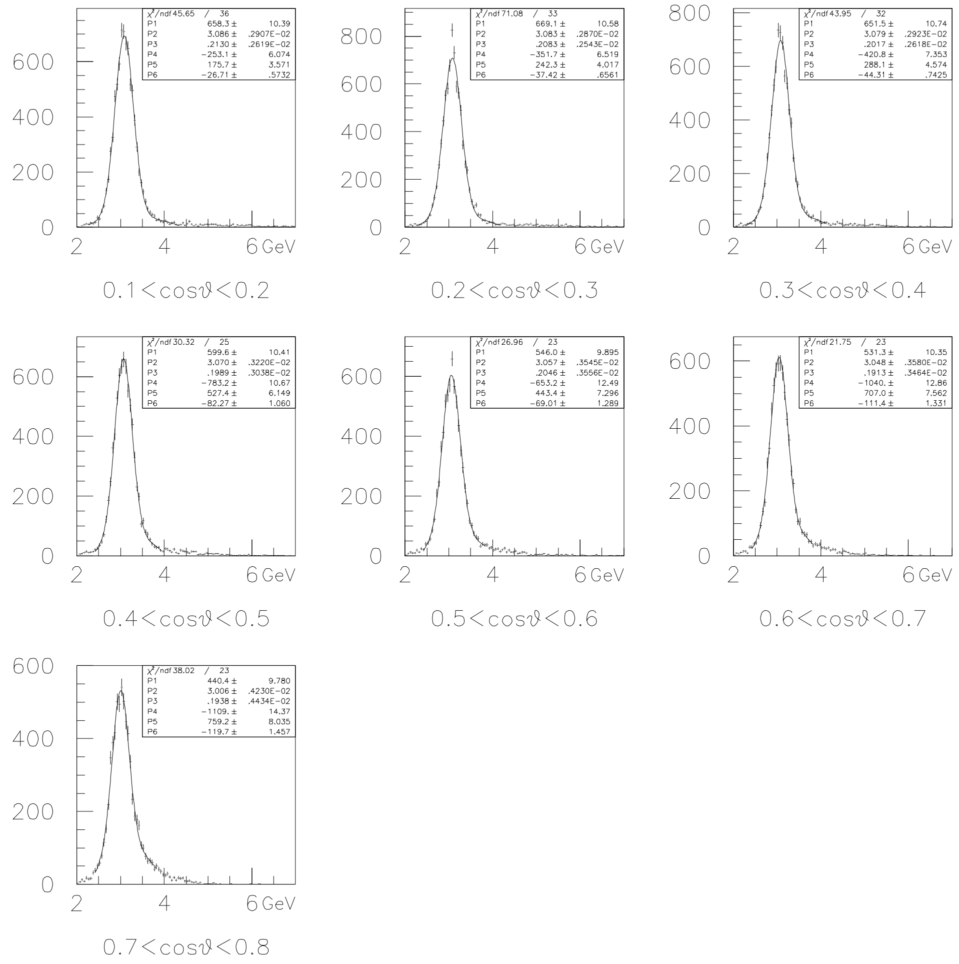

Figure B.67: Fitting of the mass spectrum: $2 < p_t < 3$ and $0.25 < x_F < 0.35$. The backgrounds were fitted to second-order polynomials, and the J/ψ's were fitted to Gaussians. The $\cos\theta$ ranges are indicated under each spectrum. The current of SM12 magnet was 2800 Ampere.

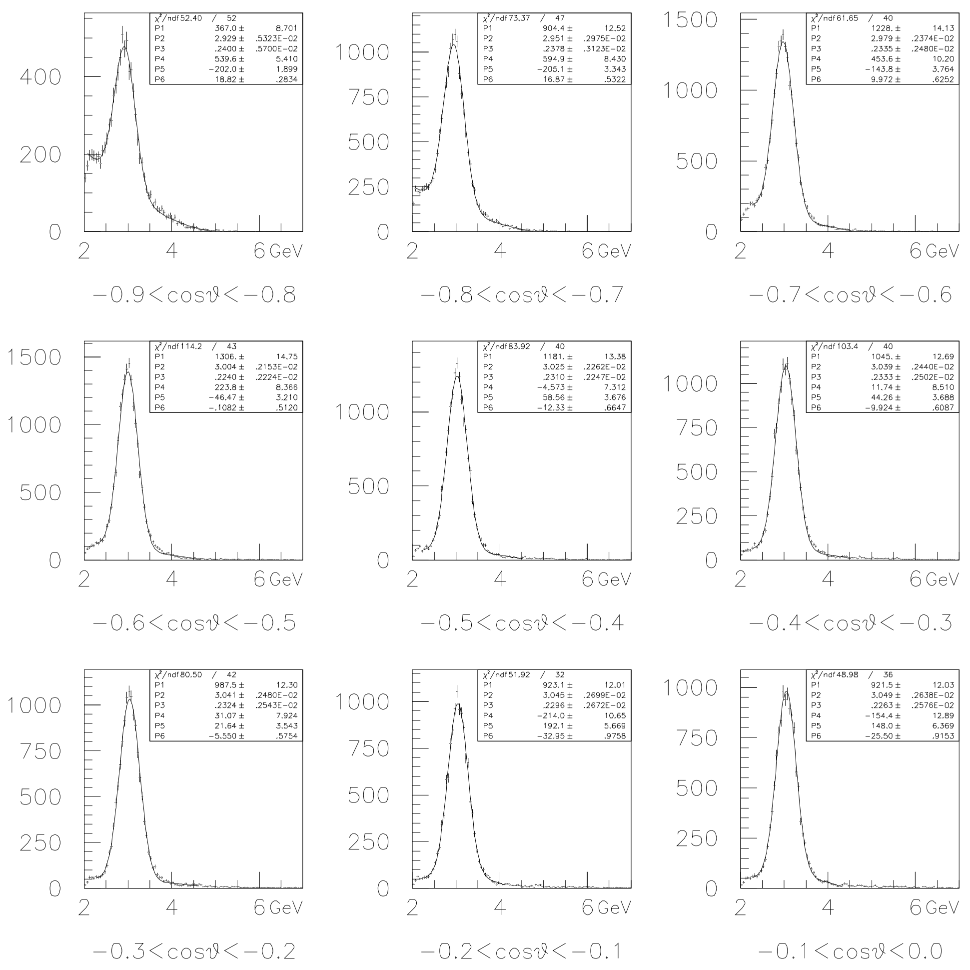

Figure B.68: Fitting of the mass spectrum: $2 < p_t < 3$ and $0.35 < x_F < 0.45$. The backgrounds were fitted to second-order polynomials, and the J/ψ's were fitted to Gaussians. The $\cos\theta$ ranges are indicated under each spectrum. The current of SM12 magnet was 2800 Ampere.

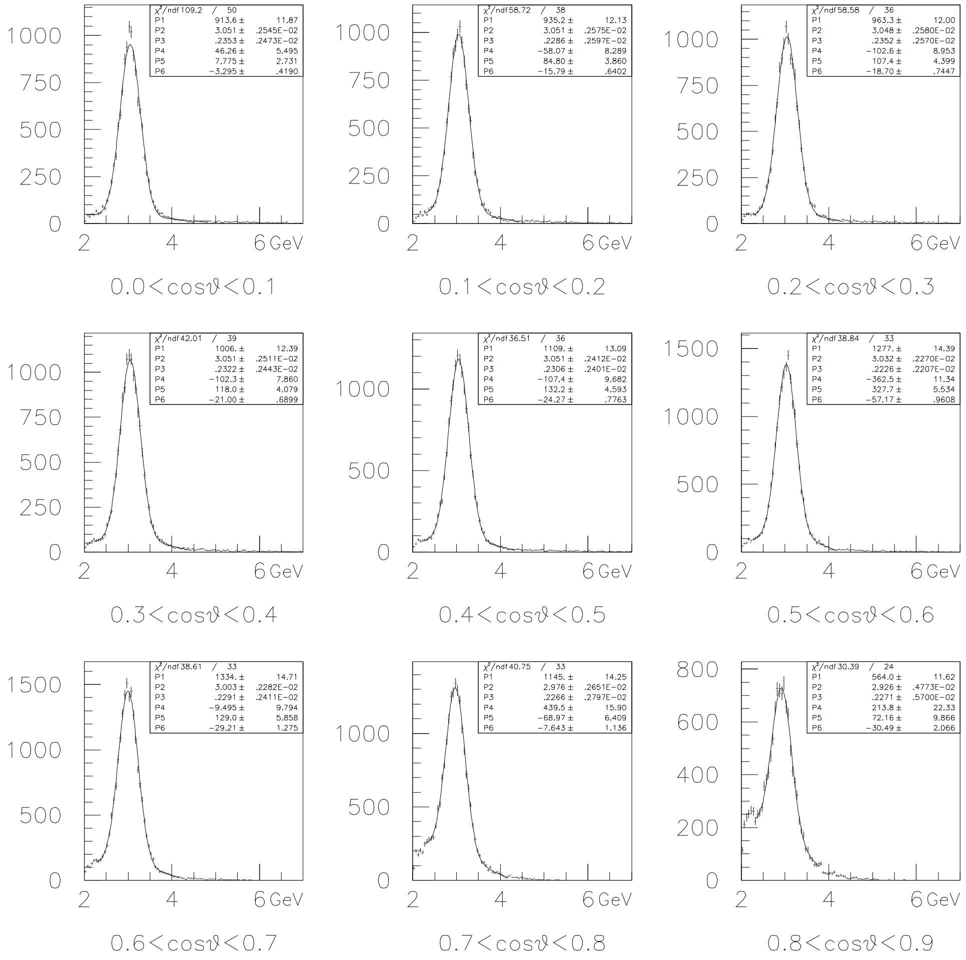

Figure B.69: Fitting of the mass spectrum: $2 < p_t < 3$ and $0.35 < x_F < 0.45$. The backgrounds were fitted to second-order polynomials, and the J/ψ's were fitted to Gaussians. The $\cos\theta$ ranges are indicated under each spectrum. The current of SM12 magnet was 2800 Ampere.

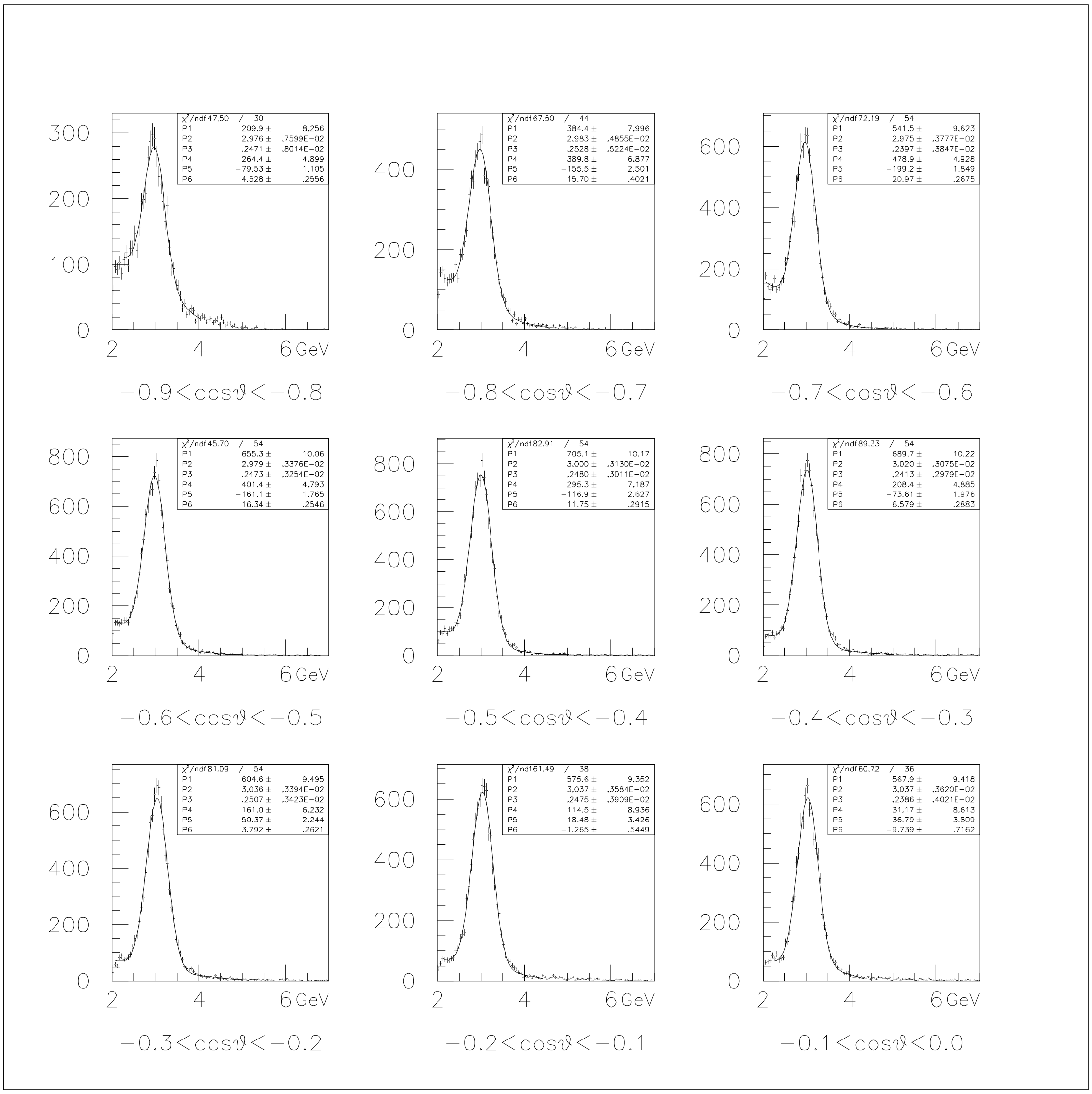

Figure B.70: Fitting of the mass spectrum: $2 < p_t < 3$ and $0.45 < x_F < 0.55$. The backgrounds were fitted to second-order polynomials, and the J/ψ's were fitted to Gaussians. The $\cos\theta$ ranges are indicated under each spectrum. The current of SM12 magnet was 2800 Ampere.

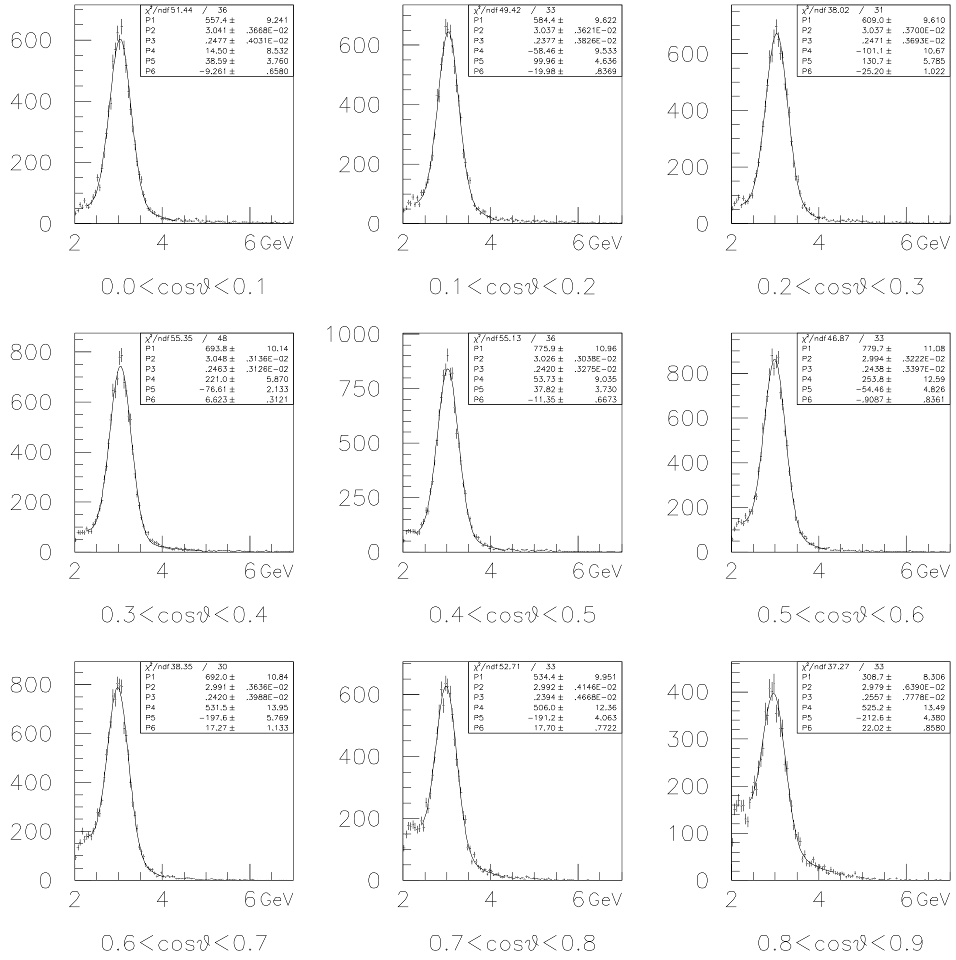

Figure B.71: Fitting of the mass spectrum: $2 < p_t < 3$ and $0.45 < x_F < 0.55$. The backgrounds were fitted to second-order polynomials, and the J/ψ's were fitted to Gaussians. The $\cos\theta$ ranges are indicated under each spectrum. The current of SM12 magnet was 2800 Ampere.

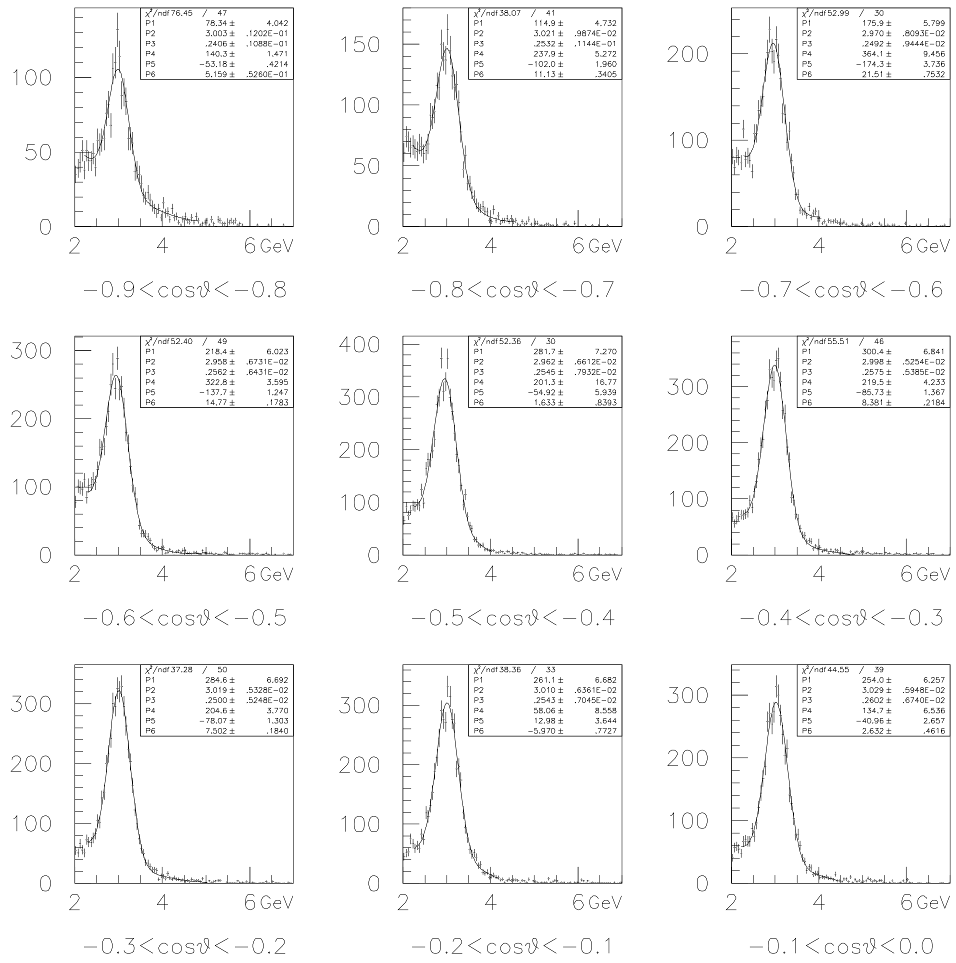

Figure B.72: Fitting of the mass spectrum: $2 < p_t < 3$ and $0.55 < x_F < 0.65$. The backgrounds were fitted to second-order polynomials, and the J/ψ's were fitted to Gaussians. The $\cos\theta$ ranges are indicated under each spectrum. The current of SM12 magnet was 2800 Ampere.

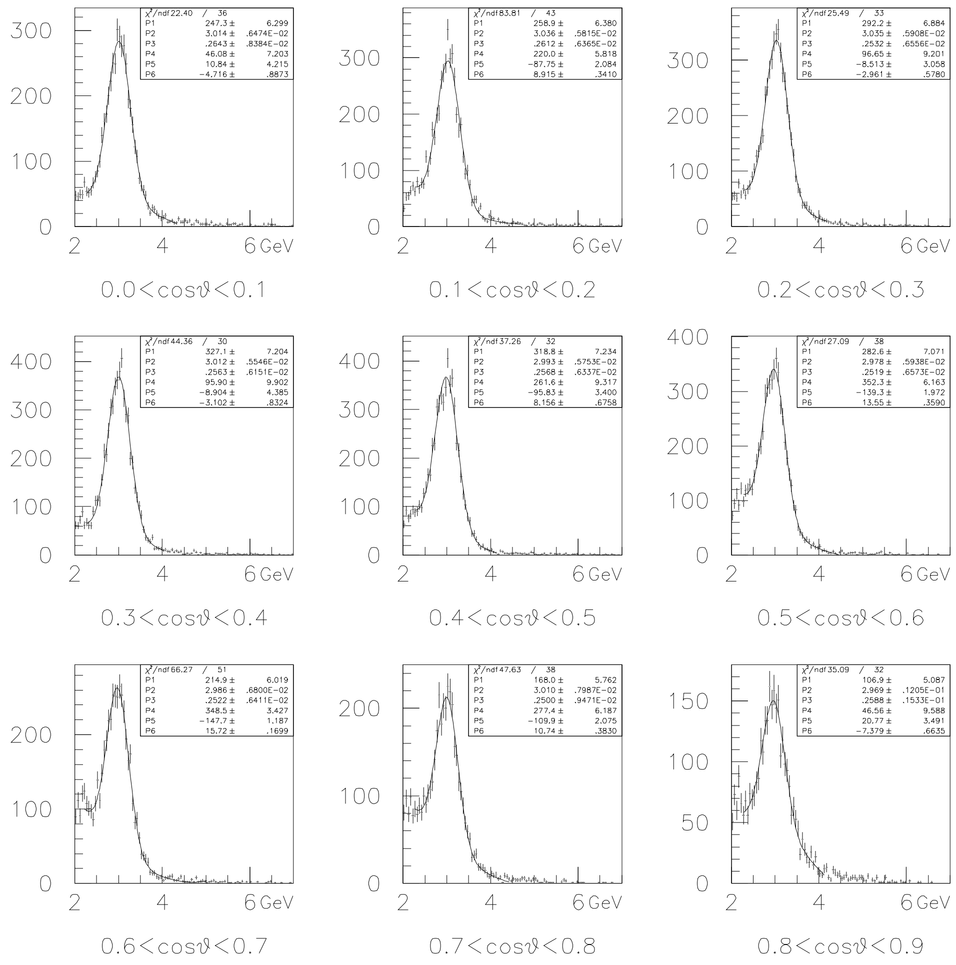

Figure B.73: Fitting of the mass spectrum: $2 < p_t < 3$ and $0.55 < x_F < 0.65$. The backgrounds were fitted to second-order polynomials, and the J/ψ's were fitted to Gaussians. The $\cos\theta$ ranges are indicated under each spectrum. The current of SM12 magnet was 2800 Ampere.

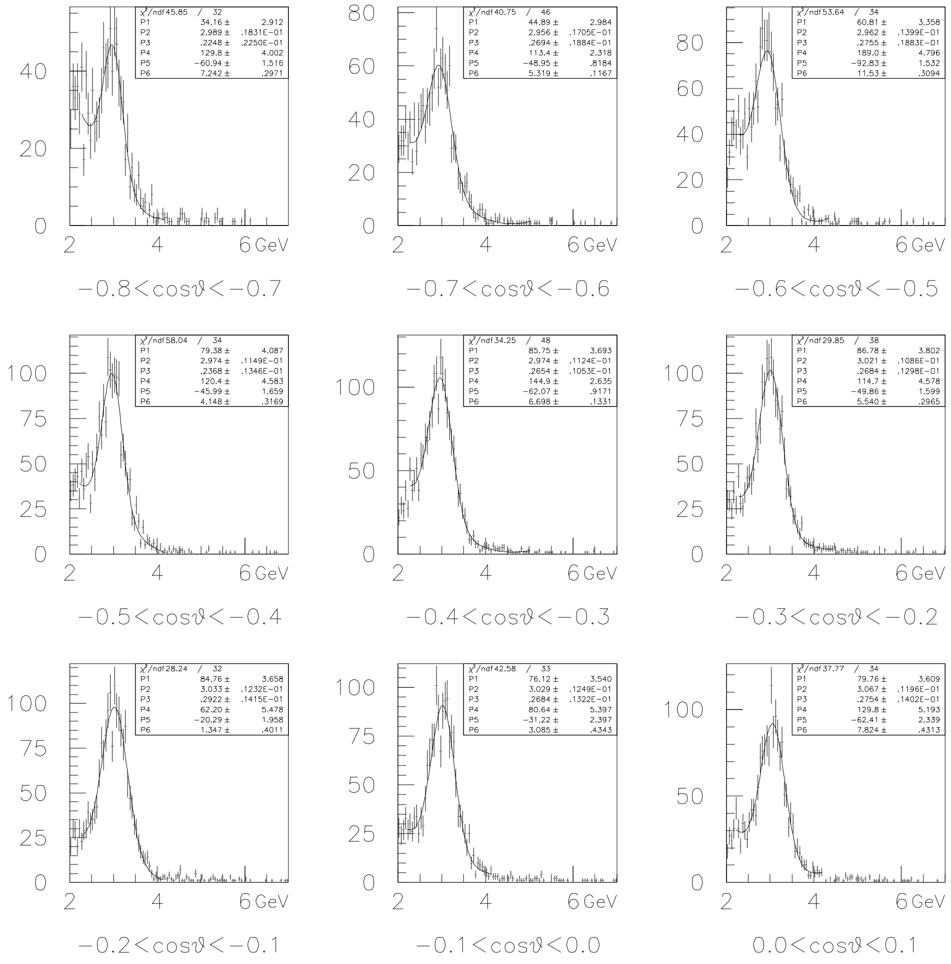

$-0.8<\cos\vartheta<-0.7$ $-0.7<\cos\vartheta<-0.6$ $-0.6<\cos\vartheta<-0.5$

$-0.5<\cos\vartheta<-0.4$ $-0.4<\cos\vartheta<-0.3$ $-0.3<\cos\vartheta<-0.2$

$-0.2<\cos\vartheta<-0.1$ $-0.1<\cos\vartheta<0.0$ $0.0<\cos\vartheta<0.1$

Figure B.74: Fitting of the mass spectrum: $2 < p_t < 3$ and $0.65 < x_F < 0.75$. The backgrounds were fitted to second-order polynomials, and the J/ψ's were fitted to Gaussians. The $\cos\theta$ ranges are indicated under each spectrum. The current of SM12 magnet was 2800 Ampere.

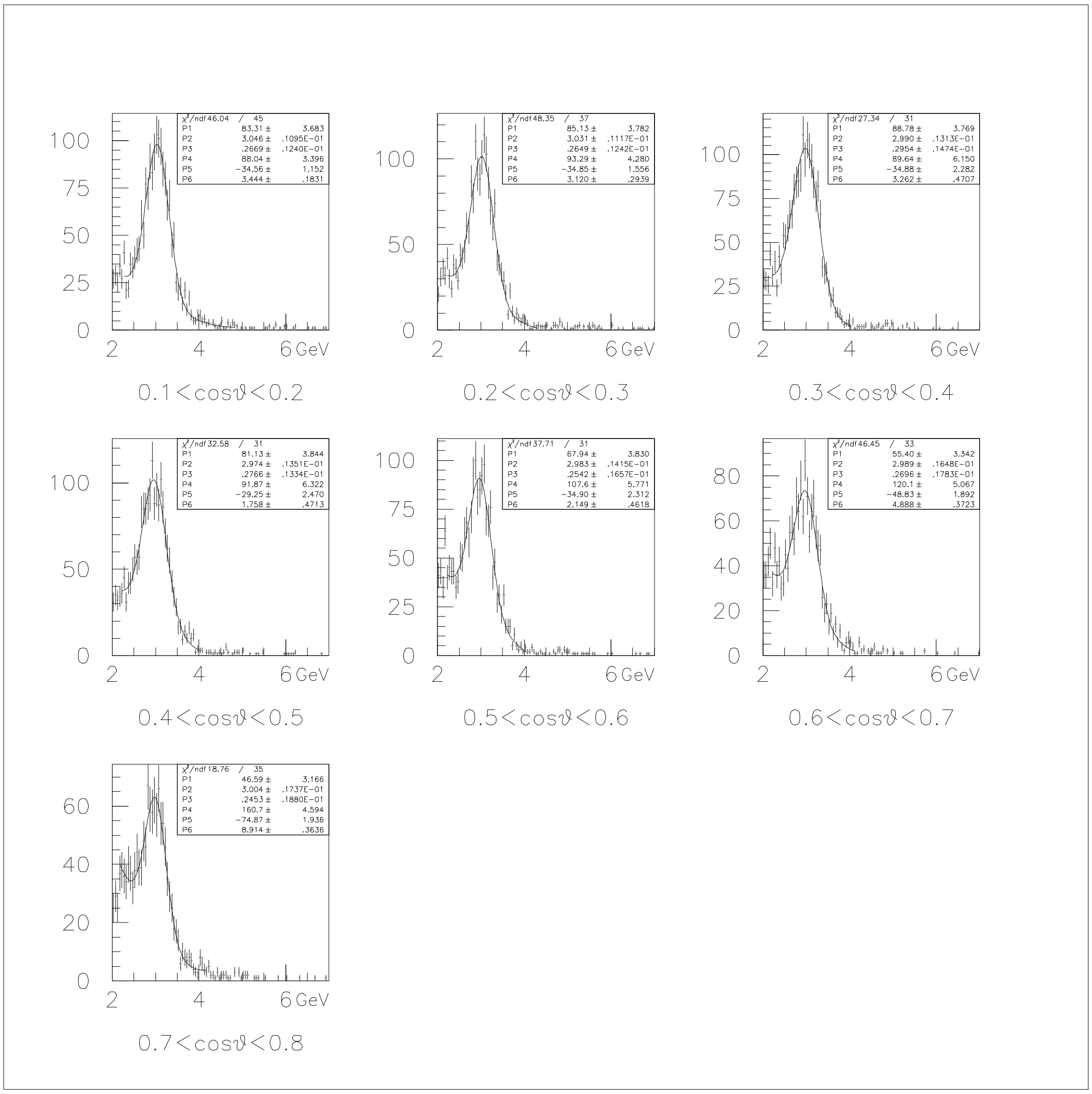

$0.1 < \cos\vartheta < 0.2$

$0.2 < \cos\vartheta < 0.3$

$0.3 < \cos\vartheta < 0.4$

$0.4 < \cos\vartheta < 0.5$

$0.5 < \cos\vartheta < 0.6$

$0.6 < \cos\vartheta < 0.7$

$0.7 < \cos\vartheta < 0.8$

Figure B.75: Fitting of the mass spectrum: $2 < p_t < 3$ and $0.65 < x_F < 0.75$. The backgrounds were fitted to second-order polynomials, and the J/ψ's were fitted to Gaussians. The $\cos\theta$ ranges are indicated under each spectrum. The current of SM12 magnet was 2800 Ampere.

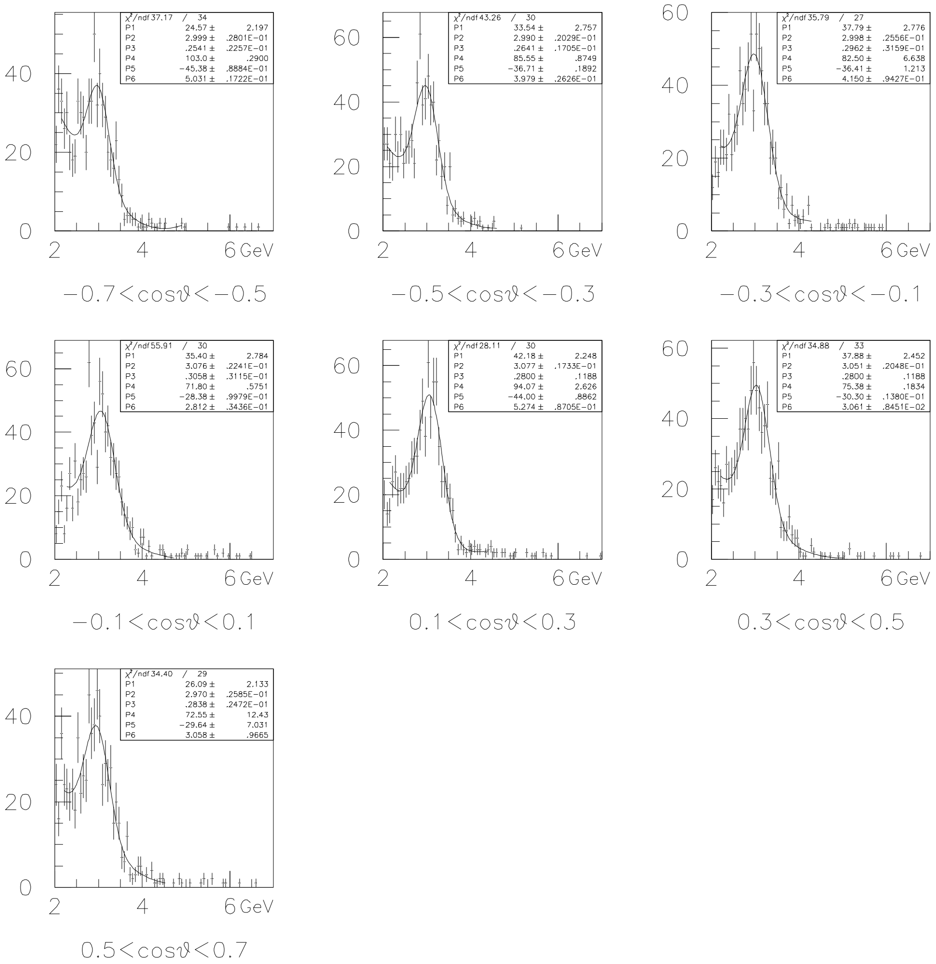

Figure B.76: Fitting of the mass spectrum: $2 < p_t < 3$ and $0.75 < x_F < 0.85$. The backgrounds were fitted to second-order polynomials, and the J/ψ's were fitted to Gaussians. The $\cos\theta$ ranges are indicated under each spectrum. The current of SM12 magnet was 2800 Ampere.

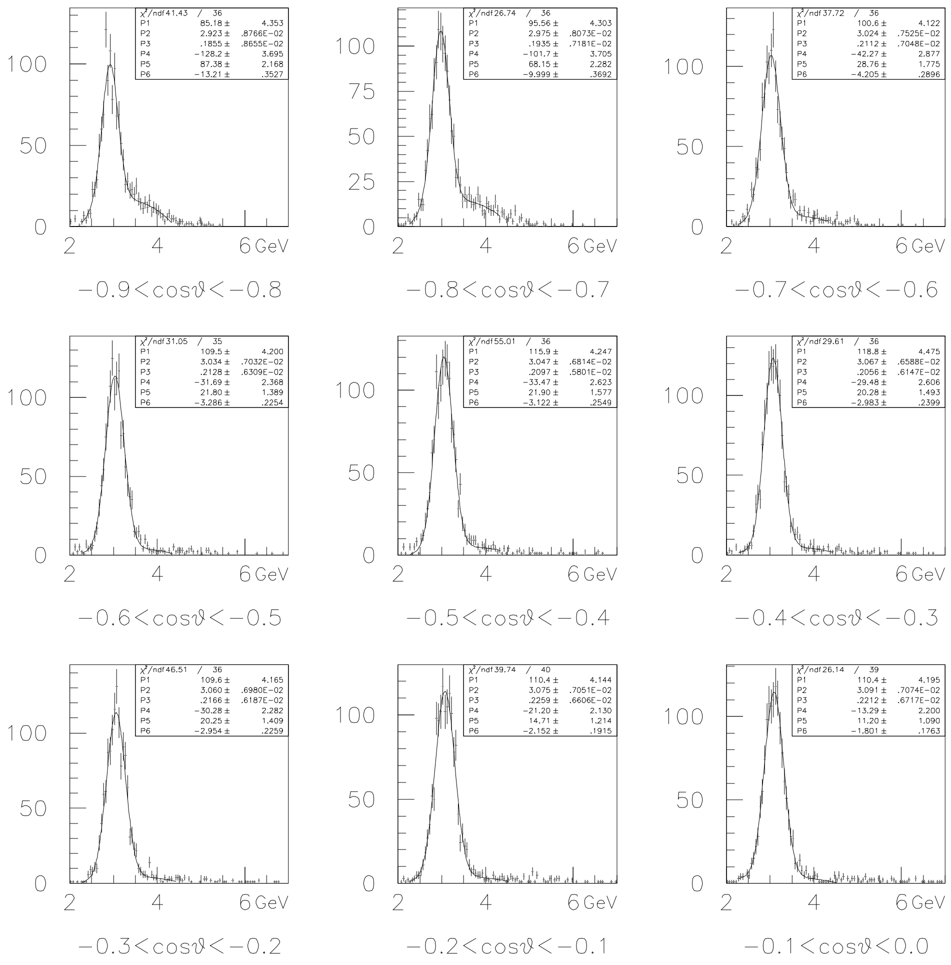

Figure B.77: Fitting of the mass spectrum: $3 < p_t$ and $0.25 < x_F < 0.35$. The backgrounds were fitted to second-order polynomials, and the J/ψ's were fitted to Gaussians. The $\cos\theta$ ranges are indicated under each spectrum. The current of SM12 magnet was 2800 Ampere.

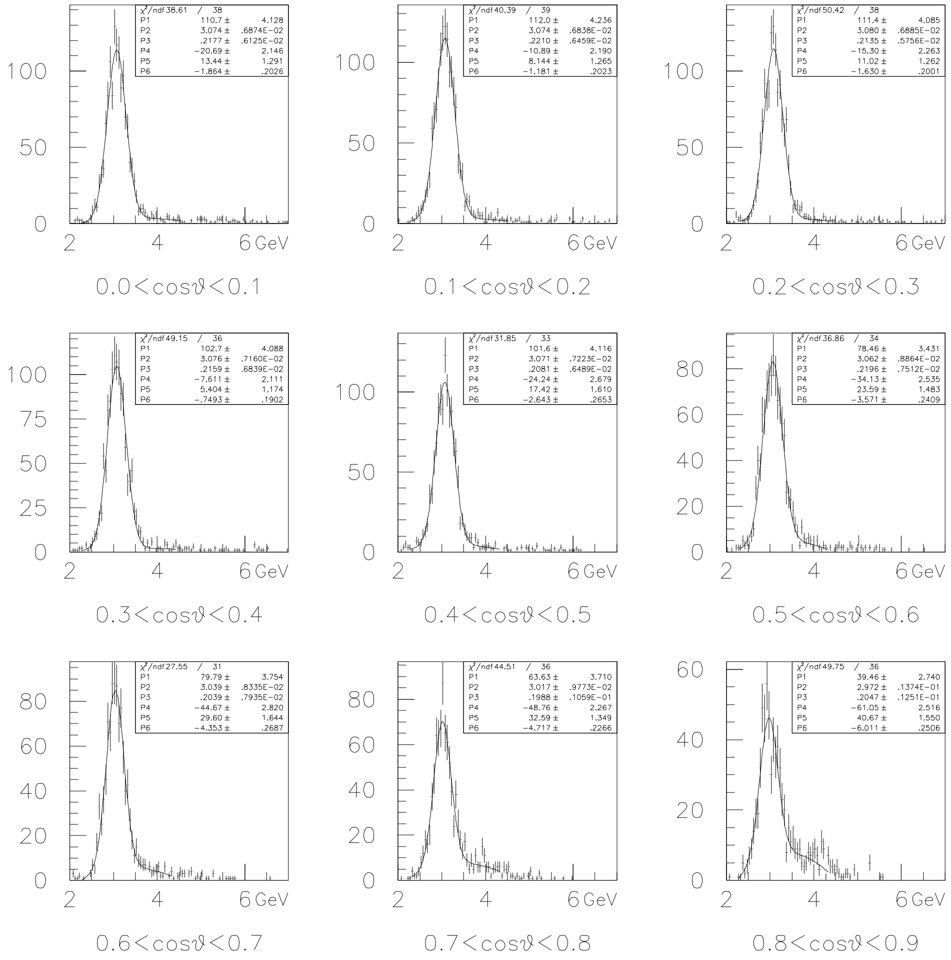

Figure B.78: Fitting of the mass spectrum: $3 < p_t$ and $0.25 < x_F < 0.35$. The backgrounds were fitted to second-order polynomials, and the J/ψ's were fitted to Gaussians. The $\cos\theta$ ranges are indicated under each spectrum. The current of SM12 magnet was 2800 Ampere.

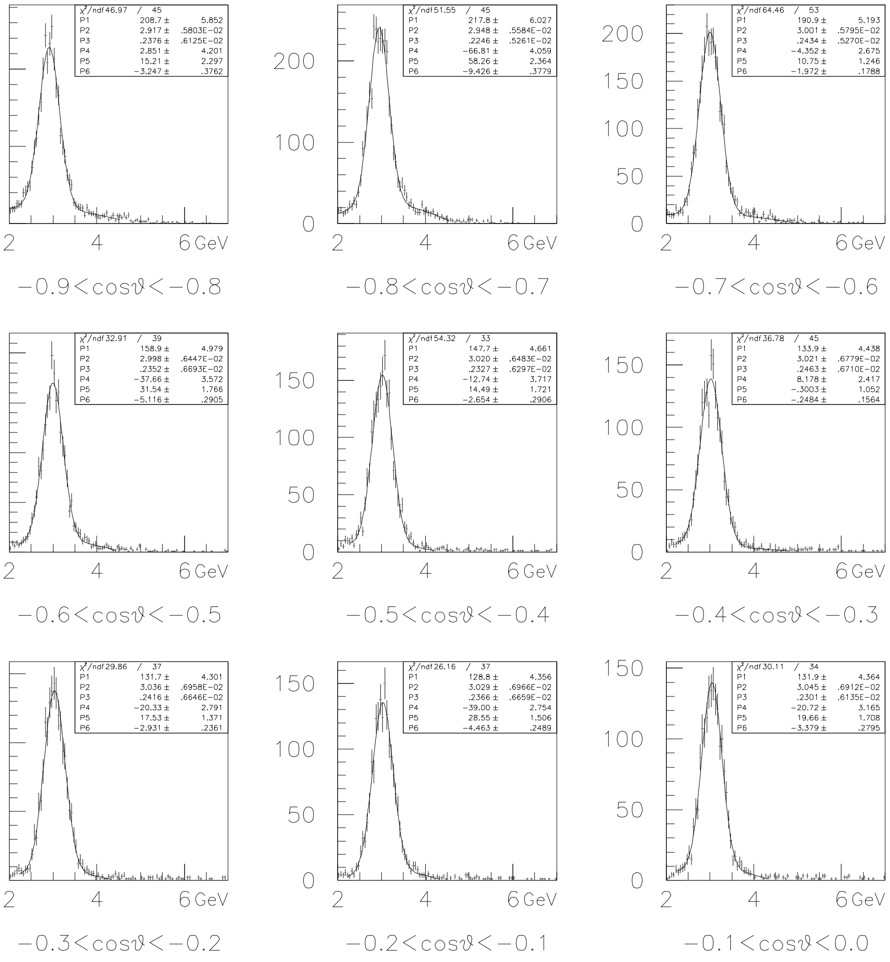

Figure B.79: Fitting of the mass spectrum: $3 < p_t$ and $0.35 < x_F < 0.45$. The backgrounds were fitted to second-order polynomials, and the J/ψ's were fitted to Gaussians. The $\cos\theta$ ranges are indicated under each spectrum. The current of SM12 magnet was 2800 Ampere.

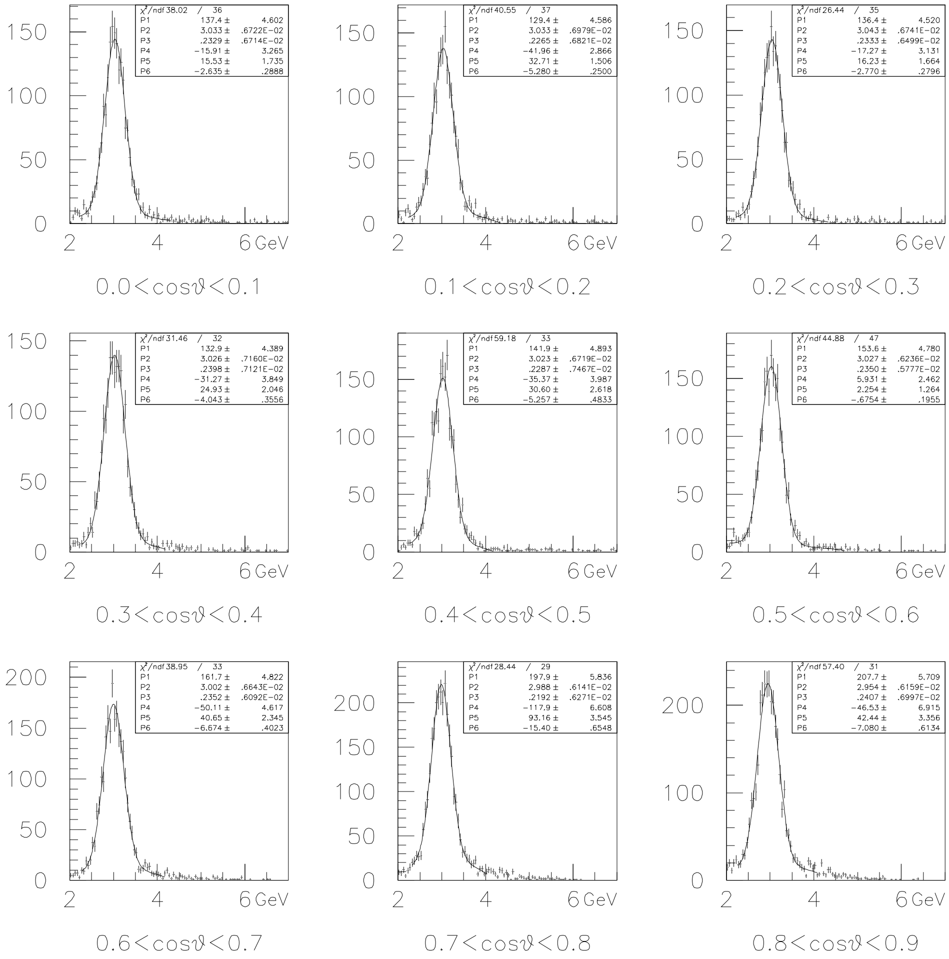

Figure B.80: Fitting of the mass spectrum: $3 < p_t$ and $0.35 < x_F < 0.45$. The backgrounds were fitted to second-order polynomials, and the J/ψ's were fitted to Gaussians. The $\cos\theta$ ranges are indicated under each spectrum. The current of SM12 magnet was 2800 Ampere.

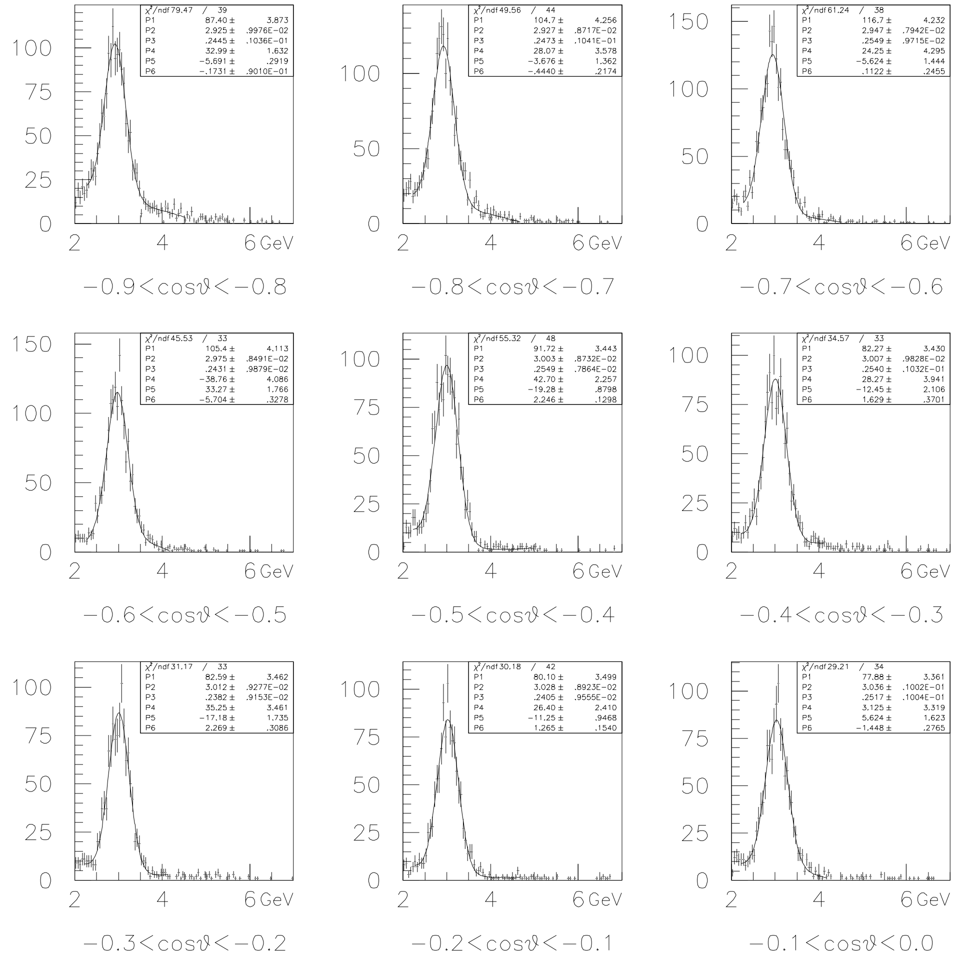

Figure B.81: Fitting of the mass spectrum: $3 < p_t$ and $0.45 < x_F < 0.55$. The backgrounds were fitted to second-order polynomials, and the J/ψ's were fitted to Gaussians. The $\cos\theta$ ranges are indicated under each spectrum. The current of SM12 magnet was 2800 Ampere.

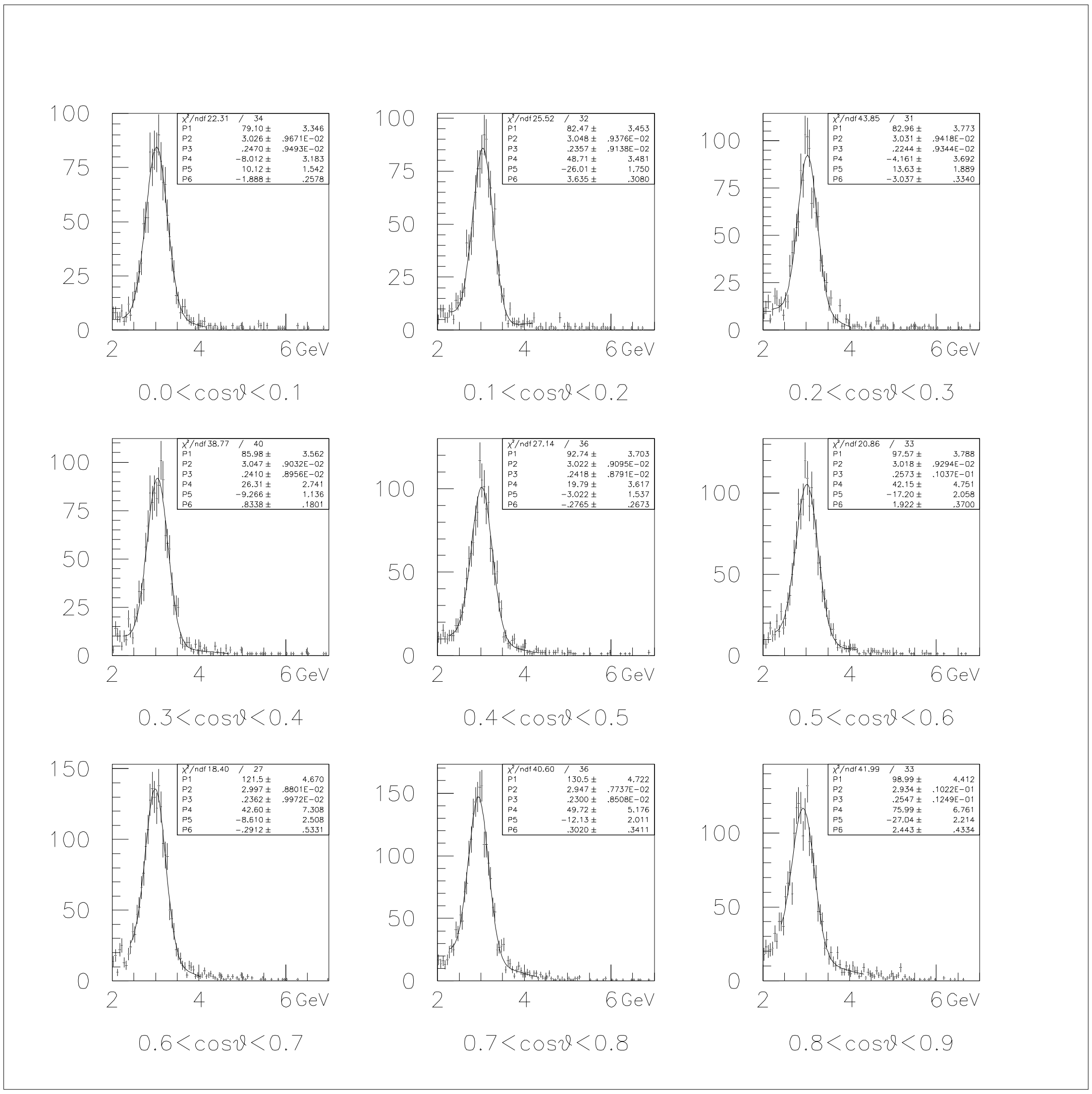

Figure B.82: Fitting of the mass spectrum: $3 < p_t$ and $0.45 < x_F < 0.55$. The backgrounds were fitted to second-order polynomials, and the J/ψ's were fitted to Gaussians. The $\cos\theta$ ranges are indicated under each spectrum. The current of SM12 magnet was 2800 Ampere.

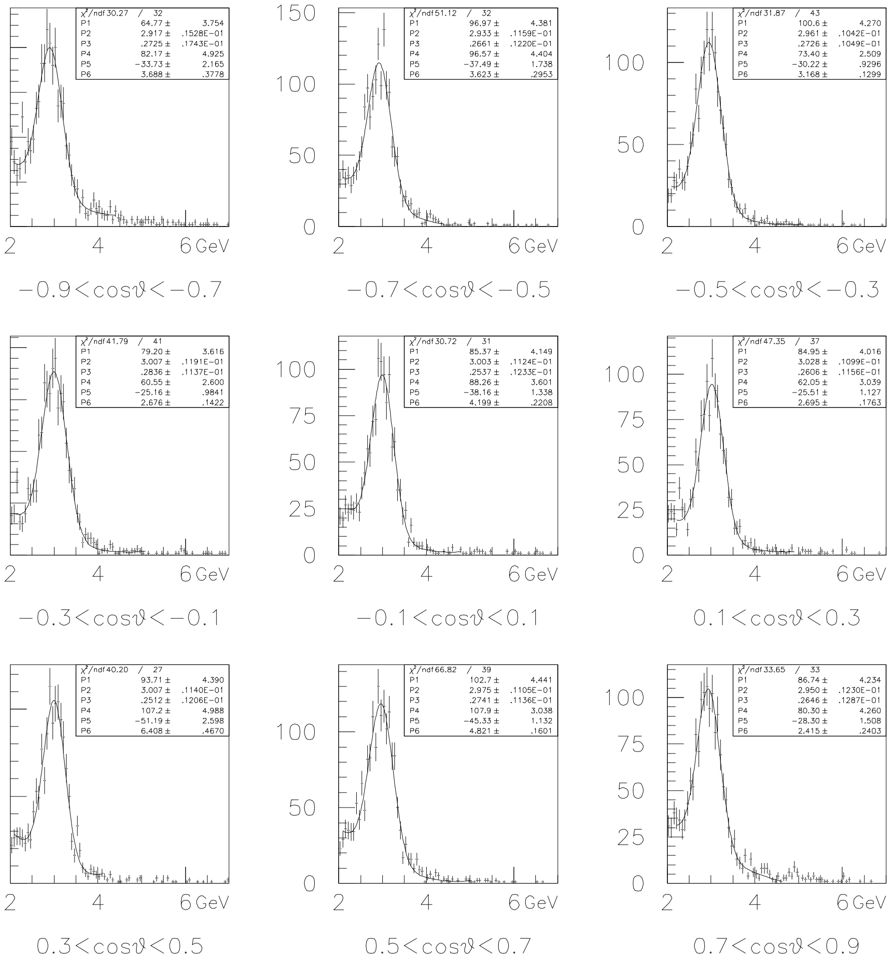

$-0.9<\cos\vartheta<-0.7$ $-0.7<\cos\vartheta<-0.5$ $-0.5<\cos\vartheta<-0.3$

$-0.3<\cos\vartheta<-0.1$ $-0.1<\cos\vartheta<0.1$ $0.1<\cos\vartheta<0.3$

$0.3<\cos\vartheta<0.5$ $0.5<\cos\vartheta<0.7$ $0.7<\cos\vartheta<0.9$

Figure B.83: Fitting of the mass spectrum: $3 < p_t$ and $0.55 < x_F < 0.65$. The backgrounds were fitted to second-order polynomials, and the J/ψ's were fitted to Gaussians. The $\cos\theta$ ranges are indicated under each spectrum. The current of SM12 magnet was 2800 Ampere.

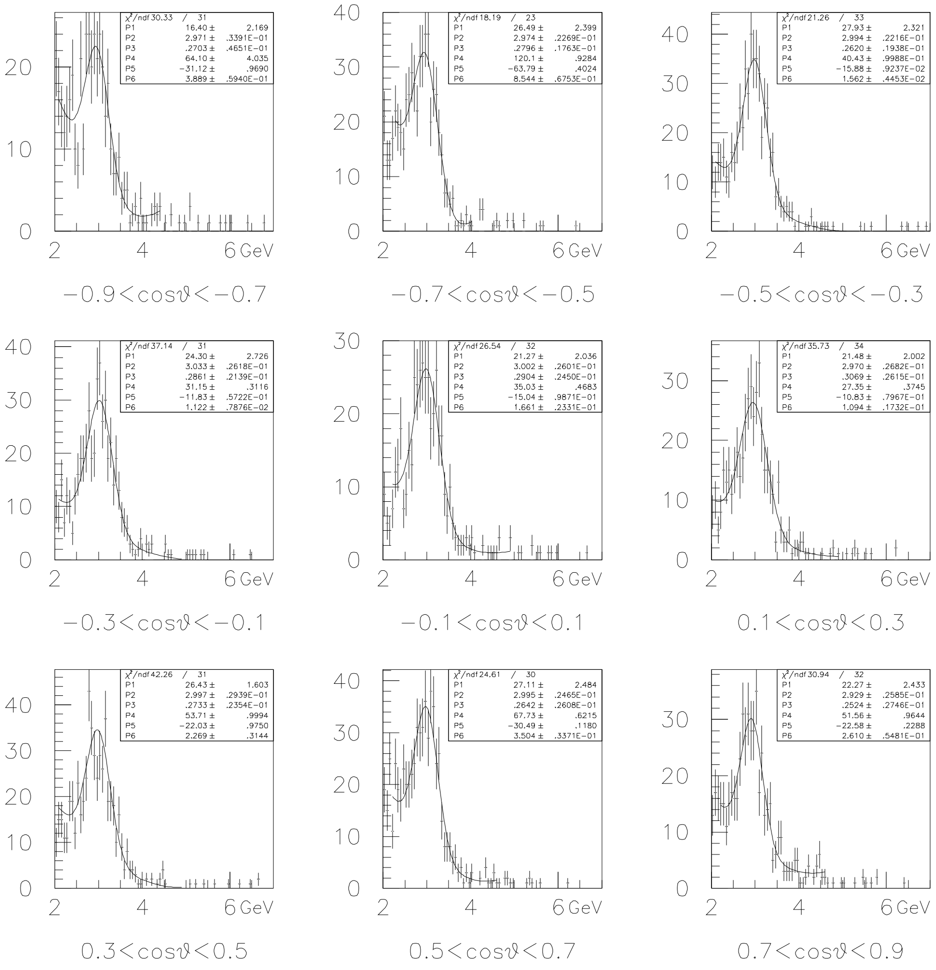

$-0.9 < \cos\vartheta < -0.7$

$-0.7 < \cos\vartheta < -0.5$

$-0.5 < \cos\vartheta < -0.3$

$-0.3 < \cos\vartheta < -0.1$

$-0.1 < \cos\vartheta < 0.1$

$0.1 < \cos\vartheta < 0.3$

$0.3 < \cos\vartheta < 0.5$

$0.5 < \cos\vartheta < 0.7$

$0.7 < \cos\vartheta < 0.9$

Figure B.84: Fitting of the mass spectrum: $3 < p_t$ and $0.65 < x_F < 0.75$. The backgrounds were fitted to second-order polynomials, and the J/ψ's were fitted to Gaussians. The $\cos\theta$ ranges are indicated under each spectrum. The current of SM12 magnet was 2800 Ampere.

C. Fitting the λ's

After the counts of the J/ψ peaks for each bin of $\cos\theta$, x_F, and p_T, were determined, the number of counts was plotted versus $\cos\theta$. This gave us the accepted $\cos\theta$ distributions for J/ψ in bins of x_F and p_T. Then those accepted $\cos\theta$ distributions were divided by the acceptance curves shown in Appendix A to obtain the true distributions. The corrected $\cos\theta$ distributions were then fitted to $1+\lambda\cos^2\theta$ times an arbitrary normalization constant. Those distributions and the fits are presented in this appendix. In Figures C1 to C6 are the curves for the "SM12=2040" data set, and from Figures C7 to C12 are the curves for the "SM12=2800" data set.

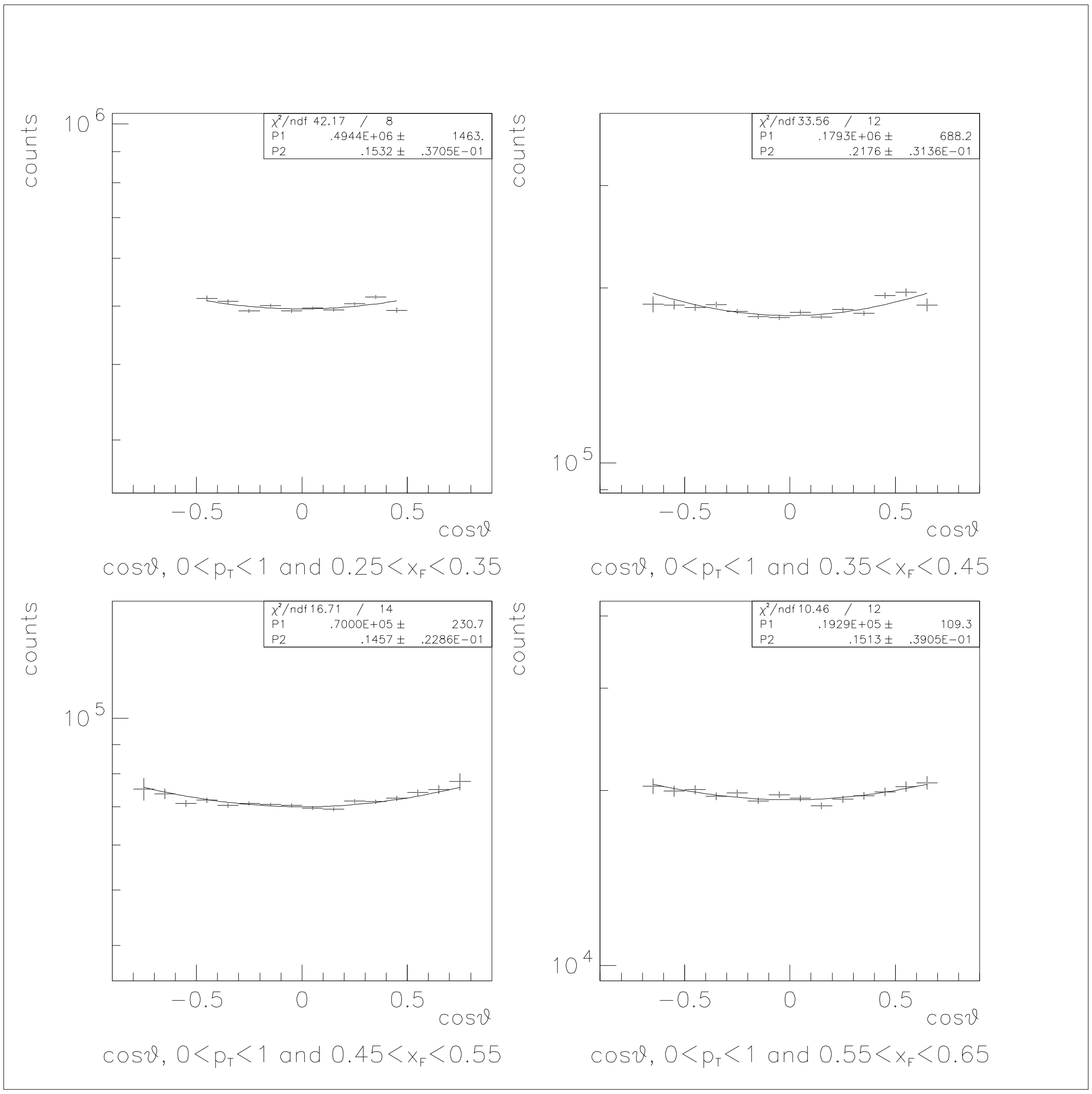

Figure C.1: The corrected $\cos\theta$ distributions and the polarization parameter λ. Upper left: $0 < p_T < 1$ and $0.25 < x_F < 0.35$. Upper right: $0 < p_T < 1$ and $0.35 < x_F < 0.45$. Lower left: $0 < p_T < 1$ and $0.45 < x_F < 0.55$. Lower right: $0 < p_T < 1$ and $0.55 < x_F < 0.65$. SM12=2040.

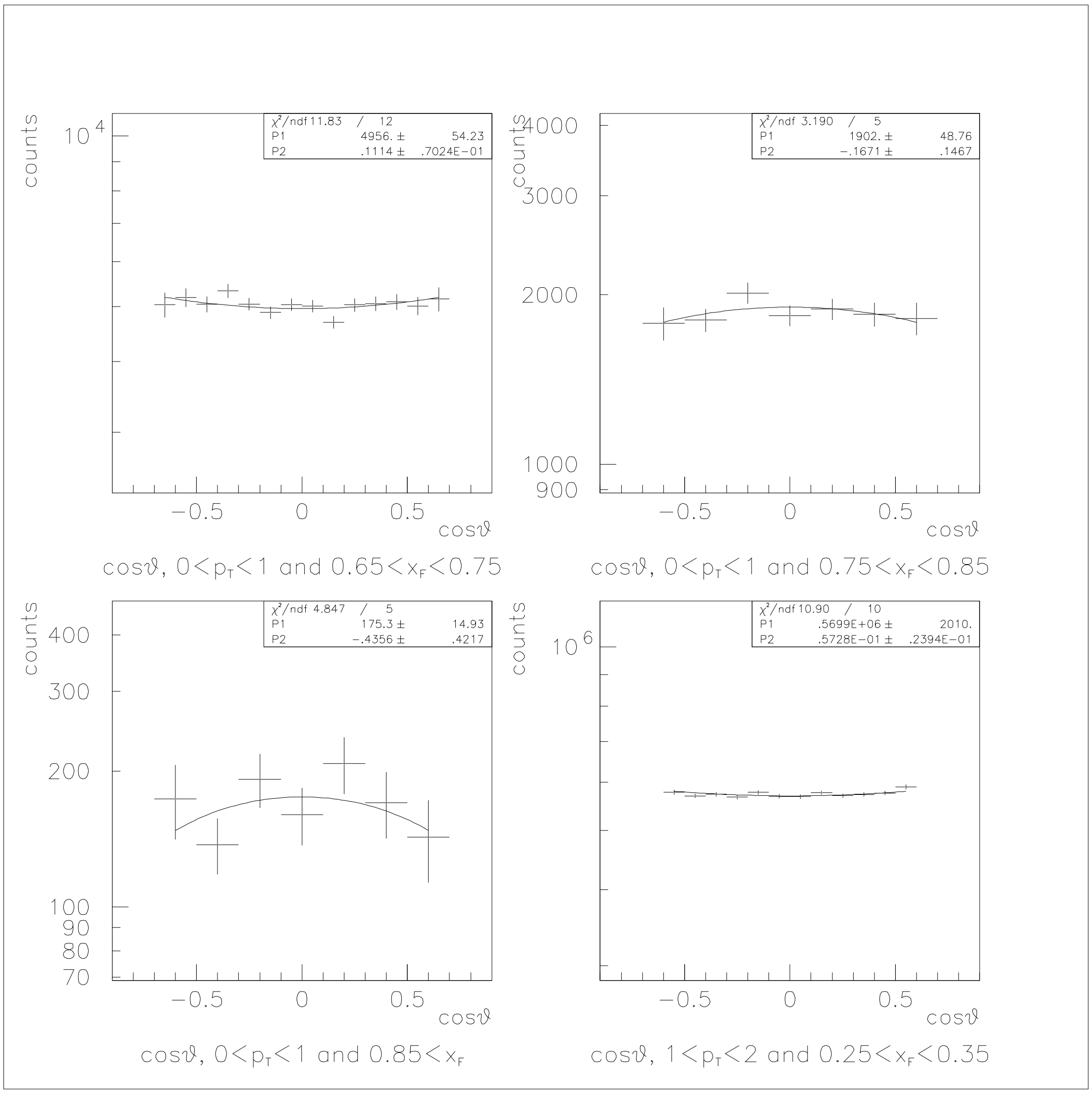

cosϑ, $0<p_T<1$ and $0.65<x_F<0.75$ cosϑ, $0<p_T<1$ and $0.75<x_F<0.85$

cosϑ, $0<p_T<1$ and $0.85<x_F$ cosϑ, $1<p_T<2$ and $0.25<x_F<0.35$

Figure C.2: The corrected $\cos\theta$ distributions and the polarization parameter λ. Upper left: $0 < p_T < 1$ and $0.65 < x_F < 0.75$. Upper right: $0 < p_T < 1$ and $0.75 < x_F < 0.85$. Lower left: $0 < p_T < 1$ and $0.85 < x_F$. Lower right: $1 < p_T < 2$ and $0.25 < x_F < 0.35$. SM12=2040.

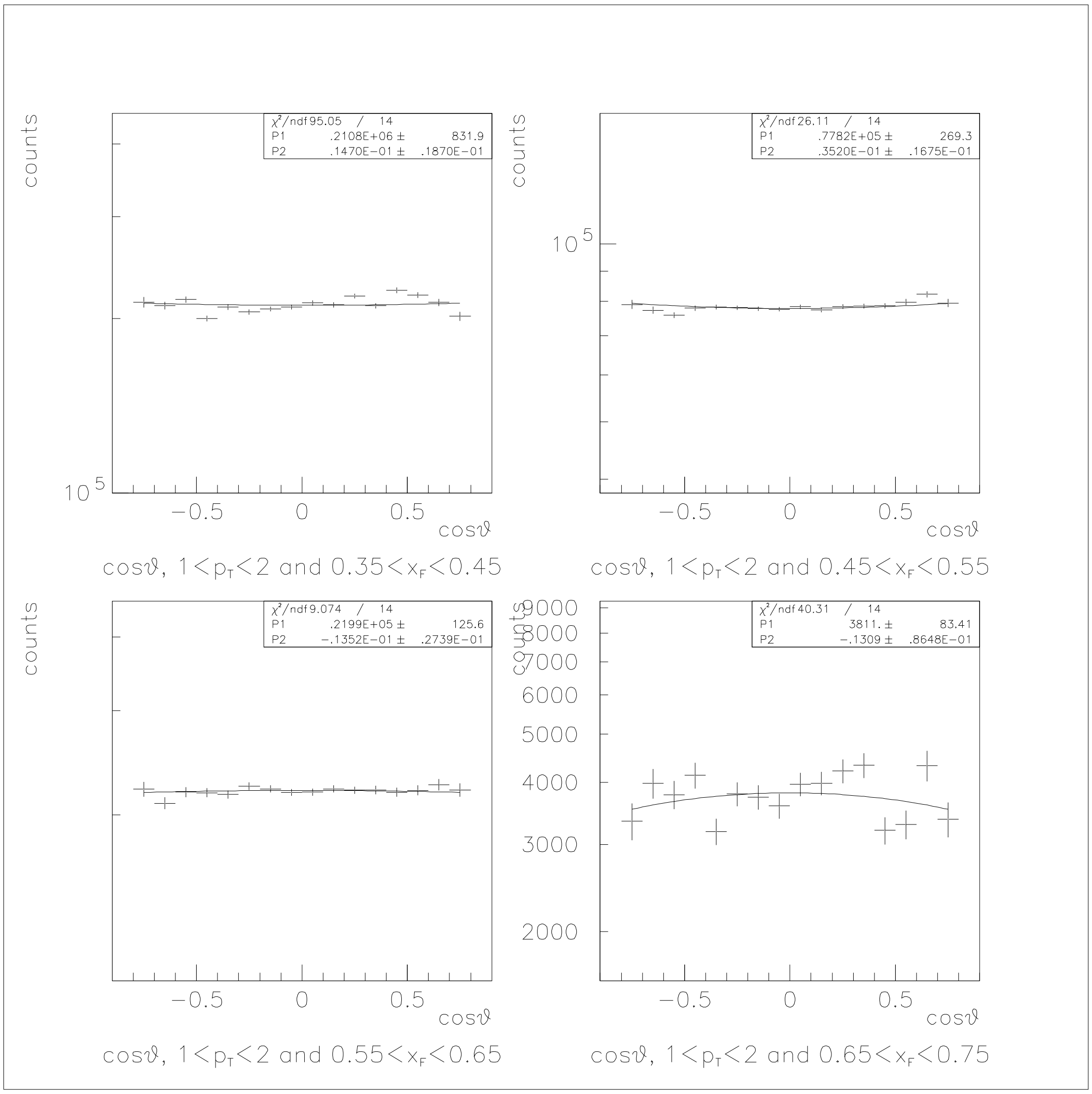

Figure C.3: The corrected $\cos\theta$ distributions and the polarization parameter λ. Upper left: $1 < p_T < 2$ and $0.35 < x_F < 0.45$. Upper right: $1 < p_T < 2$ and $0.45 < x_F < 0.55$. Lower left: $1 < p_T < 2$ and $0.55 < x_F < 0.65$. Lower right: $1 < p_T < 2$ and $0.65 < x_F < 0.75$. SM12=2040.

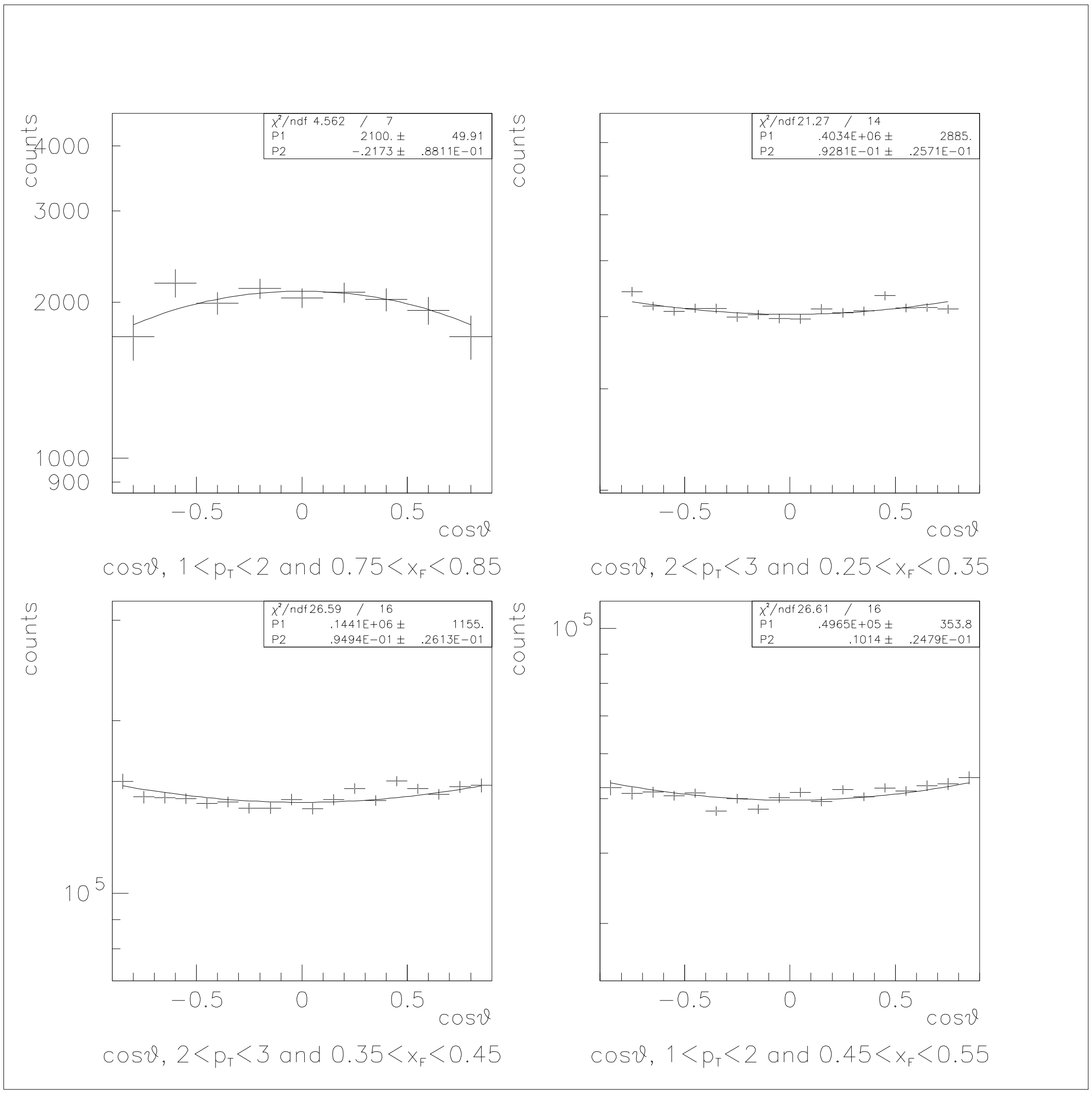

Figure C.4: The corrected $\cos\theta$ distributions and the polarization parameter λ. Upper left: $1 < p_T < 2$ and $0.75 < x_F < 0.85$. Upper right: $2 < p_T < 3$ and $0.25 < x_F < 0.35$. Lower left: $2 < p_T < 3$ and $0.35 < x_F < 0.45$. Lower right: $2 < p_T < 3$ and $0.45 < x_F < 0.55$. SM12=2040.

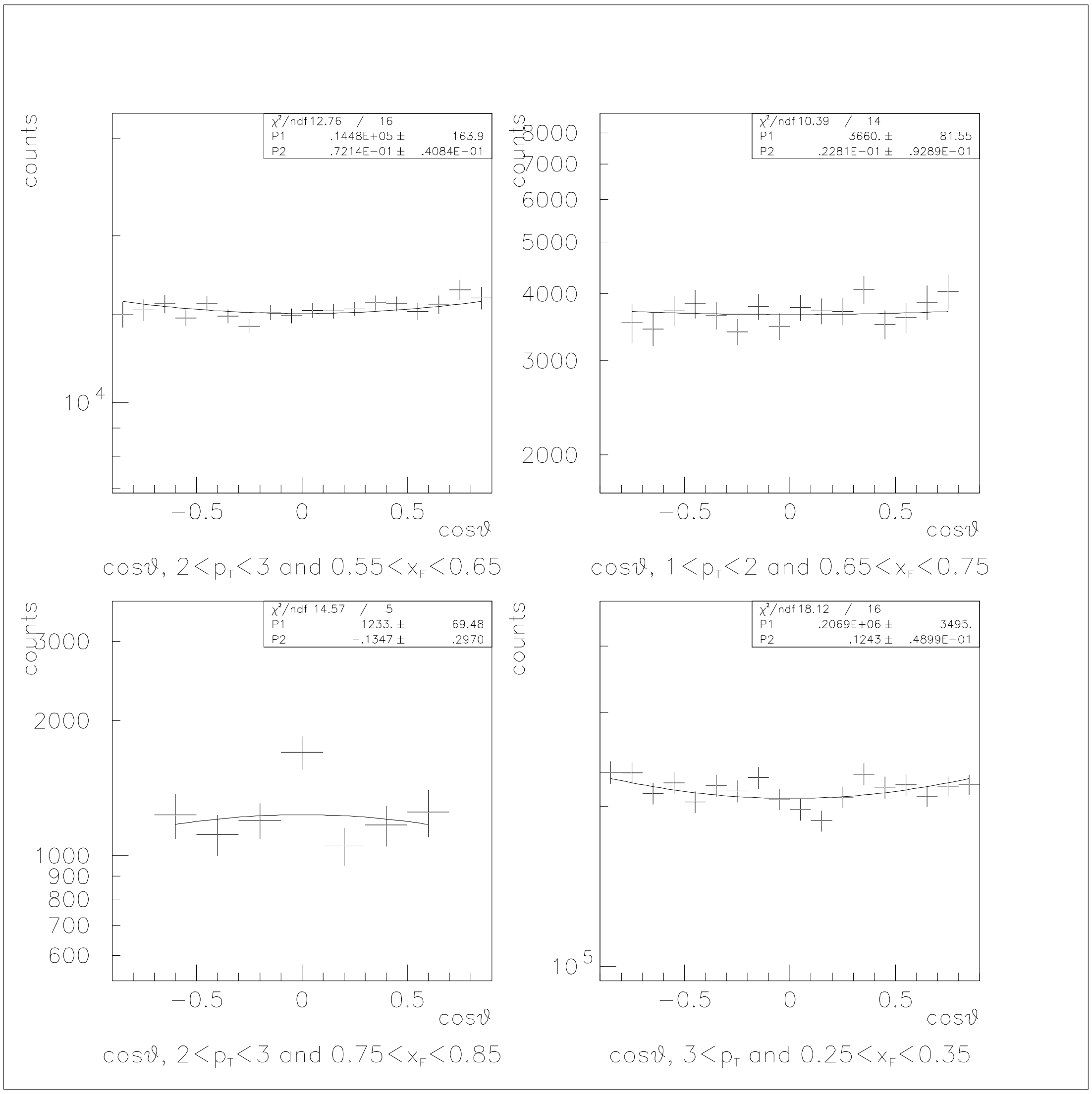

cosϑ, $2<p_T<3$ and $0.55<x_F<0.65$

cosϑ, $1<p_T<2$ and $0.65<x_F<0.75$

cosϑ, $2<p_T<3$ and $0.75<x_F<0.85$

cosϑ, $3<p_T$ and $0.25<x_F<0.35$

Figure C.5: The corrected $\cos\theta$ distributions and the polarization parameter λ. Upper left: $2 < p_T < 3$ and $0.55 < x_F < 0.65$. Upper right: $2 < p_T < 3$ and $0.65 < x_F < 0.75$. Lower left: $2 < p_T < 3$ and $0.75 < x_F < 0.85$. Lower right: $3 < p_T$ and $0.25 < x_F < 0.35$. SM12=2040.

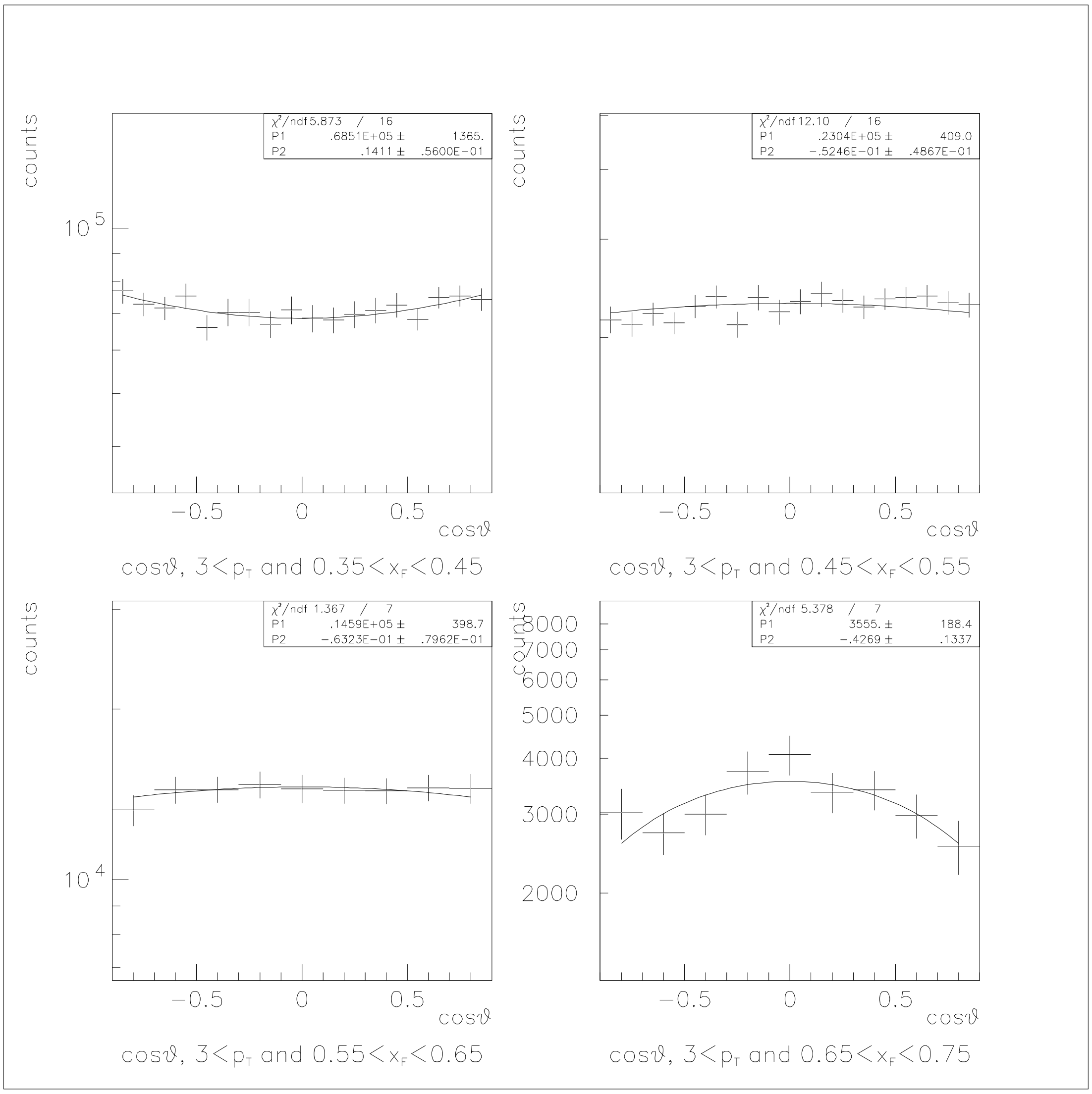

Figure C.6: The corrected $\cos\theta$ distributions and the polarization parameter λ. Upper left: $3 < p_T$ and $0.35 < x_F < 0.45$. Upper right: $3 < p_T$ and $0.45 < x_F < 0.55$. Lower left: $3 < p_T$ and $0.55 < x_F < 0.65$. Lower right: $3 < p_T$ and $0.65 < x_F < 0.75$. SM12=2040.

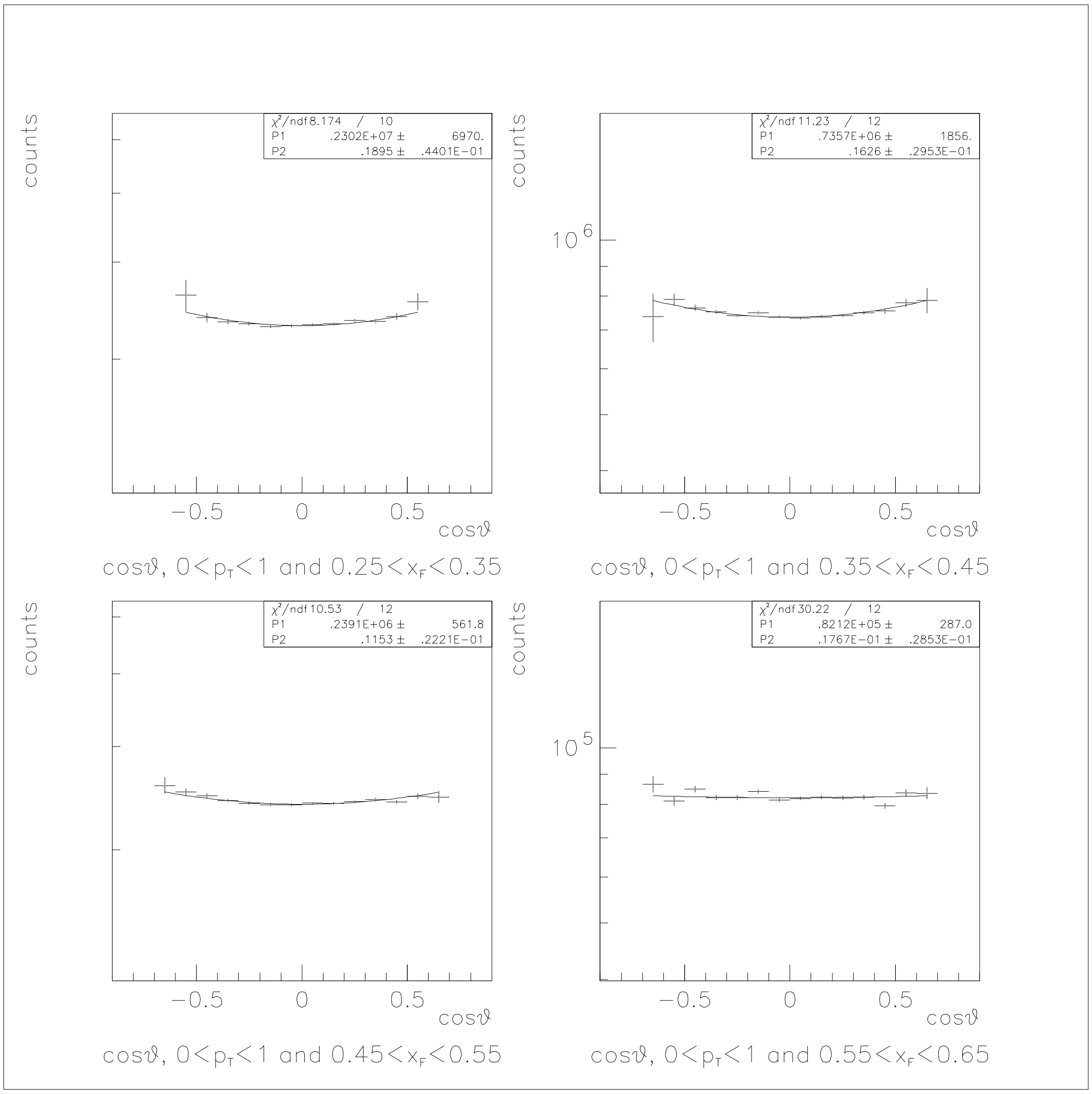

Figure C.7: The corrected $\cos\theta$ distributions and the polarization parameter λ. Upper left: $0 < p_T < 1$ and $0.25 < x_F < 0.35$. Upper right: $0 < p_T < 1$ and $0.35 < x_F < 0.45$. Lower left: $0 < p_T < 1$ and $0.45 < x_F < 0.55$. Lower right: $0 < p_T < 1$ and $0.55 < x_F < 0.65$. SM12=2800.

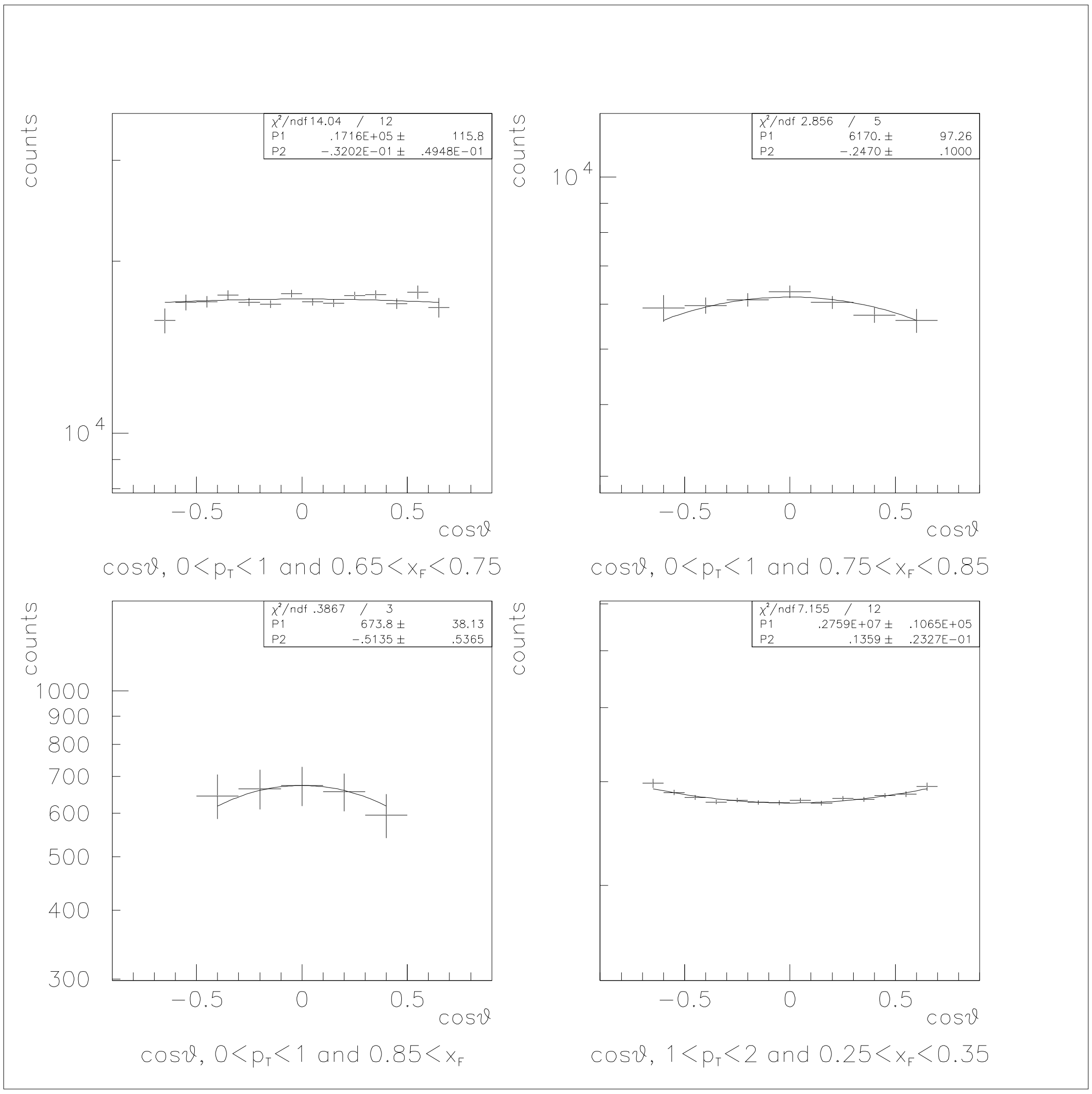

Figure C.8: The corrected $\cos\theta$ distributions and the polarization parameter λ. Upper left: $0 < p_T < 1$ and $0.65 < x_F < 0.75$. Upper right: $0 < p_T < 1$ and $0.75 < x_F < 0.85$. Lower left: $0 < p_T < 1$ and $0.85 < x_F$. Lower right: $1 < p_T < 2$ and $0.25 < x_F < 0.35$. SM12=2800.

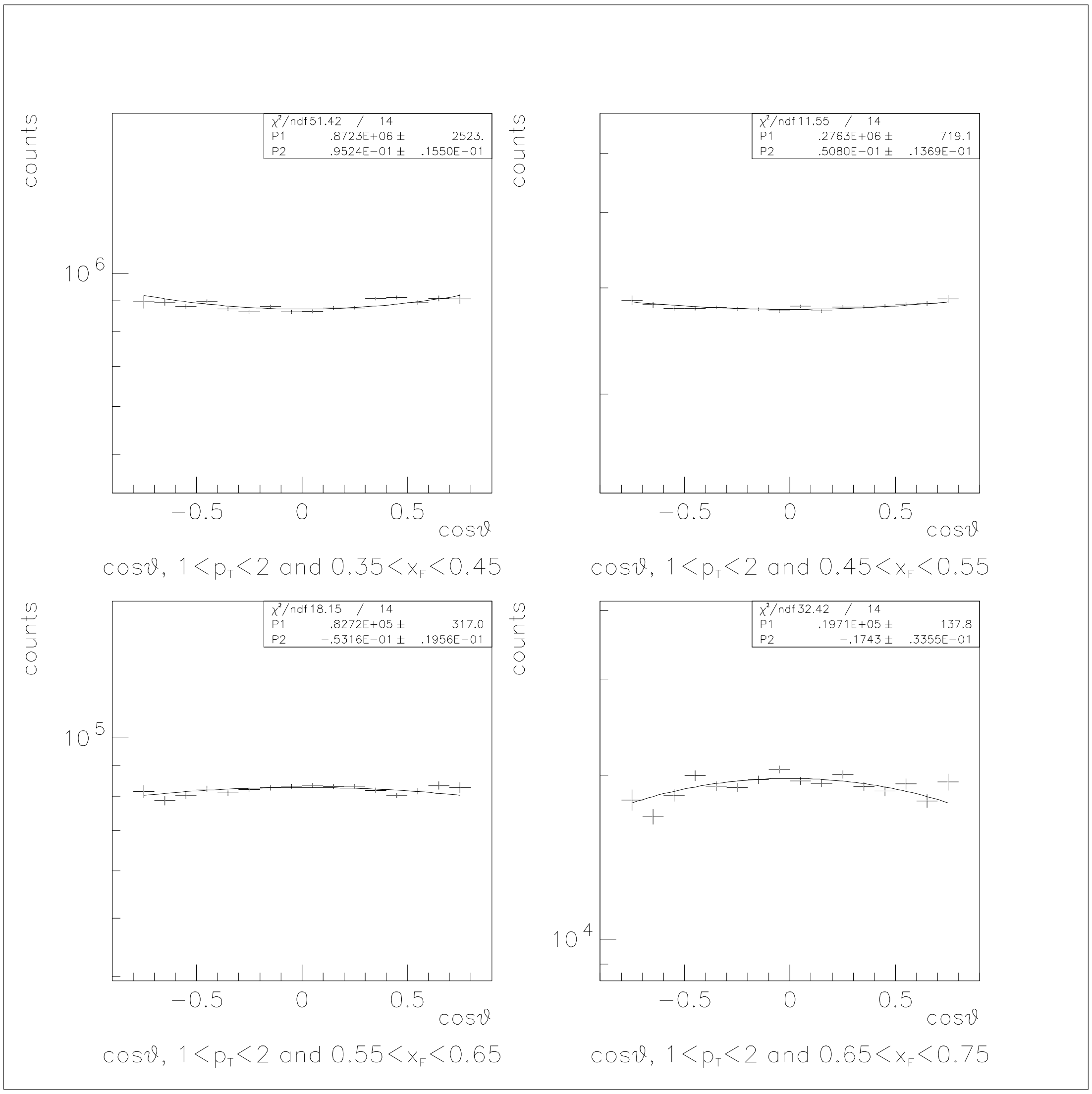

Figure C.9: The corrected $\cos\theta$ distributions and the polarization parameter λ. Upper left: $1 < p_T < 2$ and $0.35 < x_F < 0.45$. Upper right: $1 < p_T < 2$ and $0.45 < x_F < 0.55$. Lower left: $1 < p_T < 2$ and $0.55 < x_F < 0.65$. Lower right: $1 < p_T < 2$ and $0.65 < x_F < 0.75$. SM12=2800.

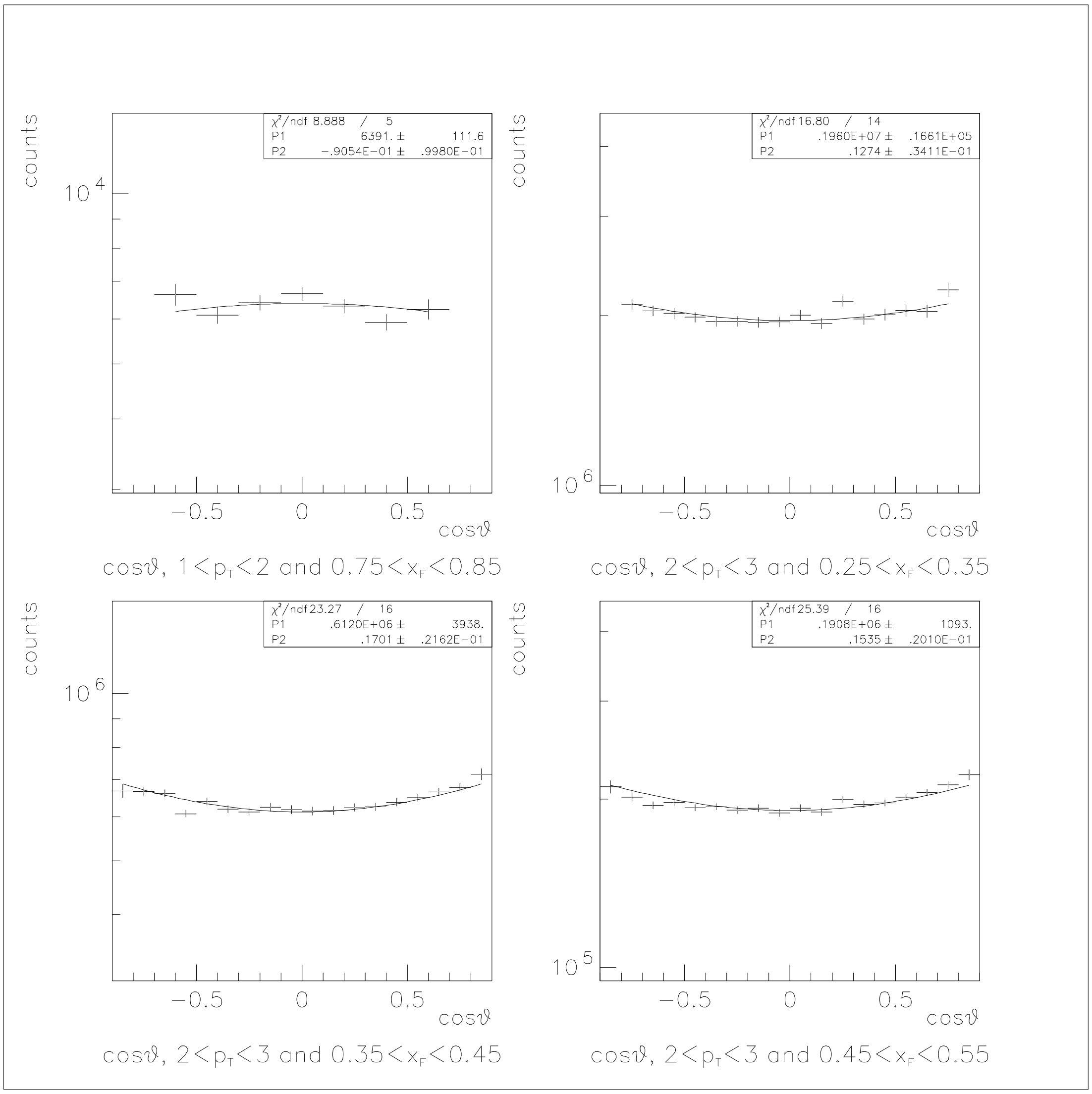

cosϑ, $1<p_T<2$ and $0.75<x_F<0.85$ cosϑ, $2<p_T<3$ and $0.25<x_F<0.35$

cosϑ, $2<p_T<3$ and $0.35<x_F<0.45$ cosϑ, $2<p_T<3$ and $0.45<x_F<0.55$

Figure C.10: The corrected $\cos\theta$ distributions and the polarization parameter λ. Upper left: $1 < p_T < 2$ and $0.75 < x_F < 0.85$. Upper right: $2 < p_T < 3$ and $0.25 < x_F < 0.35$. Lower left: $2 < p_T < 3$ and $0.35 < x_F < 0.45$. Lower right: $2 < p_T < 3$ and $0.45 < x_F < 0.55$. SM12=2800.

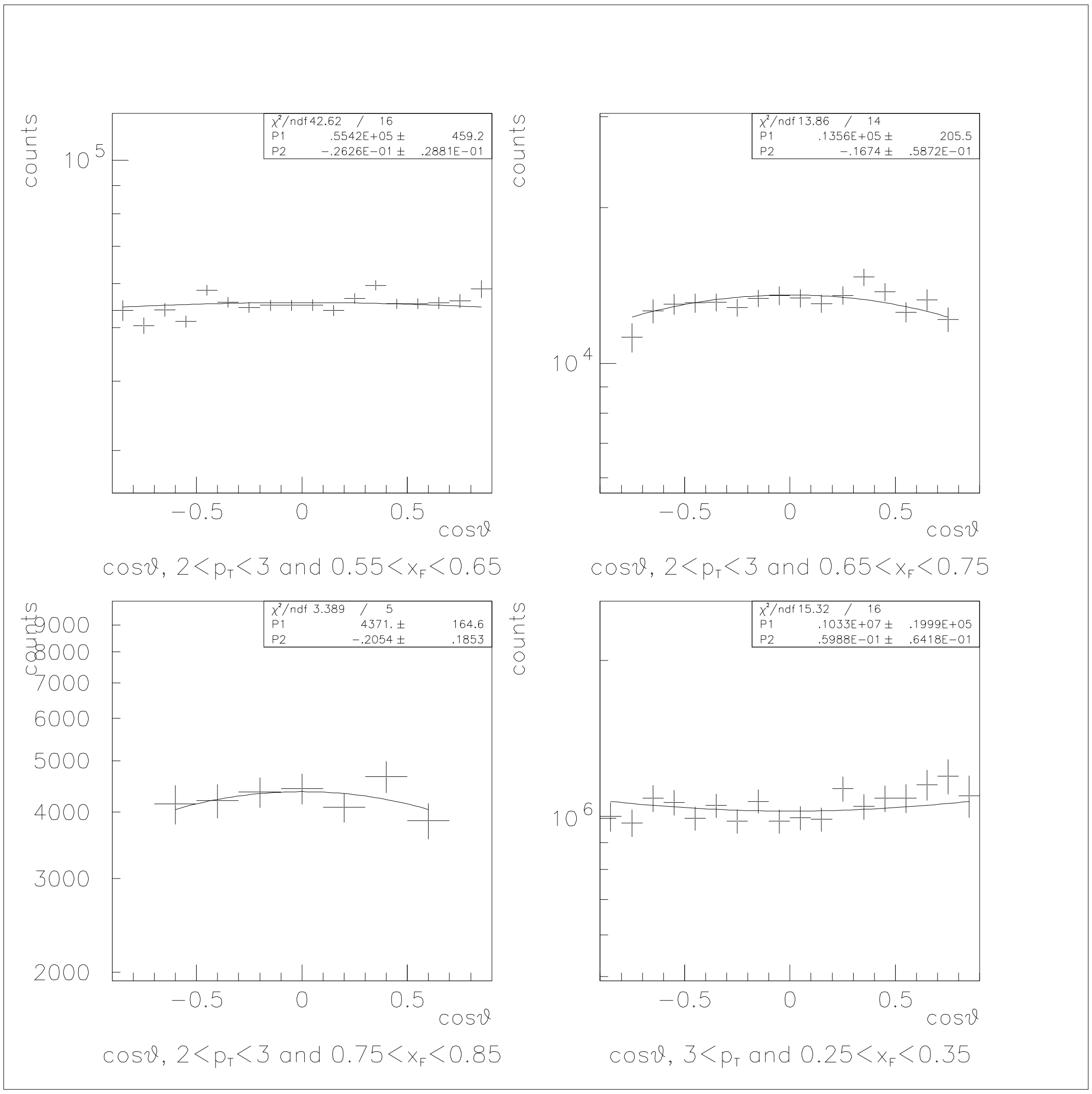

cosϑ, $2<p_T<3$ and $0.55<x_F<0.65$

cosϑ, $2<p_T<3$ and $0.65<x_F<0.75$

cosϑ, $2<p_T<3$ and $0.75<x_F<0.85$

cosϑ, $3<p_T$ and $0.25<x_F<0.35$

Figure C.11: The corrected $\cos\theta$ distributions and the polarization parameter λ. Upper left: $2 < p_T < 3$ and $0.55 < x_F < 0.65$. Upper right: $2 < p_T < 3$ and $0.65 < x_F < 0.75$. Lower left: $2 < p_T < 3$ and $0.75 < x_F < 0.85$. Lower right: $3 < p_T$ and $0.25 < x_F < 0.35$. SM12=2800.

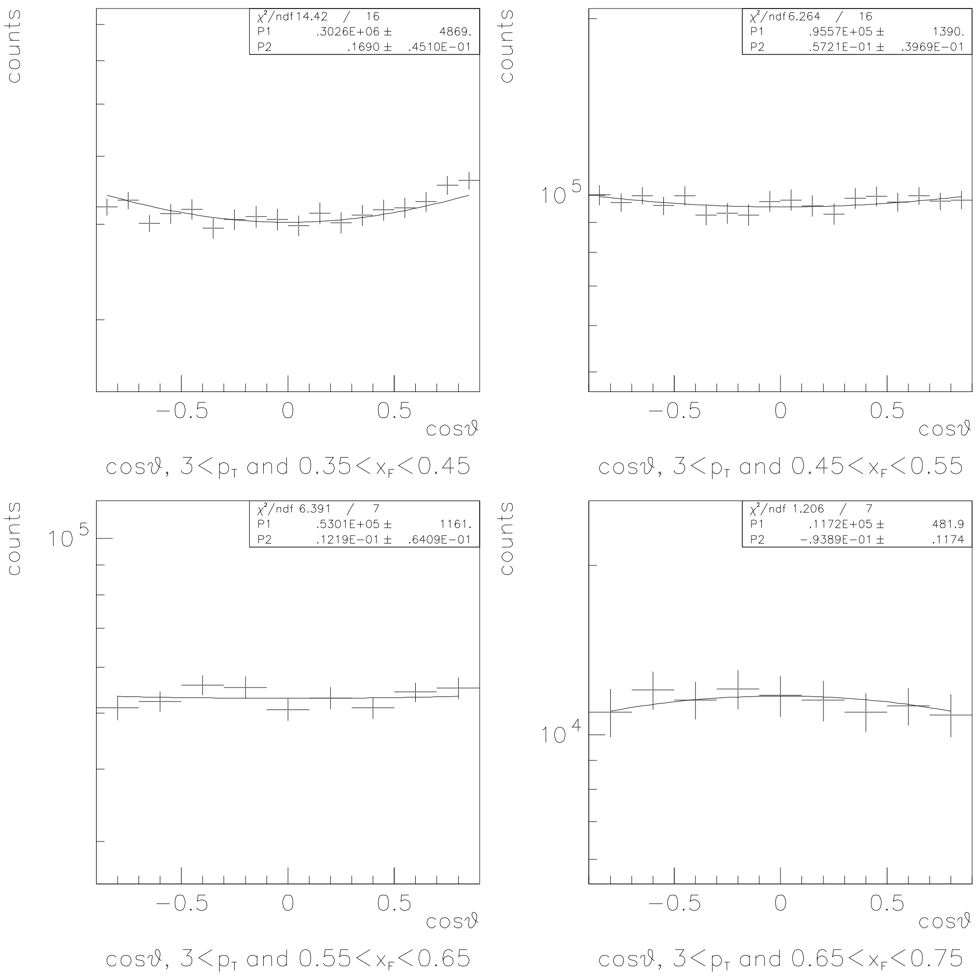

Figure C.12: The corrected $\cos\theta$ distributions and the polarization parameter λ. Upper left: $3 < p_T$ and $0.35 < x_F < 0.45$. Upper right: $3 < p_T$ and $0.45 < x_F < 0.55$. Lower left: $3 < p_T$ and $0.55 < x_F < 0.65$. Lower right: $3 < p_T$ and $0.65 < x_F < 0.75$. SM12=2800.

Bibliography

[Abe 93] F. Abe *et al.*, Phys. Rev. Lett. **70**, 1376 (1993).

[Ake 93] C. Akerlof *et al.*, Phys. Rev. **D48**, 5067(1993).

[Ale 97] T. Alexopoulos *et al.*, Phys. Rev. **D55**, 3927(1997).

[Ale 86] J.P. Alexander *et al.*, Phys. Rev. **D34**, 315(1986).

[Ali 91] J. Alitti *et al.*, Phys. Lett. **B257**, 232 (1991).

[Arn 86] G. Arnison *et al.*, Phys. Lett. **B172**, 461 (1986).

[Bar 87] R. Barate *et al.*, Z. Phys. **C33**, 505(1987).

[Ben 97] M. Beneke and M. Kramer, Phys. Rev. **D55**, 5269(1997).

[Ben 96] M. Beneke and I.Z. Rothstein, Phys. Rev. D **54**, 2005 (1996).

[Bii 87] C. Biino *et al.*, Phys. Rev. Lett. **58**, 2523(1987).

[Bnk 97] M. Beneke, Preprint hep-ph/9703429, March 1997 (Unpublished).

[Bra 96] E. Braaten, S. Fleming and T.C. Tuan, Ann. Rev. Nucl. Part. Sci. **46**, 197 (1996).

[Bra 95] E. Braaten and S. Fleming, Phys. Rev. Lett. **74**, 3327 (1995).

[Bra 94] E. Braaten, M. Doncheski, S. Fleming, and M. Mangano, Phys. Lett. **B333**, 548 (1994).

[Car 91] T.A. Carey and M.S. Kowitt, “E789 frontend DAQ system”, FNAL E789 technical note, July 1991 (unpublished).

[Cho 95] P. Cho and M.B. Wise, Phys. Lett. **B346**, 129(1995).

[Col 77] J.C. Collins and D.E. Soper, Phys. Rev. **D16**, 2219 (1977).

[Dre 70] S.D. Drell and T.M. Yan, Phys. Rev. Lett. **25**, 316 (1970).

[Fal 86] S. Falciano *et al.*, Z. Phys. **C31**, 513 (1986).

[Fri 97] S. Frixione, M.L. Mangano, P. Nason and G. Ridolfi, Preprint hep-ph/9702287, Febuary 1997 (Unpublished).

[Fri 77] H. Fritzsch, Phys. Lett. **B67**, 217(1977).

[Gag 98] C.A. Gagliardi *et al.*, Nucl. Instrum. Methods **A418**, 322(1998).

[Gee 98] D.F. Geesaman, "Angle transformation to photon rest system", E866 Memorandum, Febuary 1998 (Unpbulished).

[Gri 96] A. Gribushin *et al.*, Phys. Rev. **D53**, 4723(1996).

[Hal 77] F. Halzen, Phys. Lett. **B69**, 105(1977).

[Haw 98] E.A. Hawker, Ph.D. Thesis, Chapter 2, Texas A&M University, 1998.

[Hei 91] J.G. Heinrich *et al.*, Phys. Rev. **D44**, 1909(1991).

[Kap 82] D.M. Kaplan, "Introduction to the E605 readout System", E605 Memorandum, August 1982 (unpublished).

[Lam 78] C. Lam and W.-K. Tung, Phys. Rev. **D18**, 2447(1978).

[Mue 99] B. Mueller, "Pion-induced J/ψ production in E866 beam dump", E866 Memorandum, March 1999 (unpublished).

[Pic 95] A. Pich, Preprint hep-ph/9505231, May 1995 (Unpublished).

[Rij 95] P.J. Rijken and W.L. van Neerven, Phys. Rev. **D51**, 44 (1995).

[Roy 94] D.P. Roy and K. Sridhar, Phys. Lett. **B339**, 141(1994).

[Sch 94] G.A. Schuler, Preprint hep-ph/9403387, March 1994 (Unpublished).

[Van 95] M. Vanttinen, P. Hoyer, S.J. Brodsky and W.-K. Tang, Phys. Rev. **D51**, 3332 (1995).